

Sheffield Hallam University

Development of Novel Processing Routes for Electrical Ceramics and Glass-Ceramics

MUHAMMED, Khalid Rmaydh

Available from the Sheffield Hallam University Research Archive (SHURA) at:

<http://shura.shu.ac.uk/25513/>

A Sheffield Hallam University thesis

This thesis is protected by copyright which belongs to the author.

The content must not be changed in any way or sold commercially in any format or medium without the formal permission of the author.

When referring to this work, full bibliographic details including the author, title, awarding institution and date of the thesis must be given.

Please visit <http://shura.shu.ac.uk/25513/> and <http://shura.shu.ac.uk/information.html> for further details about copyright and re-use permissions.

Sheffield Hallam University
Materials and Engineering Research Institute

**Development of Novel Processing Routes for
Electrical Ceramics and Glass-Ceramics**

Khalid Rmaydh Muhammed

A thesis submitted in partial fulfilment of the requirements
of Sheffield Hallam University for the degree of Doctor of
Philosophy (PhD)

April 2019

Acknowledgements

First, this thesis could not have been achieved without continuous support, encouragement, guidance, and advice from Professor Paul A. Bingham. I am very proud to do my PhD research with Professor Paul A. Bingham (Director of Studies) and Dr Iasmi Sterianou (Second Supervisor). I would like gratefully to acknowledge them for insight and guidance through this research project, and I would like to express my sincere gratitude to them for many valuable suggestions, encouragement and assistance.

I have learnt many principles from Professor Paul A. Bingham, including how to do my PhD research like to be simple, patient and do not run before you walk (meaning focus on your work and do it precisely then start to make development), and how to work in a group effectively.

I am proud to work with very friendly and helpful group (Prof. Paul's group), I learnt from them, how to share information and engage with the group, I do not need to forget Dr Tony as they are very knowledgeable in XRD analysis and you can find them in time to help you as well.

I would thank all MERI lab technicians and staff, could I mention Dr Francis to help me with DTA analysis, Deebea to help me with Raman analysis and Paul Allender to help me with SEM measurements.

Big thanks to my big family including my parents, brothers and sisters for their continuous support and encouragement, as well as big thanks to my wife Randah Hmood Abdallah and kids Younis, Yaqoota and Omnia for their support, encouragement and being patient with me during my study. I appreciate my friend Ayoob Jasim for support and help me with all the request requirements in my country.

I acknowledge with much appreciation all staff in the Higher Committee for Educational Development in Iraq (HCED) for financial support; without them, I cannot study my PhD research.

Declaration

Declaration

I declare that all work in this thesis has been achieved by myself under the supervision of Professor Paul A. Bingham in the MERI labs/Sheffield Hallam University, except where otherwise referenced/acknowledged.

Abstract

The study in this project focuses on using three different processing routes, conventional solid-state sintering, microwave sintering and melt processing, to manufacture electrical ceramics and glass-ceramics in bismuth sodium titanate (BNT) and potassium sodium niobate (KNN) systems. Manufacturing electrical ceramics using a conventional solid-state processing route requires high sintering temperatures (more than 1100°C) for long times (at least 10 hours including heating and cooling), with high energy consumption (20kWh) for electrical furnaces, leading to high cost. Moreover, laboratory-scale preparation of electrical ceramics in the author's home country, Iraq, is difficult because of equipment shortages and power cuts. Therefore, in the present work, a microwave processing route using a standard kitchen microwave oven has been used to produce electrical ceramics, whilst dramatically reducing sintering times (heating between 20-25mins and cooling 2h) and thus energy consumption (0.4kWh). Also, a melt processing route has been used to manufacture electrical glass-ceramics as bulk and fibre samples, thus reducing processing steps and preparing KNN borosilicate glass-ceramic fibres for the first time.

Microwave sintering/heating depends on the generation of heating throughout the sample simultaneously. This project has used a combination of direct microwave heating of the sample itself, combined with indirect heating by microwave susceptor disks placed close to the sample. In the present project, microwave susceptor disks composed of 50wt% graphite, 30wt% SiO₂, 10wt% Mn₂O₃, 10wt% Fe₃O₄ have been used.

Both conventional solid-state sintering and microwave processing have been used to prepare four different electrical ceramic compositions: pure bismuth sodium titanate (Bi_{0.5}Na_{0.5}TiO₃), pure potassium sodium niobate (K_{0.5}Na_{0.5}NbO₃), iron-doped bismuth sodium titanate (Bi_{0.5}Na_{0.5}Ti_{1-x}Fe_xO_{3-0.5x}) and iron-doped potassium sodium niobate (K_{0.5}Na_{0.5}Nb_{1-x}Fe_xO_{3-x}), with high sintering temperatures (900-1100°C) for 2h inside an electrical furnace (conventional sintering) and short heating times (10-25 mins) inside a standard 900W kitchen microwave oven.

A melt processing route has also been used, with the aim of preparing bismuth sodium titanate (Bi_{0.5}Na_{0.5}TiO₃) and potassium sodium niobate (K_{0.5}Na_{0.5}NbO₃) by heat treatment of bismuth sodium titanium silicate, bismuth sodium titanium borate, potassium sodium niobium silicate, potassium sodium niobium borate and potassium

sodium niobium borosilicate glasses to form glass-ceramics. In addition, opportunities for preparation of potassium sodium niobium borosilicate glass and glass-ceramic fibres have been studied.

A range of structural, thermal and electrical measurements have been carried out, including differential thermal analysis (DTA), X-ray diffraction (XRD), Raman spectroscopy, scanning electron microscopy (SEM), density, polarisation and strain versus electric field measurement were carried out on the electrical ceramics and glass-ceramics.

Pure BNT ceramics have been prepared by solid-state sintering and microwave sintering. In addition, BNT-silicate and BNT-borate glasses have been prepared by melt processing, and subsequent heat treatment with the aim of forming BNT in the resulting glass-ceramics. A $\text{Bi}_{0.5}\text{Na}_{0.5}\text{TiO}_3$ phase with rhombohedral structure has been successfully produced by solid-state sintering and microwave sintering methods, however, it was not possible to produce entirely glassy materials in the silicate and borate systems studied, which instead formed glass + crystalline components upon cooling from molten. Increasing the sintering temperature from 1000°C to 1100°C for pure BNT ceramics prepared by solid-state sintering increased average grain size from ca. 0.4 μm to 2 μm and the relative density increased from approximately 83% of theoretical density to approximately 94% of theoretical density. Also, increasing sintering temperatures from 1050°C to 1100°C enhanced the remnant polarisation from approximately 22 to 40 $\mu\text{C}/\text{cm}^2$ and maximum strain increased from about 4.5 to 8%, respectively. Furthermore, increasing the microwave sintering time from 10 to 25 min for pure BNT ceramics prepared by microwave sintering processing, increased average grain size approximately 0.2 to ca 0.9 μm , and the relative density from approximately 70% to approximately 94% of theoretical density. The remnant polarisation (about 42.2 $\mu\text{C}/\text{cm}^2$) and the maximum strain (8.3%) with a saturated and typical shape for ferroelectric behaviour were obtained at higher microwave sintering times (25 mins).

Iron-doped BNT ceramics were produced by solid-state sintering and microwave sintering. A single $\text{Bi}_{0.5}\text{Na}_{0.5}\text{TiO}_3$ phase with cubic structure was successfully produced by both processing methods. Adding iron to the BNT ceramics using solid-state sintering processing increased average grain size with increasing Fe content from 0.2 μm in pure BNT to 5 μm in $(\text{Bi}_{0.5}\text{Na}_{0.5}\text{Ti}_{0.9}\text{Fe}_{0.1}\text{O}_{2.95})$ for iron doped BNT ceramics. The relative density was low (69% of theoretical density) for undoped BNT ceramics and high (97% of theoretical density) for 7 mole% Fe-BNT.

Pure KNN ceramics have been prepared by solid-state sintering and microwave sintering. In addition, KNN-silicate glasses, KNN-borate glasses, KNN-borosilicate glasses and KNN-borosilicate glass fibres have been prepared by melt processing, and subsequent heat treatment with the aim of forming KNN in the resulting glass-ceramics. A $\text{K}_{0.5}\text{Na}_{0.5}\text{NbO}_3$ phase with orthorhombic structure has been successfully produced by solid-state sintering and microwave sintering processing. Also, a main $\text{K}_{0.5}\text{Na}_{0.5}\text{NbO}_3$ phase with anorthic structure has been presented for KNN-borate glass-ceramics, KNN-borosilicate glass-ceramics and KNN-borosilicate glass-ceramic fibres by melt processing, however, it was not possible to produce entirely glassy materials in the silicate systems studied, which instead formed glass + crystalline components upon cooling from molten. Increasing the sintering temperature from 1000°C to 1100°C for pure KNN ceramics manufactured by solid-state sintering increased average grain size from ca. 0.6 μm to 5 μm and the relative density increased from ca. 69% of theoretical density to approximately 91% of theoretical density. Also, increasing sintering temperatures from 1075°C to 1100°C enhanced maximum strain increased from about 3.6 to 6%, respectively. The remnant polarisation of approximately 33 $\mu\text{C}/\text{cm}^2$ with a saturated and ideal P-E hysteresis shape related to the ferroelectric behaviour has obtained at a higher sintering temperature of 1100°C. Additionally, increasing the microwave sintering time from 10 to 25 min for pure KNN ceramics manufactured by microwave sintering processing, increased average grain size approximately 0.2 μm to approximately 3 μm , and the relative density from ca. 68% to ca. 90% of theoretical density. Also, increasing microwave sintering time from 20 to 25 mins improved maximum strain increased from about approximately 5.2 to 7.5%, respectively. The remnant polarisation of approximately 17 $\mu\text{C}/\text{cm}^2$ with a saturated and ideal P-E hysteresis shape related to the ferroelectric behaviour has obtained at a higher microwave sintering time of 25 mins. On the other hand, flat surfaces with grain growth, and slimmed P-E hysteresis shapes, indicated the absence of ferroelectric behaviour from the KNN borate glass-ceramics and KNN borosilicate glass-ceramics prepared by melt method.

Iron-doped KNN ceramics were prepared by solid-state sintering. A single $\text{K}_{0.5}\text{Na}_{0.5}\text{NbO}_3$ phase was obtained for only one iron-doped sample, $\text{K}_{0.5}\text{Na}_{0.5}\text{Nb}_{0.98}\text{Fe}_{0.02}\text{O}_{2.98}$. Adding iron to KNN ceramics increased the relative density from 73% of the theoretical density for undoped KNN ceramics to 86% of the theoretical density for $\text{K}_{0.5}\text{Na}_{0.5}\text{Nb}_{0.9}\text{Fe}_{0.1}\text{O}_{2.9}$.

Table of Content

Acknowledgements	i
Declaration	ii
Abstract	iii
Table of Content	vi
Chapter One General Introduction	1
1.1.Introduction	1
1.2.1. Electrical Ceramic and Glass-Ceramic Materials	2
1.2.1.Ferroelectric Ceramics	2
1.2.2.Piezoelectric Ceramics	3
1.2.3.Dielectrics	4
1.3.Piezoelectric Ceramic and Glass-Ceramic Materials	4
1.3.1.Lead Zirconate Titanate (PZT)	5
1.3.2.Barium Titanate (BTO)	5
1.3.3.Bismuth Sodium Titanate (BNT)	6
1.3.4.Potassium Sodium Niobate (KNN)	7
1.3.5.Dopants	7
1.4.Perovskite Structure	8
1.5.Processing Routes	10
1.5.1.Conventional Solid-State Sintering Processing	10
1.5.2.Microwave Sintering Processing	12
1.5.3.Melt Processing	13
1.6.Aims and Objectives of the Project	13
1.7.Contribution to Knowledge	14
1.8.Thesis Outline	15

Table of Contents

Chapter Two Literature Review	17
2.1. Introduction	17
2.2. Literature Review	19
2.2.1. Solid State Sintering Processing	19
2.2.1.1. BNT Ceramics	19
2.2.1.2. KNN Ceramics	23
2.2.2. Microwave Sintering Processing	28
2.2.2.1. BNT Ceramics	28
2.2.2.2. KNN Ceramics	28
2.2.3. Melt processing	29
2.2.3.1. KNN Glass- Ceramics	29
Chapter Three Experimental Procedures	31
3.1. Introduction	31
3.2. Experimental Processing Routes	31
3.2.1. Conventional Solid-State Sintering Processing	32
3.2.1.1. Bismuth Sodium Titanate (BNT) Ceramics	32
3.2.1.2. Iron-Doped Bismuth Sodium Titanate (BNTFe) Ceramics	33
3.2.1.3. Potassium Sodium Niobate (KNN) Ceramics	34
3.2.2. Microwave Sintering Processing	38
3.2.2.1. Bismuth Sodium Titanate (BNT) Ceramics	38
3.2.2.2. Iron-Doped Bismuth Sodium Titanate (BNTFe) Ceramics	39
3.2.2.3. Potassium Sodium Niobate (KNN) Ceramics	41
3.2.2.4. Microwave Susceptor Disks	42
3.2.3. Melt Processing Route	44
3.2.3.1. Bismuth Sodium Titanium Silicate (BNTSi) Glasses	44
3.2.3.2. Bismuth Sodium Titanium Borate (BNTB) Glasses	45
3.2.3.4. Potassium Sodium Niobium Silicate (KNNS) Glasses	47

Table of Contents

3.2.3.5. Potassium Sodium Niobium Borate (KNNB) Glasses and Glass-Ceramics	48
3.2.3.6. Potassium Sodium Niobium Borosilicate (KNNBS) Glasses and Glass-Ceramics	49
3.2.3.7. Potassium Sodium Niobium Borosilicate (KNNBS) Glasses and Glass-Ceramic Fibres	50
3.3. Structural Analysis	51
3.3.1. XRD (X-Ray Diffraction)	51
3.3.2. Raman Spectroscopy	52
3.3.3. Scanning Electron Microscopy (SEM)	53
3.4. Differential Thermal Analysis (DTA)	54
3.5. Density Measurements	55
3.6. Electrical Property Measurements	56
3.6.1. Electrode Preparation	56
3.6.2. Hysteresis (Polarization Versus Electric Field) and Strain Versus Electric Field Loop Measurements	56
Chapter Four Pure and Iron Doped Bismuth Sodium Titanate Ceramics and Glasses	59
4.1. Introduction	59
4.2. Pure Bismuth Sodium Titanate Ceramics and Glasses	62
4.2.1. Solid State Processing Route	62
4.2.1.1. Results	62
4.2.1.1.1. XRD	62
4.2.2. Microwave Processing Route	68
4.2.2.1. Results	69
4.2.2.1.1. XRD	69
4.2.3. Melt Processing Route	74
4.2.3.1. Bismuth Sodium Titanium Silicate Glasses	74
4.2.3.1.1. Results	74
4.2.3.1.1.1. XRD	74

Table of Contents

4.2.3.2. Bismuth Sodium Titanium Borate Glasses	77
4.2.3.2.1. Results	77
4.2.3.2.1.1. XRD	77
4.2.4. Discussion	78
4.3. Iron-Doped Bismuth Sodium Titanate Ceramics	85
4.3.1. Solid State Processing Route	85
4.3.1.1. Results	85
4.3.1.1.1. XRD	85
4.3.2. Novel Microwave Processing Route	90
4.3.2.1. Results	90
4.3.2.1.1. XRD	90
4.3.3. Discussion	95
Chapter Five Pure and Iron Doped Potassium Sodium Niobate Ceramics and Glass-Ceramics	100
5.1. Introduction	100
5.2. Pure Potassium Sodium Niobate Ceramics and glass-Ceramics	103
5.2.1. Solid State Sintering Processing	103
5.2.1.1. Results	103
5.2.1.1.1. XRD	103
5.2.1.1.2. Raman Spectroscopy	104
5.2.1.1.3. Electron Microscopy	105
5.2.1.1.4. Density	106
5.2.1.1.5. Electrical Properties	108
5.2.2. Microwave Processing Route	110
5.2.2.1. Results	110
5.2.2.1.1. XRD	110
5.2.2.1.2. Raman Spectroscopy	111
5.2.2.1.3. Electron Microscopy	113

Table of Contents

5.2.2.1.4. Density	113
5.2.2.1.5. Electrical Properties	115
5.2.3. Melt Processing Route	118
5.2.3.1. Potassium Niobium Borate glasses	118
5.2.3.2. Potassium Sodium Niobium Silicate Glasses	118
5.2.3.2.1. Results	118
5.2.3.2.1.1. XRD	118
5.2.3.2.1.2. Raman Spectroscopy	119
5.2.3.2.1.3. Electron Microscopy	120
5.2.3.2.1.4. Density	121
5.2.3.3. Potassium Sodium Niobium Borate Glass-Ceramics	121
5.2.3.3.1. Results	122
5.2.3.3.1.1. DTA	122
5.2.3.3.1.2. XRD	122
5.2.3.3.1.3. Raman Spectroscopy	124
5.2.3.3.1.4. Electron Microscopy	125
5.2.3.3.1.5. Density	126
5.2.3.3.1.6. Electrical Properties	128
5.2.3.4. Potassium Sodium Niobium Borosilicate Glass-Ceramics	128
5.2.3.4.1. Results	129
5.2.3.5.1.2. XRD	135
5.2.3.5.1.3. Raman Spectroscopy	137
5.2.3.5.1.4. Electron Microscopy	138
6.2.3. Discussion	140
5.3. Iron-Doped Potassium Sodium Niobate Ceramics	152
5.3.1. Solid State Processing Route	152
5.3.1.1. Results	152
5.3.1.1.1. XRD	152

Table of Contents

5.4. Conclusions	156
Chapter Six Conclusions and Future Work	158
6.1. Conclusions	158
6.1.1. BNT Ceramics and Glasses	158
6.1.1.1. Solid-State Sintering Processing Route	158
6.1.1.2. Microwave Sintering Processing Route	159
6.1.1.3. Melt Processing Route	159
6.1.2. Iron-Doped Bismuth Sodium Titanate Ceramics	160
6.1.2.1. Solid-State Sintering Processing Route	160
6.1.2.2. Microwave Sintering Processing Route	160
6.1.3. KNN Ceramics and Glass-Ceramics	161
6.1.3.1. Solid-State Sintering Processing Route	161
6.1.3.2. Microwave Sintering Processing Route	162
6.1.3.3. Melt Processing Route	163
6.1.4. Potassium Sodium Niobium Borosilicate Glass and Glass-Ceramic Fibres	163
6.1.5. Iron-Doped Potassium Sodium Niobate Ceramics	164
6.2. Future Work	164
References	166

Chapter One

General Introduction

1.1. Introduction

Chapter one introduces electrical ceramic materials, the perovskite structure, processing routes and the aims and objectives of the present project, as summarised in Figure 1.1.

Electrical ceramics and glass-ceramics have been extensively used in electrical and electronic applications such as communications, medical diagnostics, industrial automation, energy storage (Priya & Nahm, 2011); and sensors, transducers, memory cells, energy harvesters and actuators (Koruza et al., 2018). They can be classified into three main groups: (i) piezoelectrics (Duran & Moure, 1986); (ii) ferroelectrics (Buchanan, 1986); and (iii) dielectrics (Marghussiam, 2015; Vijaya M. S., 2013). Piezoelectrics include lead zirconate titanate (PZT) (Jaffe et al., 1971), barium titanate (BT or BTO) (Jaffe et al., 1971), bismuth sodium titanate (BNT) (Priya & Nahm, 2011) and potassium sodium niobate (KNN) (Priya & Nahm, 2011). Piezoelectrics typically have a perovskite structure of ABX_3 , where A is a cation such as Pb, Ba, Bi, Na or K; B is a cation such as Zr, Ti or Nb; and X is an anion such as O (Buchanan, 1986; Jaffe et al., 1971). Electrical ceramics and glass-ceramics can be prepared using different processing routes including conventional solid-state sintering (Malič et al., 2018), microwave sintering (Agrawal, 2013) and melt processing (Bansal & Doremus, 1986; Shelby, 2005). The solid-state sintering processing route has been extensively used over many decades to manufacture electrical ceramics. However, it has disadvantages related to the high energy consumption related to long sintering times such as 470 mins (Wei et al., 2018), 350 mins (Maqbool et al., 2014) or 340 mins (Kakroo et al., 2016), high energy consumption (20 kWh) and high sintering temperatures (1100°C) (Smart & Moore, 2016). Microwave sintering processing has been used to prepare electrical ceramics by a few researchers (Chiang et al., 2013; Feizpour et al., 2014; Ramana et al., 2011). This processing route displays some advantages, for example, reduced sintering and processing times and energy consumption. However, it has one drawback in the context of ceramic sintering which is correlated to the ability of the raw materials or green body to absorb sufficient electromagnetic energy to generate high temperatures (susceptibility) (Bykov et al., 2001; Chandrasekaran et al., 2012). Melt processing

routes have been used to prepare electrical glass ceramics, presenting a potentially reduced number of processing steps as an advantage (Fanelli et al., 2011; Yongsiri et al., 2014; Zheng et al., 2016).

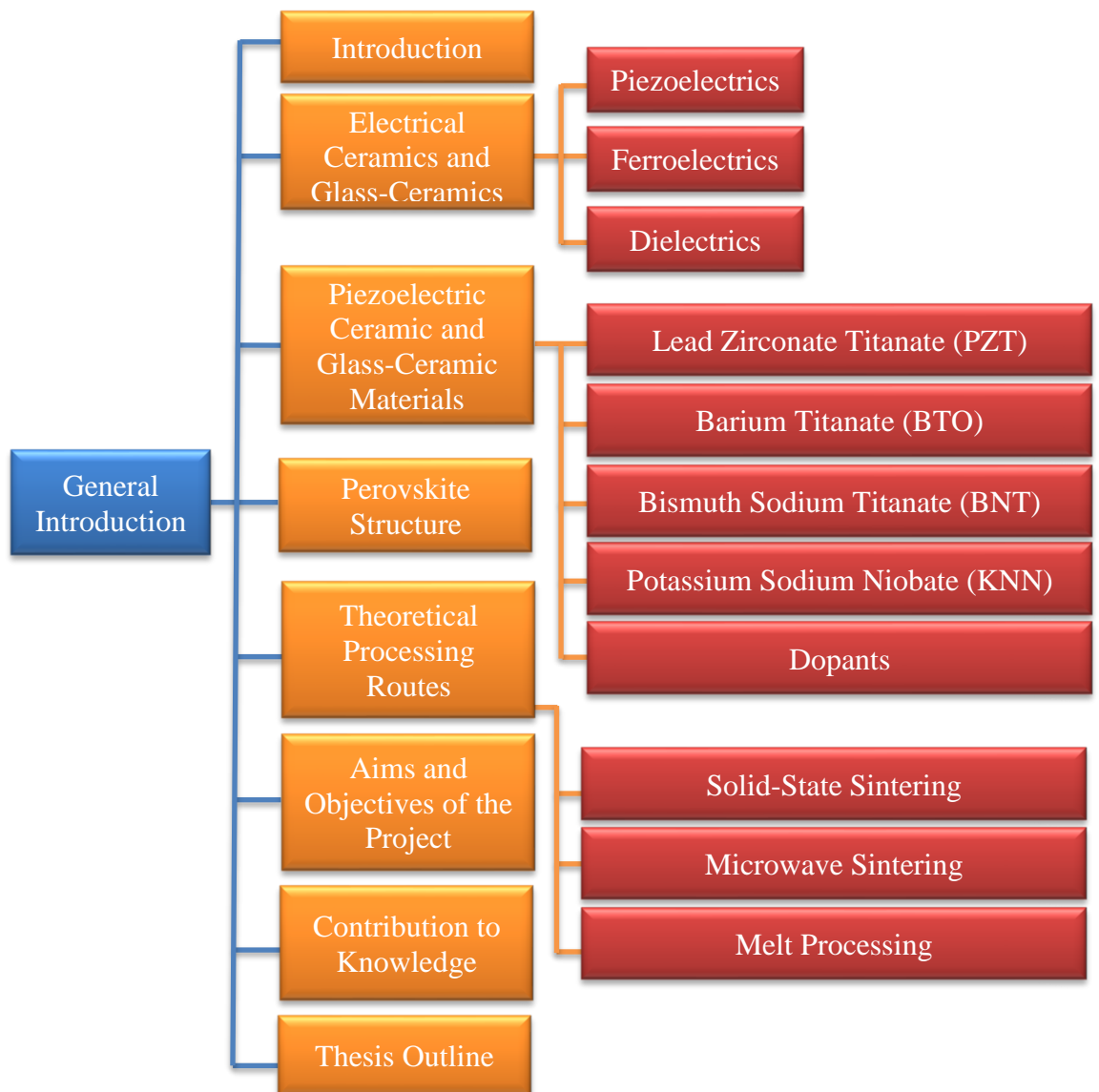


Figure 1.1. Schematic overview of the general introduction (Chapter One).

1.2.1. Electrical Ceramic and Glass-Ceramic Materials

Electrical ceramics can be classified into piezoelectric, ferroelectric and dielectric materials.

1.2.1. Ferroelectric Ceramics

Ferroelectric ceramics are characterised by the generation of spontaneous polarisation under an applied electric field or mechanical stress to form permanent

electrical dipoles, which can be reoriented (switched) by the application of an external electric field to reverse the polarisation. Valasek first discovered ferroelectricity in 1920 during work on Rochelle salt (Buchanan, 1986). Later, ferroelectric materials historically developed in terms of ceramic compositions of barium titanate (BaTiO_3), lead zirconate titanate ($\text{Pb}(\text{ZrTi})\text{O}_3$), alkali niobates ($\text{K}_{0.5}\text{Na}_{0.5}\text{NbO}_3$) and alkali bismuth titanates ($\text{Bi}_{0.5}\text{Na}_{0.5}\text{TiO}_3$) from 1940-1960, to be utilised in the many applications including sensors, transducers, memory cells, energy harvesters and actuators (Koruza et al., 2018). Ferroelectric behaviour depends significantly on the shape of the hysteresis loop (polarisation versus electric field), which shows nonlinear polarisation as a function of an electric field (Buchanan, 1986). A hysteresis loop plot of ferroelectricity depends on three main factors; coercive field (E_C) placed on the x-axis exhibiting at zero polarization, spontaneous polarization (P_S) and remnant polarisation (P_R) placed on the y-axis displaying on the zero electric fields, as shown in Figure 1.2 (Ivanov et al., 2018).

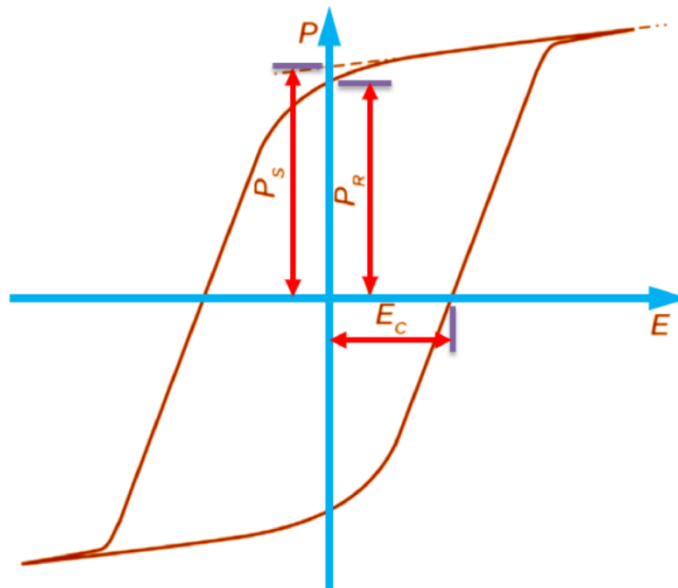


Figure 1.2. Ferroelectric hysteresis loop (Ivanov et al., 2018).

1.2.2. Piezoelectric Ceramics

Piezoelectricity can be defined as the development of an electric charge by applying mechanical stress. The generated electric field is proportional to mechanical stress (Jaffe, Cook Jr, & Jaffe, 1971). Piezoelectricity was first discovered by Pierre and Jacques Curie in 1880 when they tried to generate an electric charge by applying

pressure to single-crystal quartz (Uchino, 2012). Piezoelectric ceramics are ferroelectric materials. Ferroelectric behaviour is not exhibited above the Curie temperature (T_C), and the ferroelectric transition occurs below the Curie temperature (T_C) to induce a polar axis which leads to spontaneous polarisation. The piezoelectric state thus occurs at the same time as the ferroelectric state (Duran & Moure, 1986). Piezoelectric ceramics form a critical part of electronic ceramic materials, and have been used in many systems such as communications, medical diagnostics, industrial automation, and energy storage and harvesting (Priya & Nahm, 2011). There are two material classes, from an industrial perspective, of piezoelectric materials; lead-based piezoelectric ceramics (lead zirconate titanate ($\text{Pb}(\text{Zr}, \text{Ti})\text{O}_3$)) and lead-free piezoelectric ceramics (barium titanates (BaTiO_3), bismuth sodium titanates ($\text{Bi}_{0.5}\text{Na}_{0.5}\text{TiO}_3$)), potassium sodium niobate ($\text{K}_{0.5}\text{Na}_{0.5}\text{NbO}_3$), and bismuth layer-structured ferroelectrics) (Priya & Nahm, 2011).

1.2.2.1. Langevin Transducers

Langevin transducers are given as an industrial example of ecological piezoelectric applications, for example to find underwater fish. In Japan, Honda Electronics used the BNT lead-free piezoelectric ceramics to develop Langevin transducers for ultrasonic cleaner applications. $0.82\text{Bi}_{0.5}\text{Na}_{0.5}\text{TiO}_3-0.15\text{BaTiO}_3-0.03(\text{Bi}_{1/2}\text{Na}_{1/2})(\text{Mn}_{1/3}\text{Nb}_{2/3})\text{O}_3$ ceramics show a smaller piezoelectric constant (110pC/N), a relative permittivity (520), and a Curie point (260°C) less than that of hard $\text{Pb}(\text{Zr}, \text{Ti})\text{O}_3$ (PZT). On the other hand, the electromechanical coupling factor (41%) is larger than that of PZT. Also, it exhibits a maximum vibration velocity ($k3I$) up to 1.4m/s and a mechanical quality factor (500) (Priya & Nahm, 2011; Tou et al., 2009).

1.2.3. Dielectrics

Dielectric materials can be defined as electrical insulators, and have been used in many applications such as capacitors and transducers (Moulson & Herbert, 2003). Most ceramic materials exhibit dielectric properties. When dielectric materials are subjected to an external electric field, this leads to the modification in dimensions. The dimensional change results from transportation of charge, where positive charge (cations) transports toward the external electric field direction and negative charge (anions) move in the opposite direction, which leads to the formation of polarisation and development of a dipole moment (Marghussian, 2015; Vijaya, 2013).

1.3. Piezoelectric Ceramic and Glass-Ceramic Materials

Piezoelectric ceramics can be classified by chemical composition, and their properties are explained as follows:

1.3.1. Lead Zirconate Titanate (PZT)

Lead zirconate titanate, $\text{Pb}(\text{ZrTi})\text{O}_3$ (PZT) is one of the most important compositions, and has been widely used for many decades as a piezoelectric material (Tiwari & Srivastava, 2015). Shirane et al. first discovered $\text{Pb}(\text{ZrTi})\text{O}_3$ as a solid solution in 1952 (Kimura, Ando & Sakabe, 2010), and since then it has been extensively used in electronic applications such as piezoelectric actuators, transducers, ferroelectric memory devices, stabilizers, modulators, parametric amplifiers, and sensors (Surowiak, Kupriyanov & Czekaj, 2001; Xu et al., 2016). PZT has a perovskite structure of the ABX_3 general formula, where Pb^{2+} (ionic radius 1.18 Å) occupies the A-site, and Zr^{4+} (ionic radius 0.72 Å) and Ti^{4+} (ionic radius 0.61 Å) occupy the B-site, and O^{2-} occupies the X-site in the ABX_3 structure (Kamakshi, Rao & Rao, 2015). PZT ceramics have excellent ferroelectric and piezoelectric properties, including a coercive field of 1 kV/mm and a remnant polarisation of $35 \mu\text{C}/\text{cm}^2$, a strain of 0.1%–0.2%, and a Curie temperature between 300°C to 400°C (Rödel et al., 2009). Although PZT has excellent ferroelectric and piezoelectric properties, however, the EU banned lead from electronic devices in 2006, leading to searches for Pb-free piezoelectric ceramics. PZT faces further pressure, due to the evaporation of lead oxide (PbO) at sintering temperatures above 1280°C during the processing (Tiwari & Srivastava, 2015; Wang et al., 2001).

1.3.2. Barium Titanate (BTO)

Barium titanate, BaTiO_3 (BTO) is a lead-free piezoelectric ceramic that has been widely used for electronic applications such as multilayer ceramic capacitors, sensors, piezoelectric actuators and transducers (Alkathy et al., 2017; Dai et al., 2017). BTO was first discovered as a piezoelectric ceramic during World War II, by Wainer and Salomon in 1942, Ogawa in 1944 and Vul in 1944 (Duran & Moure, 1986; Uchino, 2012). BTO ceramics have a perovskite structure with ABX_3 general formula, where the A-site is occupied by Ba^{2+} , the B-site by Ti^{4+} and X-site by O^{2-} (Abdul Hamid et al., 2015). BTO ceramics have high dielectric constant; however their application range is limited by their low Curie temperature (120°C) which limits their high-temperature applications (Nayak et al., 2014). Barium titanate has different perovskite phases, which depend on temperature: rhombohedral (below -90°C), orthorhombic (between 5°C and -

90°C), tetragonal (between 5°C and 120°C) and cubic (above 120°C), as shown in Figure 1.3 (Villafuerte-Castrejón et al., 2016).

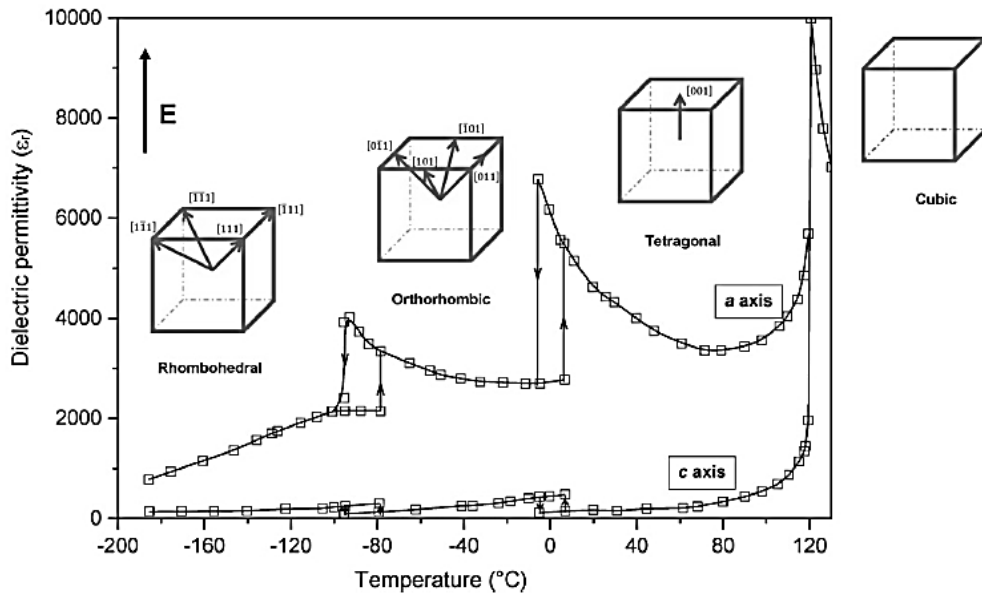


Figure 1.3. Phase temperature of BaTiO₃ (Villafuerte-Castrejón et al., 2016).

1.3.3. Bismuth Sodium Titanate (BNT)

Bismuth sodium titanate, Bi_{0.5}Na_{0.5}TiO₃ (BNT) is an important candidate lead-free piezoelectric ceramic, and was first discovered by Smolenskii and colleagues in 1960 (Priya & Nahm, 2011). BNT ceramics have been used for ecological applications such as Langevin transducers utilized for locating fish underwater (Tou et al., 2009), non-contact sensing applications (Sharma, Chauhan, & Kumar, 2016), thermal detectors (Liu et al., 2018), luminescent ferroelectrics (Pan et al., 2018), piezoelectric actuators (Zhu et al., 2018) and energy storage applications (Chandrasekhar & Kumar, 2016). BNT has a perovskite structure (ABX₃) with a rhombohedral ferroelectric phase at room temperature; where the A-site is occupied by Bi³⁺ and Na⁺, the B-site by Ti⁴⁺ and X-site by O²⁻. It has two main phase transition temperatures; one is the Curie point (tetragonal-cubic phase transition) at 320°C and another is the ferroelectric phase transition temperature (rhombohedral-tetragonal phase transition) at 200°C. BNT exhibits excellent ferroelectric properties (a large remnant polarisation of 38μC/cm²) (Jones & Thomas, 2002). However, it shows relatively high coercive field (73kV/cm) (Pardo et al., 2018).

1.3.4. Potassium Sodium Niobate (KNN)

Potassium sodium niobate, $K_{0.5}Na_{0.5}NbO_3$ (KNN) is another promising lead-free piezoelectric ceramic. It has a perovskite structure (ABX_3) with an orthorhombic phase at room temperature, where the A-site is occupied by K^+ and Na^+ , the B-site by Nb^{5+} and X-site by O^{2-} (Panda & Sahoo, 2015). It has been used in a number of many applications such as medical diagnostics (sonar) (Lusiola et al., 2016), energy harvesting (Kim et al., 2016; Kumar et al., 2016; Zheng et al., 2017; Zheng et al., 2018), energy storage (Zheng et al., 2016), optical computing and information processing (Lin et al., 2017). KNN lead-free piezoelectric ceramics have two key phase transition temperatures: one is the orthorhombic-tetragonal phase transition ($200^\circ C$), and the other is the tetragonal-cubic phase transition ($420^\circ C$). It has a relatively high Curie point ($420^\circ C$) making it potentially useful in high-temperature applications. This compound has a high remnant polarisation ($33\mu C/cm^2$). However, it is difficult to achieve a high-density ceramic because of its hygroscopic nature and volatility of alkaline oxides such as K_2O and Na_2O during processing (Jenko et al., 2005; Priya & Nahm, 2011; Shrout & Zhang, 2007).

1.3.5. Dopants

Many different dopants have been studied with the aim of improving or modifying the electrical and physical properties of bismuth sodium titanate ($Bi_{0.5}Na_{0.5}TiO_3$) and potassium sodium niobate ($K_{0.5}Na_{0.5}NbO_3$) lead-free piezoelectric ceramics. According to the perovskite structure (ABX_3), there are three types of modifiers:

- i. A-site dopants such as Th^{4+} , Sb^{3+} , La^{3+} , Nd^{3+} , Ba^{2+} , and Sr^{2+} .
- ii. B-site dopants such as Ta^{5+} , Sc^{3+} , Fe^{3+} , and Mg^{2+}
- iii. X-site dopants such as F^- and Cl^- (Panda & Sahoo, 2015).

Mainly, according to the compositional substitution of each of BNT and KNN ceramics, there are three types of modifiers used:

i. Isovalent modifiers: this kind of dopant has a similar valence and ionic radius to the replaced ion, for example, Ta^{5+} (ionic radius 0.68 \AA) substitutes Nb^{5+} (ionic radius 0.69 \AA) and Sn^{4+} (ionic radius 0.71 \AA) substitutes Ti^{4+} (ionic radius 0.68 \AA).

ii. Donor modifiers: this type of additive is a higher valence cation, that means, Ba^{2+} , Sr^{2+} , La^{3+} and Sb^{3+} for modification of the K^+ or Na^+ site; W^{6+} for substitution on the Nb^{5+} site, and Ta^{5+} and Sb^{5+} for modification of the Ti^{4+} site.

iii. Acceptor modifiers: this type of dopant is a lower valence cation, that means, Sc^{3+} , Fe^{3+} , Al^{3+} and Mg^{2+} for modification of the Ti^{4+} site; Zr^{4+} and Sn^{4+} for substitution on the Nb^{5+} site; and Ba^{2+} , Sr^{2+} and K^{+} for substitution on the Bi^{3+} site (Panda & Sahoo, 2015; Priya & Nahm, 2011).

In addition to doping with single cations, doping or mixing with multiple cations or compounds can also be performed:

i. Doped BNT: BNT ceramics have been previously doped with SrZrO_3 (Maqbool et al., 2014), $\text{Bi}(\text{Mg}_{0.5}\text{Ti}_{0.5})\text{O}_3$ (Aman Ullah et al., 2015), $(\text{Nd}_{0.5}\text{Ta}_{0.5})_x\text{O}_3$ (Cheng et al., 2015), KNbO_3 (Jiang et al., 2014), CuO and NiO (Kakroo et al., 2016), CuO (Chou et al., 2011), and Fe_2O_3 (Aksel et al., 2010), the effects of mentioned doped on the properties has explained in the chapter two literature review.

ii. Doped KNN: KNN ceramics have been previously doped with $\text{Bi}(\text{Mg}_{0.5}\text{Ti}_{0.5})\text{O}_3$ (He et al., 2013), Dy_2O_3 , Er_2O_3 , Eu_2O_3 and Pr_6O_{11} (Du et al., 2017), MnO_2 (Tian & Du, 2014), TiO_2 and ZrO_2 (Vendrell et al., 2015), Fe_2O_3 (Coondoo et al., 2015), CuO (Alkoy & Berksoy-Yavuz, 2012), ZnO (Ramajo et al., 2014) and V_2O_5 (Kambale et al., 2017), the effects of mentioned doped on the properties, as described in the next chapter literature review.

1.4. Perovskite Structure

The perovskite structure is derived from the name of Lev Perovskite, who worked on the mineral perovskite, CaTiO_3 , in 1839 in the Ural Mountains. The perovskite structure has a general formula of ABX_3 , where A is the larger cation (monovalent, divalent, or trivalent cations, such as Ba^{2+} , Bi^{3+} , Na^{+} , and K^{+}); B is the smaller cation (pentavalent, tetravalent, or trivalent elements, such as Ti^{4+} , Nb^{5+} , and Fe^{3+}) and X is an anion (usually O^{2-}) (Petrovic & Bobic, 2018). The perovskite structure shows the A-site cation at the corners, the B-site cation in the body centre, and the X anion in the centre of each face, as shown in Figure 1.4 (a). The perovskite structure has many phases; a cubic phase appears at a higher temperature than T_C , and an orthorhombic phase occurs at a lower temperature than T_C , which displays spontaneous polarisation in the [011] direction as shown in Figure 1.4 (b and c) (Zheng et al., 2013).

($\text{Bi}_{0.5}\text{Na}_{0.5}\text{TiO}_3$) and potassium sodium niobate ($\text{K}_{0.5}\text{Na}_{0.5}\text{NbO}_3$). The perovskite structure for the compounds mentioned above is explained in the previous section (section 1.3).

1.5. Processing Routes

The global ceramic material is approximately £75 (Carter & Norton, 2007). Advanced ceramics form about 17% of annual ceramics sales, which is the second largest sector of the ceramic industry. Electrical and electronic ceramics form 50% of the advanced ceramics market. These electrical ceramics include bismuth sodium titanate, potassium sodium niobate, barium titanate and lead zirconate titanate, which have been used in many applications such as capacitors, varistors and transducers (Carter & Norton, 2007). Therefore, the importance of the present project to develop new processing routes for these materials, such as microwave sintering processing and melt processing, and conventional solid-state sintering processing of electrical BNT and KNN ceramics and glass-ceramics.

1.5.1. Conventional Solid-State Sintering Processing

The most widely-used synthetic processing route for preparing solid ferroelectric (piezoelectric) ceramics is solid-state sintering processing (Figure 1.6) (Malič et al., 2018). This process is widely used in industry and in laboratories to prepare a wide range of ceramic materials. Although it is the simplest and most widely used method to prepare piezoelectric ceramics, it has drawbacks such as high sintering temperatures (500°C-2000°C) that require high energy consumption and long sintering times (Smart & Moore, 2016). Consequently, this process route is energy-intensive and contributes significantly to human-made CO₂ emissions. Solid-state sintering includes many steps; the first step is preparing the starting raw materials such as oxides and carbonates. The reactant powders are accurately weighed according to the compound stoichiometric formula. They are then mixed, milled, and calcined (Malič et al., 2018). Wet milling is often used to prepare the raw materials for piezoelectric ceramics, one of the most suitable machines to grind very fine powders with grain sizes below 10µm is ball milling (Rahaman, 2003). During the calcination step, reactions occur between reactant powders (oxides, hydroxides and carbonates) to decompose most of the hydroxides in the range (200°C-550°C) (Busca, 2014). The release of CO₂ for $\text{K}_{0.5}\text{Na}_{0.5}\text{NbO}_3$ occurs in the calcination temperature range 400°C-700°C, as shown in reaction equation 1.1 and Figure 1.6, and for $\text{Bi}_{0.5}\text{Na}_{0.5}\text{TiO}_3$ ceramics, it occurs in the calcination temperature range 500°C-650°C, as shown in reaction equation 1.2. After

calcination, the powders are wet milled again, and fine powder compacts are prepared at specific pressures using uniaxial or isostatic pressing to produce pellets. The final step is sintering the green pellets at high temperature (Malič et al., 2018). Sintering is considered one of the essential steps in ceramic processing/formation, and occurs under heating without reaching the molten state. There are two types of sintering: the first occurs when particles join together under heating without reaching the molten state during ceramic processing/formation; this is called solid-state sintering. The second type occurs when particles join together under heating whilst in the molten state for one component or more, forming ceramic component during ceramic processing/formation and cooling, which is called liquid-state sintering. The joining of particles occurs driving force effect, which leads to the surface tension and fusion of the particles, creating a solid ceramic with the formation of grain boundaries. The driving force for solid-state sintering is the difference in the free energy or chemical potential between the free surfaces of the particles and the points of contact between adjacent particles (Richerson, 2005). The sintering step reduces porosity and enhances the densification (density) and mechanical strength of ceramic components (Rahaman, 2003, Kingery, 1958).

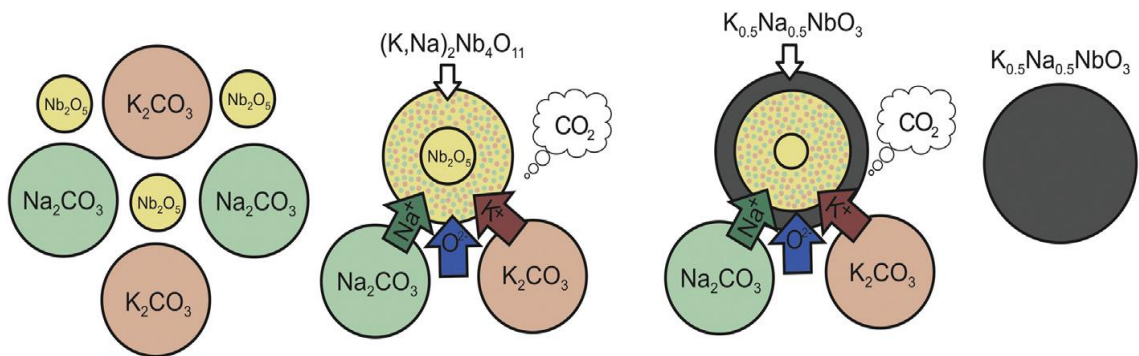


Figure 1.6. Reaction sequence during firing of KNN using conventional solid-state sintering processing, adopted from (Kingery, 1958).

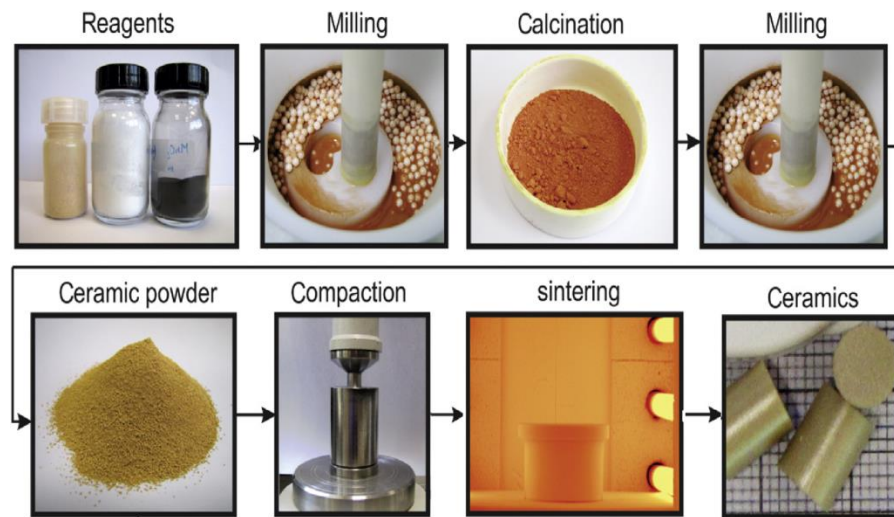


Figure 1.7. Flow diagram of solid-state sintering processing (Kingery, 1958).

1.5.2. Microwave Sintering Processing

Microwave sintering is a novel processing route for ceramic technology when compared with conventional solid-state sintering (Rajkumar & Aravindan, 2009). The main aim of using this technology in ceramic processing is saving energy and lowering sintering time, reducing processing time (energy and CO₂ emissions) (Bykov et al., 2001; Chandrasekaran et al., 2012). As described in the previous section, ceramic processing includes many steps: powder preparation, weighing, milling, calcination, pressing/forming and the final sintering step (Agrawal, 2010). Mainly, microwave sintering proceeds by internal heat generation via absorbing electromagnetic radiation with wavelength (1m-1mm) and frequency (300MHz-300GHz). The most common frequency is 2.45 GHz that is used in kitchen microwaves because there is strong coupling with water molecules at this frequency. Frequencies of 28-30 GHz and 915 MHz have been used for research and industry (Agrawal, 2013). Microwave heating depends mainly on the dielectric constant and dielectric loss factor of materials, for example; water has dielectric constant (77) and dielectric loss factor (13). Indeed, the dielectric constant refers to the storage of electric energy. However, the dielectric loss factor indicates the generation of heat by the dissipation of electrical power. Therefore, heat generation of materials by microwave radiation requires a considerable dielectric constant and high dielectric loss factor, indicated by absorbing microwaves and dissipating electromagnetic energy as heat (Birla & Pitchai, 2017; Chandrasekaran et al., 2012).

1.5.3. Melt Processing

The melt-quench method is the most commonly used process for almost all glass products. This process involves raw materials selection. Batch components consist of glass formers such as silica (SiO_2), phosphoric oxide (P_2O_5) or boric oxide (B_2O_3) to form glass; fluxes to reduce the melting temperature (e.g. Na_2O , K_2O and PbO); modifiers to improve durability and/or reduce melting temperature (e.g. MgO , CaO , SrO , BaO and ZnO) and property modifiers to adjust properties (e.g. TiO_2 , Fe_2O_3 and Al_2O_3). Drying the raw materials is then carried out to remove moisture. Following that, the raw materials are weighed according to stoichiometric batch calculations, and mixed to provide batch homogeneity. The mixed batch then passes to the final melting step to prepare the glass melt. The first step of glass melting is heating until the moisture is released and dehydration of the batch is complete, then liquid phase formation occurs by melting the carbonate raw materials and others, which form eutectic mixtures. The final stage involves dissolution of refractory oxides (e.g. SiO_2 and Al_2O_3) in the liquid phase, forming the viscous melt. Control of both melting time and temperature is essential to enable the chemical reactions to complete and the glass melt to homogenize. Finally, the glass melt is poured and formed into shapes. The fast cooling rate prevents crystallisation and instead forms an amorphous phase. Annealing of the product is then carried out to remove thermal stresses (Narottam P. Bansal & Doremus, 1986; Shelby, 2005)

1.6. Aims and Objectives of the Project

This project aims to understand the potential of novel processing routes such as microwave sintering and melt processing, to prepare lead-free electrical ceramics and glass-ceramics (bulk and fibre) using BNT and KNN compositions. BNT and KNN ceramics have been commercially manufactured using solid-state processing route. However, due to the long time to prepare ceramics (5-7days), and high energy consumption (20 kWh) through using ordinary furnaces, it was necessary to search for novel processing routes offer that lower processing CO_2 emissions and times, and energies cost of lead-free electrical ceramic production. The aims and objectives are summarised in Table 1.1.

Table 1.1. Aims and objectives of the present project.

Processing route (aim)	State of aim	Objective
Solid-State Processing 	Conventional	<ul style="list-style-type: none">• Using processing as a baseline to compare results with novel processing routes.
Microwave Processing 	Novel	<ul style="list-style-type: none">• Reducing energy consumption (0.4 kWh).• Lowering sintering time to the 20-25 mins in the present project.• Reducing processing time.
Melt Processing 	Novel	<ul style="list-style-type: none">• Reduce processing time to the three days is by reducing processing steps to 5 steps in the present project.• Preparing electrical glass-ceramic fibres.

1.7. Contribution to Knowledge

The present project offers novelty through using microwave sintering and melt processing routes with the aim of developing electrical ceramics and glass-ceramics including fibre manufacturing. The current project has contributed to:

- i. Solving the issue of uninterrupted electricity supply (> 10 hours) for electrical furnaces (conventional sintering), a major problem in many countries such as Iraq, by reducing the need for uninterrupted electricity supply (<25 min) for a microwave oven in ceramic research and production.
- ii. Producing electrical ceramics during short sintering time using developed microwave sintering processing, with single phase and enhancing the densification (density) and electrical properties (polarisation and strain versus electric field) as summarised in chapter six conclusions and future work.

- iii. Reduced sintering times and energies by using microwave sintering. Equivalent properties have been achieved between solid-state sintering processing and microwave sintering processing routes.
- iv. First use of microwave susceptor disks consisting of 50wt% graphite, 30wt% SiO₂, 10wt% Mn₂O₃, 10wt% Fe₃O₄, to accelerate sintering times (20-30 mins) for BNT and KNN ceramics.
- v. Demonstration of low cost, readily accessible firing procedures for electroceramics in developing countries.
- vi. Conventional BNT and KNN sintering processing shows enhancing the densification with increasing the sintering temperature to 1100°C/2h whilst exhibiting piezoelectric behaviour.
- vii. Fe₂O₃ doping of BNT and KNN has reduced sintering temperature with improving densification.
- viii. Developing a melt processing glass-ceramic production route with potential for KNN formation with further development.
- ix. Demonstrated the potential for KNN glass-ceramic fibre formation routes with further development.

1.8. Thesis Outline

Chapter one describes electrical materials, perovskite structure, piezoelectric ceramic materials, theoretical processing routes and the aim and objectives of the present project.

Chapter two describes previous research concerning processing routes and lead-free electrical ceramic materials which have been used.

Chapter three concerns experimental processing routes such as conventional solid-state sintered, novel microwave sintered and novel melt processing; it is also considered the analytical techniques to investigate the composition, structure and properties of electrical ceramics and glass-ceramics, X-ray diffraction, Raman spectroscopy, scanning electron microscopy, differential thermal analysis, density, and polarization and strain versus electric field.

Chapter four considers pure and iron-doped BNT ceramics prepared by three different processing routes: conventional solid-state sintering processing, microwave sintering processing and melt processing.

Chapter five concerns pure and iron-doped KNN ceramics prepared by three different processing routes: conventional solid-state sintering processing, microwave sintering processing and melt processing.

Chapter six considers conclusions and future work.

Chapter Two

Literature Review

2.1. Introduction

Chapter two considers previous research relevant to the processing routes and electrical materials studied, as shown in Figure 2.1.

The best performing piezoelectric ceramic that has been used is lead zirconate titanate, $\text{Pb}(\text{ZrTi})\text{O}_3$ (PZT), with excellent ferroelectric and piezoelectric properties. However, PZT has toxicity and volatilisation of lead oxide (PbO) at higher sintering temperatures. Also, lead was banned in electrical equipment in the EU in 2006, therefore, have been facing a limitation in use in Europe (Pal, Dwivedi & Thakur, 2014; Rahman et al., 2014; Rödel et al., 2009). So far, barium titanate (BTO) is a Pb- free piezoelectric ceramic that has been used to replace PZT ceramics (Alkathy et al., 2017; Dai et al., 2017). However, BTO ceramics have low Curie temperature (120°C) which leads to a reduction in the range of application at higher temperature than 120°C (Nayak et al., 2014). Lead-free potassium sodium niobate ceramic, $\text{K}_{0.5}\text{Na}_{0.5}\text{NbO}_3$, has been identified as a promising material for the replacement of PZT. However, it is difficult to achieve a high density in these ceramics because of their hygroscopic nature and volatility of alkaline oxides such as K_2O and Na_2O (Jenko et al., 2005; Priya & Nahm, 2011; Shrout & Zhang, 2007). Another lead-free piezoelectric ceramic is BNT, which has been used for electronic materials. BNT lead-free piezoelectric ceramics have a high Curie point (320°C) and display excellent ferroelectric properties (a large remnant polarisation of $38\mu\text{C}/\text{cm}^2$) (Jones & Thomas, 2002). However, BNT ceramics have high conductivity and relatively high coercive field ($73\text{kV}/\text{cm}$) and emit volatile materials such as Bi or Na or $\text{Bi}_{0.5}\text{Na}_{0.5}$ at higher sintering temperatures (Pardo et al., 2018). Conventional solid-state sintering (Hollenstein, Damjanovic & Setter, 2007; Li et al., 2017; Malic et al., 2005; Takao et al., 2006; Vendrell et al., 2016), hot press (Fisher et al., 2008; Qin et al., 2015), sol-gel (Kang et al., 2011; Wiegand et al., 2012; Xu et al., 2008), and hydrothermal processing (Bai et al., 2017; Hao et al., 2014; Wang et al., 2016), have all been used in the last few decades to prepare piezoelectric ceramics. However, all of these preparation methods have the disadvantage of long processing times of 4-5 days and the need for long sintering times of more than 18h to manufacture BNT and KNN ceramics (Feizpour et al., 2014). Therefore several researchers have

studied other processing routes to prepare BNT and KNN ceramics, for example reducing sintering time to 20-40min without soaking time using novel microwave sintering processing (Chiang et al., 2013; Feizpour et al., 2014; Ramana et al., 2011). In addition, melt processing has been used to manufacture electrical KNN glass-ceramics by some researchers, reducing time processing and processing steps, by excluding wet milling steps that are used in solid-state sintering that may take 2-4 days (Fanelli et al., 2011; Kioka, Honma & Komatsu, 2011a; Yongsiri et al., 2014; Zheng et al., 2016).

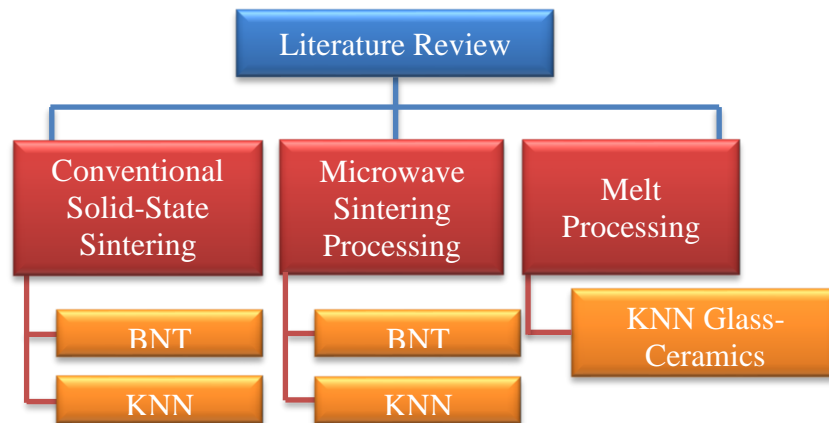


Figure 2.1. Overview of the literature review (Chapter Two).

2.2. Literature Review

The most promising properties include giant stain (45%) for 0.92BNT-0.06BT-0.02KNN ceramics prepared by solid-state sintering processing (1100°C/3h) (Zhang et al., 2007); the best remnant polarisation (43.6 $\mu\text{C}/\text{cm}^2$) for pure BNT ceramics manufactured by solid-state sintering processing with sintering temperature of 1150°C/2h (Jiang et al., 2014); the best normalised strain ($d_{33}^* = 625 \text{ pm}/\text{V}$) for 0.75KNN-0.25SrTiO₃ ceramics; and the best piezoelectric constant ($d_{33} = 700 \text{ pC}/\text{N}$) for 0.78KNN-0.22SrTiO₃ ceramics prepared by solid-state sintering processing with sintering temperature of 1175°C/2h (Duong et al., 2018). These examples represent some of the excellent characteristics of the BNT and KNN ceramics.

2.2.1. Solid State Sintering Processing

2.2.1.1. BNT Ceramics

BNT ceramics should be sintered at more than 1200°C as a high sintering temperature is needed to obtain dense ceramics. However, sintering BNT ceramics at > 1200°C causes difficulty in poling of the ceramics, which is due to the evaporation of Bi at more than 1,130°C. Therefore, the Bi_{0.5}Na_{0.5}TiO₃ should be sintered at 1,100°C and lower, as Priya and Nahm reported (Priya & Nahm, 2011). The relevant previous studies are summarised in Table 2.1.

Table 2.1. Summary of properties for undoped BNT ceramics, prepared using solid-state processing.

Citation	Calcination temperature /time	Sintering temperature /time	Properties
Maqbool et al., 2014	850°C/2h	1150°C/2h	<ul style="list-style-type: none"> • Pure BNT perovskite phase (100%). • Average grain size of 25.2 μm. • Saturated P-E hysteresis and butterfly S-E loops indicating ferroelectric properties. • Remnant polarisation ($30\mu\text{C}/\text{cm}^2$). • Coercive field (55kV/cm). • Maximum strain of 0.08%.
Aman Ullah et al., 2015	800°C/2h	1150°C/2h	<ul style="list-style-type: none"> • Single BNT perovskite phase (100%) with rhombohedral symmetry. • Average grain size of 5 μm. • Saturated P-E hysteresis and butterfly S-E loops indicating ferroelectric properties. • Remnant polarisation ($28\mu\text{C}/\text{cm}^2$). • Coercive field (58kV/cm).
Cheng et al., 2015	850°C/2h	1150°C/2h	<ul style="list-style-type: none"> • Pure BNT perovskite phase (100%). • Average grain size of 2.2 μm. • Saturated typical P-E hysteresis loops indicating ferroelectric properties. • Remnant polarisation ($24\mu\text{C}/\text{cm}^2$).
Jiang et al., 2014	-	1150°C/2h	<ul style="list-style-type: none"> • Pure BNT perovskite phase (100%) with rhombohedral symmetry. • Saturated P-E hysteresis and butterfly S-E loops indicating ferroelectric properties. • Remnant polarisation ($43.6\mu\text{C}/\text{cm}^2$). • Coercive field (53.5kV/cm). • Maximum strain of 0.07%.
Kakroo et al., 2016	750°C/2h	1100°C/2h	<ul style="list-style-type: none"> • Single BNT perovskite phase (100%) with rhombohedral symmetry. • Average grain size of 2 μm. • Remnant polarisation ($2.76\mu\text{C}/\text{cm}^2$). • Coercive field (12.31kV/cm).
Wei et al., 2018	850°C/4h	1150°C/4h	<ul style="list-style-type: none"> • Pure BNT perovskite phase (100%) with rhombohedral symmetry. • Average grain size of 7 μm. • Saturated P-E hysteresis and butterfly S-E loops indicating ferroelectric properties. • Remnant polarisation ($25\mu\text{C}/\text{cm}^2$). • Maximum strain of 0.07%.
Chou et al., 2011	800°C/3h	900-1050°C /3h	<ul style="list-style-type: none"> • Pure BNT perovskite phase (100%). • Relative density (81.8% of theoretical density), at 800°C/3h (calcination temperature) and 1000°C/3h (sintering temperature).
Khamman , 2014	-	1100°C/2h	<ul style="list-style-type: none"> • Pure BNT perovskite phase (100%) with rhombohedral symmetry. • Average grain size of 2.5 μm.
Fujii et al., 2016	-	1100°C/2h	<ul style="list-style-type: none"> • Pure BNT perovskite phase (100%). • Relative density (95% of theoretical density).

Watcharapasorn et al. (2007) (Watcharapasorn, Jiansirisomboon & Tunkasiri, 2007) investigated $\text{Bi}_{0.5}\text{Na}_{0.5}\text{Ti}_{1-x}\text{Fe}_x\text{O}_{3-0.5x}$ (Fe-BNT) ceramics using solid-state processing, where x ranged from 0 to 0.15mol%. The composition was calcined at $800^\circ\text{C}/2\text{ h}$ and sintered between 850 and $1000^\circ\text{C}/2\text{h}$. XRD showed a pure perovskite phase without secondary phases. In all Fe-BNT samples, the (200) peak position shifted to lower angle with increasing Fe_2O_3 contents. SEM images displayed very porous samples with smaller grain sizes for pure BNT ceramics and denser samples with larger grain sizes for 0.15mol%Fe-BNT ceramics sintered at 850°C . The highest relative density of 95% appeared at 1000°C for 0.15mol%Fe-BNT ceramics. In this work, Fe^{3+} substitution in the same site as Ti^{4+} can generate oxygen vacancies in the BNT perovskite structure that assisted in reducing the sintering temperature from 1000 to 850°C and promote densification.

Aksel and group (2010) (Aksel et al., 2010) investigated iron doped BNT (Fe-BNT) ceramics, synthesised by solid-state sintering using sintering temperature $1100^\circ\text{C}/2\text{h}$, and iron content ranged from 0 to 5mol%. XRD patterns showed single phase BNT for all samples. Adding iron to the BNT displayed defect complexes of oxygen vacancies in the perovskite structure, attributed to substitution of Fe^{3+} in the Ti^{4+} B-site of the perovskite structure, which leads to the formation of pseudocubic phase in the BNT lattice, due to lattice distortion of c/a for rhombohedral phase at room temperature. Also, Fe doped BNT ceramics lead to increases in the coercive field with increasing Fe_2O_3 .

A significant number of researchers have worked to improve density, microstructural, and electrical properties by studying the effect of dopants on the BNT ceramics using solid-state sintering processing route, a review of dopants effect on the density, microstructural, and electrical properties of BNT using solid-state sintering processing are described below and shown in Table 2.2.

Table 2.2. Summary of dopant effects on the properties of BNT prepared using solid-state sintering processing.

Citation	Stoichiometric formula	Sintering temperature /time	Properties
Maqbool et al., 2014	$(1-x)\text{Bi}_{0.5}\text{Na}_{0.5}\text{TiO}_3 - x\text{SrZrO}_3$, $x = 0-0.15\text{mol}\%$.	1150°C/2h	<ul style="list-style-type: none"> • Pure BNT perovskite phase (100%) with pseudocubic symmetry. • Average grain size (2.4 μm, at $x=0.10\%$). • Saturated typical P-E hysteresis and butterfly S-E loops shape identical to ferroelectric property. • Remnant polarisation (32$\mu\text{C}/\text{cm}^2$, at $x= 5\%$). • Coercive field (35kV/cm, at $x=0.05\%$). • Maximum strain (0.24%, at $x=0.09\%$).
Aman Ullah et al., 2015	$(1-x)\text{Bi}_{0.5}\text{Na}_{0.5}\text{TiO}_3 - x\text{Bi}(\text{Mg}_{0.5}\text{Ti}_{0.5})\text{O}_3$, $x = 0$ to 6 mol%.	1150°C/2h	<ul style="list-style-type: none"> • Single BNT perovskite phase (100%) with rhombohedral symmetry. • Average grain size (1 μm, at $x=0.06$). • Saturated typical P-E hysteresis loops shape identical to ferroelectric property. • Remnant polarisation (38$\mu\text{C}/\text{cm}^2$, at $x= 0.04$). • Coercive field (43kV/cm, at $x=0.04$).
Cheng et al., 2015	$\text{Bi}_{0.5}\text{Na}_{0.5}\text{Ti}_{1-x}(\text{Nd}_{0.5}\text{Ta}_{0.5})_x\text{O}_3$, $x=0$ to 1.2mol%.	1150°C/2h	<ul style="list-style-type: none"> • Pure BNT perovskite phase (100%). • Average grain size (4.9 μm, at $x= 0.06\%$). • Saturated typical P-E hysteresis loops shapes related to the ferroelectric property. • Remnant polarisation (34.7$\mu\text{C}/\text{cm}^2$, at $x=0.06\%$).
Jiang et al., 2014	$(1-x)\text{Bi}_{0.5}\text{Na}_{0.5}\text{TiO}_3 - x\text{KNbO}_3$, $x=0$ to 8mol%.	1150°C/2h	<ul style="list-style-type: none"> • Pure BNT perovskite phase (100%) with the coexistence of rhombohedral and orthorhombic symmetries. • Slimmed P-E hysteresis and S-E loops shape related to relaxer behaviour. • Remnant polarisation (1.8$\mu\text{C}/\text{cm}^2$, at $x= 0.06$). • Coercive field (5.6kV/cm, at $x= 0.06$). • Maximum strain (0.28%, at $x=0.06$).
Kakroo et al., 2016	$(\text{Na}_{0.5}\text{Bi}_{0.5})\text{TiO}_3 - x\text{CuO} - y\text{NiO}$, $x=y=0$ to 8mol%.	1100°C/2h	<ul style="list-style-type: none"> • Pure BNT perovskite phase (100%) of $x=y=0-0.04$, however appearing additional phases of $x=y=0.06$. • Average grain size (4 μm, at $x=y= 0.06$). • Remnant polarisation (9.12$\mu\text{C}/\text{cm}^2$, at $x=y=0.08$). • Coercive field (8.00kV/cm, at $x=y= 0.08$).
Wang et al., 2018	$0.94(\text{Bi}_{0.5}\text{Na}_{0.5})\text{TiO}_3 - 0.06\text{Ba}(\text{Zr}_{0.055}\text{Ti}_{0.945})\text{O}_3$	1130°C/5h	<ul style="list-style-type: none"> • Pure BNT perovskite phase (100%) with a combination of rhombohedral and tetragonal phases. • Average grain size of 1 μm. • Saturated typical P-E hysteresis loops shape related to ferroelectric behaviour. • Remnant polarisation (33.7$\mu\text{C}/\text{cm}^2$). • Maximum strain of 0.2%.

Citation	Stoichiometric formula	Sintering temperature /time	Properties
Wei et al., 2018	$(1-x)\text{Bi}_{0.5}\text{Na}_{0.5}\text{TiO}_3 - x\text{Ba}(\text{Zn}_{0.3}\text{Nb}_{0.7})\text{O}_3$, x=0 to 7% mol%.	1150°C/4h	<ul style="list-style-type: none"> • Pure BNT perovskite phase (100%) with rhombohedral symmetry (x=0-5%) and pseudocubic symmetry (x=6-7%). • Average grain size (1 μm, x=6%). • Slimmed P-E hysteresis and S-E loops shape related to relaxer behaviour at x=6%. • Remnant polarisation (5$\mu\text{C}/\text{cm}^2$, at x= 6%). • Maximum strain (0.04%, at x=5.5%).
Chou et al., 2011	CuO doped BNT, CuO = 0 to 8wt%.	900-1050°C /3h	<ul style="list-style-type: none"> • Main BNT perovskite phase and secondary CuO phase have appeared for all CuO doped BNT ceramics. • Relative density (96.7% of theoretical density), at 4wt% Cu-BNT ceramic, calcined at 700°C/3h and sintered at 950°C/3h.
Khamman, 2014	$\text{Bi}_{0.5}\text{Na}_{0.5}\text{Ti}_{1-x}\text{Ge}_x\text{O}_3$, x = 0 - 20mol%.	1100°C/2h (x=0), 1000°C/2h (x=0.05), 900°C/2h (x=0.1-0.2)	<ul style="list-style-type: none"> • Pure BNT perovskite phase (100%). • Average grain size (0.3 μm, x=0.2 and 900°C/2h sintering temperature). • Relative density (94% of theoretical density, at x=0.15 and 92% of theoretical density, at x=0.20, with 900°C/2h sintering temperature).

2.2.1.2. KNN Ceramics

Sintering temperature has a significant effect on the density, structural and electrical properties of pure KNN ceramics produced using solid-state processing. It is difficult to sinter KNN ceramics more than 1100°C, which is due to the volatilisation of alkali components such as K_2O and Na_2O . Increasing the volatility of alkali elements makes pure KNN ceramics less dense at higher than 1100°C sintering temperature. The previous studies are summarised in Table 2.3.

Several researchers have added dopants to KNN ceramics prepared by traditional solid-state sintering to improve density, microstructural, and electrical properties. A review of dopant effects on the density, microstructural, and electrical properties of KNN using solid-state sintering processing is described below and shown in Table 2.4.

Table 2.3. Summary of properties for undoped KNN ceramics, prepared using solid-state sintering processing.

Citation	Calcination temperature /time	Sintering temperature /time	Properties
Ponraj & Varma, 2016	800°C/5h	1100°C/1h	<ul style="list-style-type: none"> • Pure KNN perovskite phase (100%). • Average grain size of 3 μm. • Saturated typical P-E hysteresis loop shape, showing the ferroelectric property. • Remnant polarisation ($10\mu\text{C}/\text{cm}^2$). • Coercive field (4.86kV/cm).
He et al., 2013	900°C/8h	1130°C/2.5 h	<ul style="list-style-type: none"> • Pure KNN perovskite phase (100%) with orthorhombic symmetry. • Relative density (97.78% of theoretical density) • Saturated typical P-E hysteresis loop shapes, showing ferroelectric behaviour. • Remnant polarisation ($15\mu\text{C}/\text{cm}^2$). • Coercive field (10kV/cm).
Alkoy & Berksoy-Yavuz, 2012	900°C /1h	1100°C/4h	<ul style="list-style-type: none"> • Pure KNN perovskite phase (100%) with orthorhombic symmetry. • Average grain size (5 μm). • Saturated typical P-E hysteresis loops shape related to ferroelectric behaviour. • Remnant polarisation ($33\mu\text{C}/\text{cm}^2$).
Tian & Du, 2014	850°C/4h	1040-1140°C/2h	<ul style="list-style-type: none"> • Pure KNN perovskite phase (100%). • Saturated typical P-E hysteresis loop shape related to ferroelectric behaviour. • Remnant polarisation ($26\mu\text{C}/\text{cm}^2$). • Coercive field (16.7kV/cm).
Vendrell et al., 2015	700°C/2h	1125°C/2h	<ul style="list-style-type: none"> • Pure orthorhombic KNN perovskite phase (100%) • Average grain size (3.9 μm). • Saturated typical P-E hysteresis loop shapes, showing ferroelectric behaviour. • Remnant polarisation ($8.5\mu\text{C}/\text{cm}^2$). • Coercive field (11.4kV/cm).
Du et al., 2017	890°C/4.5h	1140°C/3.5h	<ul style="list-style-type: none"> • Pure KNN perovskite phase (100%) with orthorhombic structure. • Saturated typical P-E hysteresis and S-E loops shape corresponding to the ferroelectric property. • Remnant polarisation ($30\mu\text{C}/\text{cm}^2$). • Maximum strain of 0.05%.
Ramajo et al., 2014	-	1125°C/2h	<ul style="list-style-type: none"> • Main perovskite KNN phase with secondary $\text{K}_4\text{Nb}_6\text{O}_{17}$ phase attributed the evaporation of alkali element at the high sintering temperature. • Average grain size (1.61 μm). • Remnant polarisation ($13.8\mu\text{C}/\text{cm}^2$). • Coercive field (17.3 kV/cm).
Byun et al., 2018	-	1110°C/4h	<ul style="list-style-type: none"> • Pure KNN perovskite phase (100%) with orthorhombic structure. • Average grain size (8 μm). • Remnant polarisation ($6.12\mu\text{C}/\text{cm}^2$). • Coercive field (7.41 kV/cm)

Coondoo and group (2015) (Coondoo et al., 2015) studied pure KNN and 0.25mol%Fe-KNN (KNFN) ceramics prepared by solid-state sintering processing, where pure KNN ceramics sintered at 1090°C/2h and 0.25mol%Fe-KNN sintered at 980°C/2h. XRD results showed a pure perovskite phase with the orthorhombic phase at room temperature. SEM images displayed rectangular grains with larger grain sizes (9 μm) of 0.25mol%Fe-KNN ceramics. Adding Fe^{3+} for Nb^{5+} improved the relative density to 94% of theoretical density of 0.25mol%Fe-KNN ceramics, however, it reduces the dielectric constant from 650 (KNN) to 430 (KNFN).

Zuo and group (2009) (Zuo et al., 2009) investigated $(\text{Na}_{0.5}\text{K}_{0.5})(\text{Nb}_{1-x}\text{Fe}_x)\text{O}_{3-x}$, $\text{La}_y(\text{Na}_{0.5}\text{K}_{0.5})_{1-3y}\text{NbO}_3$ and $(\text{Na}_{0.5}\text{K}_{0.5})_{1-z}\text{La}_z(\text{Nb}_{1-z}\text{Fe}_z)\text{O}_3$ ceramic compositions prepared by solid state sintering at 1040-1130°C/4h, where x and y ranged from 0 to 4mol% and z ranged from 0 to 2mol%. XRD results showed single perovskite phase for all samples sintered at 1080°C, with orthorhombic phase (iron doped KNN) and transition from the orthorhombic to pseudocubic phase with increasing y content (lanthanum doped KNN) and z content (iron and lanthanum doped KNN). The replacement of Fe^{3+} (0.65Å) for Nb^{5+} (0.64Å) does not show any change in the crystal structure because they have similar ionic sizes, however, the replacement of La^{3+} (1.36Å) for K^+ (1.64Å) and Na^+ (1.39Å) shows a clear change in the crystal structure and creates oxygen vacancies. SEM images showed that adding Fe_2O_3 to the KNN ceramics sintered at 1100°C improved densification with increasing grain sizes from 2.5 μm (pure KNN) to the larger grain sizes of 8.0 μm (x=3mol%). High densification was obtained by adding 0.5mol% Fe_2O_3 and sintering at 1100°C for a maximum relative density of 97.9% of theoretical density. Adding 0.25mol% La- Fe_2O_3 to KNN ceramics sintered at 1080°C improved the remnant polarization to 26.5 $\mu\text{C}/\text{cm}^2$ compared with 15.1 $\mu\text{C}/\text{cm}^2$ (pure KNN) and 21.5 $\mu\text{C}/\text{cm}^2$ (0.5mol%Fe doped KNN).

Chan and group (2011) (Chan et al., 2011) studied Sb-doped KNN ($\text{Na}_{0.5}\text{K}_{0.5}\text{Nb}_{1-x}\text{Sb}_x\text{O}_3$) ceramics prepared by solid-state sintering between 1000 and 1100°C/2h, where x ranged between 0 to 0.1mol%. XRD patterns indicated that all Sb-doped KNN samples had pure perovskite structure with no secondary phases, and the phase structure was completely changed from tetragonal to orthorhombic at x= 0.07-0.1mol%. Densified ceramics with a maximum bulk density of 4.31 g/cm^3 occurred at 1075°C/2h sintering temperature and x=0.03mol%. Relaxor hysteresis loop has obtained at x=0 and 0.1mol and then changed to ferroelectric loop at x=0.3 and 0.7mol with maximum

Chapter Two| Literature Review

remnant polarisation of $12.7 \mu\text{C}/\text{cm}^2$ ($x=0.07\text{mol}$) and minimum coercive field of $9.3 \text{ kV}/\text{cm}$ ($x=0$) measured at 120°C and 60 Hz frequency.

Cheng and group (2012) (Cheng, Chen & Yang, 2012) investigated the $0.5\text{mol}\%\text{Ta}_2\text{O}_5$ doped KNN ceramics fabricated by solid-state sintering processing sintered at differed sintering temperatures from 1060 to $1140^\circ\text{C}/3\text{h}$. XRD showed a pure perovskite phase with orthorhombic symmetry. SEM micrographs exhibited a densified ceramic with maximum grain sizes of $1\text{-}2 \mu\text{m}$ at 1100°C . The maximum relative density (97.6%) was obtained at 1100°C . Hysteresis loop results exhibited maximum remnant polarisation of $22 \mu\text{C}/\text{cm}^2$ (1100°C sintering temperature) and minimum coercive field of $10 \text{ kV}/\text{cm}$ (1060°C sintering temperature).

Table 2.4. A summary of dopants effect on the properties of KNN ceramics using solid-state sintering processing, according to the previous papers.

Citation	Stoichiometric formula	Sintering temperature /time	Properties
Ponraj & Varma, 2016	$\text{K}_{0.5}\text{Na}_{0.5}\text{NbO}_3 + x(0.5\text{Li}_2\text{O} - 0.5\text{K}_2\text{O} - 2\text{B}_2\text{O}_3)$ (glass) $X=0$ to $2 \text{ wt}\%$.	$1100^\circ\text{C}/1\text{h}$	<ul style="list-style-type: none"> • Pure KNN perovskite phase of $x=0\text{-}1\text{wt}\%$ without secondary phases, however main KNN perovskite phase with secondary phases of $\text{K}_2\text{B}_4\text{O}_7$ and LiKB_4O_7 have detected at $x=1.5\text{-}2\text{wt}\%$. • Average grain size ($8 \mu\text{m}$, at $x=0.01$). • Saturated typical P-E hysteresis loop shape identical to ferroelectric property. • Remnant polarisation ($22.3\mu\text{C}/\text{cm}^2$, at $x=0.01$). • Coercive field ($10.6\text{kV}/\text{cm}$, at $x=0.01$).
He et al., 2013	$(1-x)\text{K}_{0.5}\text{Na}_{0.5}\text{NbO}_3 - x\text{Bi}(\text{Mg}_{0.5}\text{Ti}_{0.5})\text{O}_3$, $x=0$ to $4\text{mol}\%$.	1130°C ($x=0$), 1130°C ($x=0.01$), and $1210^\circ\text{C}/2.5\text{h}$ ($x=0.02\text{-}0.04$)	<ul style="list-style-type: none"> • Pure KNN perovskite phase without observed secondary phases of all samples, with introducing orthorhombic ($x=0\text{-}0.03$) and tetragonal ($x=0.04$) structure. Average grain size ($8 \mu\text{m}$, at $x=0.01$). • Relative density (98.89% of theoretical density, at $x=0.01$). • Hysteresis P-E loops detected saturated typical hysteresis shapes of $x=0\text{-}0.03$ and slimmed shape of $x=0.04$, referring to the transition of ferroelectric to relaxer behaviour. • Remnant polarisation ($22.1\mu\text{C}/\text{cm}^2$, at $x=0.01$). • Coercive field ($13.16\text{kV}/\text{cm}$, at $x=0.01$).
Alkoy & Berksoy -Yavuz, 2012	$1\text{mol}\%\text{CuO}$ doped $\text{K}_{0.5}\text{Na}_{0.5}\text{NbO}_3$	$1090^\circ\text{C}/4\text{h}$	<ul style="list-style-type: none"> • Pure KNN perovskite phase (100%) with orthorhombic symmetry. • Average grain size ($40 \mu\text{m}$). • Propeller-like P-E hysteresis loop shape identical to hard piezoelectric behaviour. • Remnant polarisation ($3\mu\text{C}/\text{cm}^2$).

Chapter Two| Literature Review

Citation	Stoichiometric formula	Sintering temperature /time	Properties
Vendrell et al., 2015	$(K_{0.5}Na_{0.5})(Nb_{1-x}Zr_x)O_{3-x}$ (KNNZ) and $(K_{0.5}Na_{0.5})(Nb_{1-x}Ti_x)O_{3-x}$ (KNNT), x=0 to 0.5mol%.	1125°C/2h	<ul style="list-style-type: none"> • Pure KNN perovskite phase (100%) with orthorhombic structure. • Average grain size (2.1 μm (0.5mol% KNNZ) and 1.7 μm (0.5mol% KNNT)). • Saturated typical P-E hysteresis loop shape identical to ferroelectric property. • Remnant polarisation (19.8 $\mu\text{C}/\text{cm}^2$ for 0.5mol% KNNT). • Coercive field (15kV/cm for 0.5mol% KNNT).
Lopez-Juarez et al., 2015	1-x $K_{0.5}Na_{0.5}NbO_{3-x}MnO$, x=0-2mol%.	1100°C/2h	<ul style="list-style-type: none"> • Pure KNN perovskite phase (100%) with orthorhombic structure. • Average grain size (3.8 μm, at x=0.02). • Adding Mn^{2+} to the KNN ceramics create dipole defects due to the generation of oxygen vacancies resulting from charges imbalance of substitution Mn^{2+} (ionic radius 0.83 Å) in the Nb^{5+} (ionic radius 0.64 Å) same B-perovskite structure. • Bulk density (4.27 g/cm^3, at x=0.02).
Du et al., 2017	Addition of 0.6wt% of each of Dy_2O_3 , Er_2O_3 , Eu_2O_3 and Pr_6O_{11} to $K_{0.5}Na_{0.5}NbO_3$ ceramics.	1140°C/ 3.5h	<ul style="list-style-type: none"> • Pure KNN perovskite phase (100%) with orthorhombic structure. • Average grain size (larger 6.91 μm (Er_2O_3 added KNN) and smaller 1.11 μm (Pr_6O_{11} added KNN)). • Saturated typical P-E hysteresis and S-E loops shape corresponding to ferroelectric behaviour. • Remnant polarisation (39$\mu\text{C}/\text{cm}^2$ for 0.6wt% Dy_2O_3 doped KNN). • Maximum strain (0.07% for 0.6wt% Pr_6O_{11} doped KNN).
Byun et al., 2018	$(K_{0.5}Na_{0.5})_{1-x}Ag_xNbO_3$, x=0-30mol%	1110°C/4h	<ul style="list-style-type: none"> • Pure KNN perovskite phase (100%) with orthorhombic structure at x= 0-20mol%, however main perovskite KNN phase with secondary phase and pseudocubic symmetry have detected at x=25-30mol%. • Average grain size (3 μm, at x= 30mol%). • Remnant polarisation (20.72 $\mu\text{C}/\text{cm}^2$, at x= 30mol%). • Coercive field (9.03 kV/cm, at x= 30mol%).
Tian & Du, 2014	$(1-x)K_{0.5}Na_{0.5}NbO_{3-x}MnO_2$, x=0 to 0.8mol%.	1040- 1140°C/2h	<ul style="list-style-type: none"> • Single KNN perovskite phase (100%) with coexistence of orthorhombic and tetragonal structure of all samples sintered at 1080°C. • Saturated typical P-E hysteresis loop shape identical to ferroelectric property. • Remnant polarisation (28.3$\mu\text{C}/\text{cm}^2$, at x= 0.004 and 1100°C). • Coercive field (13.7kV/cm., at x=0.004 and 1100°C).

Xie et al., 2018 investigated $(1-x)(\text{K}_{0.5}\text{Na}_{0.5})\text{NbO}_3-x\text{Sr}(\text{In}_{0.5}\text{Nb}_{0.5})\text{O}_3$ (KNN-xSIN) ceramics, which were synthesised using solid-state sintering, where x ranged from 0.05 to 0.25. KNN-xSIN ceramics were calcined at 950°C/5h and sintered at 1200-1270°C/5h. XRD results show single phase with a pseudo-cubic structure for all doped KNN ceramics without existing any secondary phases. Adding 0.25SIN to the KNN presented relaxor behaviour.

2.2.2. Microwave Sintering Processing

2.2.2.1. BNT Ceramics

Ramana et al. (2011) investigated $\text{Bi}_{0.5}\text{Na}_{0.5}\text{TiO}_3$ (BNT) ceramics. BNT ceramics were prepared by microwave processing, calcined and sintered at 700°C/2h (conventional furnace) and 950°C/30 mins (laboratory-modified microwave oven), respectively. XRD patterns showed a pure perovskite phase with tetragonal symmetry. SEM images displayed inhomogeneous distribution in the shape and size of grains with average grain size of 1 μm . The densification had significantly improved with a relative density of 99% of theoretical density. At room temperature, the dielectric constant and loss factor were considerably enhanced to 798 and 0.04, respectively.

Chiang et al. (2013) studied $\text{Bi}_{0.5}\text{Na}_{0.5}\text{TiO}_3+x\text{ZnO}$ (BNT+xZnO) ceramics. BNT+xZnO ceramics were manufactured by microwave processing, where x ranged from 0-3 (wt%). BNT+xZnO ceramics calcined and sintered at 800°C/2h (conventional furnace) and 750-1000°C/30 (laboratory-modified microwave oven), respectively. XRD results revealed the main perovskite BNT phase without presenting secondary phases of x=0-1. However, the main KNN perovskite phase with the secondary phase of Zn_2TiO_4 was identified at higher ZnO contents of 2-3%. At 1000°C sintering temperature, SEM micrographs showed a significant increase in average grains sizes from 2.9 to 7.3 μm of x= 0.1 to 3.0, respectively, Addition of 0.1wt%ZnO to BNT ceramics sintered at 950°C, significantly increased remnant polarization and coercive field from 9 $\mu\text{C}/\text{cm}^2$ and 39 kV/cm (pure BNT) to 38 $\mu\text{C}/\text{cm}^2$ and 58.5kV/cm, respectively.

2.2.2.2. KNN Ceramics

Feizpour and group (2014) (Feizpour et al., 2014) studied $\text{K}_{0.5}\text{Na}_{0.5}\text{NbO}_3$ (KNN) ceramics. KNN ceramics were prepared by microwave-assisted sintering method, calcined and sintered at 950°C/36min and 1115°C/36min (laboratory-modified microwave oven), respectively. XRD results showed pure KNN perovskite phase with the orthorhombic structure of the microwave sintered sample. SEM micrographs

displayed the nearly cubic-like shape of grains with average grain sizes of ca 3.8 μm . Densification was achieved with a high relative density of 93.8% of theoretical density. Hysteresis P-E loop showed typical saturated shape, indicating the achievement of ferroelectric properties. Good electrical results were achieved at room temperature, for example, remnant polarisation $18\mu\text{C}/\text{cm}^2$, coercive field $12\text{kV}/\text{cm}$, dielectric constant (427) and dielectric loss factor (0.035).

2.2.3. Melt processing

2.2.3.1. KNN Glass- Ceramics

Yongsiri and colleague (2014) (Yongsiri et al., 2014) investigated two different glass-ceramic compositions including 0.5-1.0 Er_2O_3 doped 70KNN–30 SiO_2 and 80KNN–20 SiO_2 (mol%), manufactured by incorporation processing. $\text{K}_{0.5}\text{Na}_{0.5}\text{NbO}_3$ powder was prepared without mixing with SiO_2 by solid-state sintering processing, and then KNN glasses were prepared by mixing $\text{K}_{0.5}\text{Na}_{0.5}\text{NbO}_3$ powder with SiO_2 , then melt-quenching processing melting at $1300^\circ\text{C}/15$ min. DTA analysis exhibited exothermic peaks identified at 664, 672, 601, 607°C , indicating the crystallization temperatures for 0.5 Er_2O_3 -70KNN–30 SiO_2 , 1.0 Er_2O_3 -70KNN–30 SiO_2 , 0.5 Er_2O_3 -80KNN–20 SiO_2 and 1.0 Er_2O_3 -80KNN–20 SiO_2 glasses, respectively. Heat treatment temperatures of 670 and 570°C for 4h have been used to prepare 0.5-1.0 Er_2O_3 doped 70KNN–30 SiO_2 and 0.5-1.0 Er_2O_3 doped 80KNN–20 SiO_2 glass-ceramics, respectively. XRD results showed an amorphous pattern with no sharp crystalline peaks for melted glass samples. However, crystalline sharp peaks appeared for heat treated glass samples as a result of the formation of $\text{K}_{0.65}\text{Na}_{0.35}\text{NbO}_3$ glass-ceramics. SEM images showed grains on heat treated glass samples, consistent with the formation of KNN glass-ceramics. The dielectric properties significantly improved to maximum dielectric constant (458.41) and minimum dielectric loss factor (0.001), for 0.5 Er_2O_3 doped 70KNN–30 SiO_2 and 1.0 Er_2O_3 doped 80KNN–20 SiO_2 glass-ceramics respectively, measured at room temperature and 100 kHz frequency.

Fanelli and group (2011) (Fanelli et al., 2011) studied 13 K_2O -10 Na_2O -27 Nb_2O_5 -50 SiO_2 (KNaNS) glass-ceramics prepared by melt quenching, melted at $1500^\circ\text{C}/1.5\text{h}$. DTA analysis exhibited an exothermic peak at approximately 700°C indicating the crystallisation temperature. XRD results showed a broad hump with no peaks for the melted composition, however, sharp peaks indicating crystallinity (formation of glass-ceramics) were shown for heat treated glass at $700^\circ\text{C}/10\text{h}$.

Zheng and group (2016) (Zheng et al., 2016) investigated $15\text{Na}_2\text{O}-15\text{K}_2\text{O}-30\text{Nb}_2\text{O}_5-27\text{SiO}_2-10\text{B}_2\text{O}_3-3\text{CeO}_2$ (KNNBSC) glass-ceramics prepared by melt-quenching, melted at $1400^\circ\text{C}/2\text{h}$. DTA analysis showed two exothermic peaks at 707 and 900°C , indicating the crystallisation temperatures. KNNBSC glasses were heat treated at various temperatures and times e.g. G1 ($707^\circ\text{C}/5\text{h}$), G2 ($707^\circ\text{C}/4\text{h} + 900^\circ\text{C}/1\text{h}$), G3 ($707^\circ\text{C}/3\text{h} + 900^\circ\text{C}/2\text{h}$), G4 ($707^\circ\text{C}/2\text{h} + 900^\circ\text{C}/3\text{h}$), G5 ($707^\circ\text{C}/1\text{h} + 900^\circ\text{C}/4\text{h}$) and G6 ($900^\circ\text{C}/5\text{h}$). XRD results showed the main $\text{Na}_{0.9}\text{K}_{0.1}\text{NbO}_3$ phase with sharp peaks and the presence of secondary phases for all heat treated glasses, indicating crystallisation and formation of glass-ceramics from glasses of KNNBSC composition. SEM images revealed very fine grains, with no clear grain boundaries and irregular grain shapes for glasses heat treated at G1, then clearly shown boundaries, with grain shapes becoming regular and increasing grain sizes with increasing holding time from 1 to 5h at the 900°C heat treatment temperature. The dielectric constant significantly enhanced from 121 to 270 with increasing heat treatment temperatures from 707 to $900^\circ\text{C}/5\text{h}$, respectively. Hysteresis P-E loops of KNNBSC glass-ceramics revealed unsaturated and slimmed shape, for all glass-ceramics referring to relaxor than ferroelectric property.

Kioka and group (2011) (Kioka et al., 2011b) studied $(30-x)\text{K}_2\text{O}-x\text{Na}_2\text{O}-25\text{Nb}_2\text{O}_5-45\text{SiO}_2$ (KNNS) glass-ceramic compositions, where x contents included 0, 5, 10, 20 and 30mol%, for glasses synthesized by melt-quenching processing at $1300^\circ\text{C}/1\text{h}$. DTA investigation revealed three exothermic peaks (crystallization peaks) place at 748 , 770 and 827°C for $x=0$ mol% and 764 , 852 and 877°C for $x=5\text{mol}\%$. On the other hand, they exhibited one exothermic peak identified at 754 , 749 , 739°C for each of $x=10$, 20 and 30mol% samples, respectively. XRD results exhibited perovskite $\text{K}_{0.5}\text{Na}_{0.5}\text{NbO}_3$ phase for heat treated $20\text{K}_2\text{O}-10\text{Na}_2\text{O}-25\text{Nb}_2\text{O}_5-45\text{SiO}_2$ and $10\text{K}_2\text{O}-20\text{Na}_2\text{O}-25\text{Nb}_2\text{O}_5-45\text{SiO}_2$ glass-ceramics.

Chapter Three

Experimental Procedures

3.1. Introduction

Chapter three describes the three experimental processing routes used in this study: conventional solid-state sintering, microwave sintering and melt processing. In this project a variety of measurements has been used to investigate electrical ceramics and glass-ceramics, including structural analysis (X-ray diffraction, Raman, scanning electron microscopy), differential thermal analysis, density and electrical measurements (polarization and strain versus electric field, dielectric constant and dielectric loss factor), as shown schematically in Figure 3.1.

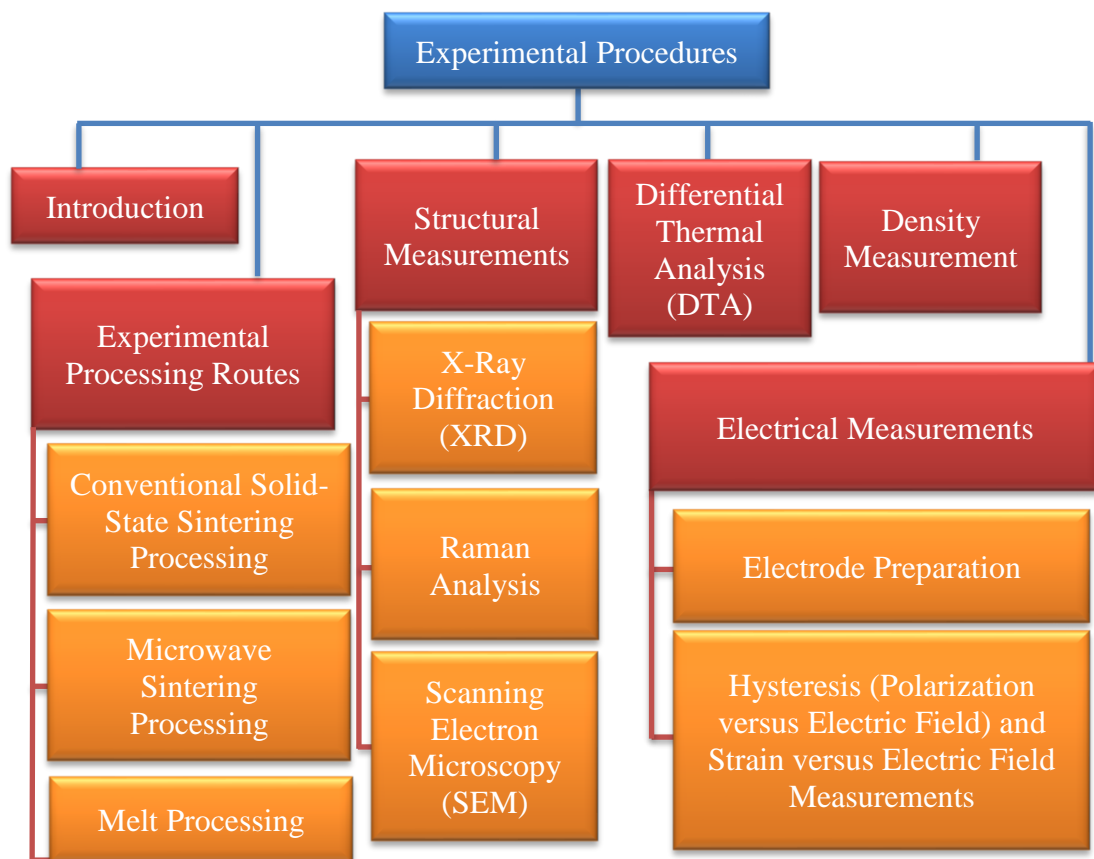


Figure 3.1. Overview of the experimental procedures (Chapter three).

3.2. Experimental Processing Routes

In the present project, three different processing routes have been used to prepare ceramics and glass ceramics, described as follows.

3.2.1. Conventional Solid-State Sintering

The solid-state sintering processing route has been used to prepare electrical ceramics, as follows:

3.2.1.1. Bismuth Sodium Titanate (BNT) Ceramics

A conventional solid-state sintering processing route was used to prepare solid-state BNT ceramics with different calcination and sintering temperatures, as presented in Table 3.1. Bi₂O₃ (99%, Alfa Aesar), Na₂CO₃ (99%, Better Equipped) and TiO₂ (99.9%, Aldrich) were used as starting raw materials, then BNT ceramic synthesis was carried out to produce ceramics according to the stoichiometric formula Bi_{0.5}Na_{0.5}TiO₃. The nominal compositions of the samples prepared in the present work are summarised in Table 3.1. The manufacturing process steps used to produce pure bismuth sodium titanate ceramics using conventional solid-state sintering are shown in Figure 3.2. The pure BNT batch compositions (30 g) were calcined in an electric furnace by ramping at 5°C / min to different calcination temperatures of 700°C and 800°C and held at these temperatures for 4h, then cooled slowly to room temperature. All of the prepared BNT pellets (10 mm diameter and 1-2 mm thickness) in the present work were sintered in one process as follows: (i) Heat from room temperature at 3°C/min to 300°C and hold at this temperature for 1h; (ii) heat at 3°C/min from 300°C to 700°C and hold at this temperature for 1h; (iii) and finally heat at 5°C/min from 700°C to different sintering temperatures, such as 1000, 1050, 1075 and 1100°C and hold at each temperature for 2h; then allow samples to cool slowly inside the furnace to room temperature.

Table 3.1. Sample name, nominal sample compositions, calcination and sintering temperatures per time.

Sample name	Nominal composition	Calcination temperature per time (T/t)	Sintering temperature per time (T/t)
B700, 1000	Bi _{0.5} Na _{0.5} TiO ₃	700°C/4h	1000°C/2h
B700, 1050	Bi _{0.5} Na _{0.5} TiO ₃	700°C/4h	1050°C/2h
B700, 1075	Bi _{0.5} Na _{0.5} TiO ₃	700°C/4h	1075°C/2h
B700, 1100	Bi _{0.5} Na _{0.5} TiO ₃	700°C/4h	1100°C/2h
B800, 1000	Bi _{0.5} Na _{0.5} TiO ₃	800°C/4h	1000°C/2h
B800, 1050	Bi _{0.5} Na _{0.5} TiO ₃	800°C/4h	1050°C/2h
B800, 1075	Bi _{0.5} Na _{0.5} TiO ₃	800°C/4h	1075°C/2h
B800, 1100	Bi _{0.5} Na _{0.5} TiO ₃	800°C/4h	1100°C/2h

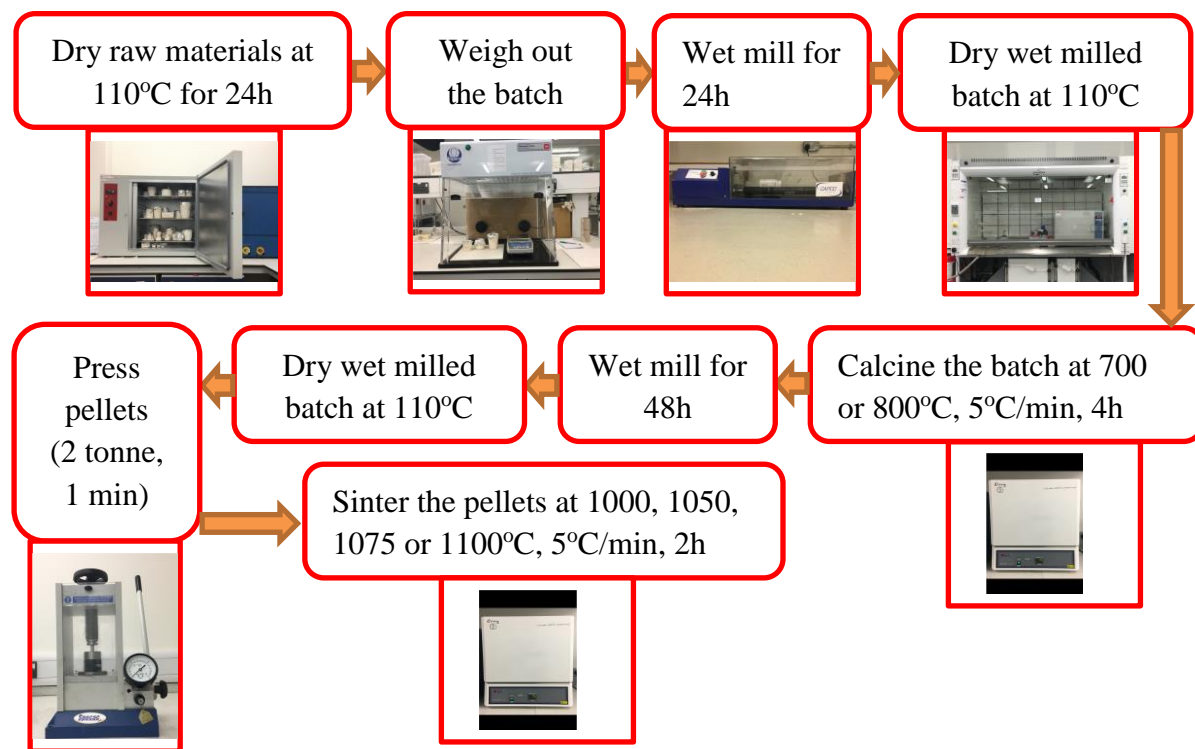


Figure 3.2. Solid-state sintering processing for pure solid-state sintered BNT ceramics.

3.2.1.2. Iron-Doped Bismuth Sodium Titanate (BNTFe) Ceramics

A conventional solid-state sintering processing route was used to prepare solid-state iron-doped BNT (BNTFe) ceramics with calcination and sintering temperatures as presented in Table 3.2. Bi_2O_3 (99%, Alfa Aesar), Na_2CO_3 (99%, Better Equipped), TiO_2 (99.9%, Aldrich) and Fe_2O_3 (>99%, Aldrich) were used as starting raw materials, then BNTFe ceramic synthesis was carried out to prepare ceramics according to the stoichiometric formula $\text{Bi}_{0.5}\text{Na}_{0.5}\text{Ti}_{1-x}\text{Fe}_x\text{O}_{3-0.5x}$ where $x = 0, 0.025, 0.0375, 0.050, 0.070$ and 0.100 . The nominal compositions of the samples prepared in the present work are summarised in Table 3.2. The manufacturing process steps used to synthesise iron-doped bismuth sodium titanate ceramics using traditional solid-state sintering are shown in Figure 3.3. The iron-doped BNT batch compositions (30 g) were calcined in an electric furnace by ramping at $5^\circ\text{C}/\text{min}$ to a calcination temperature of 700°C and held at these temperatures for 4h, then cooled slowly to room temperature. All of the prepared BNTFe pellets (10 mm diameter and 1-2 mm thickness) in the present work were sintered in one process as follows: (i) Heat from room temperature at $3^\circ\text{C}/\text{min}$ to 300°C and hold at this temperature for 1h; (ii) heat at $3^\circ\text{C}/\text{min}$ from 300°C to 700°C and hold at this temperature for 1h; (iii) and finally heat at $5^\circ\text{C}/\text{min}$ from 700°C to different sintering temperatures, such as 900°C and hold at each temperature for 2h; then allow samples to cool slowly inside the furnace to room temperature.

Table 3.2. Nominal samples, nominal compositions and sintering temperature per time.

Sample name	Nominal composition	Sintering temperature and time (T/t)
BFe0.00	$\text{Bi}_{0.5}\text{Na}_{0.5}\text{TiO}_3$	900°C/2h
BFe2.50	$\text{Bi}_{0.5}\text{Na}_{0.5}\text{Ti}_{0.975}\text{Fe}_{0.025}\text{O}_{2.9875}$	900°C/2h
BFe3.75	$\text{Bi}_{0.5}\text{Na}_{0.5}\text{Ti}_{0.9625}\text{Fe}_{0.0375}\text{O}_{2.98125}$	900°C/2h
BFe5.00	$\text{Bi}_{0.5}\text{Na}_{0.5}\text{Ti}_{0.95}\text{Fe}_{0.05}\text{O}_{2.975}$	900°C/2h
BFe7.00	$\text{Bi}_{0.5}\text{Na}_{0.5}\text{Ti}_{0.93}\text{Fe}_{0.07}\text{O}_{2.965}$	900°C/2h
BFe10.00	$\text{Bi}_{0.5}\text{Na}_{0.5}\text{Ti}_{0.9}\text{Fe}_{0.1}\text{O}_{2.95}$	900°C/2h

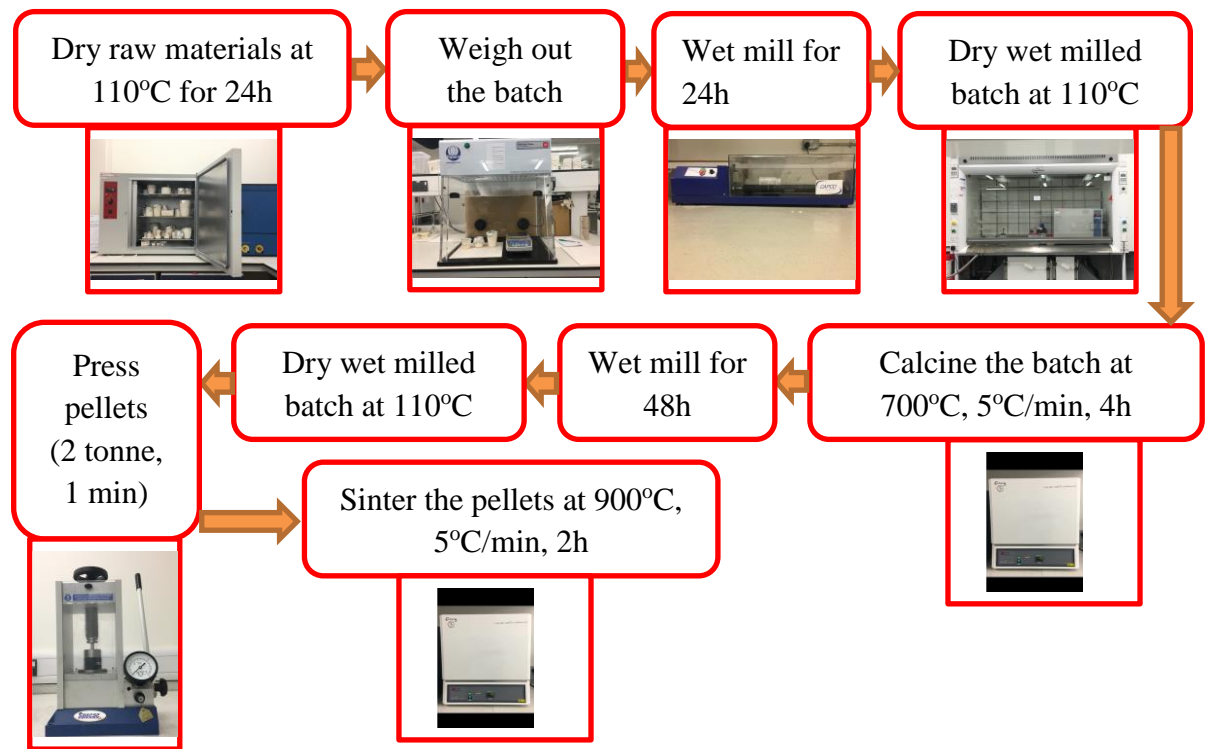


Figure 3.3. Solid-state sintering processing for iron-doped BNT ceramics.

3.2.1.3. Potassium Sodium Niobate (KNN) Ceramics

A conventional solid-state processing route was used to synthesise solid-state sintered KNN ceramics with different calcination and sintering temperatures as shown in Table 3.3. K_2CO_3 (>99%, Better Equipped), Na_2CO_3 (>99.9%, Better Equipped) and Nb_2O_5 (>99.9%, Aldrich) were used as starting raw materials, then KNN batch (30 g) prepared according to the stoichiometric formula $\text{K}_{0.5}\text{Na}_{0.5}\text{NbO}_3$. The nominal compositions of the samples prepared in the present work are summarised in Table 3.3. The

manufacturing of pure potassium sodium niobate ceramics using conventional solid-state sintering processing are shown in Figure 3.4. The pure KNN batch compositions were calcined in an electric furnace at different calcination temperatures of 700°C, and 800°C with ramping of 5°C/min and held for 4h, then cooled them gradually to room temperature. All of the KNN prepared pellets in the present work were sintered in one process as follows: (i) Heat from room temperature at 3°C/min to 300°C and hold at this temperature for 1h; (ii) heat at 3°C/min from 300°C to 700°C and hold at this temperature for 1h; (iii) and finally heat at 5°C/min from 700°C to different sintering temperatures, such as 1000, 1050, 1075 and 1100°C and hold at each temperature for 2h; then allow samples to cool slowly inside the furnace to room temperature.

Table 3.3. Nominal sample compositions, calcination temperature and sintering temperatures per time.

Sample name	Nominal composition	Calcination temperature per time (T/t)	Sintering temperature per time (T/t)
K700, 1000	$K_{0.5}Na_{0.5}NbO_3$	700°C/4h	1000°C/2h
K700, 1050	$K_{0.5}Na_{0.5}NbO_3$	700°C/4h	1050°C/2h
K700, 1075	$K_{0.5}Na_{0.5}NbO_3$	700°C/4h	1075°C/2h
K700, 1100	$K_{0.5}Na_{0.5}NbO_3$	700°C/4h	1100°C/2h
K800, 1000	$K_{0.5}Na_{0.5}NbO_3$	800°C/4h	1000°C/2h
K800, 1050	$K_{0.5}Na_{0.5}NbO_3$	800°C/4h	1050°C/2h
K800, 1075	$K_{0.5}Na_{0.5}NbO_3$	800°C/4h	1075°C/2h
K800, 1100	$K_{0.5}Na_{0.5}NbO_3$	800°C/4h	1100°C/2h

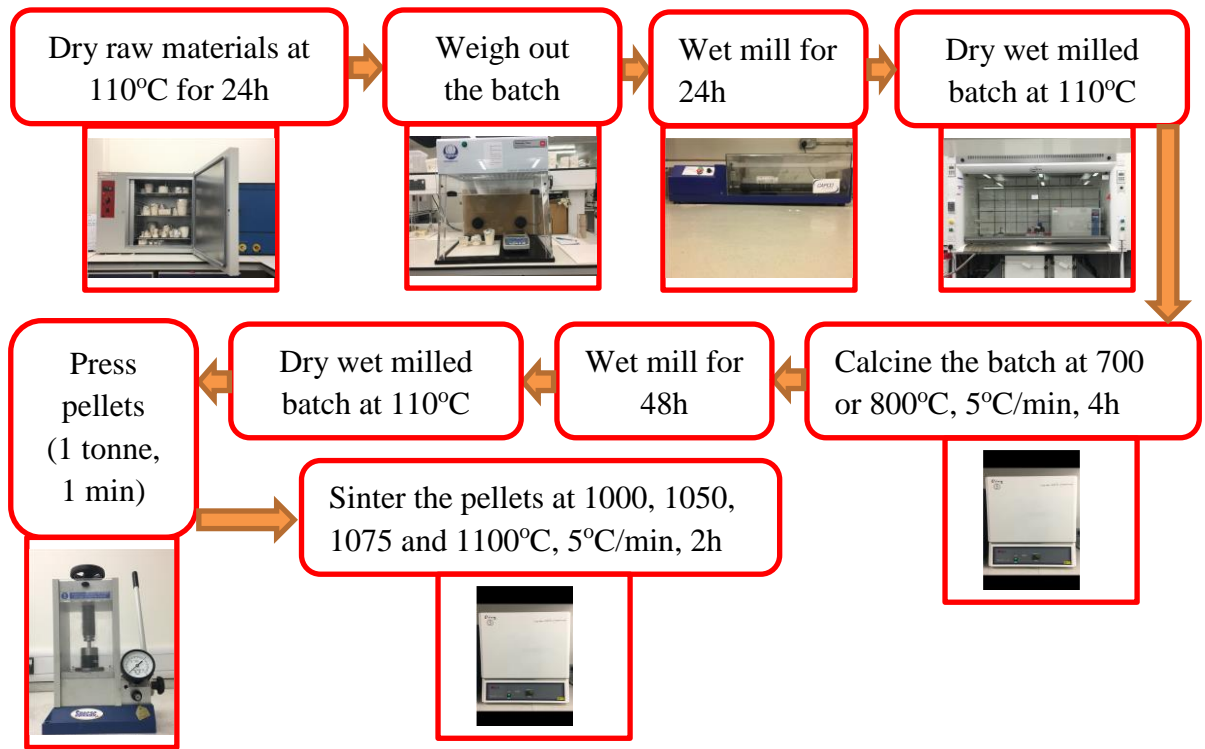


Figure 3.4. Processing flow diagram for solid-state sintered KNN ceramics.

3.2.1.4. Iron-Doped Potassium Sodium Niobate (KNNFe) Ceramics

A traditional solid-state sintering processing route was used to synthesise solid-state iron-doped KNN ceramics with calcination and sintering temperatures, as presented in Table 3.4. K_2O (99%, Alfa Aesar), Na_2CO_3 (99%, Better Equipped), Nb_2O_5 (99.9%, Aldrich) and Fe_2O_3 (>99%, Aldrich) were used as starting raw materials, then KNNFe ceramic synthesis was carried out to manufacture ceramics according to the stoichiometric formula $K_{0.5}Na_{0.5}Nb_{1-x}Fe_xO_{3-x}$ where $x = 0, 0.02, 0.025, 0.050$ and 0.100 . The nominal compositions of the samples prepared in the present work are summarised in Table 3.4. The manufacturing process steps used to synthesise iron-doped potassium sodium niobate ceramics using conventional solid-state sintering are shown in Figure 3.5. The iron-doped KNN batch compositions (30 g) were calcined in an electric furnace by ramping at $5^\circ C/min$ to a calcination temperature of $700^\circ C$ and held at these temperatures for 4h, then cooled slowly to room temperature. All the KNNFe prepared pellets (10 mm diameter and 1-2 mm thickness) in the present work were sintered in one process as follows: (i) Heat from room temperature at $5^\circ C/min$ to $300^\circ C$ and hold at this temperature for 1h; (ii) heat at $5^\circ C/min$ from $300^\circ C$ to $700^\circ C$ and hold at this temperature for 1h; (iii) and finally heat at $5^\circ C/min$ from $700^\circ C$ to different sintering

temperatures, such as 1000°C and hold at each temperature for 2h; then allow samples to cool slowly inside the furnace to room temperature.

Table 3.4. Nominal sample, nominal compositions and sintering temperature per time.

Sample name	Nominal composition	Sintering temperature per time (T/t)
KFe0.00	$K_{0.5}Na_{0.5}NbO_3$	1000°C/2h
KFe2.00	$K_{0.5}Na_{0.5}Nb_{0.98}Fe_{0.02}O_{2.98}$	1000°C/2h
KFe2.50	$K_{0.5}Na_{0.5}Nb_{0.975}Fe_{0.025}O_{2.975}$	1000°C/2h
KFe5.00	$K_{0.5}Na_{0.5}Nb_{0.95}Fe_{0.05}O_{2.95}$	1000°C/2h
KFe10.00	$K_{0.5}Na_{0.5}Nb_{0.9}Fe_{0.1}O_{2.9}$	1000°C/2h

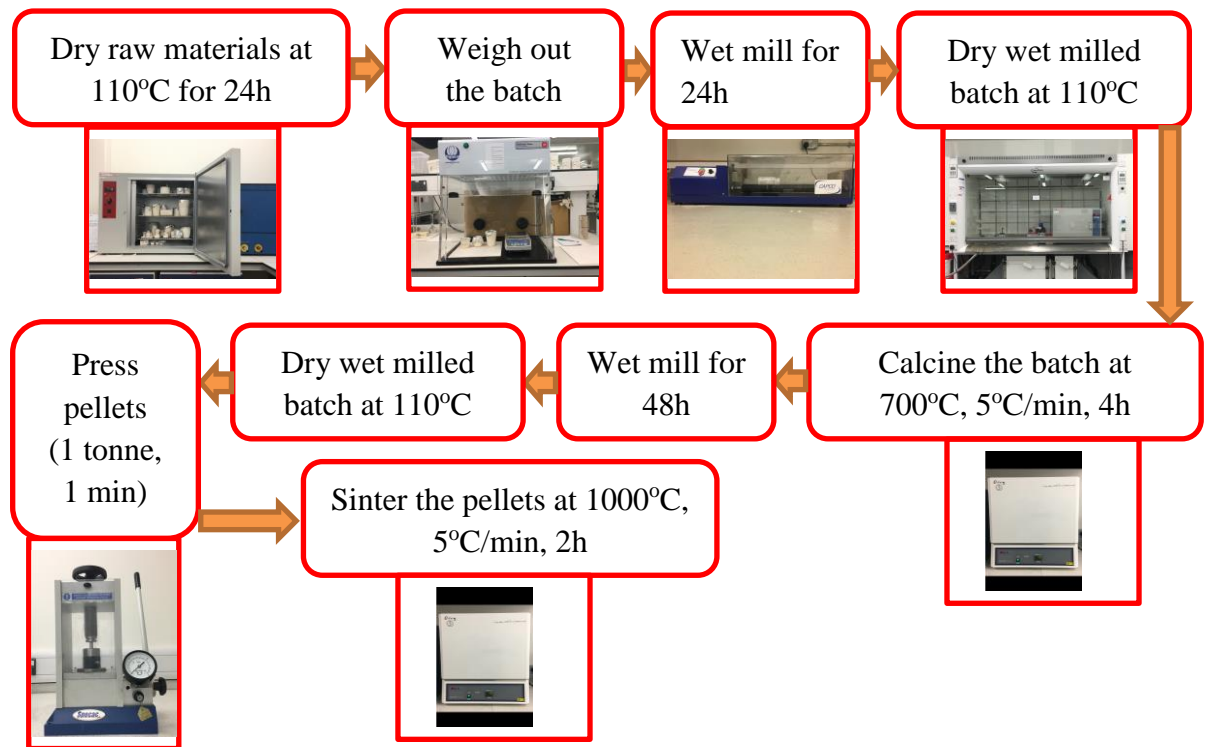


Figure 3.5. Solid-state sintering processing for iron-doped KNN ceramics.

3.2.2. Microwave Sintering Processing

The microwave sintered processing route has been used to prepare electrical ceramics, as follows:

3.2.2.1. Bismuth Sodium Titanate (BNT) Ceramics

The microwave sintering processing route was used to prepare microwave sintered BNT ceramics. The starting raw materials in the present work consist of Bi_2O_3 (99%, Alfa Aesar), Na_2CO_3 (99%, Better Equipped) and TiO_2 (99.9%, Aldrich) which were used to synthesise BNT ceramics according to the stoichiometric formula $\text{Bi}_{0.5}\text{Na}_{0.5}\text{TiO}_3$. Details of BNT samples prepared using microwave processing are summarised in Table 3.5. A process diagram of the preparation of bismuth sodium titanate ceramics using the microwave sintering process studied here is shown in Figure 3.6. The prepared compositions were calcined individually inside the furnace at ramping rate $5^\circ\text{C}/\text{min}$ with different temperatures (700°C and 800°C) for 4h. All BNT pellets were sintered inside a standard kitchen microwave oven for different sintering (10, 15, 20 and 25mins) times as shown in Figure 3.6.

Table 3.5. Sample name, nominal sample compositions, calcination temperatures per time and microwave sintering time.

Sample name	Nominal composition	Calcination temperature per time ($^\circ\text{C}/\text{t}$)	Sintering time (mins)
MKB700, 10	$\text{Bi}_{0.5}\text{Na}_{0.5}\text{TiO}_3$	$700^\circ\text{C}/4\text{h}$	10
MKB700, 15	$\text{Bi}_{0.5}\text{Na}_{0.5}\text{TiO}_3$	$700^\circ\text{C}/4\text{h}$	15
MKB700, 20	$\text{Bi}_{0.5}\text{Na}_{0.5}\text{TiO}_3$	$700^\circ\text{C}/4\text{h}$	20
MKB700, 25	$\text{Bi}_{0.5}\text{Na}_{0.5}\text{TiO}_3$	$700^\circ\text{C}/4\text{h}$	25
MKB800, 10	$\text{Bi}_{0.5}\text{Na}_{0.5}\text{TiO}_3$	$800^\circ\text{C}/4\text{h}$	10
MKB800, 15	$\text{Bi}_{0.5}\text{Na}_{0.5}\text{TiO}_3$	$800^\circ\text{C}/4\text{h}$	15
MKB800, 20	$\text{Bi}_{0.5}\text{Na}_{0.5}\text{TiO}_3$	$800^\circ\text{C}/4\text{h}$	20
MKB800, 25	$\text{Bi}_{0.5}\text{Na}_{0.5}\text{TiO}_3$	$800^\circ\text{C}/4\text{h}$	25

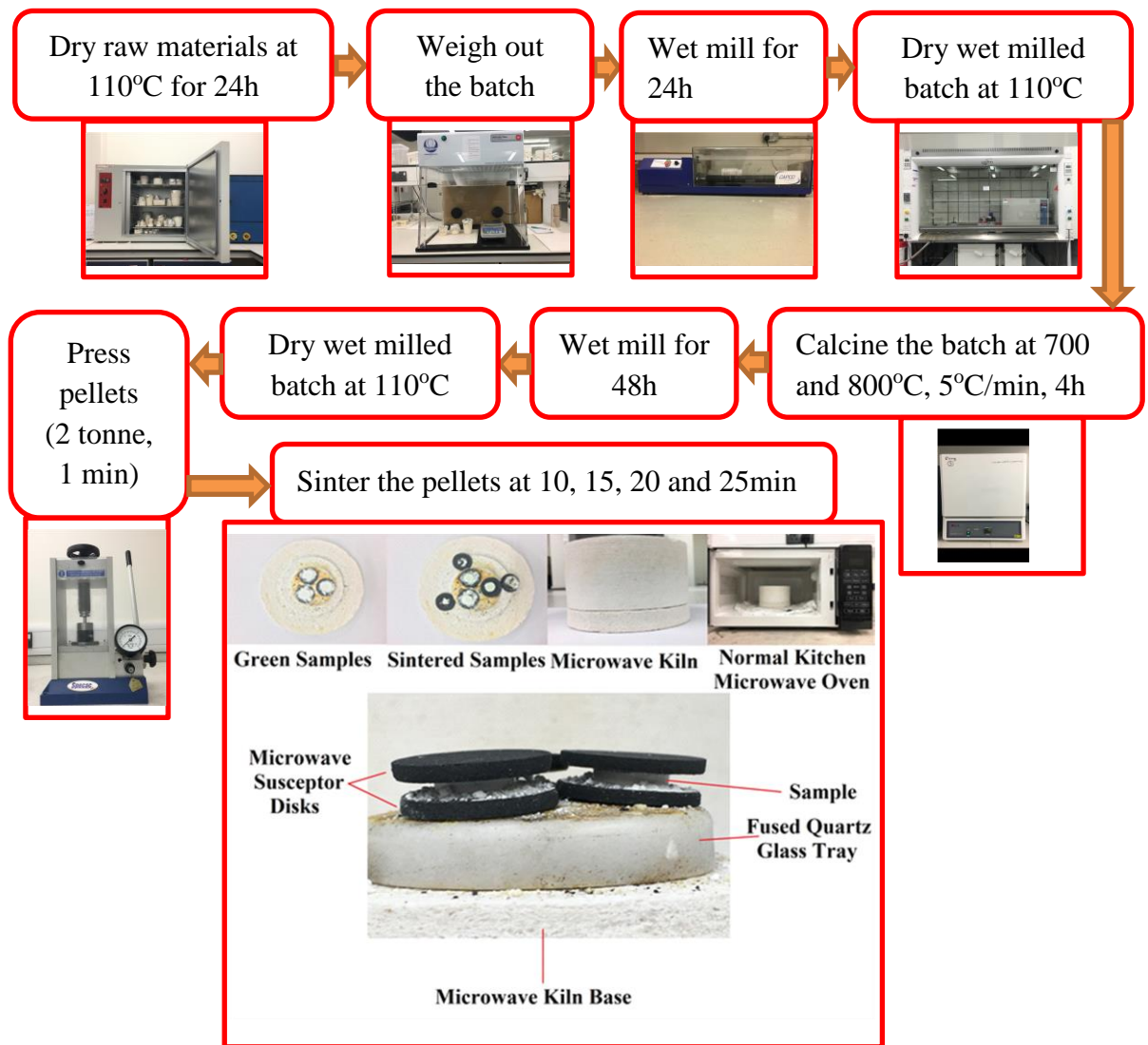


Figure 3.6. Process diagram of microwave sintering processing of pure microwave sintered BNT ceramics.

3.2.2.2. Iron-Doped Bismuth Sodium Titanate (BNTFe) Ceramics

A microwave sintering processing route was used to prepare microwave sintered BNTFe ceramics. The starting raw materials in the present work consist of Bi_2O_3 (99%, Alfa Aesar), Na_2CO_3 (99%, Better Equipped), TiO_2 (99.9%, Aldrich) and Fe_2O_3 (>99%, Aldrich), which were used to synthesise iron modified BNT ceramics according to the stoichiometric formula $\text{Bi}_{0.5}\text{Na}_{0.5}\text{Ti}_{1-x}\text{Fe}_x\text{O}_{3-0.5x}$, where $x = 0, 0.025, 0.0375, 0.050, 0.070$ and 0.100 . Details of Fe-BNT samples prepared using microwave processing are summarised in Table 3.6. A process diagram of preparation of iron-doped bismuth sodium titanate ceramics using the microwave sintering process studied here is shown in Figure 3.7. The prepared compositions were calcined inside an electric furnace at ramping rate 5°C/min with temperatures (700°C) for 4h. All BNT pellets were sintered

inside a standard kitchen microwave oven (0.4 kWh) on full power for sintering (20 mins) time, as shown in Figure 3.7.

Table 3.6. Sample name, nominal sample compositions, and microwave sintering time.

Sample name	Nominal composition	Sintering time (mins)
MKBF _e 0.00	Bi _{0.5} Na _{0.5} TiO ₃	20
MKBF _e 2.50	Bi _{0.5} Na _{0.5} Ti _{0.975} Fe _{0.025} O _{2.9875}	20
MKBF _e 3.75	Bi _{0.5} Na _{0.5} Ti _{0.9625} Fe _{0.0375} O _{2.98125}	20
MKBF _e 5.00	Bi _{0.5} Na _{0.5} Ti _{0.95} Fe _{0.05} O _{2.975}	20
MKBF _e 7.00	Bi _{0.5} Na _{0.5} Ti _{0.93} Fe _{0.07} O _{2.965}	20
MKBF _e 10.00	Bi _{0.5} Na _{0.5} Ti _{0.9} Fe _{0.1} O _{2.95}	20

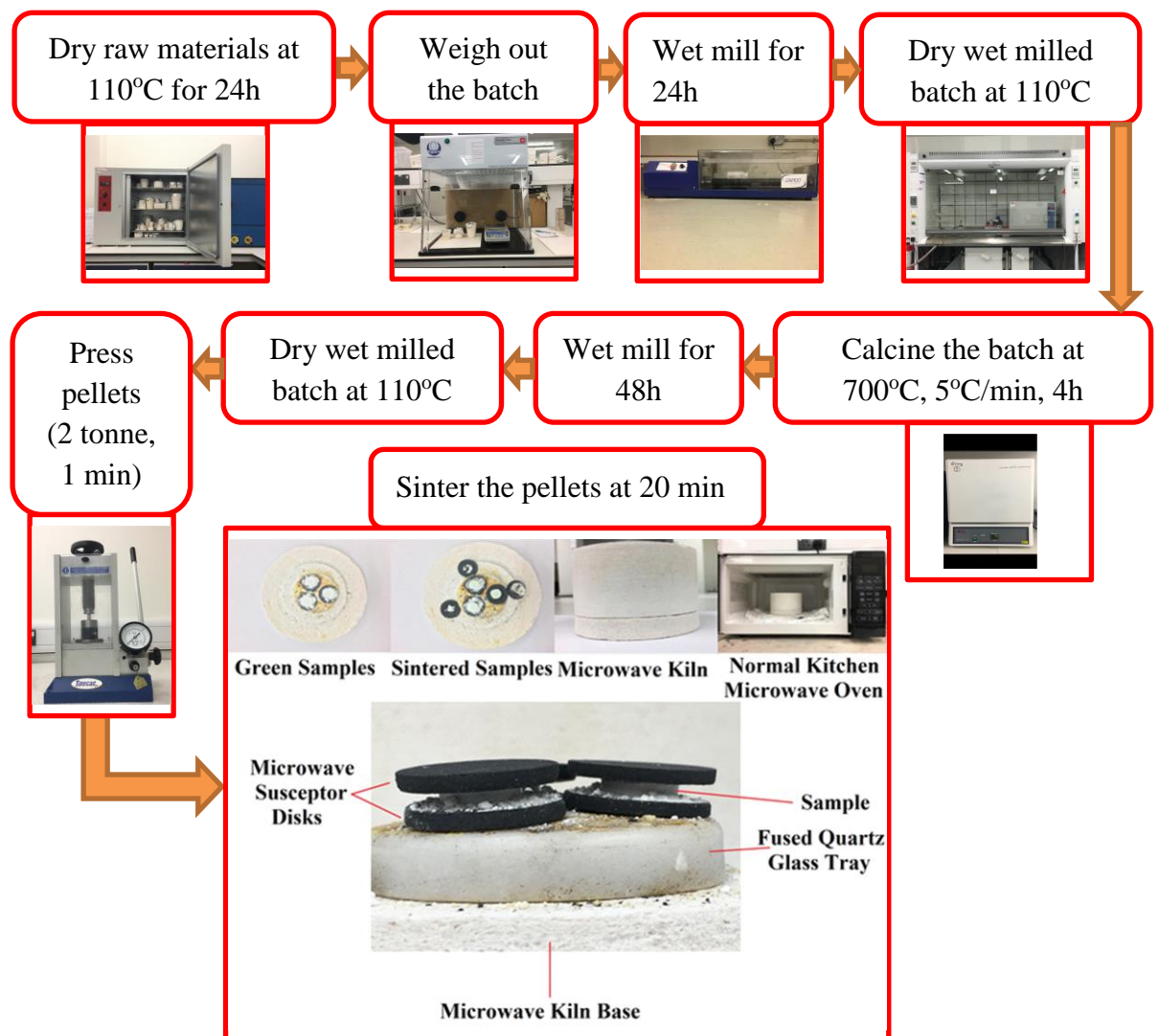


Figure 3.7. Process diagram of microwave sintering processing of microwave sintered iron modified BNT ceramics.

3.2.2.3. Potassium Sodium Niobate (KNN) Ceramics

A microwave sintering processing route was used to manufacture microwave sintered KNN ceramics with different calcination and microwave sintering times, as shown in Table 3.7. The starting raw materials in the present work consist of K_2CO_3 (>99%, Better Equipped), Na_2CO_3 (>99.9%, Better Equipped) and Nb_2O_5 (>99.9%, Aldrich) were used to prepared pure microwave sintered KNN ceramic compositions according to stoichiometry formula of $K_{0.5}Na_{0.5}NbO_3$. The nominal compositions of the microwave sintered KNN ceramic samples made in the present work are summarised in Table 3.7. A flow diagram of the preparation of pure potassium sodium niobate ceramics using microwave sintering processing is shown in Figure 3.8. The pure KNN batch compositions were calcined in an electric furnace at different calcination temperatures of 700°C and 800°C with ramping of 5°C/min and held for 4h, then cooled them gradually to room temperature. All of the KNN prepared pellets in the present work were sintered in kitchen standard microwave oven using different microwave sintering times, such as 10, 15, 20 and 25 mins without holding time; then allow samples to cool slowly inside microwave oven during 2h to reach approximately room temperature.

Table 3.7. Nominal sample compositions, calcination temperatures per time and microwave sintering times.

Sample name	Nominal composition	Calcination temperature (°C/t)	Sintering time (mins)
MKK700, 10	$K_{0.5}Na_{0.5}NbO_3$	700°C/4h	10
MKK700, 15	$K_{0.5}Na_{0.5}NbO_3$	700°C/4h	15
MKK700, 20	$K_{0.5}Na_{0.5}NbO_3$	700°C/4h	20
MKK700, 25	$K_{0.5}Na_{0.5}NbO_3$	700°C/4h	25
MKK800, 10	$K_{0.5}Na_{0.5}NbO_3$	800°C/4h	10
MKK800, 15	$K_{0.5}Na_{0.5}NbO_3$	800°C/4h	15
MKK800, 20	$K_{0.5}Na_{0.5}NbO_3$	800°C/4h	20
MKK800, 25	$K_{0.5}Na_{0.5}NbO_3$	800°C/4h	25

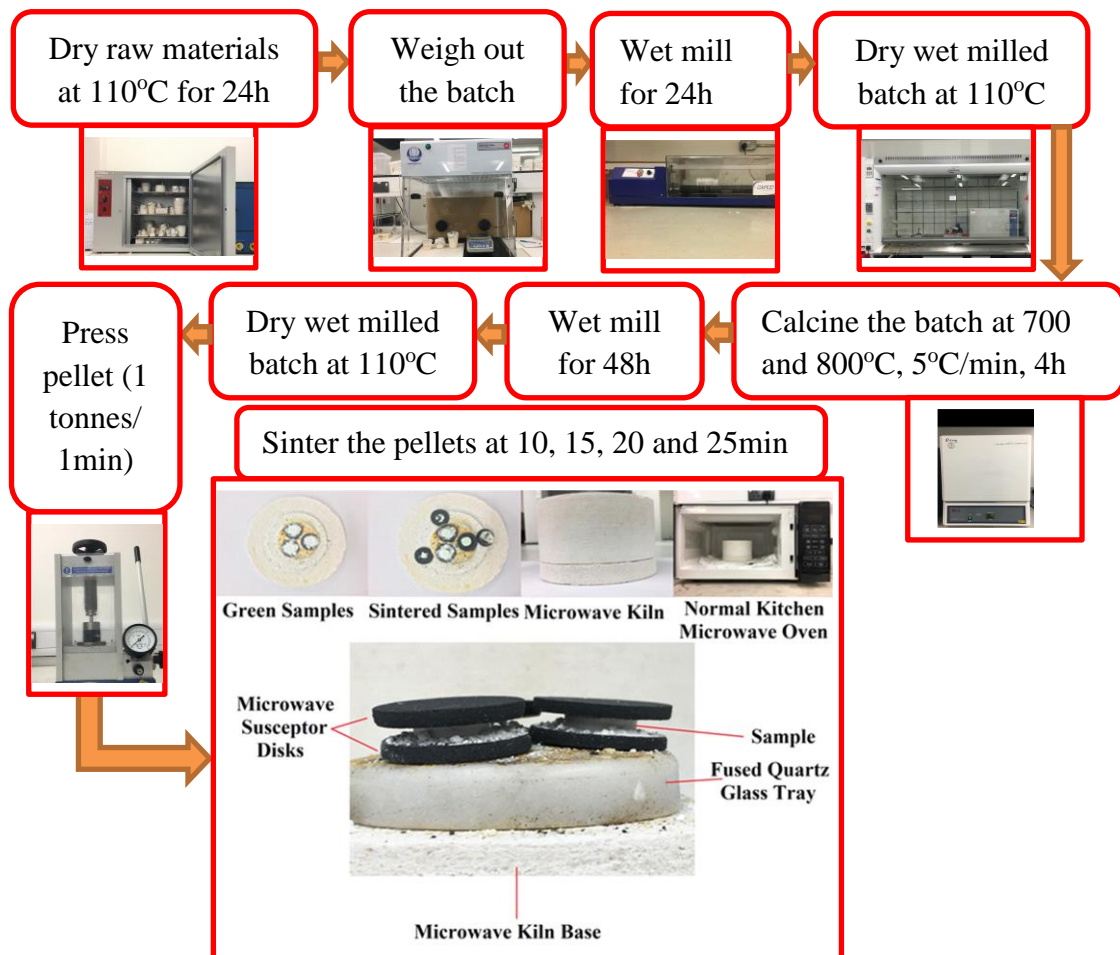


Figure 3.8. Processing flow diagram for microwave sintered KNN ceramics.

3.2.2.4. Microwave Susceptor Disks

Microwave susceptor disks were made by solid-state sintering processing. The starting materials consisted of 50wt% graphite (99.9%, Timothy Sleight), 30wt% SiO₂ (99.9%, Better Equipped), 10wt% MnO₂ (99%, Aldrich), 10wt% Fe₃O₄ (97%, Alfa Aesar). The prepared composition of microwave susceptor disks was designed based on the materials presented in Table 3.8 (Rao et al., 1999). As shown by the data in the table, MnO₂ and Fe₃O₄ provide high temperature under microwave irradiation. Early attempts to use susceptor disks made from pure MnO₂ or Fe₃O₄ failed due to these materials melting during the experiments. Graphite was therefore added to provide a different high-temperature susceptor, and SiO₂ was added to provide stability as a refractory material to reduce the effects of MnO₂ / Fe₃O₄ melting during processing. This formulation was not optimised, but was found to be sufficient for the processing times of up to 25 minutes.

To prepare the microwave susceptor disks, the starting materials were dried at 110°C for 24h, then weighed into a 40g batch. The batch was wet milled and mixed using propanol and zirconia milling media in 250 mL polyethene (PE) bottles, and milled in a planetary ball mill for 10h. The milled powder was then removed and dried at 110°C in an oven placed in a fume cupboard. The prepared compositions were then calcined individually inside a furnace at different temperatures (700°C) with ramp rate 5°C/min for 1h, then wet milled again for 10h. The milled powder was then removed and dried at 110°C in an oven placed in a fume cupboard. The disks were pressed using a hydraulic press with 10 tons per 20mm diameter disk. The final step was to sinter the green microwave susceptor disks at 900°C with a ramp rate 5°C/min for 2h. The final microwave susceptor disks that were used to sinter sample pellets in the microwave oven, were used by placing the ceramic pellet between two microwave susceptor disks in a "sandwich" arrangement. A bed of powdered sample material was used to separate the pellet from the susceptor discs, as shown in Figure 3.9. Inside the microwave oven was placed a "hot pot" constructed from a high-porosity, low-density Al_2O_3 material. Samples and their surrounding powder bed and susceptor disks were placed inside the "hot-pot" and these were used to absorb the microwave energy from room temperature, generating heat, and to transmit this heat to the sample pellet.

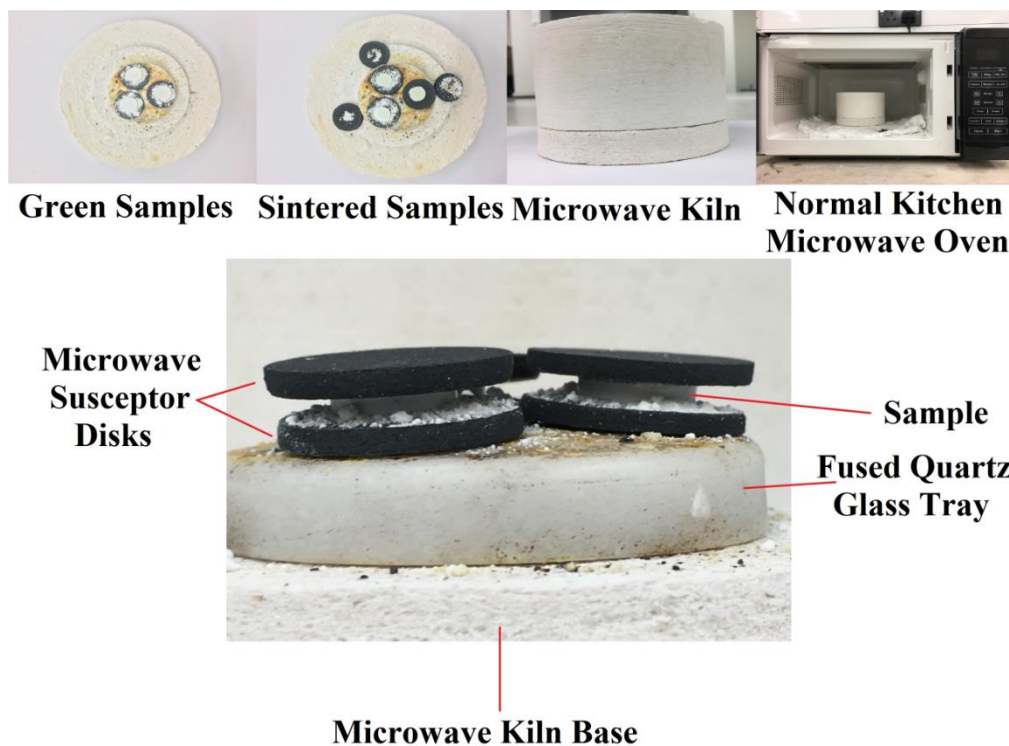


Figure 3.9. Microwave susceptor disks and microwave sintering step.

Table 3.8. Microwave active elements, natural minerals and compounds (Rao et al., 1999).

element/mineral/compound	time (min) of microwave exposure	T, K	element/mineral/compound	time (min) of microwave exposure	T, K
Al	6	850	NiO	6.25	1578
C (amorphous, <1 μm)	1	1556	V ₂ O ₅	11	987
C (graphite, 200 mesh)	6	1053	WO ₃	6	1543
C (graphite, < 1 μm)	1.75	1346	Ag ₂ S	5.25	925
Co	3	970	Cu ₂ S (chalcocite)	7	1019
Fe	7	1041	CuFeS ₂ (chalcopyrite)	1	1193
Mo	4	933	Fe _{1-x} S (pyrrhotite)	1.75	1159
V	1	830	FeS ₂ (pyrite)	6.75	1292
W	6.25	963	MoS ₂	7	1379
Zn	3	854	PbS	1.25	1297
TiB ₂	7	1116	PbS (galena)	7	956
Co ₂ O ₃	3	1563	CuBr	11	995
CuO	6.25	1285	CuCl	13	892
Fe ₃ O ₄ (magnetite)	2.75	1531	ZnBr ₂	7	847
MnO ₂	6	1560	ZnCl ₂	7	882

3.2.3. Melt Processing Route

3.2.3.1. Bismuth Sodium Titanium Silicate (BNTSi) Glasses

A melt processing route was used to manufacture six samples of bismuth sodium titanium silicate glasses. The glasses in the present work were manufactured using the starting raw materials such as Bi₂O₃ (99%, Alfa Aesar), Na₂CO₃ (99%, Better Equipped), TiO₂ (99.9%, Aldrich) and SiO₂ (99%, Better Equipped) in various moles percentages, as shown in Table 3.9. The preparation of bismuth sodium titanium silicate glasses using melt processing route are shown in Figure 3.10. All prepared glasses were melted at 1450°C/1h or 5h separately with 5°C/min heating rate, then poured melt directly on a metallic casting plate to make glasses. However, all melted compositions have crystallised completely or partly.

Table 3.9. Sample name, nominal sample compositions and oxides concentration for bismuth sodium titanium silicate glasses.

Sample name	Mol%					Melting (T/t)
	Bi ₂ O ₃	Na ₂ O	TiO ₂	SiO ₂	Total	
MBS50, 1h	12.50	12.50	25.00	50.00	100.00	1450°C/1h
MBS60, 1h	10.00	10.00	20.00	60.00	100.00	1450°C/1h
MBS70, 1h	7.50	7.50	15.00	70.00	100.00	1450°C/1h
MBS70, 5h	7.50	7.50	15.00	70.00	100.00	1450°C/5h
MBS75, 5h	6.25	6.25	12.50	75.00	100.00	1450°C/5h
MBS80, 1h	5.00	5.00	10.00	80.00	100.00	1450°C/1h

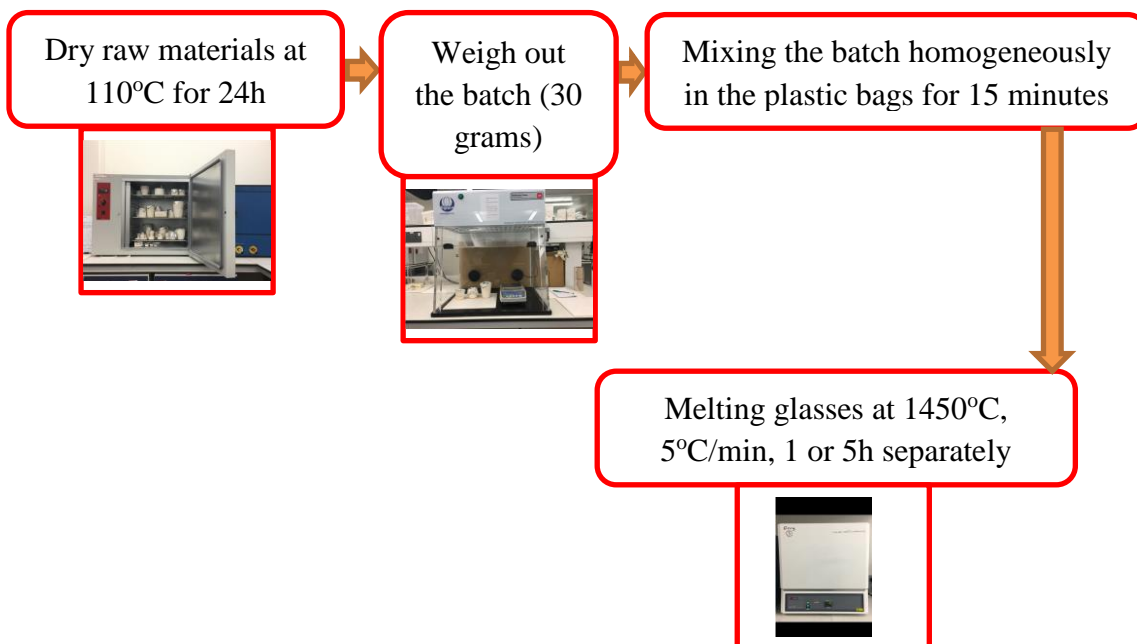


Figure 3.10. Melt processing for bismuth sodium titanium silicate glasses.

3.2.3.2. Bismuth Sodium Titanium Borate (BNTB) Glasses

A melt processing route was used to manufacture three samples of bismuth sodium titanium borate glasses. The glasses in the present work were prepared using the starting raw materials such as Bi_2O_3 (99%, Alfa Aesar), Na_2CO_3 (99%, Better Equipped), TiO_2 (99.9%, Aldrich) and H_3BO_2 (99%, Better Equipped) in various mole percentages, as shown in the Table 3.10. The synthesis of bismuth sodium titanium borate glasses using melt processing route is shown in Figure 3.11. All prepared glasses were melted in Al_2O_3 crucibles at $1300^\circ\text{C}/1\text{h}$ separately with $5^\circ\text{C}/\text{min}$ heating rate, then poured melt directly on a metallic casting plate to make glasses. However, all melted compositions have crystallised completely or partly.

Table 3.10. Sample name, nominal sample compositions and oxides concentration for bismuth sodium titanium borate glasses.

Sample name	Mol%					Melting (T/t)
	Bi_2O_3	Na_2O	TiO_2	H_3BO_3	Total	
MBB30	17.50	17.50	35.00	30.00	100.00	$1300^\circ\text{C}/1\text{h}$
MBB50	12.50	12.50	25.00	50.00	100.00	$1300^\circ\text{C}/1\text{h}$
MBB70	7.50	7.50	15.00	70.00	100.00	$1300^\circ\text{C}/1\text{h}$

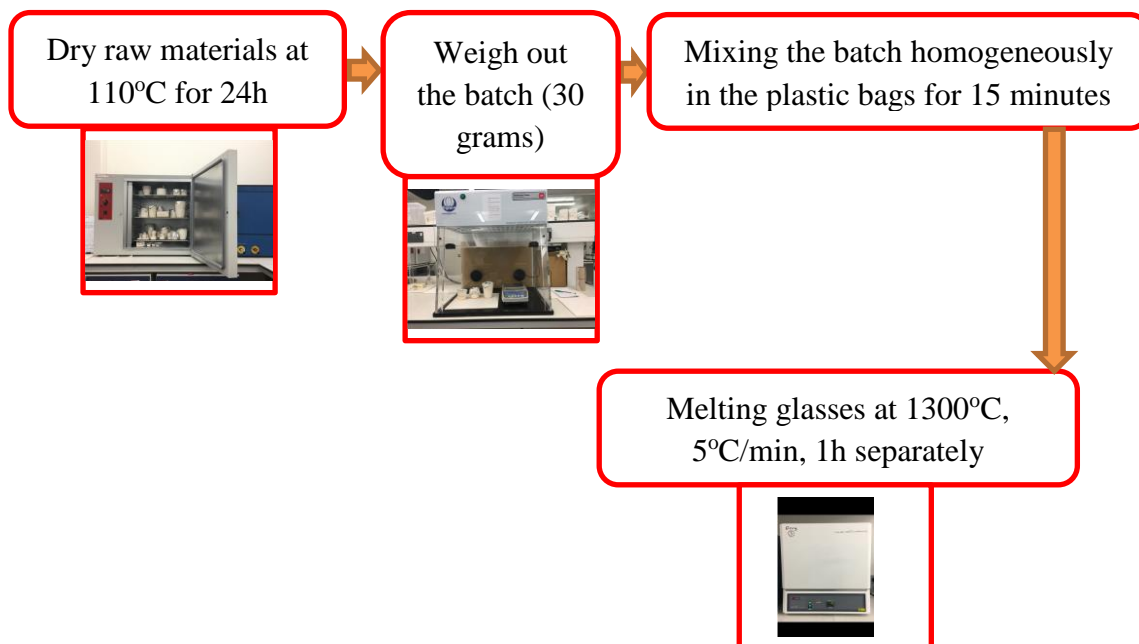


Figure 3.11. Melt processing for bismuth sodium titanium borate glasses.

3.2.3.3. Potassium Niobium Borate (KNB) Glasses and Glass-Ceramics

The melt processing route was used to manufacture potassium niobium borate (KNB) glasses with different mol% contents of starting raw materials, as shown in Table 3.11. The glasses in the present work were prepared using the starting raw materials such as K_2CO_3 (>99%, Better Equipped), Nb_2O_5 (>99.9%, Aldrich), and H_3BO_3 (>99.9%, Better Equipped). In the present work, the nominal compositions of the prepared samples are presented in Table 3.11. The manufacturing of KNB glasses using novel melt processing are revealed in Figure 3.12. The mixed compositions placed in recrystallised alumina crucibles, then melt them at 1300°C for specific time separately, then poured melt directly on a metallic casting plate to make glasses. Two of the prepared glasses were visibly amorphous, and one was partly crystalline.

Table 3.11. Nominal sample compositions and oxides concentration for potassium niobium borate glasses.

Sample Name	Mol%			Melting (T/t)
	K ₂ O	Nb ₂ O ₅	B ₂ O ₃	
25K25Nb50B	25	25	50	1300°C/1h
30K30Nb40B	30	30	40	1300°C/1h
35K35Nb30B	35	35	30	1300°C/1h
40K30Nb30B	40	30	30	1300°C/1h
40K35Nb25B	40	35	25	1300°C/1h
40K40Nb20B	40	40	20	1300°C/1h

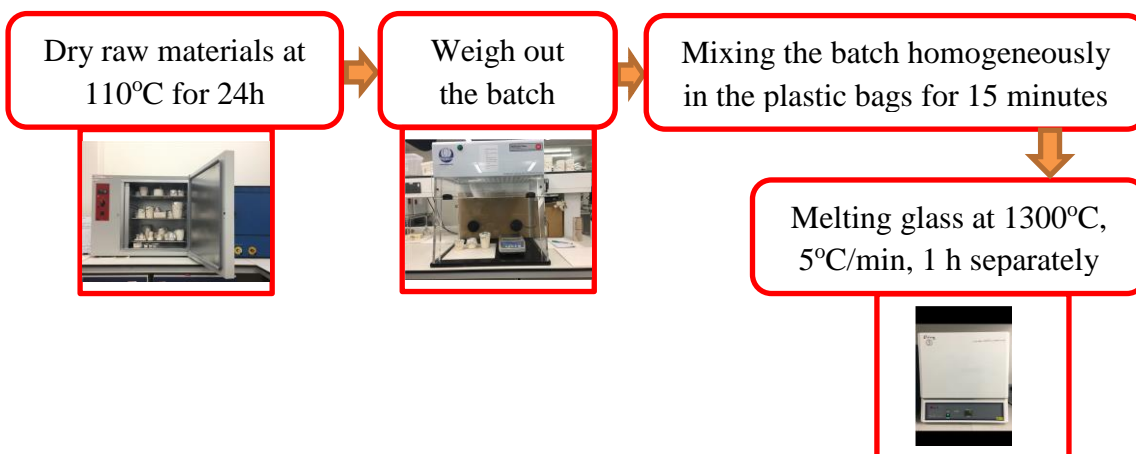


Figure 3.12. Melt processing for potassium niobium borate glasses.

3.2.3.4. Potassium Sodium Niobium Silicate (KNNS) Glasses

The melt processing route was used to manufacture potassium sodium niobium silicate (MKS) glasses with different mol% contents of starting raw materials, as shown in Table 3.12. The glasses in the present work were manufactured using the starting raw materials such as K₂CO₃ (>99%, Better Equipped), Na₂CO₃ (>99.9%, Better Equipped) and SiO₂ (>99.9%, Better Equipped). In the current work, the nominal compositions of the prepared samples are summarised in Table 3.12. The synthesis of MKS using novel melt processing is shown in Figure 3.13. The mixed compositions put in a recrystallised alumina crucible, then melt them at 1450°C for identified time separately, then poured melt directly on a metallic casting plate to make glasses. However, all melted compositions have crystallized completely or partly.

Table 3.12. Nominal sample compositions and oxides concentration for potassium sodium niobium silicate glasses.

Sample name	Mol%					Melting (T/t)
	K ₂ O	Na ₂ O	Nb ₂ O ₅	SiO ₂	Total	
MKS50, 1h	12.50	12.50	25.00	50.00	100.00	1450 ⁰ C/1h
MKS60, 1h	10.00	10.00	20.00	60.00	100.00	1450 ⁰ C/1h
MKS65, 1h	8.75	8.75	17.50	65.00	100.00	1450 ⁰ C/1h
MKS70, 1h	7.50	7.50	15.00	70.00	100.00	1450 ⁰ C/1h
MKS70, 4h	7.50	7.50	15.00	70.00	100.00	1450 ⁰ C/4h
MKS75, 5h	6.25	6.25	12.50	75.00	100.00	1450 ⁰ C/5h

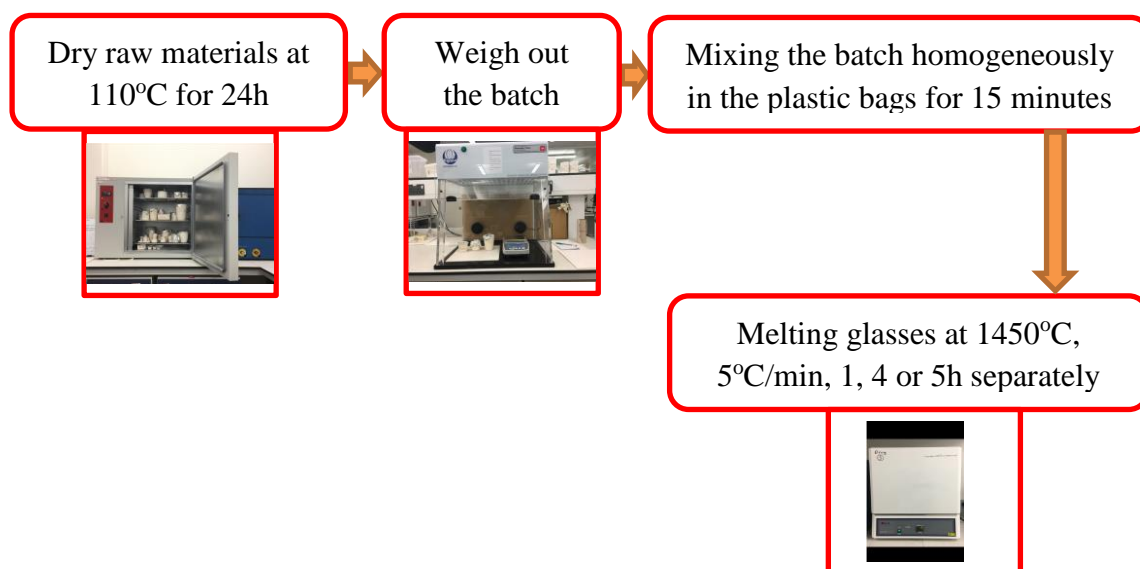


Figure 3.13. Melt processing for potassium sodium niobium silicate glasses.

3.2.3.5. Potassium Sodium Niobium Borate (KNNB) Glasses and Glass-Ceramics

The novel melt processing route was used to manufacture potassium sodium niobium borate (KNNB) glasses with different mol% contents of starting raw materials, as shown in Table 3.13. The glasses in the present work were prepared using the starting raw materials such as K₂CO₃ (>99%, Better Equipped), Na₂CO₃ (>99.9%, Better Equipped), Nb₂O₅ (>99.9%, Aldrich), and H₃BO₃ (>99.9%, Better Equipped). In the present work, the nominal compositions of the prepared samples are presented in Table 3.13. The manufacturing of KNN borate glasses and glass-ceramics using melt processing are revealed in Figure 3.14. The mixed compositions put in a recrystallised alumina crucible, then melt them at 1300°C for specific time separately, then poured

melt directly on a metallic casting plate to make glasses. Two of the prepared glasses appeared completely amorphous, and one of them appeared partly crystallised.

Table 3.13. Nominal sample compositions and oxides concentration for KNN borate glasses and glass-ceramics.

Sample Name	Mol%				Melting (T/t)
	K ₂ O	Na ₂ O	Nb ₂ O ₅	B ₂ O ₃	
40KNa30Nb30BSi	20	20	30	30	1300 ⁰ C/1h
40KNa35Nb25BSi	20	20	35	25	1300 ⁰ C/1h
40KNa40Nb20BSi	20	20	40	20	1300 ⁰ C/1h

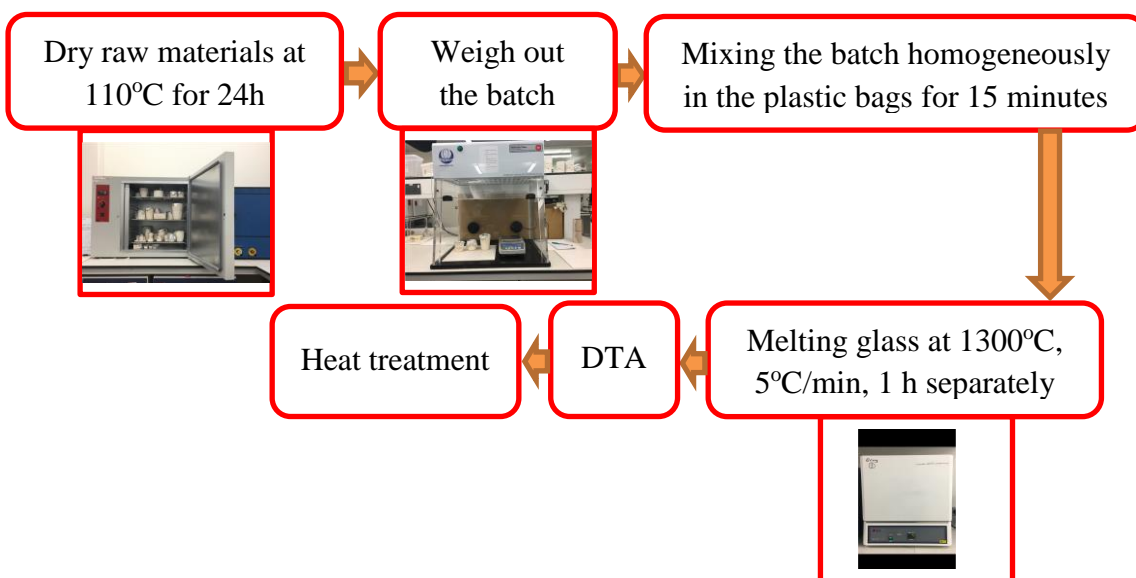


Figure 3.14. Melt processing for potassium sodium niobium borate glasses and glass-ceramics.

3.2.3.6. Potassium Sodium Niobium Borosilicate (KNNBS) Glasses and Glass-Ceramics

Potassium sodium niobium borosilicate (KNNBS) glasses were manufactured using novel melt processing route, with different mol% contents of starting raw materials, as presented in Table 3.14. The glasses in the present work were made using the starting raw materials such as K₂CO₃ (>99%, Better Equipped), Na₂CO₃ (>99.9%, Better Equipped), Nb₂O₅ (>99.9%, Aldrich), H₃BO₃ (>99.9%, Better Equipped) and SiO₂ (>99.9%, Better Equipped). In the current work, the nominal compositions of the prepared glasses are stated in Table 3.14. The preparation of KNNBSi glasses and glass-

ceramics using melt processing are shown in Figure 3.15. The mixed compositions were placed in a recrystallised alumina crucible, then melted at 1300°C for 1h, then poured melt directly on a metallic casting plate to make glasses. All glasses appeared entirely amorphous.

Table 3.14. Nominal sample compositions and oxides concentration for KNN borosilicate glasses and glass-ceramics.

Sample Name	Mol%					Melting (T/t)
	K ₂ O	Na ₂ O	Nb ₂ O ₅	B ₂ O ₃	SiO ₂	
40KNa30Nb30BSi	20	20	30	15	15	1300 ⁰ C/1h
40KNa35Nb25BSi	20	20	35	12.5	12.5	1300 ⁰ C/1h
40KNa40Nb20BSi	20	20	40	10	10	1300 ⁰ C/1h

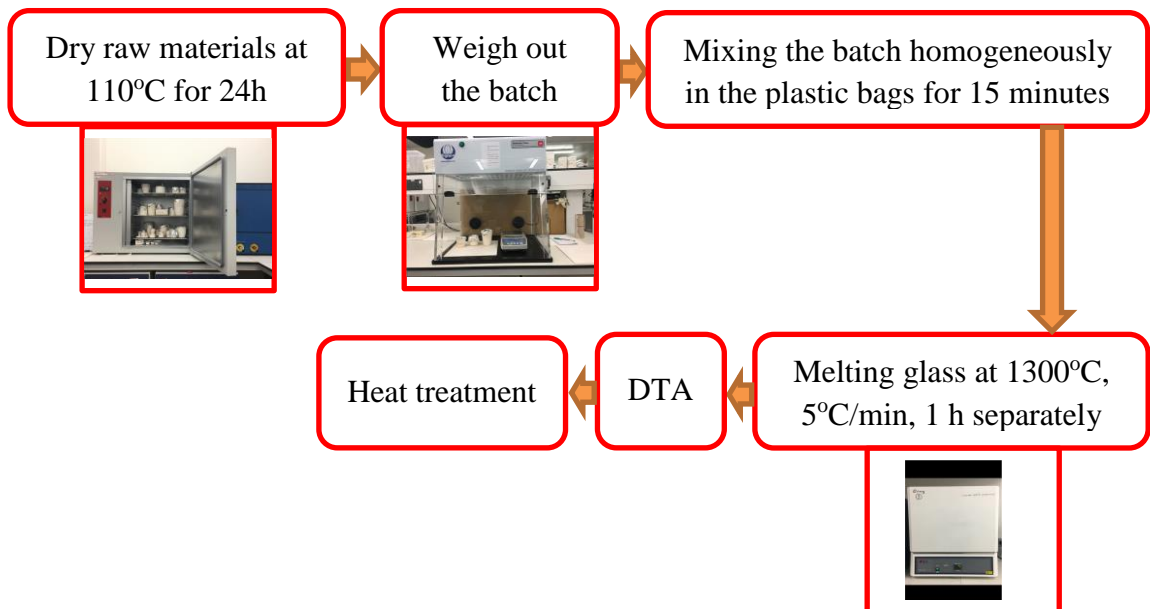


Figure 3.15. Melt processing for KNN borosilicate glasses and glass-ceramics.

3.2.3.7. Potassium Sodium Niobium Borosilicate (KNNBS) Glasses and Glass-Ceramic Fibres

Potassium sodium niobium borosilicate (KNNBSi) glass and glass-ceramic fibres were prepared using a melt processing route, with different mol% contents of starting raw materials, as presented in Table 3.15. The glass fibres were made using the starting raw materials K₂CO₃ (>99%, Better Equipped), Na₂CO₃ (>99.9%, Better Equipped), Nb₂O₅ (>99.9%, Aldrich), H₃BO₃ (>99.9%, Better Equipped) and SiO₂ (>99.9%, Better Equipped). In the present work, the nominal compositions of the prepared glass and glass-ceramic fibres are identified in Table 3.15. The manufacturing process diagram of

KNNBSi glass and glass-ceramic fibres using melt processing are shown in Figure 3.16. The mixed batch compositions were placed in a recrystallised alumina crucible, and then melted at a heating rate (5°C/min) to 1300°C then held for 1h, then glass fibres were drawn from the molten glass in the alumina crucible using borosilicate glass rods.

Table 3.15. Nominal sample compositions and oxides concentration for KNN borosilicate glass and glass-ceramic fibres.

Sample Name	Nominal Mol%				
	K ₂ O	Na ₂ O	Nb ₂ O ₅	B ₂ O ₃	SiO ₂
40KNa30Nb30BSi	20	20	30	15	15
40KNa35Nb25BSi	20	20	35	12.5	12.5
40KNa40Nb20BSi	20	20	40	10	10

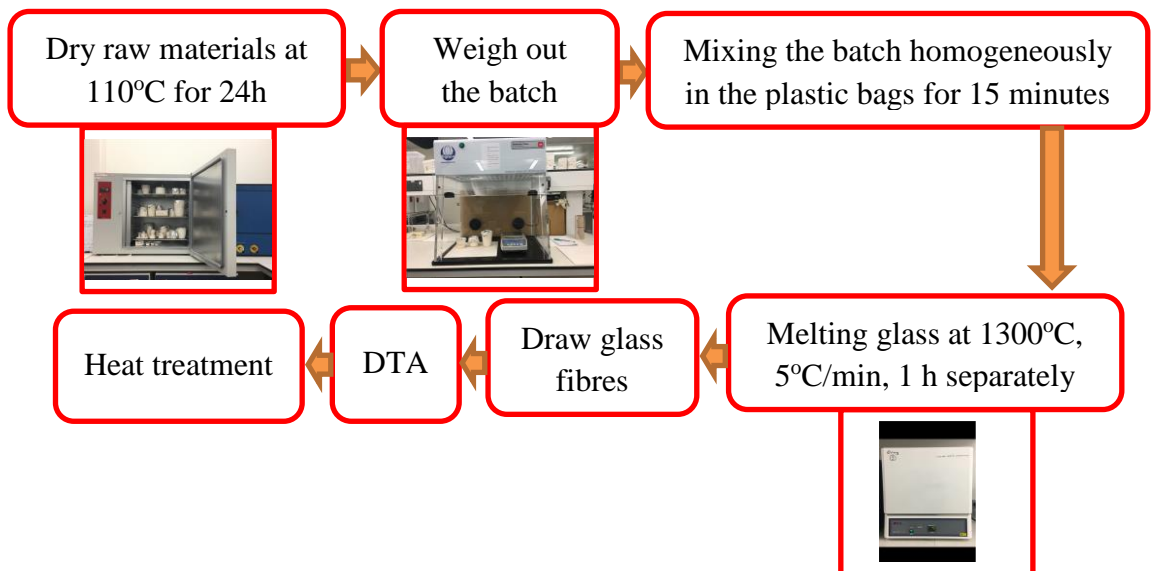


Figure 3.16. Melt processing for KNN borosilicate glass and glass-ceramic fibres.

3.3. Structural Analysis

3.3.1. XRD (X-Ray Diffraction)

All ceramic pellets, glasses and glass-ceramics powders were analysed using a Philips X-Pert Pro X-ray diffractometer (Panalytical, Netherlands) or an Empyrean X-ray diffractometer (Panalytical, Netherlands) at room temperature, using Cu K α radiation ($\lambda=1.5405\text{\AA}$) over the range 10 to 80 °2 θ . The results were interpreted for phase identification using X'Pert HighScore Plus software.

XRD can be used to identify the atomic structure, phases and grain size for crystalline materials (Ingham & Toney, 2014). The principle of the technique depends on the generation of X-rays by a cathode ray tube to produce X-rays which are focused on the sample. The incident X-rays interact with the sample producing diffraction of X-rays, which takes place through constructive interference, as described by Bragg's law (Equation 3.1) and shown schematically in Figure 3.17.

$$n\lambda=2d_{hkl} \sin(\theta) \quad \text{Equation 3.1}$$

Where n is the order of diffraction, λ is the wavelength of the incoming beam, d_{hkl} is the lattice spacing, and θ is the angle of the diffracted beam (Epp, 2016).

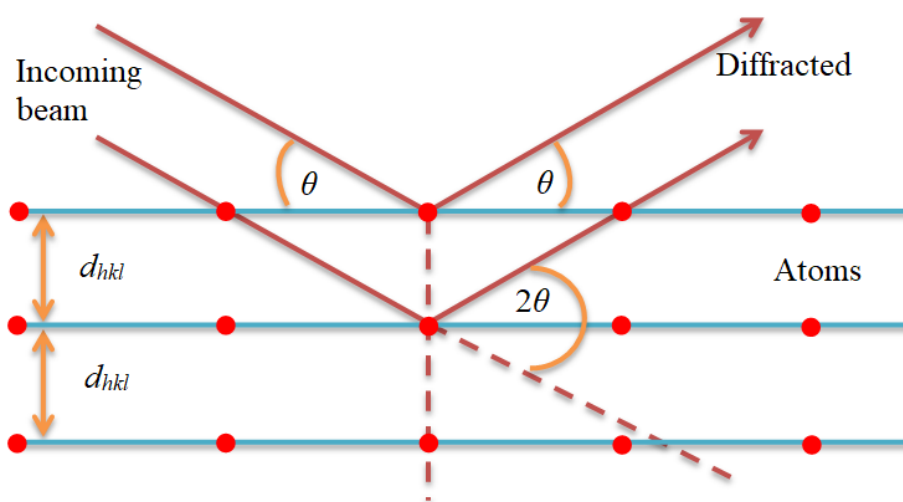


Figure 3.17. Schematic representation of the XRD principle (Epp, 2016).

All powders and pellets were measured using a spinning sample stage during 2-4h measurement time for each sample. After obtaining XRD results, phase identity was determined using X'Pert HighScore Plus software. Phase identification proceeds by fitting peaks, and then matching ICDD profiles stored in the software to obtain fits between peaks from ICDD database and sample data peaks according to the specific elements or components.

3.3.2. Raman Spectroscopy

Material structures were analysed using Raman spectroscopy (DXR2 Raman Microscope, Thermo Fisher Scientific, USA) using a 532nm laser, applied at room temperature. Raman spectroscopy is a vibrational spectroscopy technique that has been used to describe molecular structure by characterising fundamental vibrations and studying the vibrational modes of molecules in different materials (Larkin, 2018).

Raman spectroscopy depends on the light scattered from incident light on the sample; which can be divided into two types. The first type is Rayleigh scattered light. This is elastically scattered light and has a wavelength equal to that of the incident light. The second type is Raman scattered light. This is inelastically scattered light and has a wavelength different to that of the incident light. The loss in energy between the energy of the incident light and Raman scattered light is named the Raman shift, which is equal to the vibrational energy of a molecule in the sample (Ebnesajjad, 2011). The molecular structure can be interpreted depending on the Raman shift, Raman intensity and band shape, according to the Raman vibrational bands obtaining by a graph of Raman intensity (polarizability) against Raman shift (energy) (Ebnesajjad, 2011; Larkin, 2018).

Powders, bulk and pellet samples were analysed using Raman spectroscopy and measured at room temperature. The Raman results were collected using Omnic software; this proceeds by warming and switching the laser on and then calibrating and aligning the instrument using a silicon substrate and 10 μ m lens. After that scan, sample scans using exposure time (5-20 second) and sample exposures (accumulation) ranged between 1 to 20 time were used for collecting Raman spectra.

3.3.3. Scanning Electron Microscopy (SEM)

The microstructure of ceramics, glasses and glass-ceramics was analysed using scanning electron microscopy (Nova Nano SEM, Czech Republic). Prior to analysis, all samples were polished using SiC paper with water (100, 200, 400, 800, 1200, and 2500 grit size); then polished using diamond polish (1 μ m). The polished samples were thermally etched at 800°C in an electric furnace for 1 hour to reveal grains boundaries, and then polished samples were coated with a thin layer of carbon (20-30nm thickness) to collect smooth micrographs. Silver paint was applied on the three sides to provide electrical contact between the sample and sample holder.

Conventional linear intercept measurements estimated to measure the grain size by measuring the grain length as a line measurement from edge to edge through grain boundary of particle.

SEM is one of the most important techniques used to investigate the surface and microstructure of ceramics and glass-ceramics. The carbon coated surface must be connected by a thin layer of silver or gold (electrically conductive) to the metallic sample holder to pass electrons from surface of the sample to the sample holder, which

prevents charge aggregation on the surface of the sample that would cause disturbances in the imaging.

The SEM working principle depends on the formation of a magnified image from emitted electrons from the sample surface. At first, samples are placed inside vacuum cavity, and then the electron gun fires an electron beam at the sample surface, which has high energy and is transmitted through magnetic lenses to concentrate the incident electrons on the sample surface accurately. A small probe is used to raster electrons across the sample surface. The incident electrons penetrate the sample surface to produce emitted electrons, resulting from beam interactions with sample composition. Finally, the emitted electrons accumulate and analyse to the black and white images using a detector (Ebnesajjad, 2011; Sinha Ray, 2013).

Secondary electron imaging originates close to the sample surface as a result of having low energy <50 eV and inelastic interactions between the primary electron beam and the sample, which is useful for sample surface detection.

Backscattered electron imaging originates from high-energy electrons in the electron beam; the backscattered electron interacts elastically with sample atoms, this leads to scan sample volume, which is useful for chemical composition detection (Goldstein et al., 1981).

3.4. Differential Thermal Analysis (DTA)

Thermal behaviour of samples was analysed using differential thermal analysis (DTA). The aim of using DTA was to identify the crystallisation peak temperatures of glasses through the exothermic peaks enabling targeted heat treatment to form glass-ceramics. The analysis was carried out using a NETZSCH STA 449 F5 Jupiter instrument. All samples were ground to fine powders, then weighed out as 30 mg against the same quantity of a 99.9% purity α - Al₂O₃ inert reference material. After that, the fine powders were heated from room temperature to 1300°C at 5°C/min and the data collected.

DTA is an important technique to determine phase transition temperatures of materials, for example, glass transition temperature, crystallisation temperatures and melting points. The DTA working principle mainly depends on recording the temperature difference between the sample and the inert reference material ($T_s - T_r$). Data processing is carried out during heating of both sample and reference materials inside

the furnace. The heating process is controlled by a specific programmer controlling the furnace (Klančnik, Medved & Mrvar, 2010; Turi, 2012), as represented in Figure 3.18.

The DTA data were collected using STA 409PG software ramping to 1300°C at 5°C/min, then calibrating the NETZSCH STA 449 F5 instrument using a reference crucible and empty sample crucible to obtain baseline data, and then repeating the process using 30 mg of powder to collect the data.

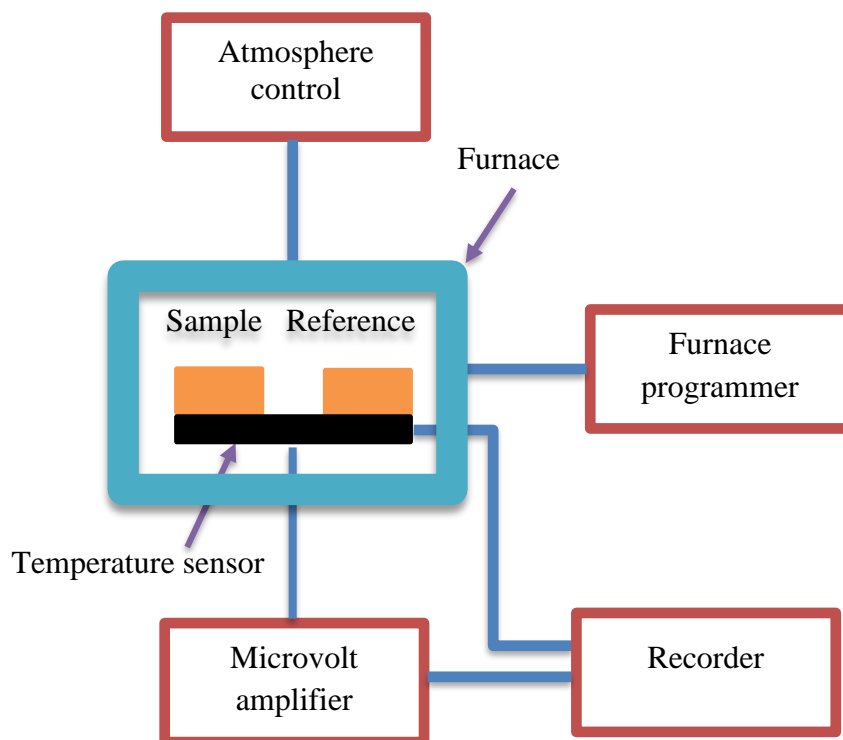


Figure 3.18. Schematic representation of typical DTA instrument (Turi, 2012).

3.5. Density Measurements

The bulk density of glasses and glass-ceramics was measured according to the Archimedes principle. The relative density of ceramic samples was calculated according to the bulk density, as presented in Equation 3.2:

$$\rho_r = (\rho_m/\rho_t) \times 100 \quad \text{Equation 3.2}$$

Where ρ_m is bulk density (mass per volume), and ρ_t is theoretical density based on the composition, which is obtained from references or ICDD card number by X'Pert HighScore Plus software. The bulk density was measured using a density balance and vacuum desiccator, where the dried pellet was weighed out in the air (W1), then the air

was evacuated from the vacuum desiccator for 30 mins. After that, the vacuumed sample was immersed in the liquid (distilled water) inside the vacuum desiccator for 10 min to allow the water to penetrate inside the open pores. Then the wet sample was weighed out in water (W2), and in the air (W3). The bulk density was then calculated using Equation 3.3 and theoretical density calculated for iron doped BNT or KNN ceramics using Equation 3.4:

$$\rho_m = (W1/W3-W2) \times \text{Liquid Density} \quad \text{Equation 3.3}$$

$$\rho_t = M_{\text{BNT or KNN}} + M_{\text{Fe}_2\text{O}_3} / [(M_{\text{BNT or KNN}}/\rho_{\text{BNT or KNN}}) + (M_{\text{Fe}_2\text{O}_3}/\rho_{\text{Fe}_2\text{O}_3})] \quad \text{Equation 3.4}$$

where $M_{\text{BNT or KNN}}$, $M_{\text{Fe}_2\text{O}_3}$, $\rho_{\text{BNT or KNN}}$, and $\rho_{\text{Fe}_2\text{O}_3}$ represent the mass of BNT or KNN composition, the mass of Fe_2O_3 , the theoretical density of BNT (5.97 g/cm^3 , ICDD 04-017-0216) or KNN (4.49 g/cm^3 , ICDD no 98-018-6360) composition, and the theoretical of Fe_2O_3 (5.12 g/cm^3 , ICDD no 032-0469).

3.6. Electrical Property Measurements

In the present project, polarisation versus electric field (hysteresis) and strain versus electric field loops have been measured, as described below:

3.6.1. Electrode Preparation

Sample electrodes were prepared using a coating instrument for electrical measurements, and then the electrodes were made using gold sputter coating with a sputtering current (10 mA), sputtering time (600 seconds) and tooling factor (2.7) parameters. Both faces of each sample pellet were coated, were pellet thickness ranged from 1 to 3 mm and diameter ranged from 8 to 10 mm.

3.6.2. Hysteresis (Polarization Versus Electric Field) and Strain Versus Electric Field Loop Measurements

In the present project, hysteresis (P-E) and strain-electric field (S-E) loops have been used to investigate the electrical properties of ceramics and glass-ceramics. The P-E and S-E loops are essential to the classification of electrical ceramic materials, for example, whether piezoelectric, relaxor (non-piezoelectric) or dielectric, as shown in Figure 3.19.

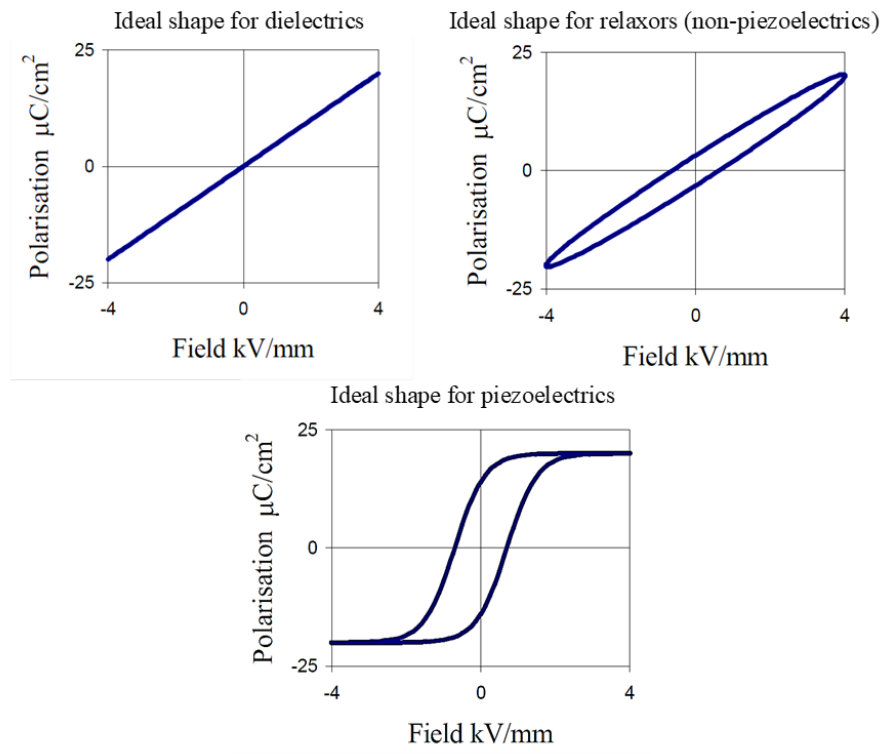


Figure 3.19. Classification of ideal P-E shapes for electrical materials (Stewart, Cain, & Hall, 1999).

A hysteresis loop (Figure 3.21) is essentially affected by parameters such as polarisation (P), stored electrical charge (Q), the area of the sample surface (A), the electric field (E), spontaneous polarisation (P_s), remnant polarisation (P_r) and coercive field (E_c).

Hysteresis (polarisation vs electric field, P-E) (Figure 3.20) and strain vs electric field (S-E) (Figure 3.21) loops were measured using an AixACT (GMBH, Germany) system. The measurements in the present work were carried out using a laser interferometer system, which mainly depends on measuring the displacement of laser beams through the splitting of the monochromatic light source (here, a He-Ne laser) to the two beams. One of the beams is a reference beam acting as a fixed path, and the second beam is heading towards the sample and returns to join the reference beam to create interference fringes, which are used to identify the displacement. For obtaining the P-E and S-E loops, the system is constructed of a generator, a high voltage amplifier and PC (AixPlover Software) software, where the generator is used to form the initial wave, and then the wave is amplified by a high voltage amplifier during transmitting it to the sample. The applied field and accumulated charge on the sample surface are

recorded and downloaded to PC software to analyse and collect the data (Stewart et al., 1999).

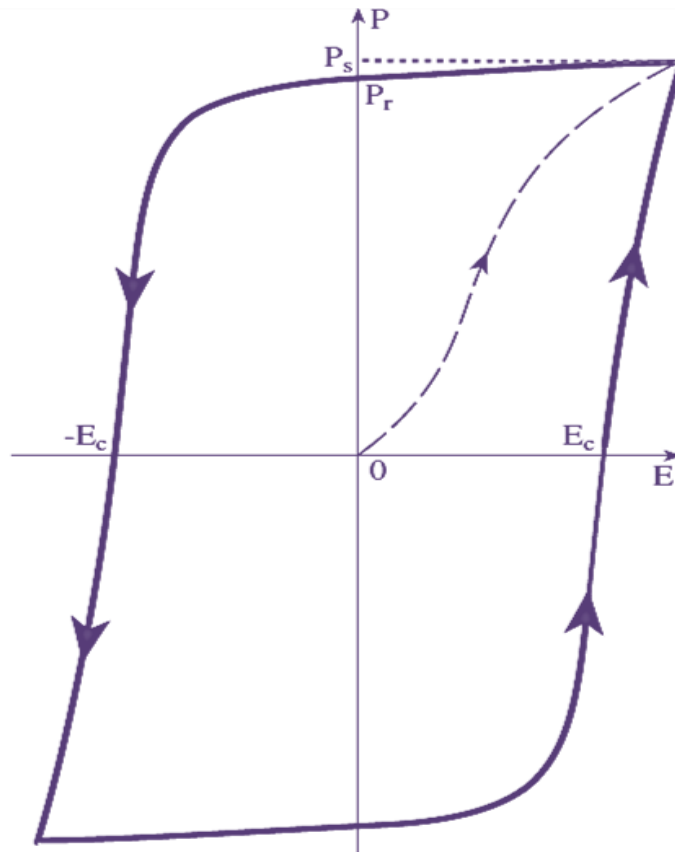


Figure 3.20. Typical shape of hysteresis loop for ferroelectric materials (Carter & Norton, 2007).

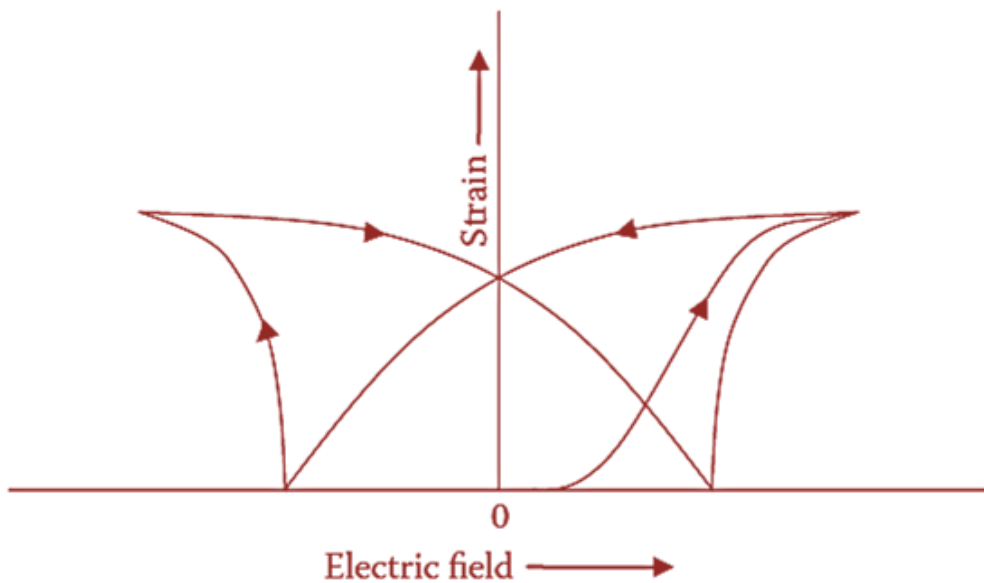


Figure 3.21. Typical shape of strain versus electric field for piezoelectric materials (Vijaya, 2012).

Chapter Four

Pure and Iron Doped Bismuth Sodium Titanate Ceramics and Glasses

4.1. Introduction

Chapter four considers the pure and iron doped BNT ceramics prepared by three different processing routes, including conventional solid-state sintering processing, microwave sintering processing and melt processing, as shown in Figure 4.1.

BNT ceramics have been essentially chosen as risk-free electrical materials, indicating to their excellent piezoelectric properties (remnant polarisation ($38 \mu\text{C}/\text{cm}^2$)) (Jones & Thomas, 2002). BNT was discovered by Smolenskii in 1960 (Priya & Nahm, 2011). BNT has been utilised in electronic applications such as resonators and filters, piezoelectric motors, transducers, and actuators (Priya & Nahm, 2011; Yuan et al., 2010). However, BNT ceramics have drawbacks such as difficulties in poling due to their high coercive field ($73 \text{ kV}/\text{cm}$) (Pardo et al., 2018), and evaporation of volatile Bi_2O_3 (melting temperature 817°C) and Na_2O (melting temperature 1132°C) during processing, that leads to porous ceramics (Kang et al., 2013; Panda & Sahoo, 2015; Wu et al., 2011). BNT ceramics have been prepared using conventional solid-state sintering processing for several decades. However, this method has drawbacks such as long sintering times of about 340 mins (1100°C , $5^\circ\text{C}/\text{min}$, 2h) and consequently high energy consumption (Fujii et al., 2016; Khamman, 2014). Adding flux materials to BNT has been studied by many researchers as one mechanism of reducing sintering temperatures and/or times to reduce energy demand. Such additions have included MgO (Chou et al., 2010), CuO (Chou et al., 2011), BiFeO_3 (Fujii et al., 2016) and Fe_2O_3 (Watcharapasorn, Jiansirisomboon & Tunkasiri, 2007). However, any such additions also affect electrical physical and/or electrical properties of the resulting ceramics. Alternative processing routes have also been used to reduce energy consumption and develop electrical and physical properties, for example soft combustion processing (Razak, Yip & Sreekantan, 2011), sol-gel processing (Cernea et al., 2012; Dargham et al., 2016), solution combustion processing (Ma et al., 2013), and hydrothermal processing (Ma et al., 2006; Trelcat et al., 2011). However, reducing the energy consumption and sintering time in

BNT sintering as well as enhancing the electrical and physical properties are still under study.

In the present chapter, three processing routes have been used to synthesise pure and iron-doped bismuth sodium titanate ceramics. One processing route has also been used to prepare bismuth sodium titanate glass-ceramics. Microwave sintering processing has been successfully used to prepare BNT ceramics as an alternative method to replace solid-state sintering, with three motivations: reducing sintering time; reducing energy consumption; and using a low-cost microwave oven in comparison to a conventional furnace. A novel melt processing route has been studied to manufacture bismuth sodium titanate glass-ceramics as an alternative process to replace solid-state sintering processing for two reasons: reducing the processing steps and reducing the processing time. Conventional solid-state sintering processing has been used as a baseline to compare the results with other novel ones.

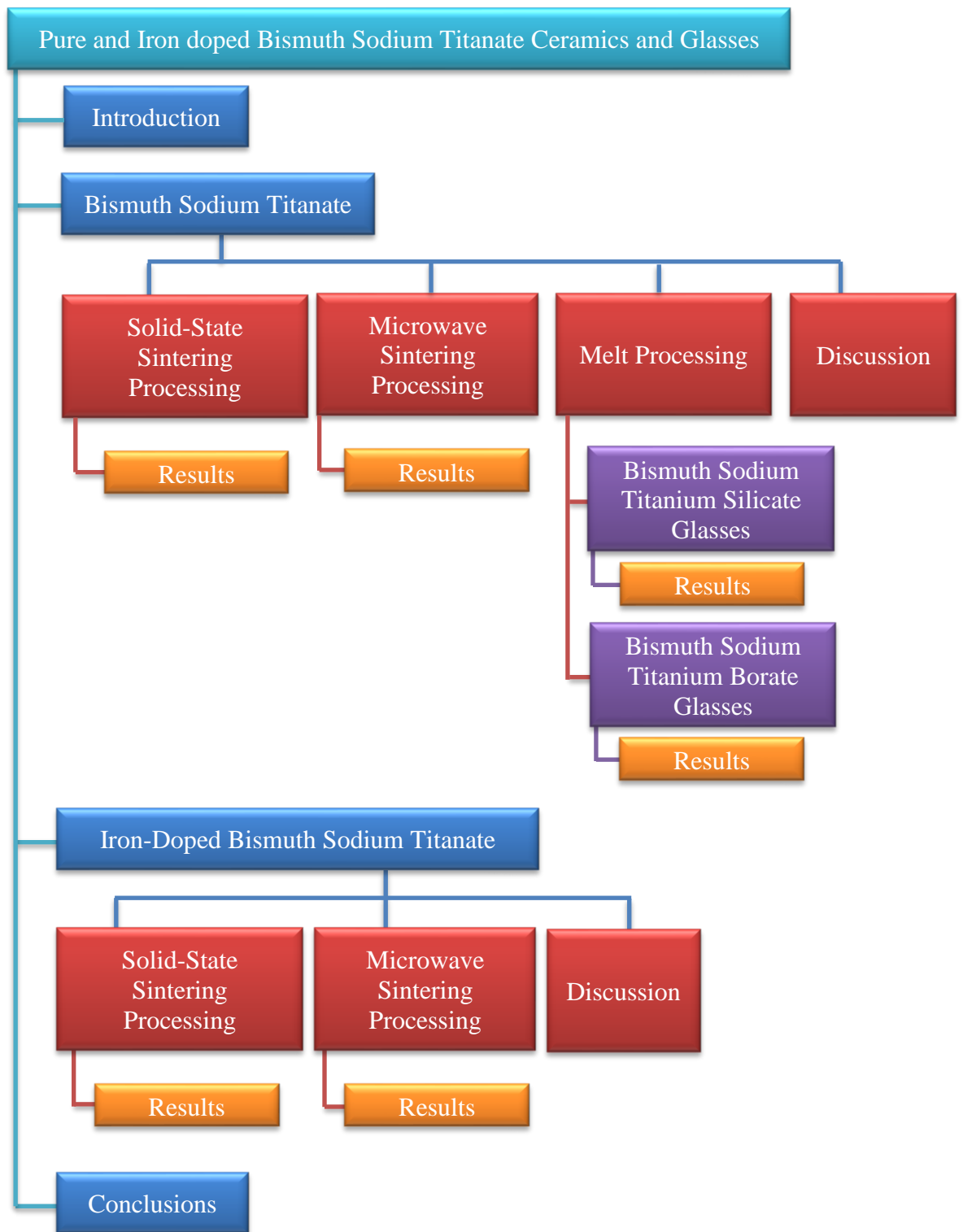


Figure 4.1. Overview of pure and iron-doped bismuth sodium titanate ceramics and glasses (Chapter Four).

4.2. Pure Bismuth Sodium Titanate Ceramics and Glasses

In the present work, pure BNT ceramics were prepared by three processing routes, as presented in Figure 4.1.

4.2.1. Solid State Processing Route

The experimental procedure for solid-state sintering processing of pure BNT ceramics was described in chapter three, section 3.2.1.1. Also, the nominal compositions of the solid-state sintered pure BNT ceramics synthesised in the present work are summarised in Table 3.1.

4.2.1.1. Results and Discussion

4.2.1.1.1. XRD

Figure 4.2 shows diffraction patterns for all solid-state BNT ceramics measured at room temperature with an angle (2θ) ranged from 10 to 80 degrees. Phase analysis identified that all samples are single-phase $\text{Bi}_{0.5}\text{Na}_{0.5}\text{TiO}_3$ with rhombohedral symmetry (ICCD no 04-017-0216). There are two parts to Figure 4.2: part (a) corresponds to BNT ceramics prepared with 700°C/4h calcination temperature/time and different sintering temperatures/time (1000, 1050, 1075, 1100°C/2h), and part (b) shows BNT ceramics prepared with 800°C/4h calcination temperature/time and different sintering temperatures/time (1000, 1050, 1075, 1100°C/2h).

XRD results show a single perovskite lead-free $\text{Bi}_{0.5}\text{Na}_{0.5}\text{TiO}_3$ phase with no traces of intermediate phases for all solid-state sintered BNT ceramic samples, which is consistent with rhombohedral structure as indicated by ICDD no 04-017-0216, as shown in Figure 4.2. XRD results shows broad peaks at lower sintering temperature, due to the smaller crystallite size (Abdul Razak, Yip, & Sreekantan, 2011), as shown in Figure 4.2 (c) and (d). The rhombohedral structure is exhibited at room temperature, which is consistent with pure BNT polymorphism reported by Priya and Nahm (Priya & Nahm, 2011). According to the rhombohedral structure for pure BNT ceramics, XRD results have good agreement with previous studies of Prado-Espinosa et al (Prado-Espinosa et al., 2017), Pourianejad and Movahedi (Pourianejad & Movahedi, 2015), Aman Ullah et al (Aman Ullah et al., 2015) and Pattipaka et al (Pattipaka et al., 2018).

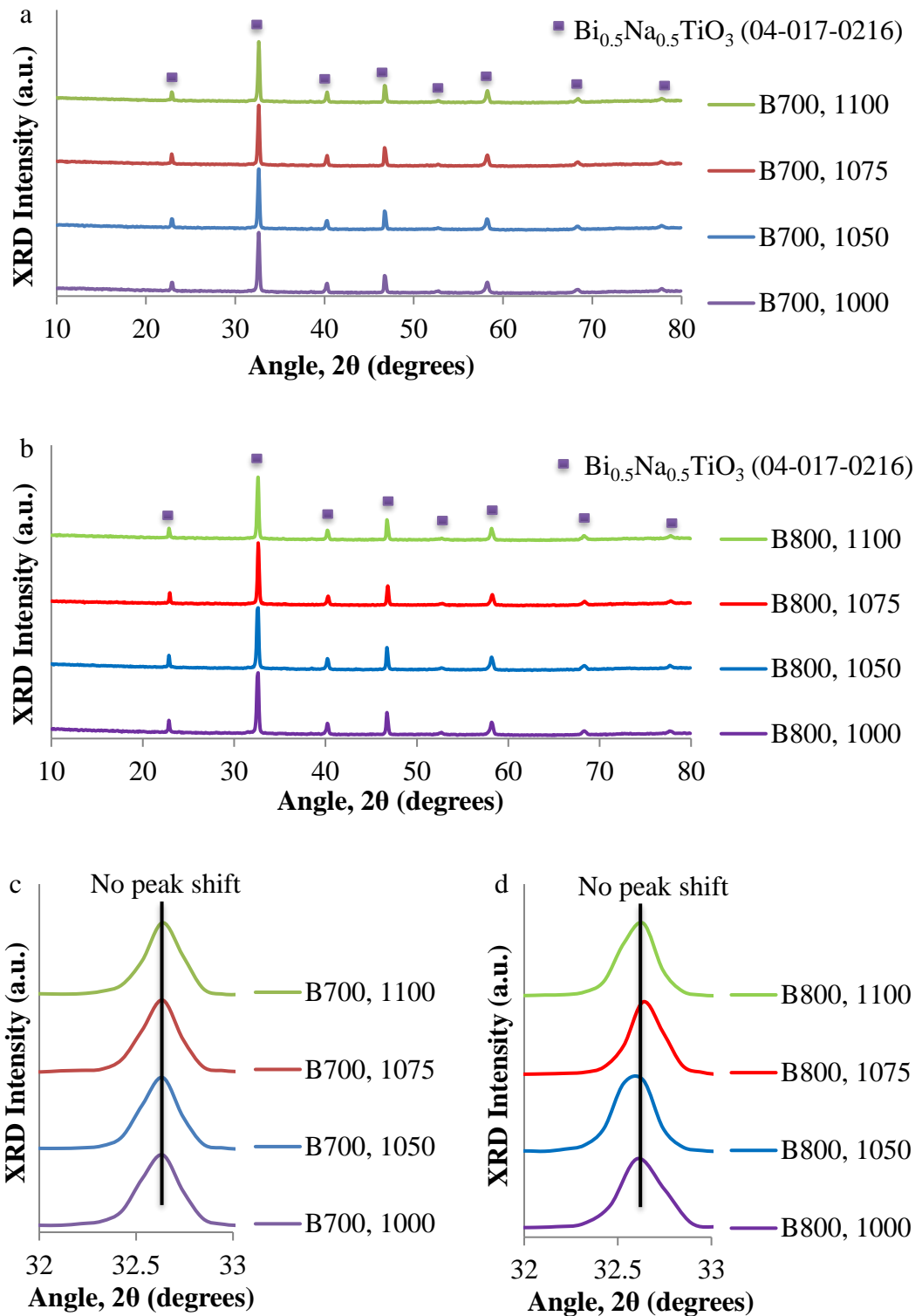


Figure 4.2. X-Ray diffraction patterns for solid sintered BNT ceramics with (a) 700°C/4h calcination conditions, (b) 700°C/4h calcination conditions, and different sintering temperatures/time as shown. Peak position (2 theta) shifting (c and d) for solid-state sintered Bi_{0.5}Na_{0.5}TiO₃ ceramics.

4.2.1.1.2. Raman Spectroscopy

Figure 4.3 presents Raman spectra for solid-state sintered BNT ceramics measured at room temperature with a Raman shift from 100 to 1000 cm^{-1} . Raman spectra exhibit six peaks for all BNT ceramic samples. Figure 4.3 is divided into two parts: part (a) shows Raman spectra for BNT ceramics synthesised with 700°C/4h calcination conditions and different sintering conditions (1000, 1050, 1075, 1100°C/2h), and part (b) shows Raman spectra for BNT prepared with 800°C/4h calcination conditions and different sintering conditions (1000, 1050, 1075, 1100°C/2h).

Raman spectra (Figure 4.3) shows six peaks at room temperature for all solid-state sintered BNT ceramics samples, consistent with Gallegos-Melgar et al. (Gallegos-Melgar et al., 2015) and Rout et al. (Rout et al., 2017) reports. The first band has one peak (peak A) located between 100 to 200 cm^{-1} , indicating a vibrational bending mode, which is assigned to the Na-O band as A-site cation in the ABO_3 perovskite structure (Sumang et al., 2017). However, a Bi-O band is not expected to exist to 100 cm^{-1} due to the larger mass of Bi (Pattipaka et al., 2018). The second band has one peak (peak B) with the highest Raman intensity placed between 200 and 450 cm^{-1} , referring to the broad stretching vibrational mode, which is assigned as a Ti-O band with A_1 -symmetry (Bai et al., 2016). The third band has two peaks (peak C and peak D) located at 450 – 700 cm^{-1} , referring to the broad stretching vibrational mode, which is allocated as TiO_6 band (Sumang et al., 2017). The fourth band shows a lower Raman intensity and contains two peaks (peaks F and G) placed in between 700 and 900 cm^{-1} , corresponding to the broad stretching vibrational mode, which is likely to be A_1 (longitudinal optical) and E mode (longitudinal optical) overlapping bands that show very broad stretching vibrational mode (Bai et al., 2017).

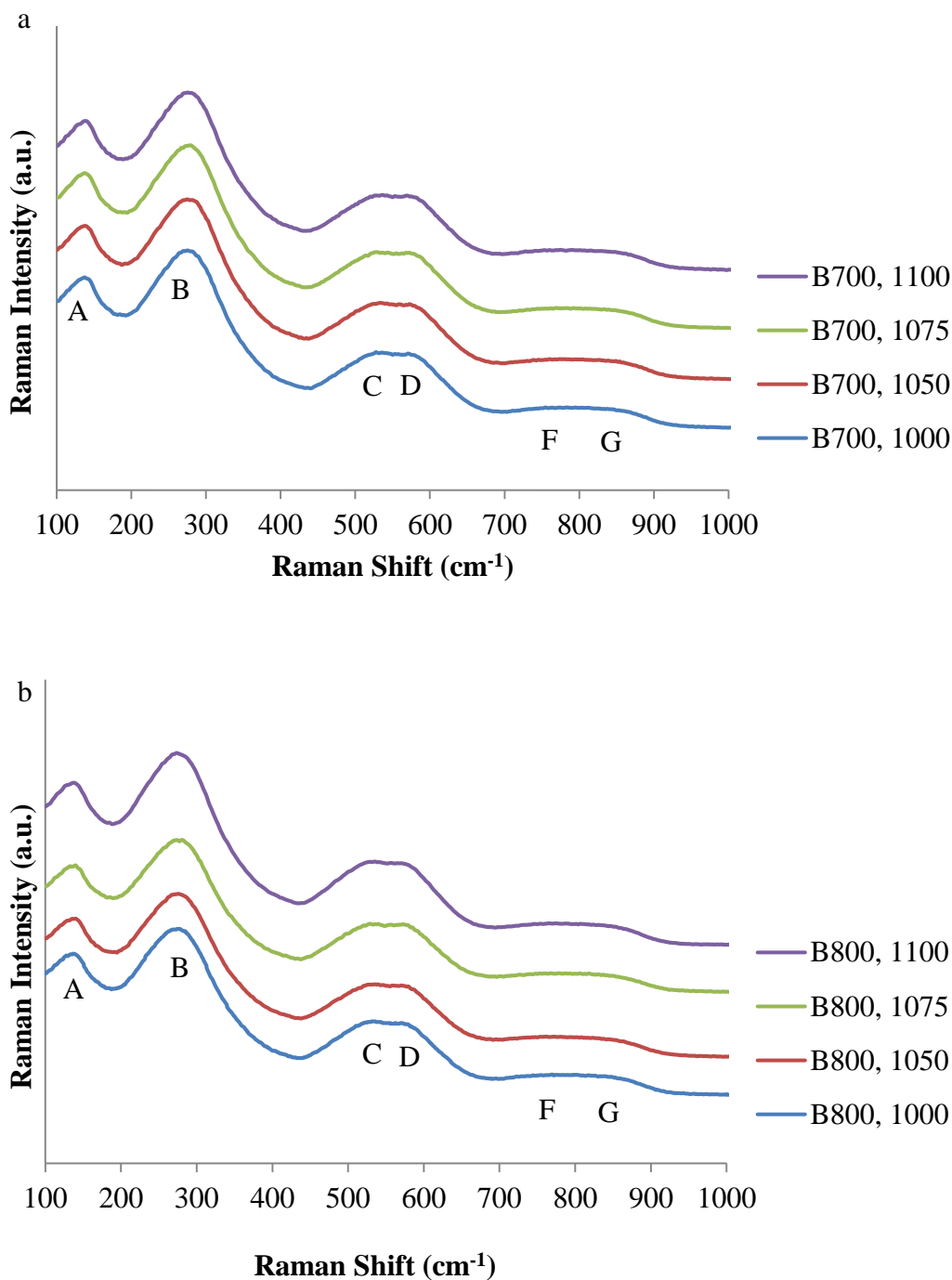


Figure 4.3. Raman spectra for solid-state sintered BNT ceramics with (a) 700°C/4h calcination condition and (b) 700°C/4h condition temperature, and different sintering conditions as shown.

4.2.1.1.3. Electron Microscopy

Figure 4.4 shows Secondary SEM micro-images for solid-state sintered BNT ceramics measured at room temperature with 60,000x magnification and 2 μm scale. It can be seen that all pure BNT ceramic samples sintered at 1000°C are porous with fine

grains. Densification and average grain size increase with increasing sintering temperatures, as shown in Figure 4.4.

SEM micro-images clearly show irregular grain shapes for all solid-state sintered BNT ceramics, as shown in Figure 4.4. It can be observed that the grain sizes have increased with increasing the sintering temperature. Porous ceramics with smaller average grain sizes (approximately $400 \text{ nm} \pm 10$) were obtained for BNT ceramics processed at $1000^\circ\text{C}/2\text{h}$ sintering conditions, and average grain sizes increased, coinciding with higher densification, the larger average grain sizes of approximately $2 \mu\text{m} \pm 0.1$ at higher 1100°C sintering temperatures. The level of densification in the SEM micro-images is consistent with the relative density, exhibiting porous with lower relative density (approximately 83% of theoretical density) and densified ceramics with higher relative density (approximately 94% of theoretical density), obtained for BNT ceramics sintered at 1000 and 1100°C respectively, as shown in Figure 4.4 and Table 4.1. Moreover, the higher average grain sizes obtained (approximately $2 \mu\text{m}$) are closely similar to values of approximately $2.5 \mu\text{m}$ stated by Khamman (Khamman, 2014), however, it is clearly smaller than these of about $2.9 \mu\text{m}$ reported by Fujii et al. (Fujii et al., 2016), for pure BNT ceramics.

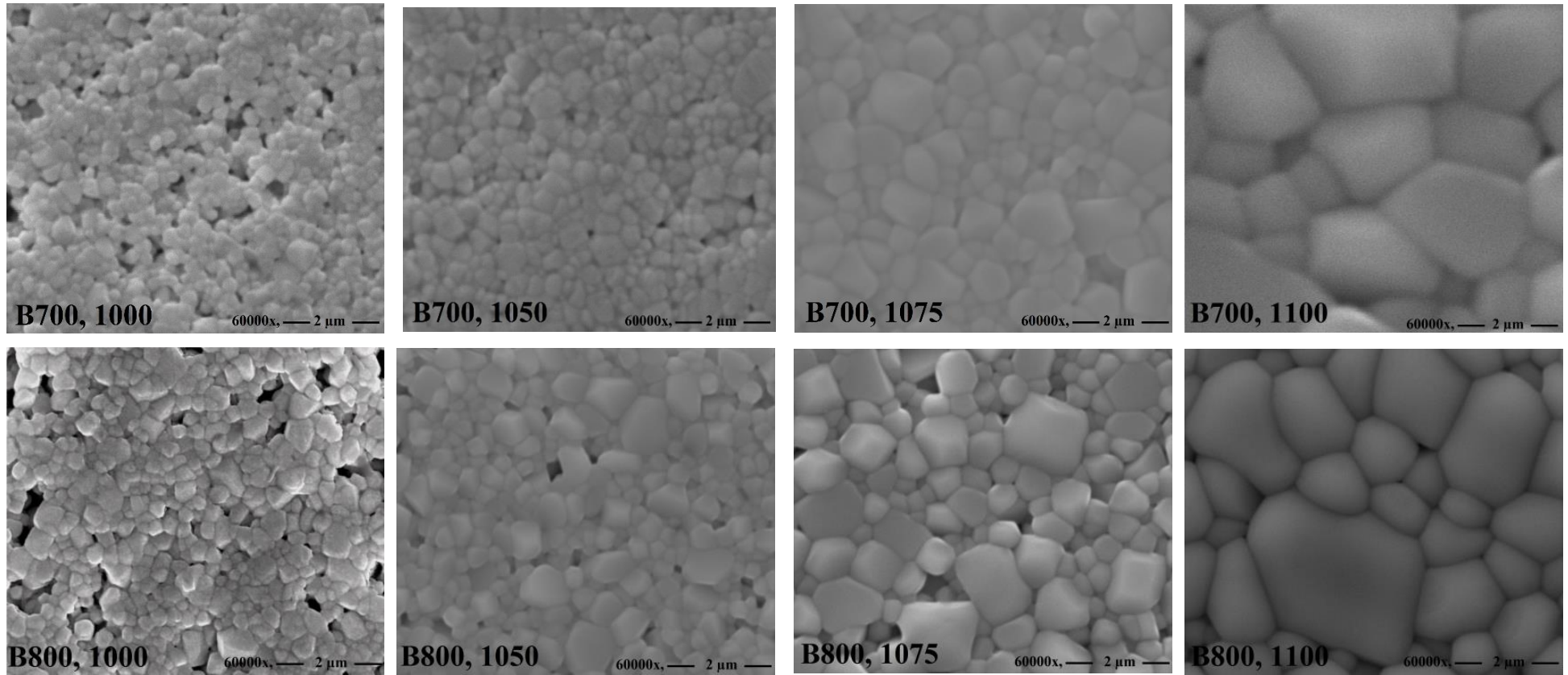


Figure 4.4. Secondary SEM images for solid sintered BNT ceramics with different calcination temperatures and sintering temperatures, as shown.

4.2.1.1.4. Density

Table 4.1 presents bulk and relative density results for all solid-state sintered BNT ceramics made with different calcination and sintering temperatures as presented.

The relative density results show increasing relative density with increasing sintering temperature, as shown in table 4.1. Pure BNT ceramics with lower (1000°C) sintering temperatures are identified with lower relative density (approximately 83% of theoretical density), then reaching higher relative density (approximately 94% of theoretical density) at higher (1100°C) sintering temperature. The higher relative density (approximately 94% of theoretical density) demonstrates good agreement with those of about 93% of theoretical density reported by Khamman (Khamman, 2014). However, it is lower than the 95% of theoretical density reported by Fujii et al. (Fujii et al., 2016), for pure BNT ceramics.

Table 4.1. Relative density results for solid-state sintered $\text{Bi}_{0.5}\text{Na}_{0.5}\text{TiO}_3$ ceramics.

Sample names	Bulk density (g/cm ³)	Relative density (%)	Sample names	Bulk density (g/cm ³)	Relative density (%)
B700, 1000	5.09±0.05	85.1±0.5	B800, 1000	4.98±0.05	83.3±0.5
B700, 1050	5.46±0.05	91.4±0.5	B800, 1050	5.42±0.05	90.5±0.5
B700, 1075	5.60±0.05	93.8±0.5	B800, 1075	5.62±0.05	93.9±0.5
B700, 1100	5.65±0.05	94.6±0.5	B800, 1100	5.64±0.05	94.1±0.5

4.2.1.1.5. Electrical Properties

Figure 4.5 shows hysteresis (P-E) loops and polarisation for all solid-state sintered BNT ceramics measured at room temperature, 70kV/cm electric field and 1 Hz frequency in a bipolar field. Figure 4.5 includes two parts: part (a) shows results for solid-state sintered BNT ceramics prepared with 700°C/4h calcination conditions and various sintering conditions (1000, 1050, 1075, 1100°C/2h), and part (b) shows results for solid-state sintered BNT ceramics prepared with 800°C/4h calcination conditions and different sintering conditions (1000, 1050, 1075, 1100°C/2h).

The remnant polarisation increased from about 22 to 40 $\mu\text{C}/\text{cm}^2$, with increasing sintering temperatures from 1050 to 1100°C, respectively. It is anticipated that, at lower (1000°C) sintering temperature and lower relative density (approximately 83% of theoretical density), the absence of hysteresis (P-E) loops is due to current leakage

through pores in the BNT samples, corresponding to the high porosity (Wiegand et al., 2012; Woo et al., 2017). At low (1050°C) sintering temperature for ceramic samples (named B700, 1050 and B800, 1050), hysteresis (P-E) loops appeared in a lemon (round) like-shape with no saturation, indicating high conductivity resulting in current leakage, caused by lower relative density (approximately 91% of theoretical density) and resulting porosity (Kang et al., 2011; Wiegand et al., 2012). The saturated and typical shape of ferroelectric hysteresis loops appeared at 1075°C and 1100°C sintering temperatures and higher relative densities of about 93% and 94% (of theoretical density), respectively. The maximum remnant polarisation ($40\mu\text{C}/\text{cm}^2$) appeared at higher 1100°C sintering temperature and relative density (94% of theoretical density), for ceramics (named B700, 1100) shows an improvement in comparison with $30\mu\text{C}/\text{cm}^2$ (Fujii et al., 2016; Maqbool et al., 2014), $30\mu\text{C}/\text{cm}^2$ (Aman Ullah et al., 2015), however, it is less than $43.6\mu\text{C}/\text{cm}^2$ (Jiang et al., 2014), for pure BNT ceramics.

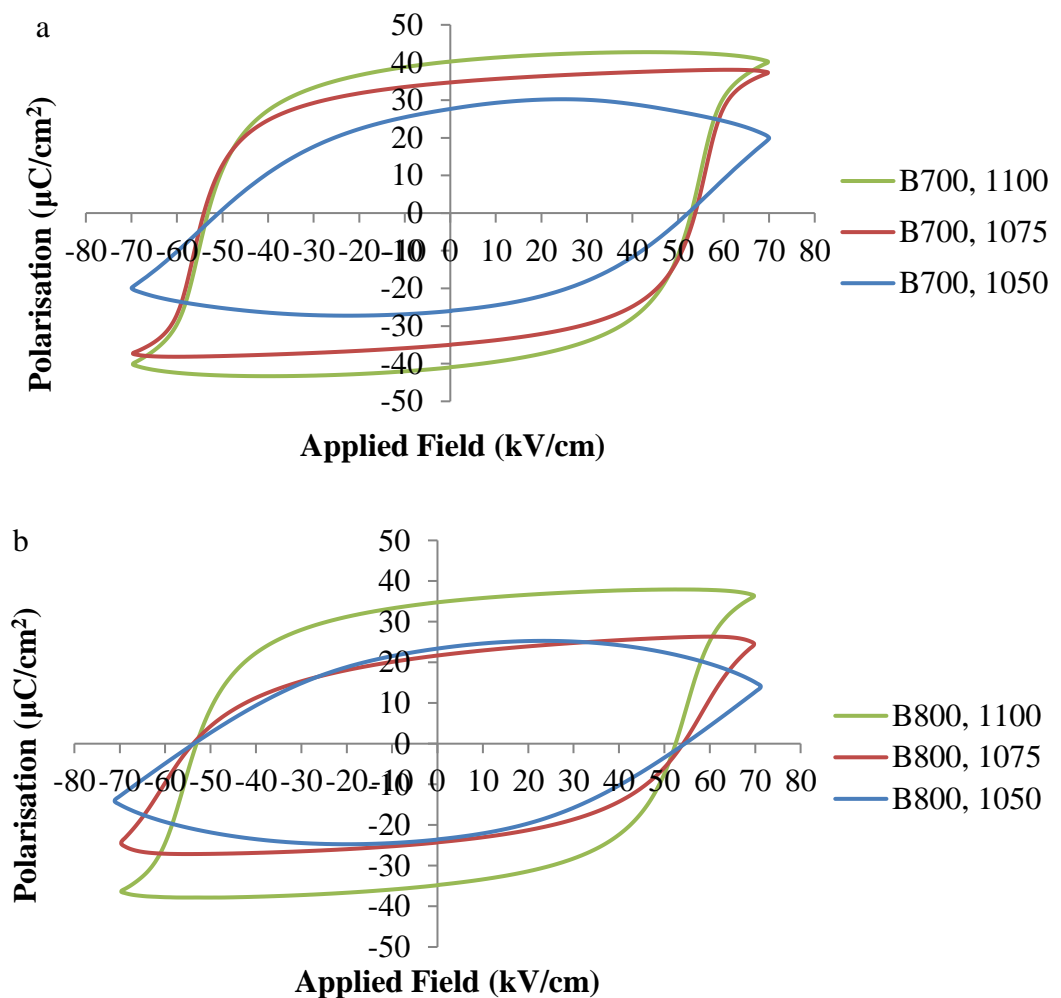


Figure 4.5. Polarisation vs electric field response at room temperature and 1Hz frequency using the bipolar measurement for solid sintered BNT ceramics with (a) 700°C/4h calcination conditions and (b) 800°C/4h calcination conditions, and different sintering temperatures as shown.

Figure 4.6 presents strain-electric field (S-E) loops of all solid-state sintered BNT ceramics measured at room temperature, 70kV/cm electric field and 1 Hz frequency in a bipolar field. There are two parts shown in Figure 4.6: part (a) corresponds to solid-state sintered BNT ceramics prepared with 700°C/4h calcination condition and various sintering conditions (1000, 1050, 1075, 1100°C/2h), and part (b) shows solid-state sintered BNT prepared using 800°C/4h calcination condition and different sintering conditions (1000, 1050, 1075, 1100°C/2h). It is observed that the butterfly S-E loop shapes showing lower and upper strain occurred in the (1050-1100°C) temperatures sintered BNT ceramics, respectively.

The maximum strain increased from about 0.045% to 0.08%, with increasing the sintering temperature from 1050 to 1100°C, respectively. The typical butterfly shape of S-E loops is present for all solid-state BNT ceramic samples sintered at 1050, 1075 and 1100°C, indicating ferroelectric behaviour (Priya & Nahm, 2011). However, at lower (1000°C) sintering temperature, the S-E loops disappeared. This may be due to current leakage through the pores of the ceramics, corresponding to lower relative density (83% of theoretical density). The maximum strain of 0.08% is consistent with other results for solid-state sintered BNT ceramics (named B700, 1100) in comparison with 0.08% (Maqbool et al., 2014) and higher than 0.07% (Rahman et al., 2014).

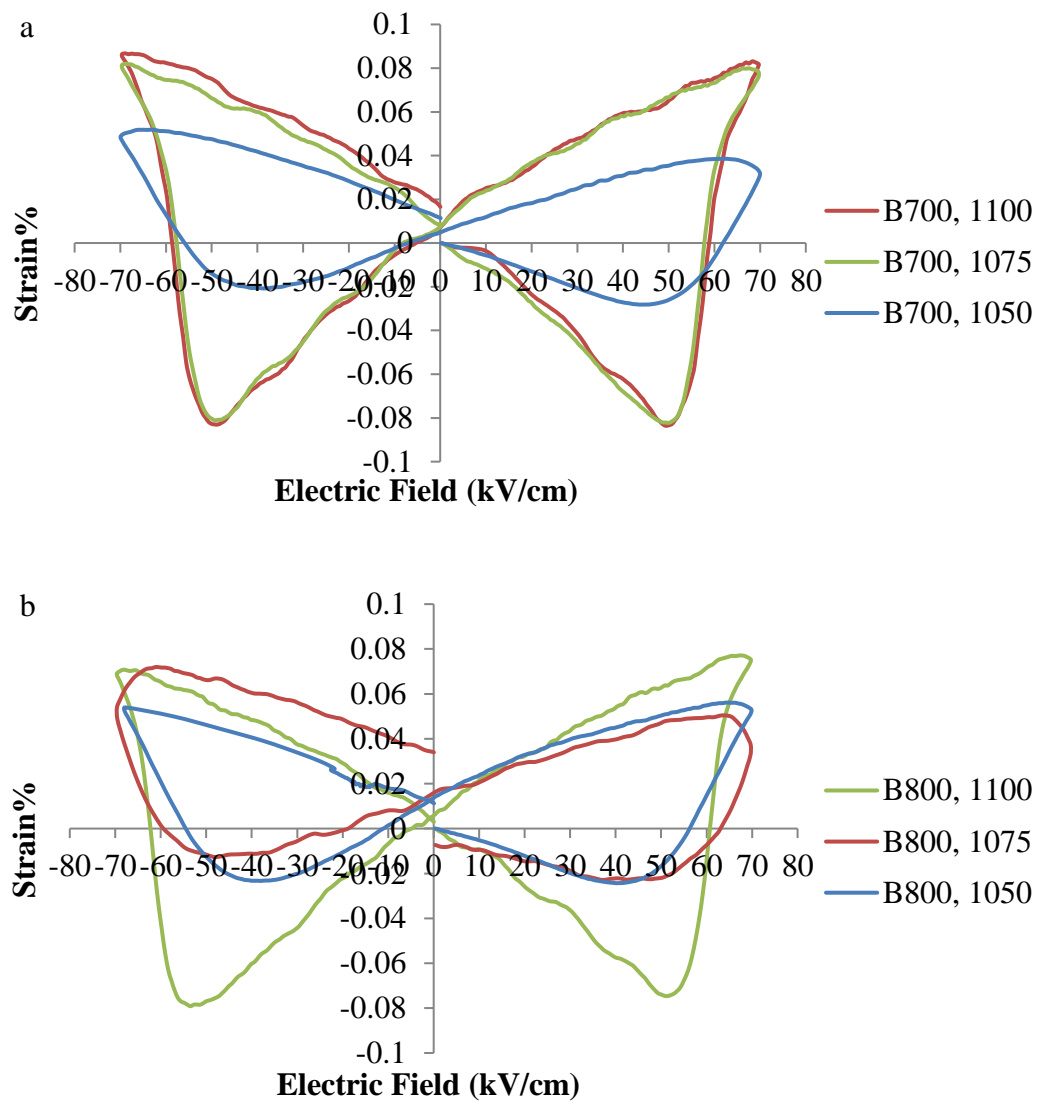


Figure 4.6. Electric field induced strain at room temperature and 1Hz frequency using the bipolar measurement for solid sintered BNT ceramics with (a) 700°C/4h calcination conditions and (b) 700°C/4h calcination conditions, and different sintering conditions.

4.2.2. Microwave Processing Route

The experimental procedure of microwave sintering processing for pure BNT ceramics has explained in chapter three, section 3.2.2.1. Also, the nominal compositions of the microwave sintered pure BNT ceramics prepared in the present work are summarised in Table 3.5.

4.2.2.1. Results and Discussion

4.2.2.1.1. XRD

XRD analysis shows a single $\text{Bi}_{0.5}\text{Na}_{0.5}\text{TiO}_3$ (ICCD no 04-017-0216) perovskite phase with the rhombohedral structure for all microwave sintered BNT ceramics applied

at 10 to $80^\circ 2\theta$, as shown in Figure 4.7. Figure 4.7 is divided into parts: part (a) microwave sintered BNT ceramics prepared with $700^\circ\text{C}/4\text{h}$ calcination conditions and different microwave sintering times (10, 15, 20, 25mins), and part (b) microwave sintered BNT ceramics prepared with $800^\circ\text{C}/4\text{h}$ calcination conditions and various microwave sintering times (10, 15, 20, 25mins).

XRD results exhibit a pure phase of perovskite $\text{Bi}_{0.5}\text{Na}_{0.5}\text{TiO}_3$ ceramics without the presence of any secondary phases for all microwave sintered BNT ceramic samples, which is consistent with rhombohedral structure as indicated by ICDD no 04-017-0216, as shown in Figure 4.7. XRD results shows broad peaks at lower sintering time, indicating to the smaller crystallite size (Abdul Razak, Yip, & Sreekantan, 2011), as shown in Figure 4.7 (c) and (d). The rhombohedral structure of pure BNT ceramics at room temperature has been reported by previous studied of Prado-Espinosa et al (Prado-Espinosa et al., 2017), Pourianejad and Movahedi (Pourianejad & Movahedi, 2015), Aman Ullah et al (Aman Ullah et al., 2015) and Pattipaka et al (Pattipaka et al., 2018). In addition, XRD results related to the rhombohedral structure of microwave sintered BNT ceramics show excellent agreement with those of solid-state sintered BNT ceramics, as shown in Figure 4.7 and Figure 4.2, respectively.

XRD patterns of pure microwave and solid-state sintered BNT ceramics displays no changes in the peak position and peak shape for a strong peak allocated between 32 and 33 degree, which shows a good consistent with rhombohedral structure indicating by ICDD no 04-017-0216, for BNT ceramics manufactured by microwave and solid-state sintering processing, as shown in Figure 4.8.

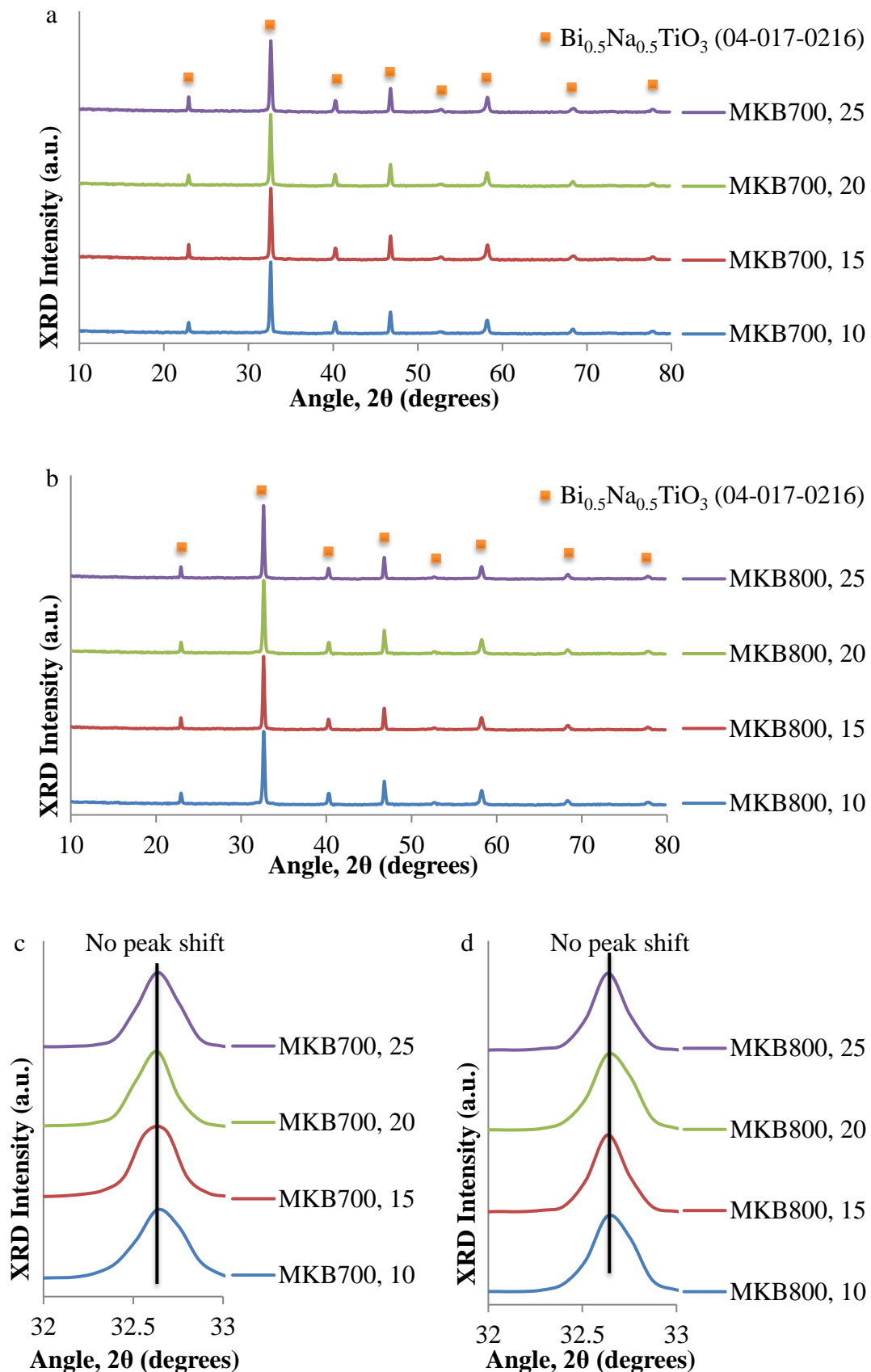


Figure 4.7. X-Ray diffraction patterns for microwave sintered BNT ceramics with (a) 700°C/4h calcination conditions (b) 800°C/4h calcination conditions, and different sintering times, and peak position (2 theta) shifting (c and d) for microwave sintered Bi_{0.5}Na_{0.5}TiO₃ ceramics.

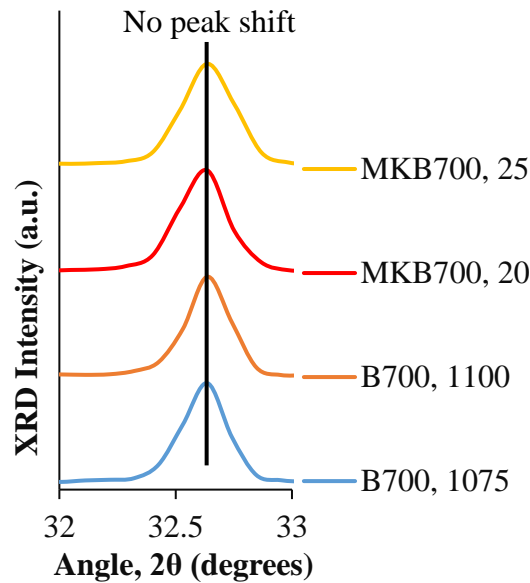


Figure 4.8. X-Ray diffraction patterns for microwave and solid-state sintered BNT ceramics with peak position (2 theta) shifting.

4.2.2.1.2. Raman Spectroscopy

Raman results present six peaks for all microwave sintered BNT ceramic samples, measured at room temperature with Raman shifts between 100 to 1000 cm^{-1} , as shown in Figure 4.9. Figure 4.9 has two parts; part (a) corresponds to microwave sintered BNT ceramics made with 700°C/4h calcination conditions and different microwave sintering times (10, 15, 20, 25 mins), and part (b) indicates to microwave sintered BNT ceramics prepared with 800°C/4h calcination conditions and different microwave sintering times (10, 15, 20, 25 mins). Peak A is located in the middle of the first region and lower Raman shift of 100 to 200 cm^{-1} , indicating a vibrational bending mode, which is assigned as an A-site cation in the ABO_3 perovskite structure as Na-O band. However, a Bi-O band is not present at 100 cm^{-1} due to the larger mass of Bi (Pattipaka et al., 2018). Peak B is placed in the middle of the second region between 200 and 450 cm^{-1} . This region shows the highest Raman intensity due to the broad vibrational stretching mode, which is assigned as Ti-O band with A_1 -symmetry (W. Bai et al., 2016). It is observed that association of peaks C and D in the third region between 450 and 700 cm^{-1} , indicating a broad vibrational stretching mode and allocated as a TiO_6 band (Sumang et al., 2017). The fourth region is an association of peaks F and G at 700 to 900 cm^{-1} . This region shows lower Raman intensity that corresponds to the broad vibrational stretching mode, which is likely to be A_1 (longitudinal optical) and E mode (longitudinal optical) overlapping bands (Bai et al., 2017). No changes were observed in the peak shape of

Raman spectra for microwave sintered BNT ceramics achieved, which is in good agreement with the Raman results for solid-state sintered BNT ceramics, as revealed in Figure 4.9 and Figure 4.3, respectively.

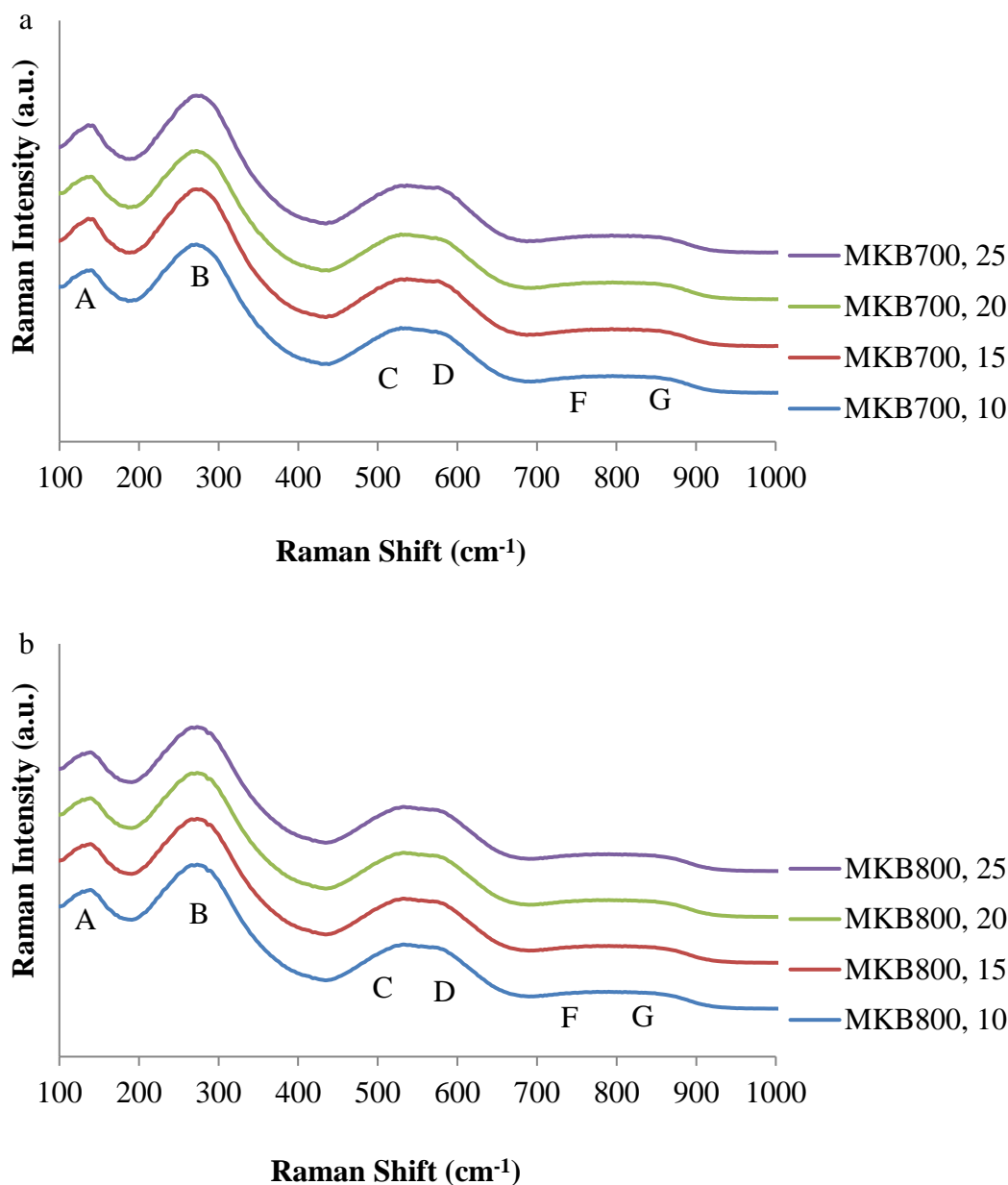


Figure 4.9. Raman spectra for microwave sintered BNT ceramics with (a) 700°C/4h calcination conditions and (b) 800°C/4h calcination conditions, and different sintering times.

4.2.2.1.3. Electron Microscopy

Secondary SEM micro-images for solid-state BNT ceramic samples measured at room temperature with 60,000x magnification and 2 μ m scale are shown in Figure 4.10. A porous sample was obtained for BNT ceramics sintered at 10 mins microwave

sintering time, and the level of densification increased with increasing microwave sintering times, as shown in Figure 4.10.

SEM micrographs show irregular grains for all microwave sintered BNT ceramic samples, as shown in Figure 4.10. The average grain size consistently increases from approximately 200 to 900 nm \pm 150 nm with microwave sintering time increasing from 10 to 25 mins, respectively. More porous samples with separately grains occurred at shorter microwave sintering times of 10 mins, and samples densified with an increasing agglomeration of grains with increasing microwave sintering time to 25 mins, as shown in Figure 4.10. Densification shows a close relationship with the relative density, for example a very porous surface ceramic with lower relative density (approximately 70% of theoretical density) and a densified surface ceramic with higher relative density (approximately 94% of theoretical density), obtained for microwave sintered BNT ceramic samples at 10 and 25 mins respectively, as shown in Figure 4.10 and Table 4.2.

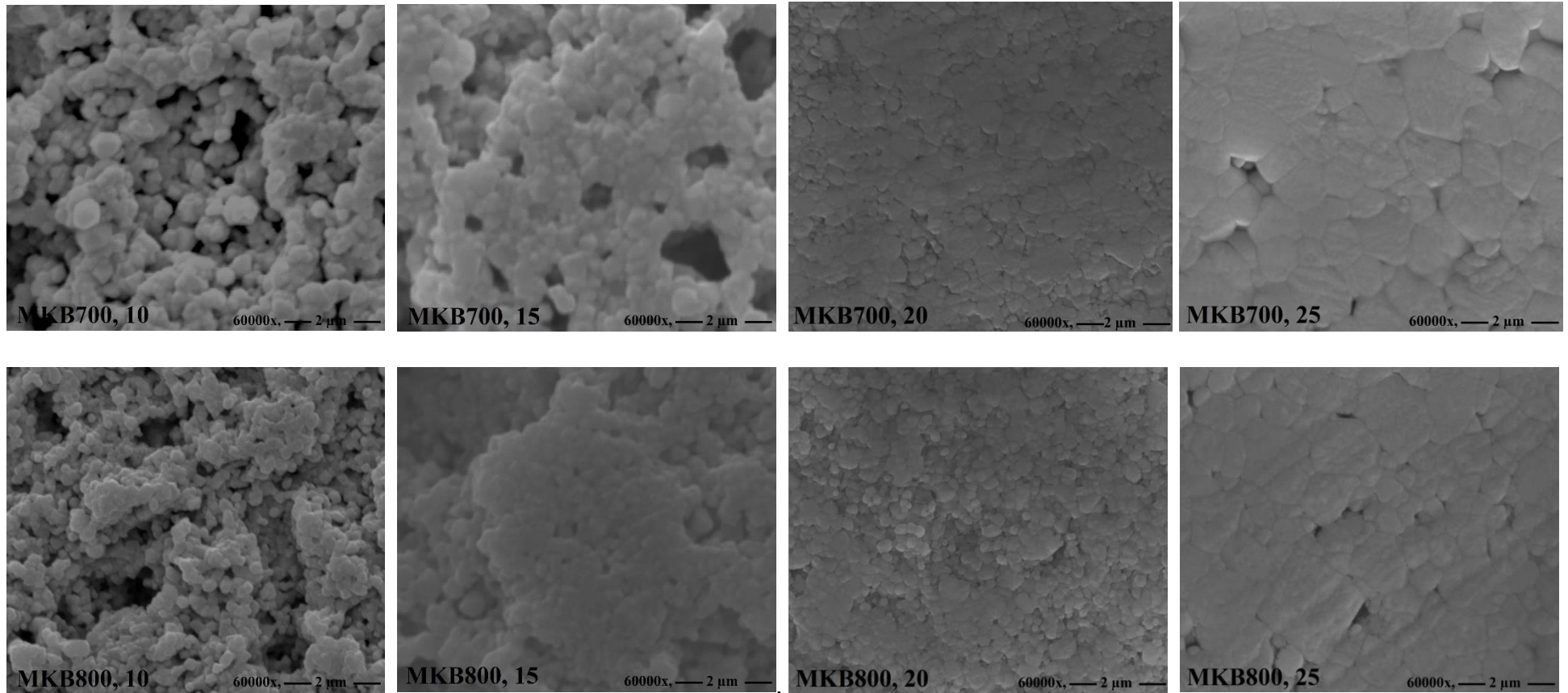


Figure 4.10. Secondary electron SEM images for microwave sintered BNT ceramics with different calcination temperatures and sintering timed (10-25 mins).

4.2.2.1.4. Density

Table 4.2 presents the dependence of bulk and relative density of microwave sintered BNT ceramics as a function of microwave sintering time.

The relative density results show increasing relative density with increasing microwave sintering time, as shown in Table 4.2. At shorter microwave sintering times of 10 mins, lower relative density (approximately 70% of theoretical density), and increasing the microwave sintering time to 25 mins, which increases the relative density to the maximum (approximately 94% of theoretical density). At longer 25 mins microwave sintering time, the maximum relative density (approximately 94% of theoretical density) for microwave sintered BNT ceramics shows excellent agreement with these of solid-state sintered BNT ceramics. In addition, the higher relative density (approximately 94% of theoretical density) exhibits good agreement with those of about 93% of theoretical density reported by Khamman (Khamman, 2014), however, it is lower than 95% of theoretical density reported by Fujii et al. (Fujii et al., 2016).

Table 4.2. Relative density results for pure microwave sintered $\text{Bi}_{0.5}\text{Na}_{0.5}\text{TiO}_3$ ceramics.

Sample names	Bulk density (g/cm^3)	Relative density (%)	Sample names	Bulk density (g/cm^3)	Relative density (%)
MKB700, 10	4.27±0.03	71.2±0.3	MKB800, 10	4.15±0.03	69.3±0.3
MKB700, 15	4.73±0.03	79.0±0.3	MKB800, 15	4.86±0.03	80.7±0.3
MKB700, 20	5.06±0.03	84.5±0.3	MKB800, 20	4.95±0.03	82.7±0.3
MKB700, 25	5.64±0.03	94.1±0.3	MKB800, 25	5.61±0.03	93.7±0.3

4.2.2.1.5. Electrical Properties

Figure 4.11 displays polarisation versus applied field at room temperature, in a bipolar field for microwave BNT ceramics sintered at 25 microwave sintering time and calcined at 700°C and 800°C. Polarisation increased with increasing an applied field and shows saturated hysteresis loop shape at higher 70kV/cm electric field.

Figure 4.12 displays hysteresis (P-E) loops and polarisation applied at room temperature, 70kV/cm electric field in a bipolar field for microwave sintered BNT

ceramics. It can be seen; saturated hysteresis P-E loop has appeared for microwave sintered BNT ceramics calcined at 700 and 800°C with microwave sintering time of 25 mins.

A low remnant polarisation of about $8 \mu\text{C}/\text{cm}^2$ detected for microwave sintered ceramics such sample MKB800, 25, and higher remnant polarisation of about $42.2 \mu\text{C}/\text{cm}^2$ was observed for the microwave sintered ceramic named MKB700, 25. At lower (10, 15, 20 mins) microwave sintering times and lower relative density (approximately 80, 80, 83% of theoretical density, respectively), there is an absence of hysteresis (P-E) loops, which is due to passing current leakage through pores in the BNT ceramics (current leakage, high conductivity), related to the high porosity (Wiegand et al., 2012; Woo et al., 2017), which led to the uptake by the BNT ceramic sample of the silicone oil during P-E measurements. The saturated shape of ferroelectric P-E loops was obtained for samples prepared at 25 minutes microwave sintering time and higher relative densities of about 94% (of theoretical density). Microwave sintering processing here has confirmed that a obtaining good remnant polarisation (e.g. $42.2\mu\text{C}/\text{cm}^2$) can be achieved for pure BNT ceramics with very short (25 mins) microwave sintering time, compared with previous studies of remnant polarisation on the basis of pure BNT ceramics from solid-state sintering processing with very long (340 mins) sintering time, as stated in Table 4.3.

Table 4.3. Remnant polarisation for pure BNT ceramics prepared by microwave sintering processing in the present study and solid-state sintering processing in the present and previous studies.

Citation	Remnant polarisation ($\mu\text{C}/\text{cm}^2$)
MKB700, 25 (Figure 4.12)	42.2
B700, 1100 (Figure 4.6)	40
Maqbool et al., 2014	30
Aman Ullah et al., 2015	28
Jiang et al., 2014	43.6
Cheng et al., 2015	24
Wei et al., 2018	25

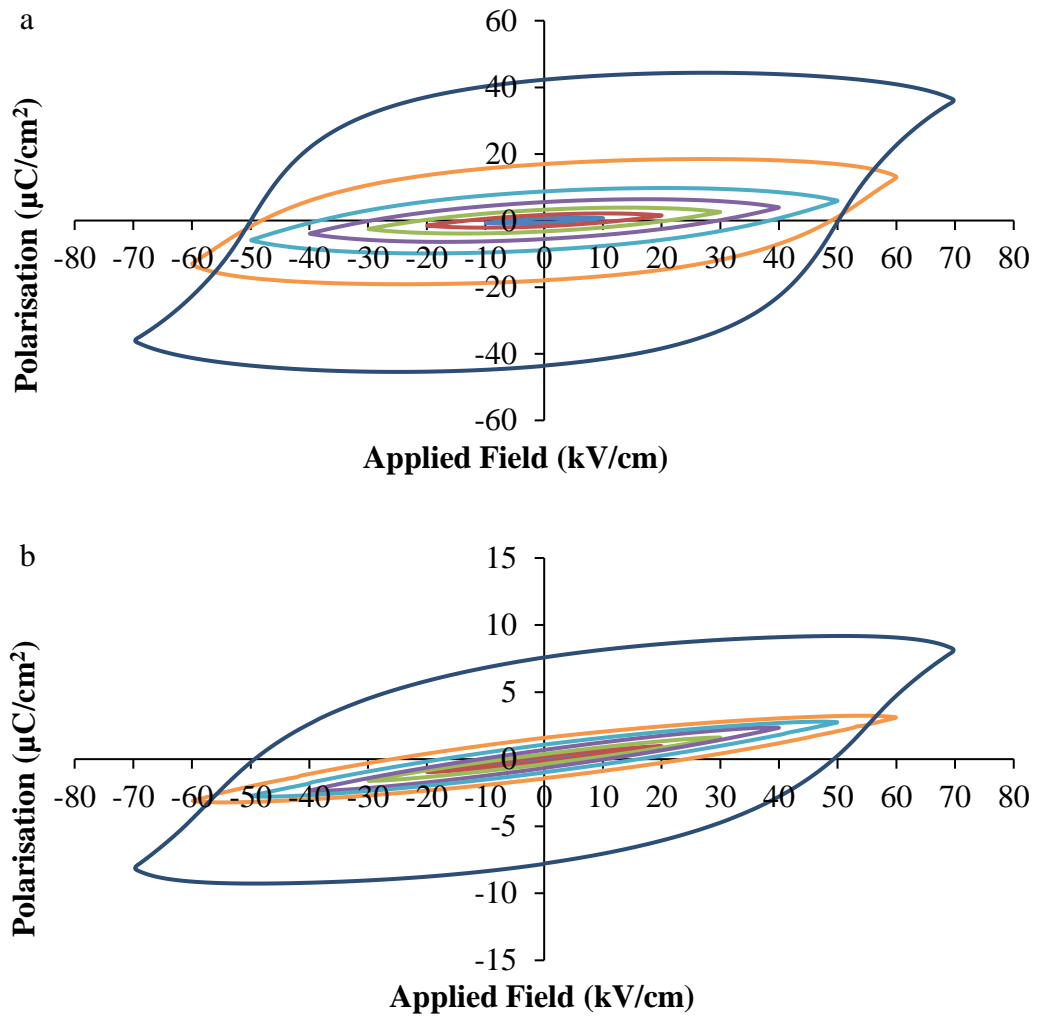


Figure 4.11. Polarisation vs electric field response at room temperature using bipolar measurement for microwave sintered BNT ceramics calcined at (a) 700°C and (b) 800°C, and sintered at 25 microwave sintering time.

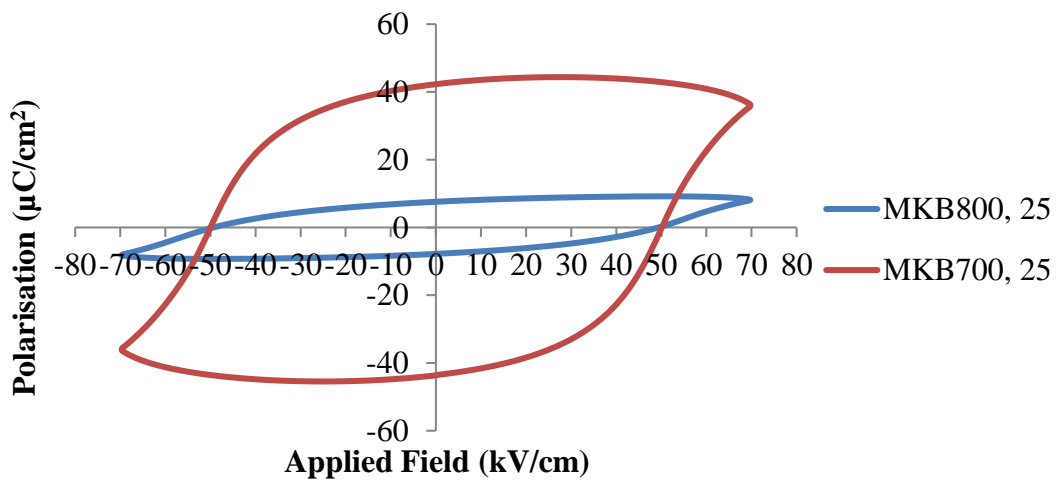


Figure 4.12. Polarisation vs electric field response at room temperature using bipolar measurement for microwave sintered BNT ceramics.

Figure 4.13 shows strain versus applied field at room temperature, in a bipolar field for microwave BNT ceramics sintered at 25 microwave sintering time and calcined at 700°C and 800°C. Maximum strain increased with increasing an applied field and shows butterfly shape for S-E loops at higher 70kV/cm electric field.

Figure 4.14 presents strain-electric field (S-E) loops and strain applied at room temperature, 70kV/cm electric field in a bipolar field for microwave sintered BNT ceramics. The butterfly shape of the S-E loop was obtained for microwave sintered BNT ceramics calcined at 700 and 800°C with microwave sintering time of 25 mins.

A lower maximum strain of about 0.055% was detected for the microwave sintered ceramics MKB800, 25, and a higher strain of about 0.083% detected for the microwave sintered ceramics MKB700, 25. At lower (10, 15, 20 mins) microwave sintering times and lower relative density (approximately 80, 80, 83% of theoretical density) respectively, the absence of S-E loops is due the current leakage through the BNT ceramics, resulting from high porosity (Wiegand et al., 2012; Woo et al., 2017). The typical butterfly shape of S-E loops was detected for all microwave sintered BNT ceramic samples sintered at 25 mins microwave sintering time, indicating ferroelectric properties (Priya & Nahm, 2011). A typical butterfly shape of S-E loops with maximum strain (0.083%) is presented for pure BNT ceramics synthesised with very short (25 mins) microwave sintering times, comparing with previous studies of strain on the basis of pure BNT ceramics synthesis by solid-state sintering processing with very long (340 mins) sintering times, as stated in Table 4.4.

Table 4.4. Maximum stain for pure BNT ceramics prepared by microwave sintering processing in the present study and solid-state sintering processing in the present and previous studies.

Citation	Maximum train%
MKB700, 25 (Figure 4.13)	0.083
B700, 1100 (Figure 4.7)	0.08
Maqbool et al., 2014	0.08
Jiang et al., 2014	0.07
Wei et al., 2018	0.07

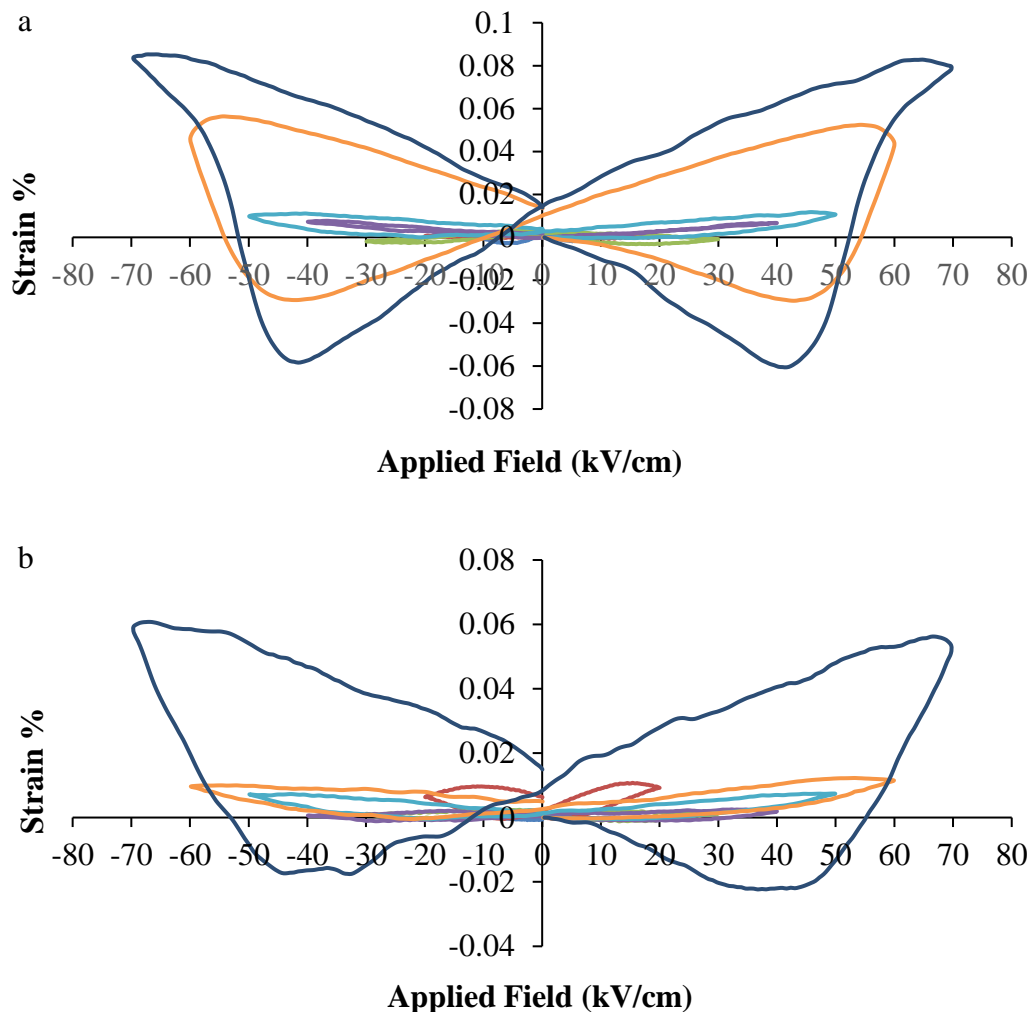


Figure 4.13. Electric field induced strain at room temperature using bipolar measurement for microwave sintered BNT ceramics calcined at (a) 700°C and (b) 800°C, and sintered at 25 microwave sintering time.

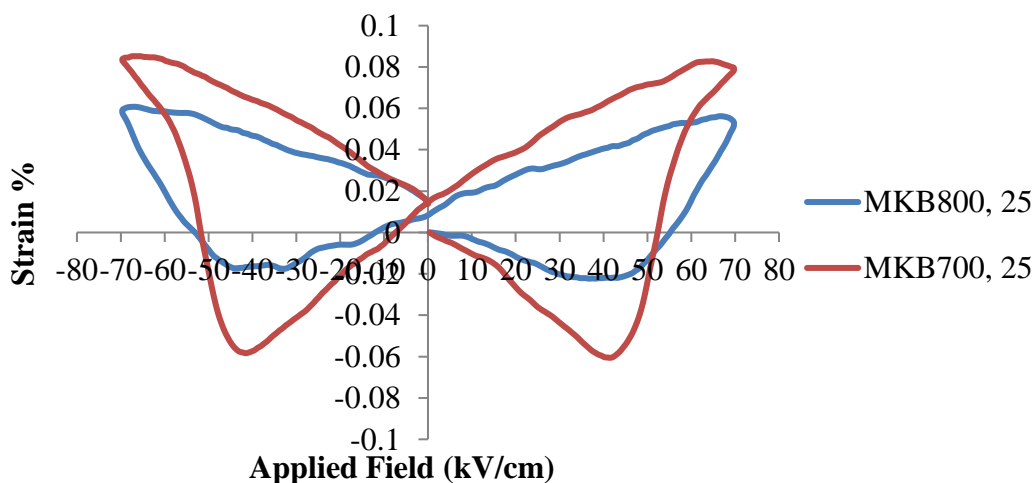


Figure 4.14. Electric field induced strain at room temperature using the bipolar measurement for microwave sintered BNT ceramics.

4.2.3. Melt Processing Route

The experimental procedures of melt processing for BNT silicate and BNT borate glasses have explained in chapter three, section 3.2.3.

4.2.3.1. Bismuth Sodium Titanium Silicate Glasses

The nominal compositions of the BNT silicate glasses prepared in the present work are summarised in Table 3.10.

4.2.3.1.1. Results and Discussion

4.2.3.1.1.1. XRD

Bismuth sodium titanium silicate glasses were ground to a fine powder and placed in XRD sample metallic holders separately to measure the crystalline structures using XRD analysis. At room temperature, XRD analysis from 10 to 80° 2θ and shows an amorphous phase and one crystalline phase, identified as $Ti_2Bi_2O_7$, for all bismuth sodium titanium silicate crystalline glasses, as shown in Figure 4.15.

It can be seen from Figure 4.13, all sharp peaks are consistent with ICDD no 04-014-2416, showing cubic crystalline structure of $Ti_2Bi_2O_7$ (bismuth titanium oxide) phase, at room temperature wide featureless peaks are consistent with amorphous phase. This indicates that Na^+ is not present in the crystalline structure. It may be evaporated during sample syntheses at higher 1450°C melting temperature, which is due to lower melting point of Na_2O of 1132°C (Li et al., 2013), or incorporated in the amorphous phase. Ten peaks were obtained for all glasses except one glass (named MBS70, 1h), however, this reduced to 3 peaks for glass (named as MBS70, 1h). This may be due to the presence of phase separation in glass MBS70, 1h composition, as shown in Figure 4.15.

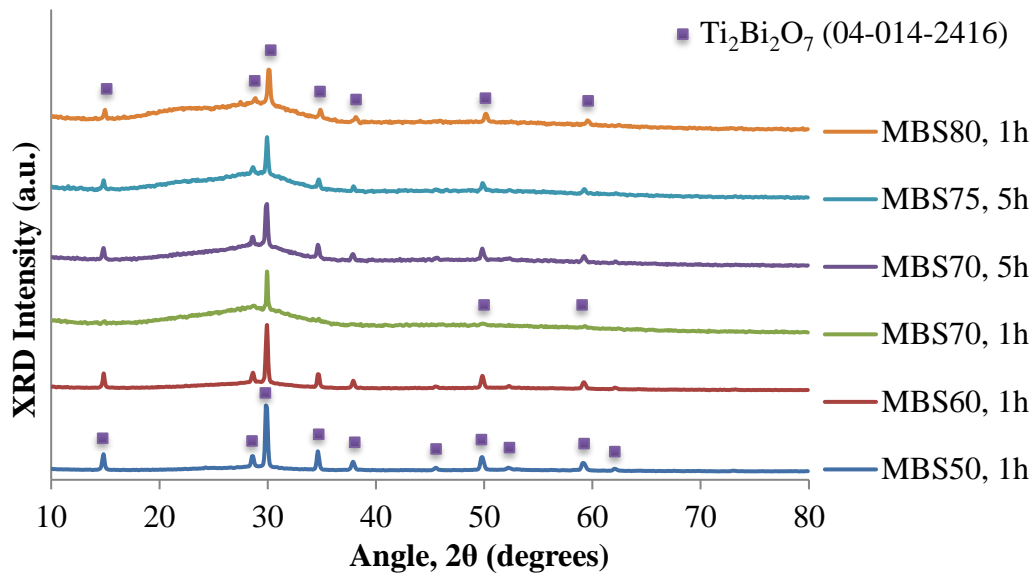


Figure 4.15. XRD patterns of as-quenched of bismuth sodium titanium silicate glasses.

4.2.3.1.1.2. Raman Spectroscopy

Raman spectra for bismuth sodium titanium silicate glasses measured at room temperature with Raman shift ranged from 50 to 1800 cm^{-1} , are shown in Figure 4.16. It can be observed that Raman spectra have sharp, strong peaks at lower than 100 cm^{-1} , however, at higher than 100 cm^{-1} , these became very broad and weak peaks. It can be seen from Figure 4.16, that peaks marked as a and b, located less than 100 cm^{-1} , can be assigned to the vibrational bending mode, which is assigned as Bi-O band due to the larger mass of Bi as reported by Pattipaka et al. (Pattipaka et al., 2018). Peak c, at approximately 283 cm^{-1} is assigned as Ti-O band, which is shown weak and broad band (Bai et al., 2016). Peak d is placed at $\sim 453 \text{ cm}^{-1}$, which is identified as a motion of Si versus its tetrahedral oxygen cage with a weak movement of oxygen from it is a position or assigned as bridging Si-O-Si band with the vibrational bending mode (Madheshiya, Gautam & Upadhyay, 2018). Peaks e and f at approximately 554 and 750 cm^{-1} are assigned to TiO_6 and TiO_5 bands respectively, which show very weak and broad peaks with vibrational stretching modes (Sumang et al., 2017; Inoue et al., 2006). The last band g, is identified at approximately 954 cm^{-1} , and is assigned to Si-O-Ti bonds formed from non-bridging oxygen of Si-O^- in Q^2 species linked with Ti^{4+} , exhibiting a weak and broad peak with vibrational stretching modes (Bouchouicha et al., 2016; Cheng, Brow & Chen, 2017; Rezazadeh et al., 2014; Shen et al., 2018).

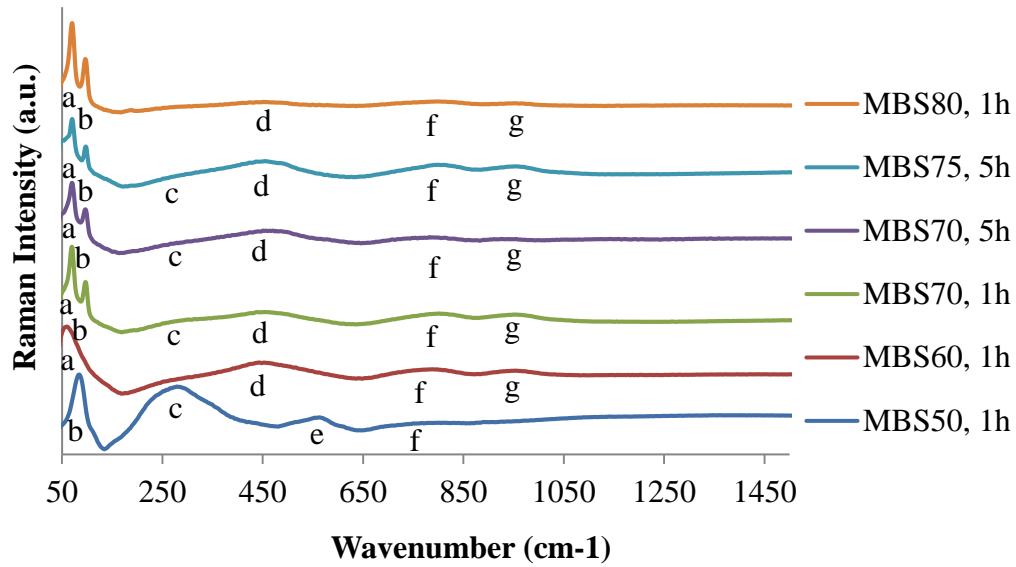


Figure 4.16. Raman spectra of bismuth sodium titanium silicate glasses.

4.2.3.1.1.3. Electron Microscopy

Secondary SEM micro-images for bismuth sodium titanium silicate glasses were measured at room temperature with 60,000x magnification and 2 μm scale. It can be observed that all glassy samples reveal grains on the surface, as shown in Figure 4.17.

Secondary SEM micrographs of bismuth sodium titanium silicate glasses revealed grains growth in the bulk of all samples except one (named MBS70, 1h), as shown in Figure 4.17. As can be anticipated, no grains were observed on the micro-surface of glass named MBSi70, 1h. This may demonstrate an amount of phase separation based on XRD result (Figure 4.15). However, the presence of grains on the glass surface, evidence of crystallisation of bismuth sodium titanium silicate, is in agreement with XRD results (Figure 4.15). It can be seen from SEM micrographs that maximum and minimum average grain size of approximately 200 and 50 nm \pm 10 nm for glasses named MBSi70, 5h and MBSi80, 1h, respectively. The fine structure of the crystalline phase is consistent with homogeneous nucleation and growth.

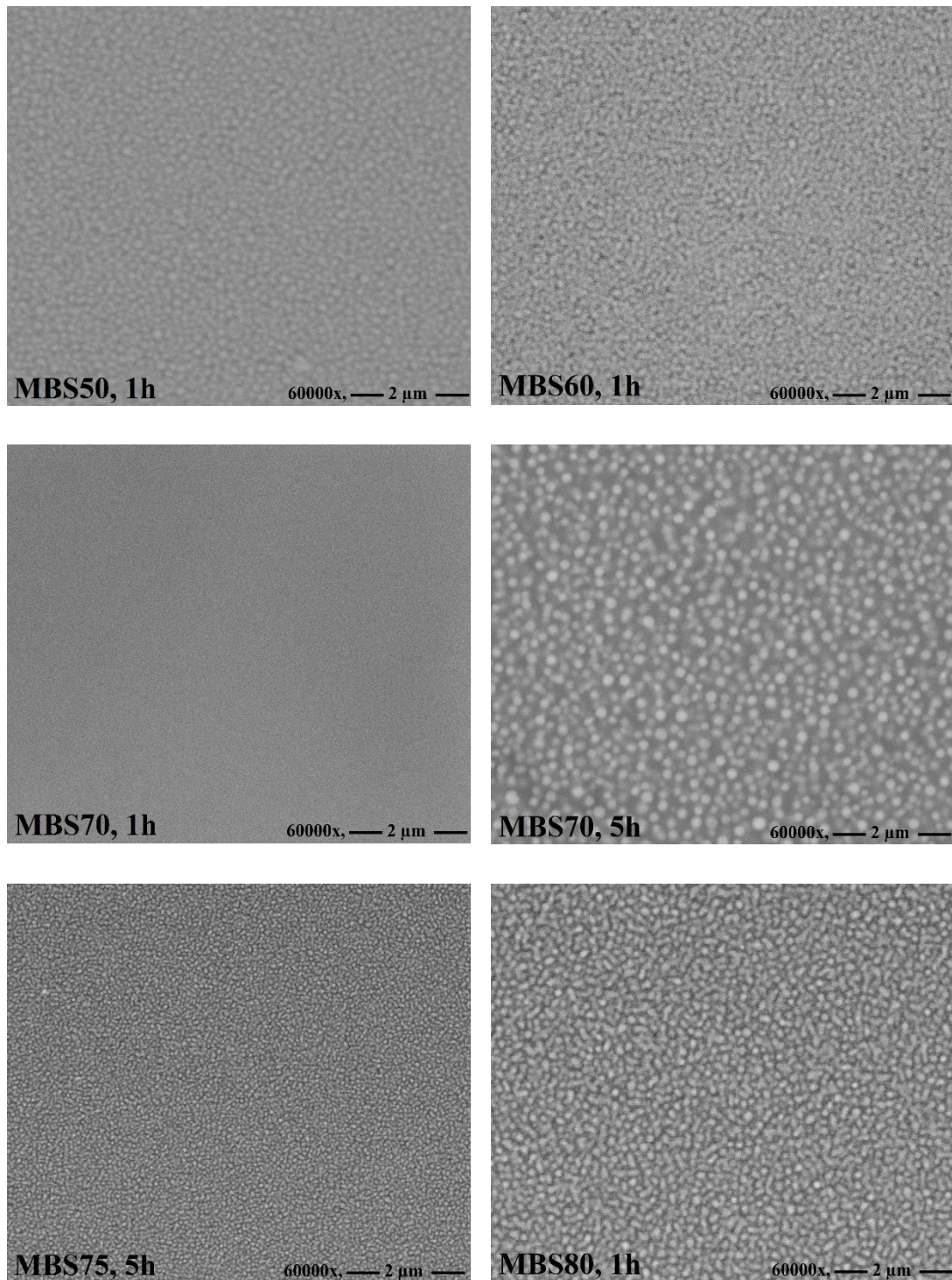


Figure 4.17. SEM images for bismuth sodium titanium silicate glasses.

4.2.3.1.1.4. Density

Table 4.5 reveals the dependence of bulk densities for bismuth sodium titanium silicate glasses as a function of composition. It can be observed that the bulk density of bismuth sodium titanium silicate glasses decreased with increasing SiO_2 content, as expected on the basis of decreasing Bi_2O_3 content.

Bulk densities of bismuth sodium titanium silicate glasses exhibit a maximum density of 4.0 g/cm³ and a minimum density of 3.0 g/cm³ of glasses MBSi50, 1h and MBSi80, 1h, respectively. Table 4.5 shows that the bulk density of bismuth sodium titanium silicate glasses decreased with increasing of SiO₂, attributing to the increasing of SiO₂ and decreasing Bi₂O₃, Na₂O and TiO₂ mol% contents.

Table 4. 5. Bulk density results for bismuth sodium titanium silicate glasses.

Sample name	Bulk density (g/cm ³)
MBS50, 1h	4.0±0.3
MBS60, 1h	3.7±0.3
MBS70, 1h	3.5±0.3
MBS70, 5h	3.2±0.3
MBS75, 5h	3.2±0.3
MBS80, 1h	3.0±0.3

4.2.3.2. Bismuth Sodium Titanium Borate Glasses

The nominal compositions of the BNT borate glasses prepared in the present work are summarised in Table 3.11.

4.2.3.2.1. Results and Discussion

4.2.3.2.1.1. XRD

Bismuth sodium titanium borate (MBB) glasses were ground to the fine powder and placed in the XRD sample metallic holders separately to measure the crystalline structures using XRD analysis. XRD diffraction patterns for all MBB glasses were measured at room temperature with an angle (2θ) ranged from 10 to 80° 2θ. XRD results show an amorphous phase and two crystalline phases identified as TiO₂ (01-078-1509) and Bi₄Ti₃O₂ (00-047-0398) for bismuth sodium titanium borate glasses, as shown in Figure 4.18.

Figure 4.18 shows that two of the bismuth sodium titanium borate glasses (named MBB30 and MBB50) have two crystalline phases, identified as TiO₂ (01-078-1509) and Bi₄Ti₃O₂ (00-047-0398), and one glass (named as MBB70) has one crystalline phase identified as TiO₂ (01-078-1509), at room temperature. This indicates that Na⁺ is not present in the crystalline structure. Most likely it is present in the amorphous phase, but

it could also be evaporated at sample syntheses at higher (>1300°C) melting temperature (H. Li et al., 2013).

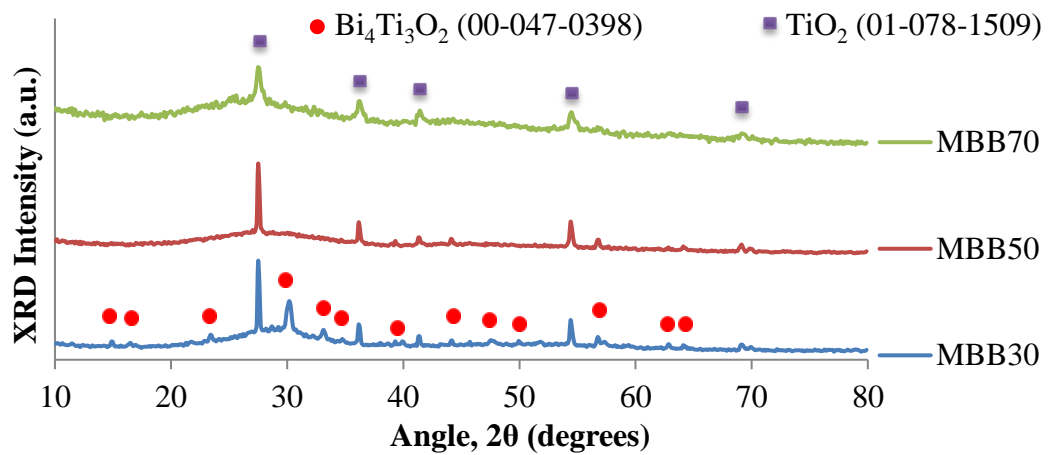


Figure 4.18. XRD results of bismuth sodium titanium borate glasses.

4.3. Iron-Doped Bismuth Sodium Titanate Ceramics

In the present work, iron-doped BNT ceramics were prepared by two processing routes, as presented in Figure 4.1.

4.3.1. Solid State Processing Route

The experimental procedure for solid-state sintering processing for iron doped BNT ceramics has described in chapter three, section 3.2.1.2. Also, the nominal compositions of the solid-state sintered pure BNT ceramics synthesised in the present work are summarised in Table 3.2.

4.3.1.1. Results and Discussion

4.3.1.1.1. XRD

Figure 4.19 shows diffraction patterns for all iron-doped BNT ceramics measured at room temperature with 2θ ranged from 10 to 80°. Phase analysis identified that all samples are phase pure Bi_{0.5}Na_{0.5}TiO₃ (89-3109) with cubic structure. There are three parts to Figure 4.19: part (a) relates to Fe-BNT ceramics measured at 2θ ranged from 10 to 80°, part (b) shows Fe-BNT ceramics analysed at 2θ ranged from 32 to 33°, and part (c) corresponds to Fe-BNT ceramics measured at 2θ ranged from 46 to 47°.

X-Ray diffraction (XRD) analysis at room temperature shows a pure Rhombohedral perovskite phase for $\text{Bi}_{0.5}\text{Na}_{0.5}\text{TiO}_3$, as indicated by the ICDD powder diffraction file pattern (04-017-0216) (Chou et al., 2011), without secondary phases, as shown in Figure 4.19(a). This confirms that iron forms a solid solution in BNT for all compositions studied, i.e. up to $x = 0.1$. In addition, the single-phase region has thus been demonstrated for the first time at higher Fe contents of doped BNT ceramics. A slight shift to lower angles occurred with the addition of Fe to BNT, as presented in Figure 4.19(b and c) for the main peak at circa $32.7^\circ 2\theta$ and $46.6^\circ 2\theta$. This slight shift is due to the fact that Fe^{3+} has a larger ionic radius (Shannon, 1976) (0.645 \AA) than Ti^{4+} (0.605 \AA) on the B-site of Fe-BNT perovskite ceramics, which causes changes in the unit cell dimensions and thus changes in d-spacings (Shannon & Prewitt, 1969).

Rietveld refinement (Rietveld, 1969) using FULLPROF (Rodríguez-Carvajal, 1993) was carried out on these data to refine crystal structure parameters. The $\text{Bi}_{0.5}\text{Na}_{0.5}\text{TiO}_3$ structure (Anton et al., 2012) was used as a starting model for Rietveld refinement. For the doped samples Fe and Ti were disordered over the same site. The Rietveld refinement has enhanced the structural and quantitative analysis. The structural analysis shows pseudocubic cell symmetry (Pm-3m) in agreement with the Vijayeta group (Pal, Dwivedi, & Thakur, 2017) and Fukuchi and colleagues (Fukuchi et al., 2002). The quantitative analysis displays unit cell lengths ($a=b=c$), cell volume, and d spacing of 32-33 (2θ) as shown in Table 4.6. The expansion of unit cell lengths ($a=b=c$) from 3.8829 to 3.8893 \AA is due to Fe (larger ionic radius, 0.645 \AA) occupying in the Ti (smaller ionic radius, 0.605 \AA) site of the pseudocubic perovskite structure in agreement with the slight shift of 32-33 (2θ), as shown in Figure 4.19(b), as well as the unit cell volume has expanded from 58.618 \AA^3 for BFe0.00 pure ceramics to the maximum 58.832 \AA^3 for BFe10.00 iron doped ceramics. The d spacing of 32-33 (2θ) increases with increasing the iron content in the BNT ceramics, as shown in Figure 4.20. All the above quantitative results exhibited important changes in the values that due to the addition of Fe_2O_3 in BNT ceramics.

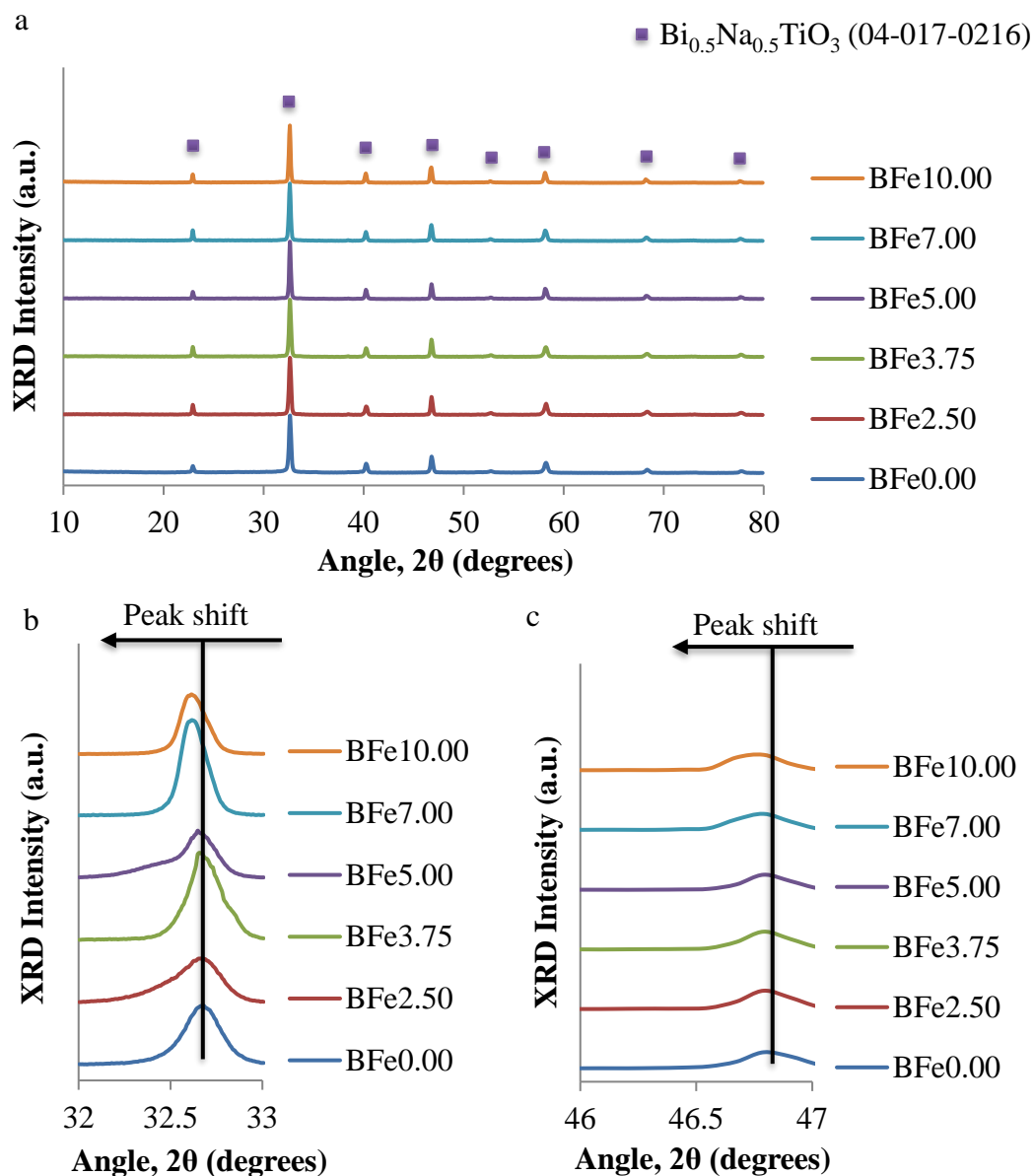


Figure 4.19. X-Ray diffraction patterns (a) and Peak positions (2 theta) shifting (b and c) for solid-state sintered $\text{Bi}_{0.5}\text{Na}_{0.5}\text{Ti}_{1-x}\text{Fe}_x\text{O}_{3-0.5x}$ ceramics ($x = 0.0000-0.1000$).

Table 4.6. Unit cell lengths and volume, d spacing at 32-33 (2θ), and X-ray densities for $\text{Bi}_{0.5}\text{Na}_{0.5}\text{Ti}_{1-x}\text{Fe}_x\text{O}_3$ ceramics ($x = 0.0000, 0.0250, 0.0375, 0.0500, 0.0700$ and 0.1000).

Sample name	Unit cell lengths (a=b=c) Å	Unit cell volume Å ³	d spacing (Å) of 32-33 (2θ)
BFe0.00	3.8846(4)	58.618(10)	2.7468
BFe2.50	3.8853(3)	58.653(8)	2.7474
BFe3.75	3.8865(3)	58.704(8)	2.7482
BFe5.00	3.8870(3)	58.726(7)	2.7485
BFe7.00	3.8881(3)	58.779(8)	2.7493
BFe10.00	3.8893(2)	58.832(6)	2.7502

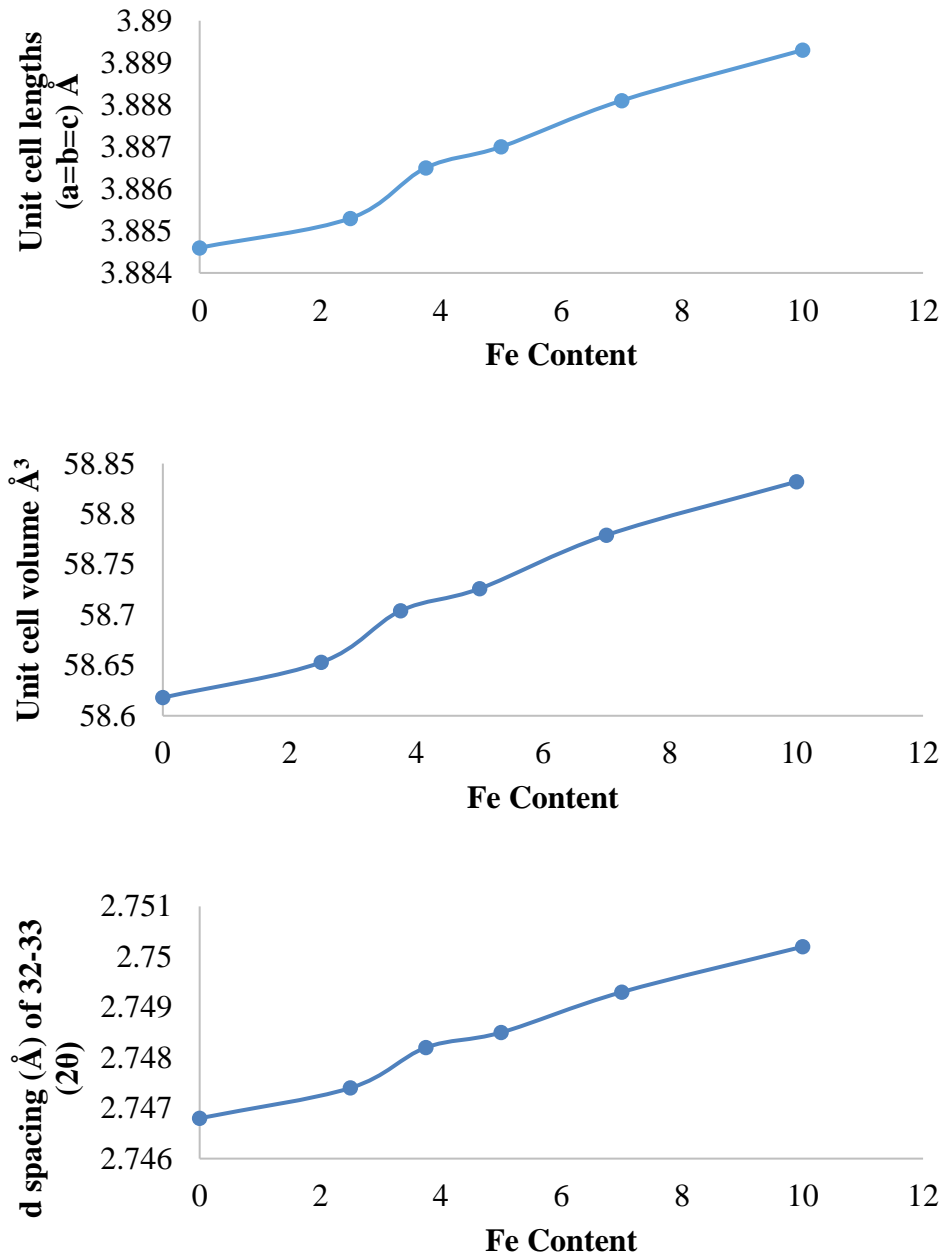


Figure 4.20. Unit cell lengths and volume, d spacing at 32-33 (2θ), and X-ray densities for $\text{Bi}_{0.5}\text{Na}_{0.5}\text{Ti}_{1-x}\text{Fe}_x\text{O}_3$ ceramics ($x = 0.0000, 0.0250, 0.0375, 0.0500, 0.0700$ and 0.1000).

4.3.1.1.2. Raman Spectroscopy

Figure 4.21 presents Raman spectra for solid-state sintered BNT ceramics measured at room temperature with Raman shift from 100 to 1000 cm^{-1} . Raman spectra exhibit six peaks for all BNT ceramic samples. Figure 4.21 is divided to two parts: part (a) displays Raman spectra for iron doped BNT ceramics measured at Raman shift from 100 to 1000 cm^{-1} , and part (b) indicates to iron doped BNT ceramics analysed at Raman shift from 200 to 350 cm^{-1} .

Figure (4.21(a)) shows room temperature Raman spectra for all samples with six peaks. Peaks at lower Raman shifts of 100 cm^{-1} to 200 cm^{-1} refer to the A-site cation in the ABO_3 perovskite structure and are assigned to vibrations of Na-O (Wang, Zhou, & Xue, 2006). However, no Bi-O bands are expected to exist. The Bi-O band should be allocated at lower than 100 cm^{-1} Raman shift due to the large mass of Bi, as Wang et al. explained (Wang et al., 2006). The results exhibit no large changes with increasing Fe content in the Raman spectra for peak A. The second spectral region contains peak B located at Raman shifts between 200 cm^{-1} and 400 cm^{-1} , which is assigned to the Ti-O bond (A_1 -symmetry) that shows broad stretching vibration and highest Raman intensity (Kreiselt et al., 2000). The third main region centred between 450 cm^{-1} and 650 cm^{-1} contains peaks C and D, which are assigned to TiO_6 oxygen octahedra (Bai et al., 2016). The two peaks C and D are mainly due to oxygen displacements, as Lidjici et al. described (Lidjici et al., 2015), and exhibit broad stretching vibration and lower Raman intensity in comparison with peaks A and B (Anthoniappen et al., 2015). The fourth region located between 700 cm^{-1} and 900 cm^{-1} and peaks F and G are likely to be A_1 (longitudinal optical) and E mode (longitudinal optical) overlapping bands that show very broad stretching vibration and lower Raman intensity in comparison with the three lower Raman shift regions (Rout et al., 2010). Raman spectra exhibit no significant changes upon adding iron at peak B, as shown in Figure 4.21(b).

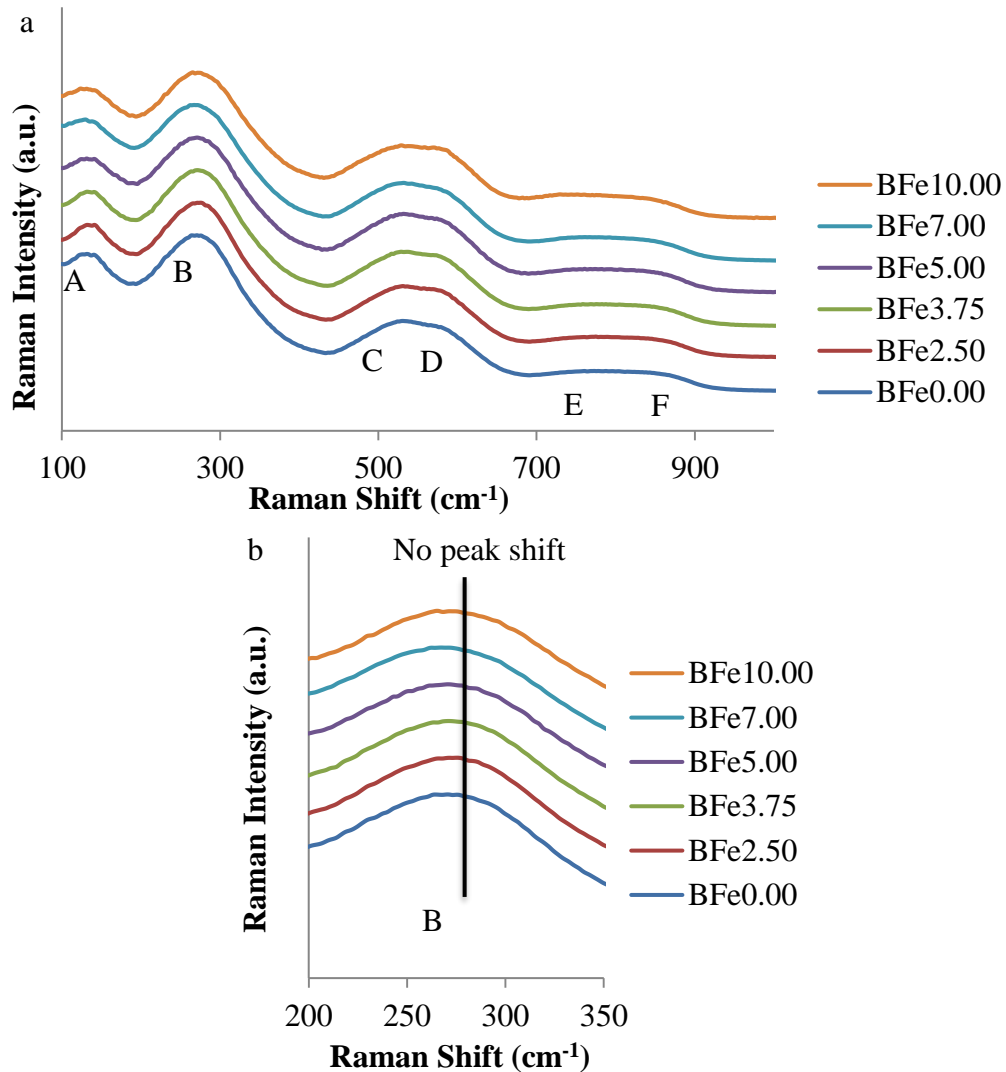


Figure 4. 21. Raman spectra for solid-state sintered $\text{Bi}_{0.5}\text{Na}_{0.5}\text{Ti}_{1-x}\text{Fe}_x\text{O}_{3-0.5x}$ ceramics ($x = 0.0000-0.1000$).

4.3.1.1.3. Electron Microscopy

Figure 4.22 shows Secondary SEM micro-images for solid-state sintered Fe-BNT ceramics measured at room temperature with 32,000x magnification and 5 μm scale. It can be seen that all pure BNT ceramic pellets sintered at 900°C are porous with fine grains. Densification and average grain size increase with increasing iron dopant, as shown in Figure 4.22.

Secondary SEM imaging showed a distribution of grain sizes, which increased with increasing Fe content from 200 nm in pure BNT to 5 μm in ($x = 0.1$) Fe-BNT, as shown in Figure 4.22. It can be observed that, with a 900°C sintering temperature, as for pure BNT, SEM shows a porous microstructure and small average grain size, and as increasing amounts of iron are introduced into the material, the microstructure becomes

progressively more densified, with a larger average grain diameter. SEM imaging is thus qualitatively in agreement with the relative density measurements of samples where $x=0$ of 69.2% and sample $x=0.1$, with a relative density of 96.5% at 900°C sintering temperature as presented in Table 4.7.

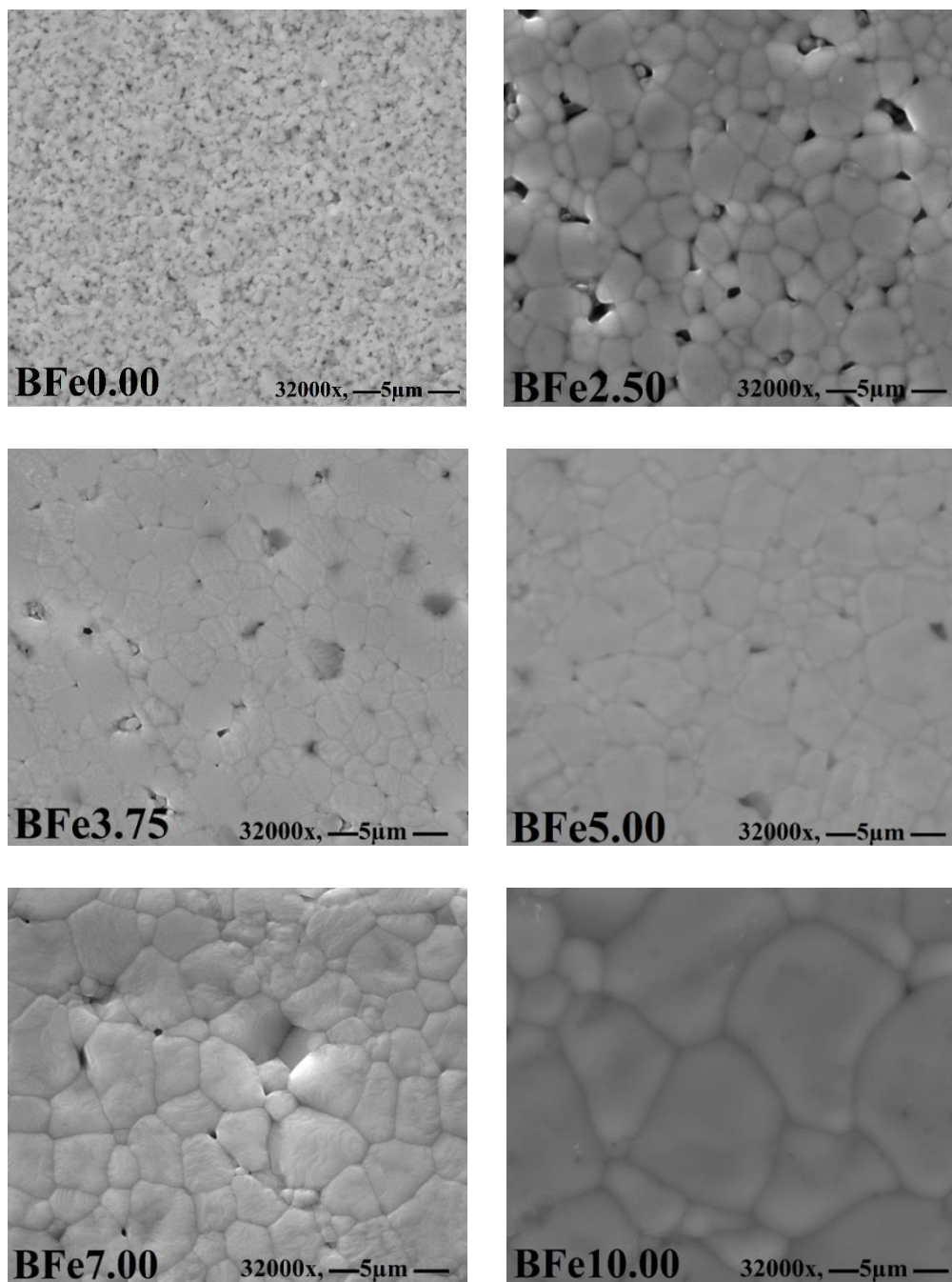


Figure 4. 22. Secondary SEM images for solid-state sintered Bi_{0.5}Na_{0.5}Ti_{1-x}Fe_xO_{3-0.5x} ceramics ($x = 0.0000-0.1000$).

4.3.1.1.4. Density

Bulk and relative density results for pure and iron modified BNT ceramics are presented in Table 4.7.

The relative density results show increasing relative density with increasing iron oxide content, as shown in Table 4.7. Lower relative density (69%) occurred for undoped BNT ceramics, and then increased reaching a value of about 97% relative density for 7mole% Fe-BNT ceramic. Then, the relative density is slightly reduced at 10mole% Fe-BNT.

Table 4.7. Relative density results for $\text{Bi}_{0.5}\text{Na}_{0.5}\text{Ti}_{1-x}\text{Fe}_x\text{O}_{3-0.5x}$ ceramics ($x = 0.0000, 0.0250, 0.0375, 0.0500, 0.0700$ and 0.1000).

Sample names	Theoretical density (g/cm^3)	Bulk density (g/cm^3)	Relative density (%)
BFe0.00	5.97	4.13±0	69.2±0
BFe2.50	5.97	5.47±0.01	91.7±0.1
BFe3.75	5.97	5.57±0.02	93.3±0.2
BFe5.00	5.97	5.70±0.03	95.6±0.3
BFe7.00	5.95	5.81±0.05	97.6±0.5
BFe10.00	5.94	5.73±0.06	96.5±0.6

4.3.1.1.5. Electrical Properties

Figure 4.23 shows hysteresis (P-E) loops and polarisation for all solid-state sintered BNT ceramics measured at room temperature, 70kV/cm electric field and 10 Hz frequency in a bipolar field. Figure 4.23 shows unsaturated and very slim hysteresis (P-E) loops for solid-state sintered iron modified BNT ceramics.

A significant reduction of remnant polarisation is displayed for iron modified bismuth sodium titanate ceramics, compared with high remnant polarisation ($38\mu\text{C}/\text{cm}^2$) for pure BNT ceramics (Li et al., 2013; Panda & Sahoo, 2015). The ferroelectric hysteresis response displays slimmed loops at the applied electric field by adding iron to the BNT ceramics. Adding Fe to the BNT ceramics makes the hysteresis loop slimmer and significantly decreases both remnant polarisation and coercive field to $1.18\mu\text{C}/\text{cm}^2$ and 21.92, respectively for sample BFe2.5 at 10Hz and applied field 60kV/cm. BNT ceramics doped with Fe contain oxygen vacancies which have been shown to assist

electrical breakdown through black spots (leaky or electrically conductive) at frequencies lower than 10Hz (Dong et al., 2015; Fujii et al., 2016; Hu et al., 2018; Shi et al., 2014; Zhao et al., 2018).

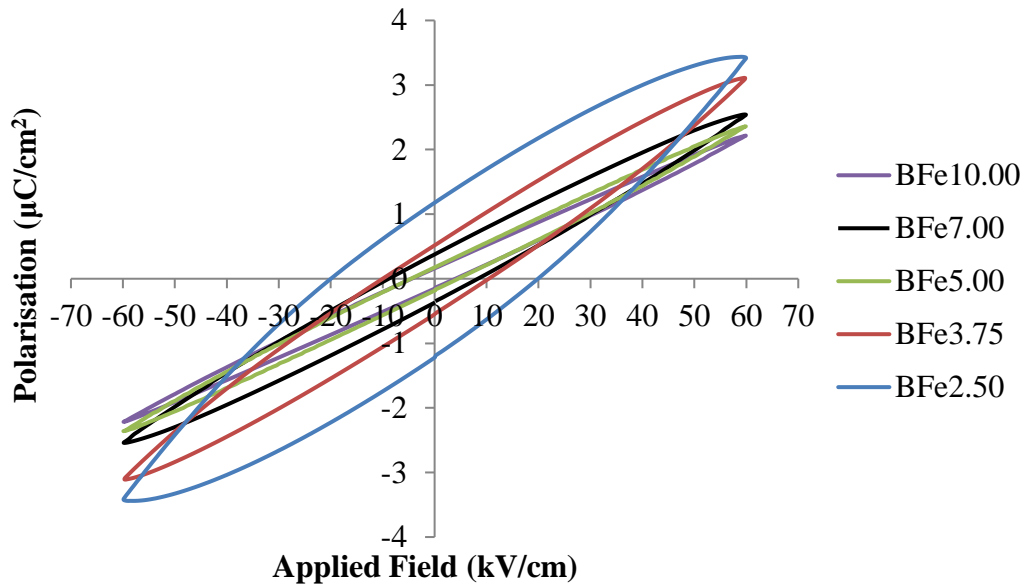


Figure 4.23. Polarisation vs. electric field response at room temperature using bipolar measurement for solid-state sintered $\text{Bi}_{0.5}\text{Na}_{0.5}\text{Ti}_{1-x}\text{Fe}_x\text{O}_{3-0.5x}$ ceramics ($x = 0.0000-0.1000$).

4.3.2. Microwave Processing Route

4.3.2.1. Results and Discussion

4.3.2.1.1. XRD

Figure 4.24 shows a single perovskite phase for all iron-doped BNT ceramics measured at room temperature with 2θ ranged from 10 to 80°. There are three parts into Figure 4.24: part (a) shows Fe-BNT ceramics measured at 2θ ranged from 10 to 80°, part (b) corresponds to Fe-BNT ceramics analysed at 2θ ranged from 32 to 33°, and part (c) refers to Fe-BNT ceramics measured at 2θ ranged from 46 to 47°.

At room temperature, X-Ray diffraction (XRD) analysis shows a single Rhombohedral perovskite phase for $\text{Bi}_{0.5}\text{Na}_{0.5}\text{TiO}_3$ without any observed secondary phases for all MKBFe samples as shown by ICDD powder diffraction file pattern (04-017-0216) (Chou et al., 2011), as shown in Figure 4.24 (a). Moreover, the pure perovskite BNT phase of all microwave sintered Fe-BNT ceramic samples (Figure

4.24(a) shows good agreement with all solid state sintered Fe-BNT ceramic samples (Figure 4.19(a)). There is a clear shift to lower angles is presented with the addition of Fe to BNT as presented in Figure 4.24 (c) for the peak at approximately $46.6^{\circ}2\theta$. This clear shift is due to the fact that Fe^{3+} has a larger ionic radius (Shannon, 1976) (0.645 \AA) than Ti^{4+} (0.605 \AA) on the B-site of Fe-BNT perovskite ceramics.

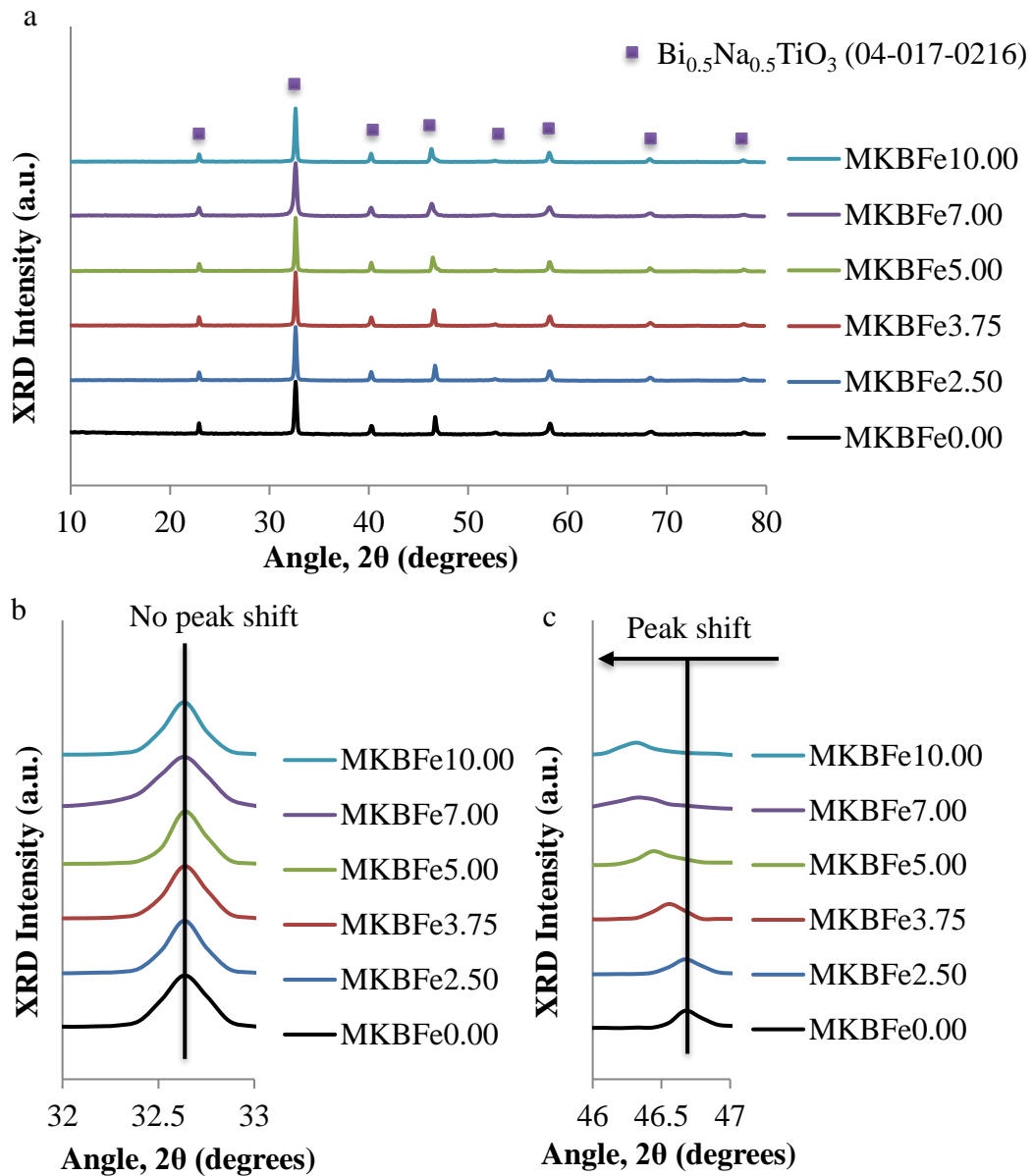


Figure 4.24. X-Ray diffraction patterns (a) and Peak positions (2θ) shifting (b and c) for microwave sintered $\text{Bi}_{0.5}\text{Na}_{0.5}\text{Ti}_{1-x}\text{Fe}_x\text{O}_{3-0.5x}$ ceramics ($x = 0.0000-0.1000$).

4.3.2.1.2. Raman Spectroscopy

Figure 4.25 shows Raman results for microwave sintered BNT ceramics analysed at room temperature with Raman shift ranged from 100 to 1000 cm^{-1} . Raman spectra

reveal six peaks for all BNT ceramic samples, as shown. Figure 4.25 is divided into two parts: part (a) corresponds to iron modified BNT ceramics measured at Raman shift ranged from 100 to 1000 cm^{-1} , and part (b) shows iron doped BNT ceramics analysed at Raman shift ranged from 200 to 350 cm^{-1} .

At room temperature, Raman spectra (Figure 4.25(a)) detect six main peaks for four bands in the Raman shift range of 100-1000 cm^{-1} for all MKBFe ceramic samples, in good agreement with Zannen et al (Zannen et al., 2012). It can be observed that the first spectrum corresponds to the peak A at lower Raman shifts of 100 cm^{-1} to 200 cm^{-1} is a bending vibrational mode of the A-site cation in the ABO_3 perovskite structure and is identified in vibrations of Na-O, as reported by Parija group (Parija et al., 2012). On the other hand, The Bi-O band expected to be placed at lower than 100 cm^{-1} Raman shift, due to the large mass of Bi, as Wang group reported (Wang et al., 2006). The second spectrum observed at peak B shows strong Raman intensity located at Raman shifts between 200 cm^{-1} and 400 cm^{-1} , which is attributed to the Ti-O band (A_1 -symmetry) that exhibits broad stretching vibration (Kreiselt et al., 2000). However, it can be seen for the second peak B position, Raman spectra exhibit no shifts with the substitution of Fe-O in the same site of Ti-O of perovskite structure, as shown in the Fig. 4.25(b). The third main region contains peaks C and D between 450 cm^{-1} and 650 cm^{-1} , which is assigned to TiO_6 oxygen octahedra (Bai et al., 2016). The third region displays broad stretching vibration and lower Raman intensity in comparison with peaks A and B (Anthoniappen et al., 2015). The fourth region placed between 700 cm^{-1} and 900 cm^{-1} and peaks F and G are likely to be A_1 (longitudinal optical) and E mode (longitudinal optical) overlapping bands that present very broad stretching vibration and lower Raman intensity in comparison with the three lower Raman shift regions (Rout et al., 2010).

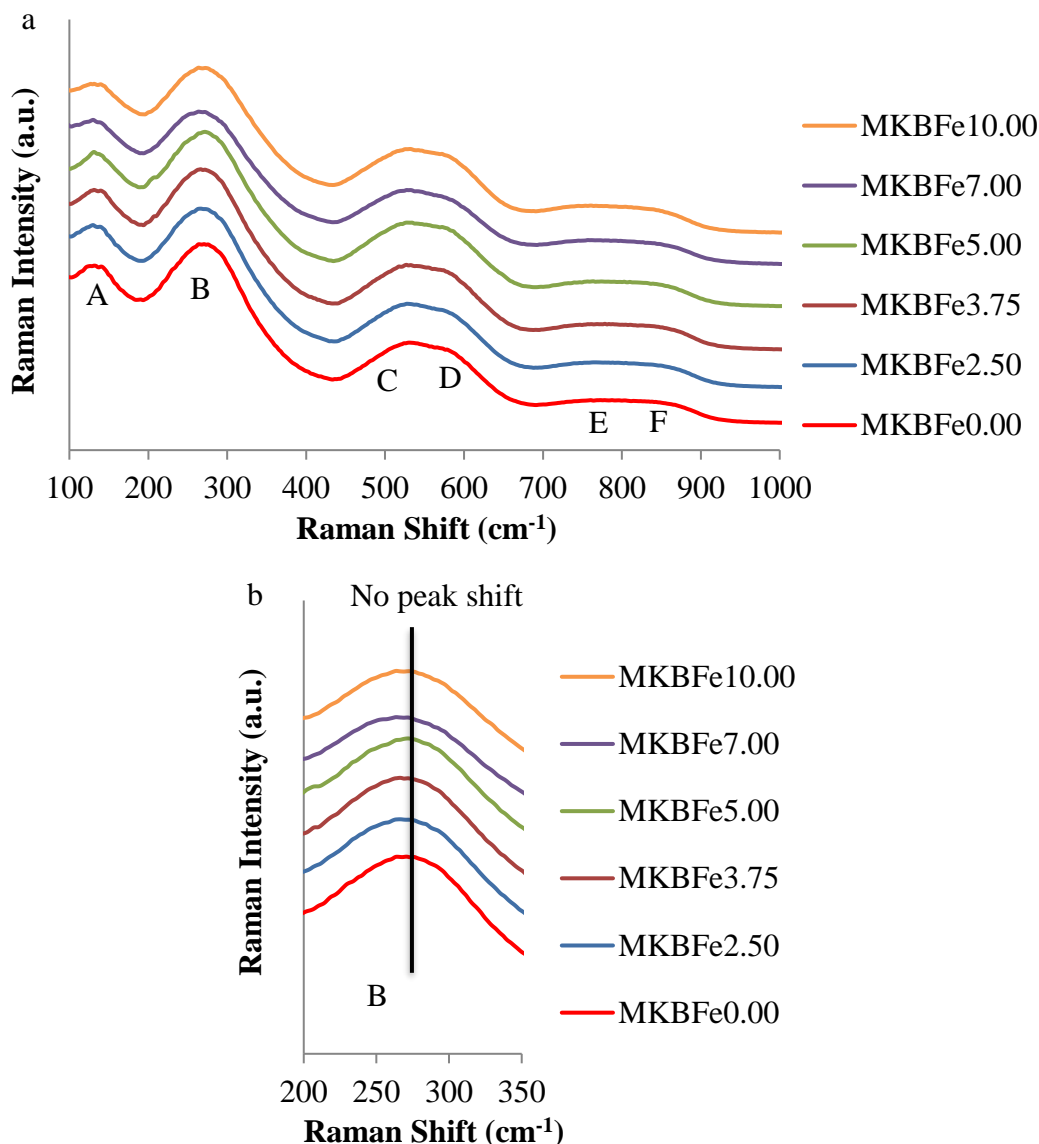


Figure 4. 25. Raman spectra for microwave sintered $\text{Bi}_{0.5}\text{Na}_{0.5}\text{Ti}_{1-x}\text{Fe}_x\text{O}_3$ ceramics ($x = 0.0000-0.1000$).

4.3.2.1.3. Electron Microscopy

Figure 4.26 shows Secondary SEM micrographs for solid-state sintered Fe-BNT ceramics measured at room temperature with 32,000 x magnification and 5 μm scale. Porous with fine grains were obtained for pure BNT ceramics sintered at 20 min microwave sintering time. Densification and average grain size increase with increasing iron content, as shown in Figure 4.26.

Secondary SEM micrographs show a distribution of grains size for all microwave sintered iron doped BNT (MKBFe) ceramics, as shown in Figure 4.26. It is seen that, inhomogeneous grain size distribution is obtained for all MKBFe ceramic samples; in addition to increases of grain sizes from (100 nm) to (4 μm) for the

Chapter Four| Pure and Iron Doped Bismuth Sodium Titanate Ceramics and Glasses

microwave sintered ceramics MKBFe0.00 and MKBFe10.00, respectively. Very fine grains were obtained for pure BNT ceramics microwave sintered with 20 mins sintering time. Also, the growth of grains was significantly increased in average grain diameter and the microstructure becomes progressively more densified, with increasing additions of iron.

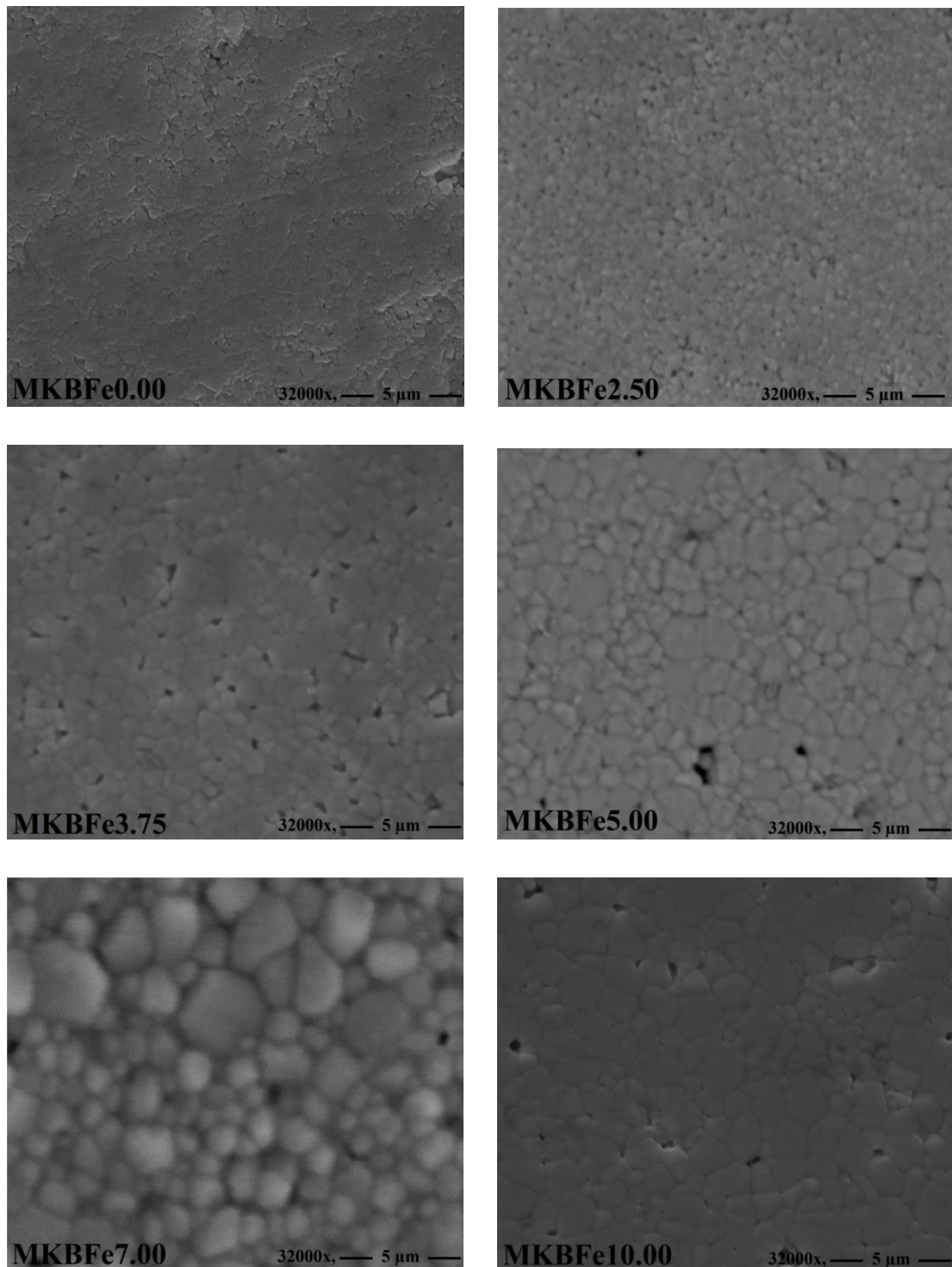


Figure 4. 26. Secondary SEM images for microwave sintered Bi_{0.5}Na_{0.5}Ti_{1-x}Fe_xO_{3-0.5x} ceramics (x = 0.0000-0.1000).

4.3.2.1.4. Density

Table 4.8 presents the dependence of bulk and relative density of microwave sintered iron doped BNT ceramics as a function of iron dopant, which are microwave sintered at 20 mins microwave sintering time. The very low relative density (approximately 84%) has obtained for Pure BNT, and the relative density increased with increasing iron oxide content, reaching a maximum value of approximately 98% relative density for 7mole% Fe-BNT ceramic, then the relative density is slightly reduced at 10mole% Fe-BNT.

Table 4.8. Relative density results for microwave sintered $\text{Bi}_{0.5}\text{Na}_{0.5}\text{Ti}_{1-x}\text{Fe}_x\text{O}_{3-0.5x}$ ceramics ($x = 0.0000, 0.0250, 0.0375, 0.0500, 0.0700$ and 0.1000).

Sample Names	Theoretical density (g/cm^3)	Bulk density (g/cm^3)	Relative Density (%)
MKBF _e 0.00	5.97	5.06± 0.00	84.5 ± 0.0
MKBF _e 2.50	5.97	5.08± 0.01	85.1 ± 0.1
MKBF _e 3.75	5.97	5.65± 0.02	94.8 ± 0.2
MKBF _e 5.00	5.97	5.80± 0.03	97.4 ± 0.3
MKBF _e 7.00	5.95	5.84± 0.05	98.1 ± 0.5
MKBF _e 10.00	5.94	5.81± 0.06	97.7 ± 0.6

4.3.2.1.5. Electrical Properties

Figure 4.27 shows hysteresis (P-E) loops and polarisation of microwave sintered BNT ceramics measured at room temperature, 70kV/cm electric field and 10 Hz frequency in a bipolar field. It can be observed that Figure 4.27 shows slimmed hysteresis (P-E) loops for microwave sintered iron doped BNT ceramics.

A major reduction of remnant polarisation is presented for all MKBF_e ceramic samples, compared with high remnant polarisation ($38\mu\text{C}/\text{cm}^2$) for pure BNT ceramics (Li et al., 2013; Panda & Sahoo, 2015). The ferroelectric hysteresis response displays linear dielectric P-E hysteresis loops for MKBF_e ($x=3.75-7.00$), which is suitable for the high energy storage (Patel, Chauhan, & Vaish, 2014), then a clear change to slimmed P-E hysteresis loops is shown by adding 10mol%Fe to the microwave sintered BNT ceramic (Tan et al., 2009). Adding iron to the BNT ceramics made the P-E loop

slimmer, and it significantly decreases the remnant polarisation to $0.68 \mu\text{C}/\text{cm}^2$ for microwave sintered ceramic MKBFe10.00 at 10Hz and applied field $60\text{kV}/\text{cm}$. The absence of P-E hysteresis loops for the microwave sintered ceramic MKBFe2.50 at frequencies lower than 10Hz, is due to electrical breakdown (leaky or electrically conductive), possibly resulting from oxygen vacancies generated from partial substitution of Fe^{3+} by Ti^{4+} on the B-site of the BNT perovskite structure (Dong et al., 2015; Fujii et al., 2016; Hu et al., 2018; Shi et al., 2014; Zhao et al., 2018).

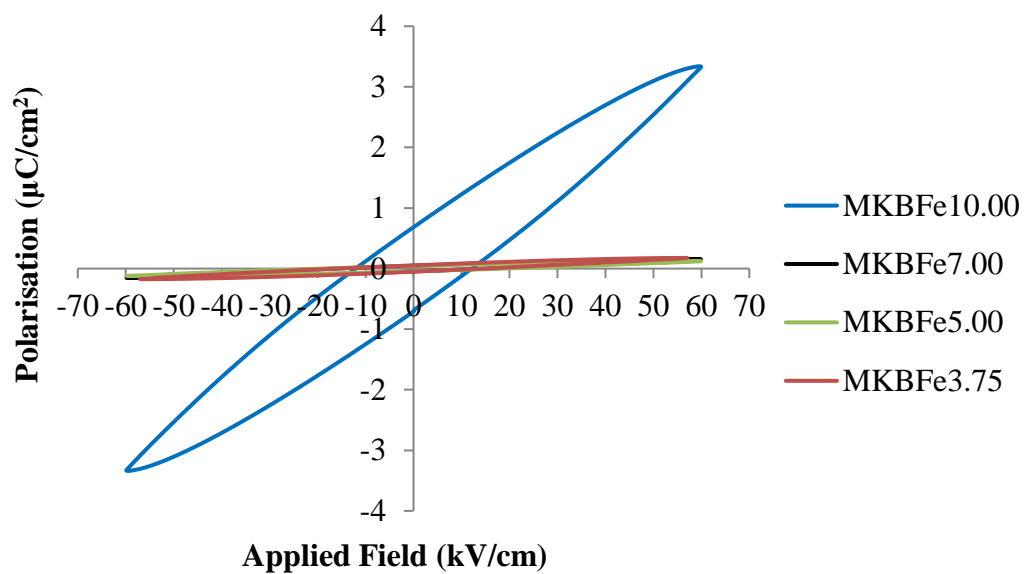


Figure 4.27. Polarisation vs. electric field response at room temperature using bipolar measurement for solid-state sintered $\text{Bi}_{0.5}\text{Na}_{0.5}\text{Ti}_{1-x}\text{Fe}_x\text{O}_3$ ceramics ($x = 0.0000-0.1000$).

4.4. Conclusions

Pure bismuth sodium titanate (BNT) ceramics were successfully produced using solid state and microwave sintering processing routes; however, it was difficult to produce single phase BNT using the silicate glass ceramic melt processing route, due to partial crystallisation of all silicate glasses to form $\text{Ti}_2\text{Bi}_2\text{O}_7$. The relative density shows a maximum value of 94.1% of the theoretical density for pure microwave sintered BNT ceramics, in comparison with these of 94.6% of the theoretical density for pure solid-state sintered BNT ceramics, on the other hand, the bulk density increased with increasing Bi_2O_3 , Na_2O and TiO_2 contents and reducing SiO_2 . SEM imaging showed enhanced densification of ceramic specimens via increasing sintering temperatures

(solid-state sintering processing) and microwave sintering time (microwave sintering one), also, showing a higher average grain size of approximately 2 μm and 900 nm for solid-state sintering and microwave sintering processing routes, respectively. On the other hand, SEM imaging showed the presence of grains on the surfaces of BNT silicate glassy samples indicating partial crystallisation of the samples. The saturated hysteresis (P-E) loops for samples prepared at higher sintering temperatures (1075-1100°C, solid-state sintering processing) and time (25 mins, microwave sintering processing), showed similar remnant polarization of 42.2 $\mu\text{C}/\text{cm}^2$ for microwave sintered BNT (named as MKB700, 25) ceramics and 40 $\mu\text{C}/\text{cm}^2$ identified for solid-state sintered BNT (named as B700, 1100) ceramics. The butterfly S-E loops shape for samples prepared at higher sintering temperatures (1050-1100°C, solid-state sintering processing) and time (25 mins, microwave sintering processing), and produced strain% of ca 0.083% stated for microwave sintered BNT (named as MKB700, 25) ceramics and approximately 0.08% exhibited for solid-state sintered BNT (named as B700, 1100) ceramics.

Iron-doped bismuth sodium titanate (Fe-BNT) ceramics were successfully produced using two processing routes; conventional solid state processing and novel microwave processing. Partial replacement of Ti^{4+} by Fe^{3+} on the B-site of the BNT perovskite structure enabled lower sintering temperatures of 900°C and microwave sintering time of 20 mins whilst enhancing the densification to up to 97% of relative density. Iron concentrations ranged from $x = 0.0$ to $x = 0.1$ according to the formula $\text{Bi}_{0.5}\text{Na}_{0.5}\text{Ti}_{1-x}\text{Fe}_x\text{O}_{3-0.5x}$. XRD analysis showed pure perovskite BNT phase for all studied Fe dopant levels. SEM imaging showed smaller average grain diameter of approximately 200 nm to 4 μm for microwave sintered Fe-BNT ceramics, in comparison with approximately 1-4 μm for solid-state Fe-BNT ceramics. Iron doping produced slimmed P-E hysteresis loops with relaxor and non-ferroelectric property. In conclusion, the addition of iron enables a significant reduction in sintering temperatures for solid-state sintered BNT ceramics, and in microwave sintering time for microwave sintered Fe-BNT ceramics, whilst enhancing relative density, but this is accompanied by reductions in the remnant polarisation, coercive field, and the ferroelectric properties of Fe-BNT.

As discussed above the main results for BNT and iron doped BNT ceramics prepared by solid-state sintering and microwave sintering processing. The larger average grains size for ceramics prepared by solid-state processing, appeared in the long hold sintering time

to give enough time for grains growth and that leading to increase the densification with shown higher relative density. At lower sintering temperature, XRD results shows broad peaks due to the smaller crystallite size.

Chapter Five

Pure and Iron Doped Potassium Sodium Niobate Ceramics and Glass-Ceramics

5.1. Introduction

Chapter Five considers the pure and iron-doped KNN ceramics prepared by three different processing routes: conventional solid-state sintering processing, microwave sintering processing and melt processing, as shown in Figure 5.1.

A microwave sintering processing has been successfully used to manufacture microwave sintered KNN ceramics as an alternative method to replace solid-state sintering processing, with three motivations: reducing sintering time and energy consumption, and use of a low-cost microwave oven in comparison with a conventional furnace. A melt processing route has been studied to attempt to prepare potassium sodium niobium glass-ceramics as an alternative process to replace solid-state sintering processing for three reasons: reducing the processing steps, processing time and manufacturing KNN borosilicate glass and glass-ceramic fibres with potential for sensing and actuating applications. A traditional solid-state sintering processing route has been used as a baseline to enable comparison of results.

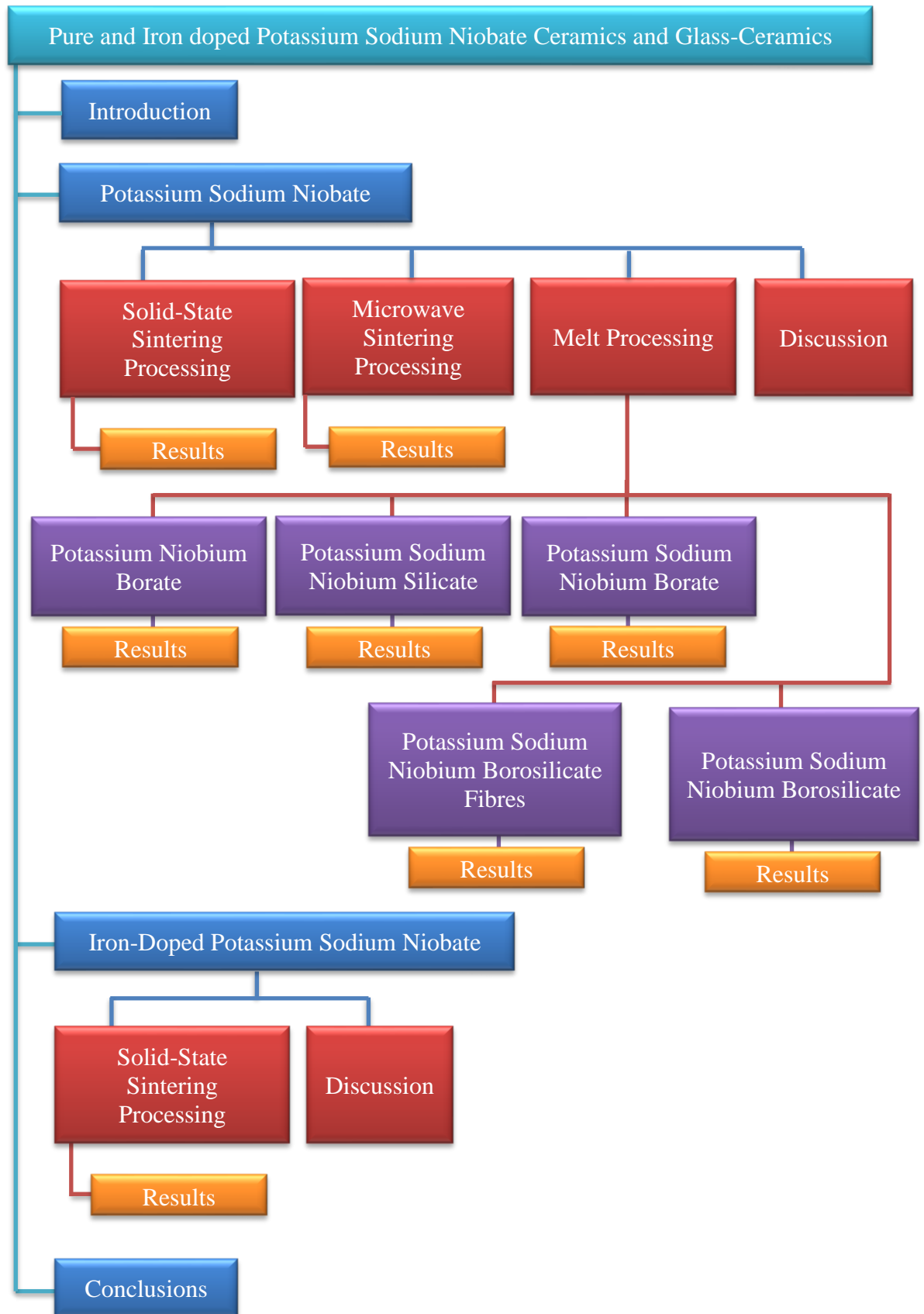


Figure 5.1. Overview of pure and iron-doped potassium sodium niobate ceramics and glass-ceramics (Chapter Five).

5.2. Pure Potassium Sodium Niobate Ceramics and Glass-Ceramics

5.2.1. Solid State Sintering Processing

5.2.1.1. Results and Discussion

5.2.1.1.1. XRD

Figure 5.2 shows XRD results for all solid-state sintered KNN ceramics analysed at room temperature with an angle (2θ) ranged from 10 to 80. All XRD results show a single phase $K_{0.5}Na_{0.5}NbO_3$ (04-017-0216) with the orthorhombic structure for All KNN ceramic samples. There are two parts to Figure 5.2: part (a) shows XRD patterns for KNN ceramics prepared with 700°C/4h calcination conditions and different sintering conditions (1000, 1050, 1075, 1100°C/2h), and part (b) presents XRD patterns for KNN ceramics synthesised with 800°C/4h calcination conditions and different sintering conditions (1000, 1050, 1075, 1100°C/2h).

XRD results show that all solid-state sintered KNN ceramic samples consisted of a single perovskite $K_{0.5}Na_{0.5}NbO_3$ phase, as anticipated. No any of secondary phases are observed, as shown in Figure 5.2. XRD patterns for the pure solid-state sintered KNN ceramics are consistent with ICDD no 04-017-0216, with no changes in the peak positions or shapes (Figure 5.2 (c) and (d)), which is consistent with the orthorhombic structure at room temperature. The peak splitting identified between 45 and 47 ° 2θ as two peaks, indicates homogeneous solid solution and orthorhombic structure of KNN ceramics, (Rani, Yadav, & Prakash, 2012; Chaiyo et al., 2009; Ramajo, Taub, & Castro, 2014). XRD results related to the orthorhombic structure at room temperature are consistent with previous studied of Jean and group (Jean et al., 2018), Ramajo and group (Ramajo et al., 2014), Agustinawati and group (Agustinawati, Isnaini, & Suasmoro, 2017) and Nuraini and group (Nuraini et al., 2018).

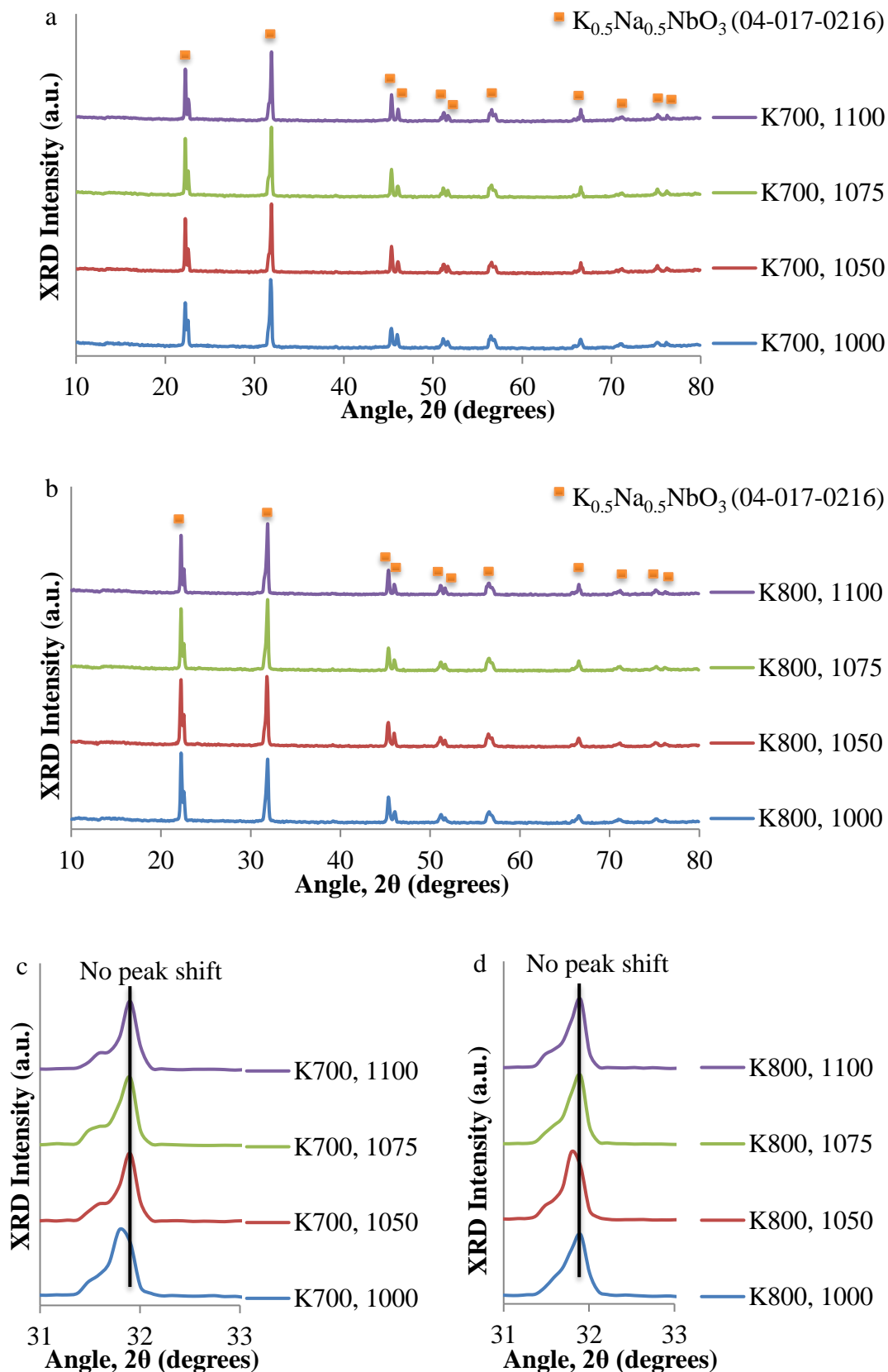


Figure 5.2. X-Ray diffraction patterns for solid sintered KNN ceramics with (a) 700°C/4h calcination temperature/time and (b) 700°C/4h calcination temperature/time, and different sintering temperatures/time as shown. Peak position (2θ) shifting (c and d) for solid-state sintered $K_{0.5}Na_{0.5}NbO_3$ ceramics.

5.2.1.1.2. Raman Spectroscopy

Figure 5.3 shows Raman results applied for solid-state sintered KNN ceramics analysed at room temperature with Raman shift from 100 to 1000 cm^{-1} . Raman spectra have four regions with eight bands for all KNN ceramic samples. Figure 5.3 is divided into two parts, part (a) shows Raman spectra for KNN ceramics manufactured with 700°C/4h calcination temperature/time and different sintering temperatures/time (1000, 1050, 1075, 1100°C/2h), and part (b) shows Raman spectra for KNN ceramics prepared with 800°C/4h calcination temperature/time and different sintering temperatures/time (1000, 1050, 1075, 1100°C/2h).

All main sharp peaks are marked as ν_1 to ν_6 and show vibrational modes, consistent with NbO_6 octahedra. The vibrational stretching modes assigned as ν_1 to ν_3 which are shown at higher Raman shift (300 and 800 cm^{-1}) and the vibrational bending modes assigned as ν_4 to ν_6 which are displayed at lower Raman shift (150 and 300 cm^{-1}) (Wang et al., 2016; Wu et al., 2014). The Raman spectra shown in Figure 5.3, are consistent with perovskite $\text{K}_{0.5}\text{Na}_{0.5}\text{TiO}_3$ structure as reported by Lingfei and group (Lingfei et al., 2009) and Singh and group (Singh et al., 2013). A shoulder noted as ν_1 and ν_2 vibrational modes indicates the orthorhombic phase (Yan et al., 2018), and the ν_6 vibrational mode identified on the beginning of shoulder underneath ν_5 vibrational mode (less than 200 cm^{-1}), could be assigned as translational mode of K^+ cation and rotations of the NbO_6 octahedron (Singh et al., 2013). Moreover, the very weak peak at 130 cm^{-1} could be matched to the Na^+/K^+ cations versus rotation of NbO_6 octahedra (Liu et al., 2013). The association of ν_1 and ν_5 (Nb_2O_5) vibrational modes for the peak in between 800 and 900 cm^{-1} , indicates the nonexistence of cubic phase of pure KNN perovskite structure (Chen et al., 2018; Yan et al., 2018).

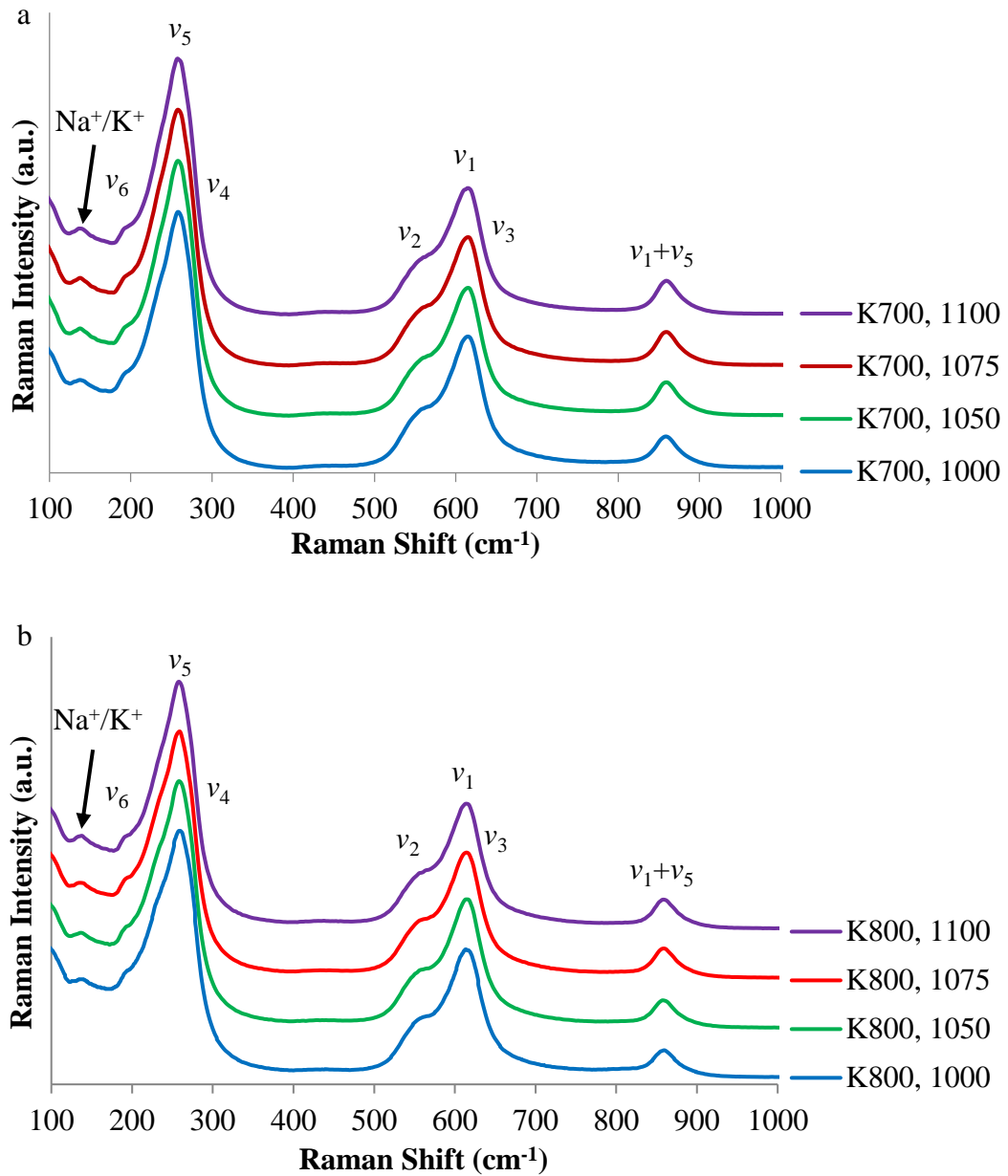


Figure 5.3. Raman spectrum for solid sintered KNN ceramics with (a) 700°C/4h calcination temperature/time and (b) 700°C/4h calcination temperature/time, and different sintering temperatures/time as shown.

5.2.1.1.3. Electron Microscopy

Figure 5.4 shows Secondary SEM micrographs for solid-state sintered KNN ceramic samples measured at room temperature with 8,000x magnification and 20 μm scale. It can be observed that small grains are detected for solid-state sintered KNN ceramics manufactured at the 1000°C/2h sintering temperature, and then the average grain size increases with increasing sintering temperature, as shown in Figure 5.4.

SEM images show irregular grains shapes and inhomogeneous grain size distributions for all solid-state sintered KNN ceramics, made with different calcination temperatures (700 and 800°C) and sintering temperatures (1000, 1050, 1075 and 1100°C), as shown in Figure 5.4. The average grain size of solid-state sintered KNN ceramics increased from approximately 600 nm to ca 5 μm with increasing sintering temperature from 1000 to 1100°C, respectively. SEM images show separated grains obtained at a lower sintering temperature of 1000°C, and then the grains agglomerated and may have potentially melted to give flat areas with no clear grain boundaries at higher sintering temperatures of 1050-1100°C, maybe that due to the lower melting temperature of alkalis (Na_2O and K_2O). The higher average grains size of about 5 μm displays good agreement with 5 μm grains presented by Alkoy and Berksoy-Yavuz (Alkoy & Berksoy-Yavuz, 2012) and larger than 3 μm grains reported by Ponraj and Varma (Ponraj & Varma, 2016). On the other hand, this is smaller than 8 μm grains reported by Byun and colleagues (Byun et al., 2018), for pure KNN ceramics.

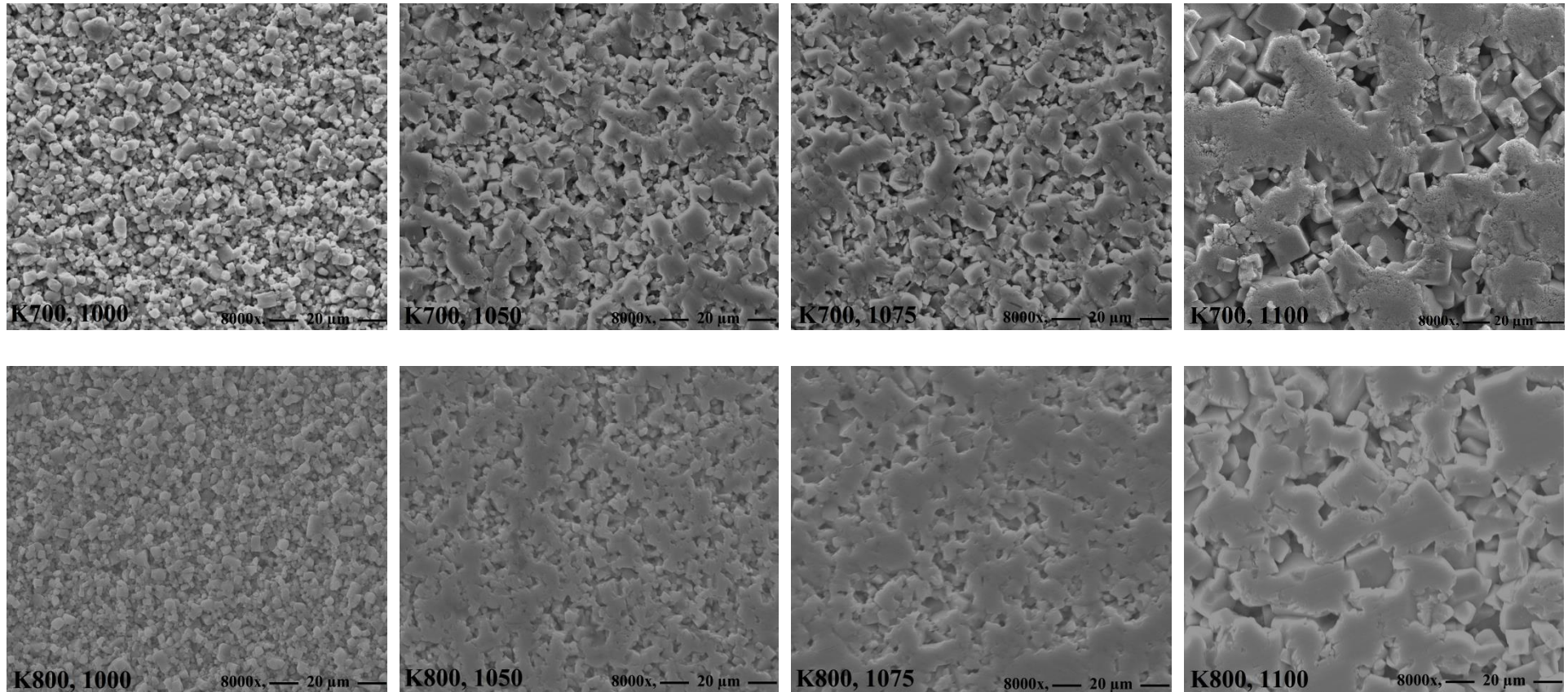


Figure 5.4. Secondary SEM images for solid-state sintered KNN ceramics with different calcination temperatures and sintering temperatures.

5.2.1.1.4. Density

Table 5.1 shows bulk and relative density results for all solid-state sintered KNN ceramic samples manufactured with different calcination and sintering temperatures.

The relative density increases with increasing sintering temperature of solid-state sintered KNN ceramics, as shown in Table 5.1. The lower relative density of approximately 69% of theoretical density, at 1000°C sintering temperature of solid-state sintered KNN (K800, 1000) ceramic calcined at 800 °C, increased to a maximum relative density of approximately 91% of theoretical density, at higher 1100°C sintering temperature of solid-state sintered KNN (K700, 1100) ceramic calcined at 700°C. The density results show a constant difference between samples calcined at 700°C and those calcined at 800°C, which is due to that the samples calcined at different calcination temperatures have sintered at the same sintering temperature, presenting close difference at each sintering temperature. The maximum relative density (approximately 91% of theoretical density) is greater than 84% of theoretical density (Agustinawati, Isnaini, & Suasmoro, 2017), however, it is clearly lower than those of about 94% and 98% of theoretical density (Lopez-Juarez et al., 2015) and (He et al., 2013) respectively, obtained by other researchers for pure KNN ceramics.

Table 5.1. Bulk and relative density results for solid-state sintered $K_{0.5}Na_{0.5}NbO_3$ ceramics.

Sample names	Bulk density (g/cm ³)	Relative density (%)	Sample names	Bulk density (g/cm ³)	Relative density (%)
K700, 1000	3.30±0.01	73.4±0.1	K800, 1000	3.14±0.01	69.6±0.1
K700, 1050	3.75±0.01	83.5±0.1	K800, 1050	3.56±0.01	79.4±0.1
K700, 1075	3.89±0.01	86.5±0.1	K800, 1075	3.84±0.01	85.5±0.1
K700, 1100	4.09±0.01	91.2±0.1	K800, 1100	4.07±0.01	90.7±0.1

5.2.1.1.5. Electrical Properties

Figure 5.5 presents hysteresis (P-E) loops, and polarisation for all solid-state sintered KNN ceramics analysed at room temperature, 70kV/cm electric field and 1 Hz frequency in a bipolar field. It can be seen, Figure 5.5 contains two parts, part (a) refers to solid-state sintered KNN ceramics manufactured with 700°C/4h calcination

temperature and different sintering temperatures (1000, 1050, 1075, 1100°C/2h), and part (b) corresponds to solid-state sintered KNN ceramics prepared with 800°C/4h calcination temperature and various sintering temperatures (1000, 1050, 1075, 1100°C/2h). Saturated hysteresis P-E loops are observed at a higher 1100°C sintering temperature for all KNN ceramic samples.

Hysteresis loop shape can be affected by sintering temperature resulting from densification and higher relative density. At higher sintering (1100°C) temperature and relative density (approximately 91% of theoretical density), the ideal hysteresis loop shape was detected, indicating the existence of ferroelectric behaviour. However, at low sintering (1075°C) temperature and relative density (approximately 86% of theoretical density), a lemon hysteresis loop shape was obtained indicating high conductivity, which is attributed to current leakage, resulting from the greater porosity (Kang et al., 2011; Wiegand et al., 2012). On the other hand, the absence of hysteresis loops for lower sintering (less than 1050°C) temperature ceramics, relative density less than 83% of theoretical density, is due to current loss through pores (current leakage), corresponding to the high porosity and low density (Wiegand et al., 2012, Woo et al., 2017). The remnant polarization of approximately $33 \mu\text{C}/\text{cm}^2$ for K700, 1100 ceramics exhibits an excellent enhancement in comparison with $26 \mu\text{C}/\text{cm}^2$ (Tian & Du, 2014) and $10 \mu\text{C}/\text{cm}^2$ (Ponraj & Varma, 2016); however, it is similar to $33 \mu\text{C}/\text{cm}^2$ (Alkoy & Berksoy-Yavuz, 2012), for pure KNN ceramics.

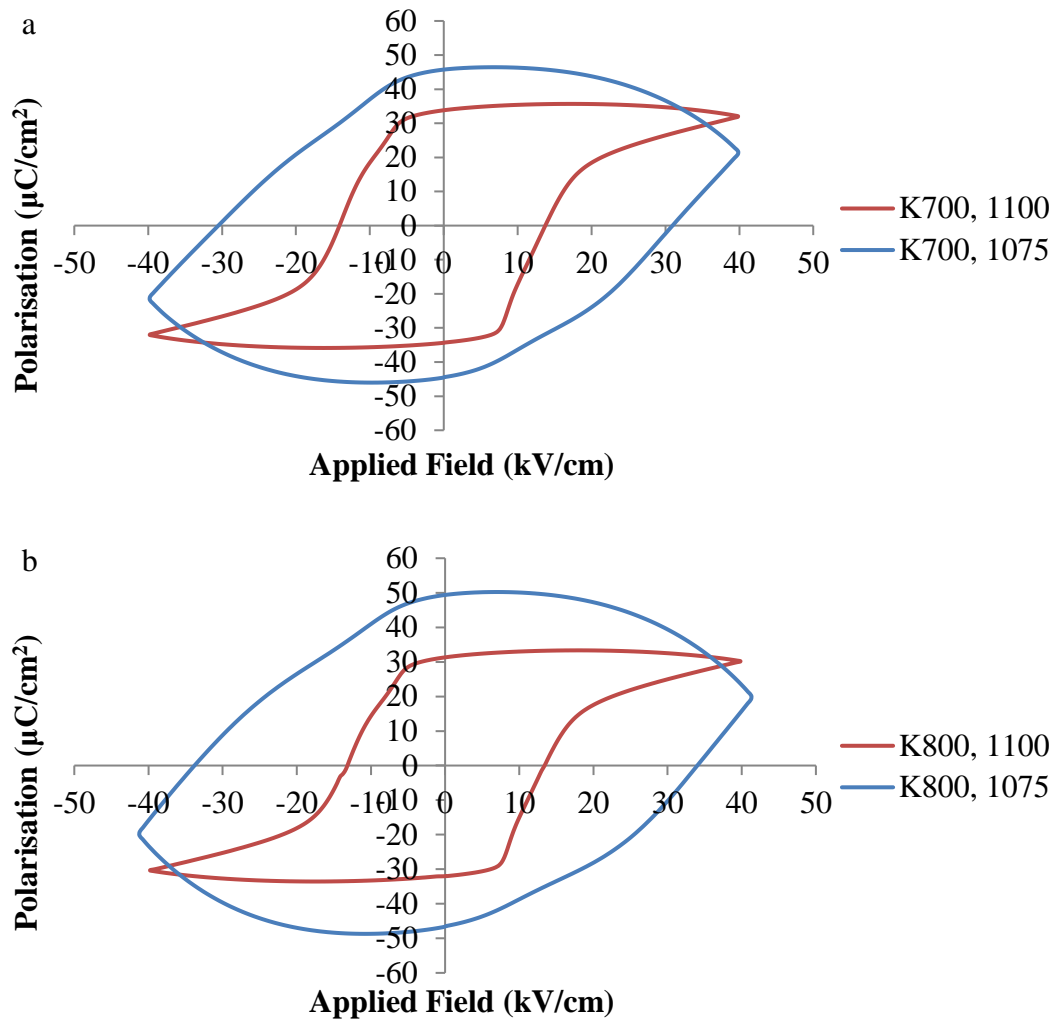


Figure 5.5. Polarisation vs electric field response at room temperature and 1Hz frequency using the bipolar measurement of solid sintered KNN ceramics with (a) 700°C/4h calcination temperature and (b) 700°C/4h calcination temperature, and different sintering temperatures as presented.

Figure 5.6 shows strain-electric field (S-E) loops of all solid-state sintered KNN ceramics investigated at room temperature, 70kV/cm electric field and 1 Hz frequency in a bipolar field. It can be observed, there are two parts presented in Figure 5.6: part (a) relates to solid-state sintered KNN ceramics made with 700°C/4h calcination temperature and different sintering temperatures (1000, 1050, 1075, 1100°C/2h), and part (b) indicates to solid-state sintered KNN ceramics prepared with 800°C/4h calcination temperature and various sintering temperatures (1000, 1050, 1075, 1100°C/2h). It can be seen that the butterfly P-E loops with lower and maximum strain% were obtained for lower 1075°C and 1100°C sintered BNT ceramics, respectively.

The maximum strain increased from approximately 0.036% to 0.06%, with increasing sintering temperatures from 1075 to 1100°C and relative density from approximately 86% to 91% of the theoretical density. The typical butterfly shape of S-E loops shows ferroelectric behaviour (Priya & Nahm, 2011). However, the absence of strain vs electric field (S-E) loops for lower sintering (less than 1050°C) temperature and relative density (less than 83% of theoretical density), is due to current leakage. The maximum strain of approximately 0.06% shows good enhancement in comparison with 0.05% (Du et al., 2017), however, it is less than other obtained values of 0.012% (Dahiya, Thakur, & Juneja, 2013), 0.09% (Palei, Sonia, & Kumar, 2012) and 0.08% (Matsubara, Yamaguchi, Kikuta, & Hirano, 2005).

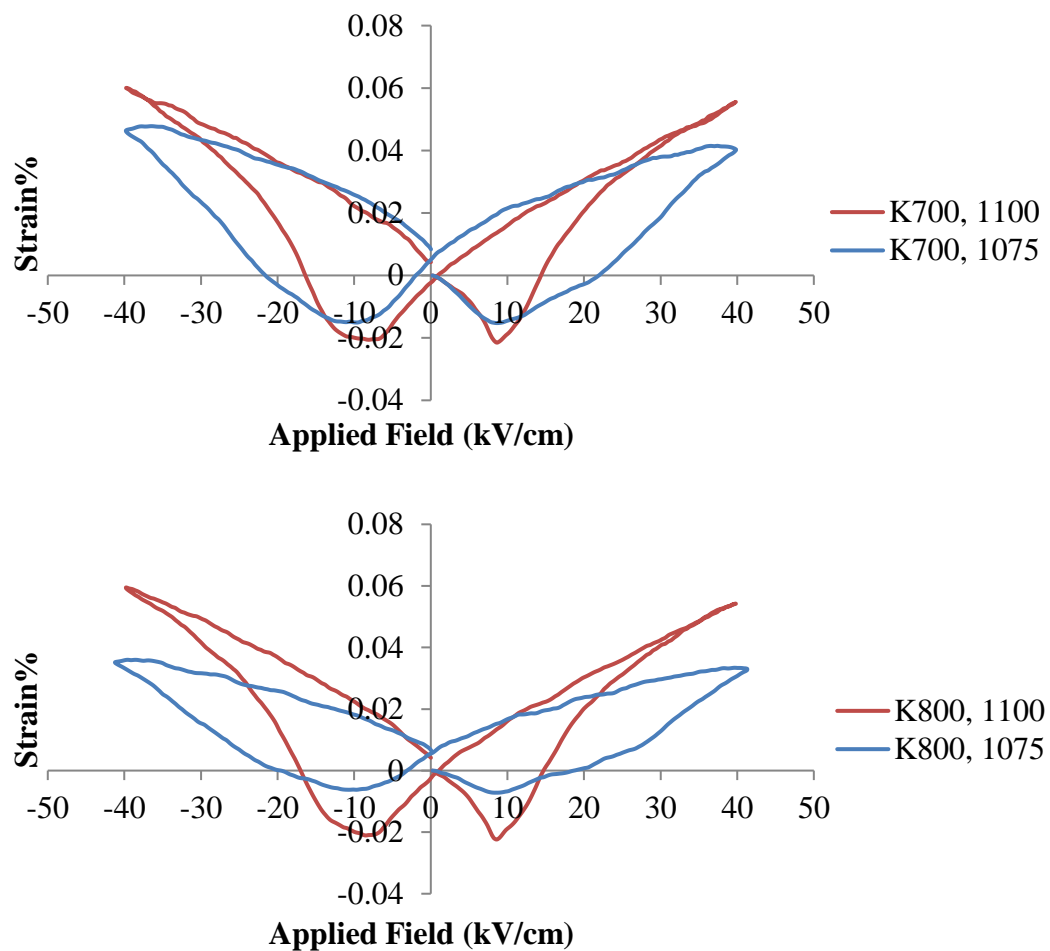


Figure 5.6. Electric field induced strain at room temperature and 1Hz frequency using the bipolar measurement of solid-state sintered KNN ceramics with (a) 700°C/4h calcination temperature and (b) 700°C/4h calcination temperature, and different sintering temperatures.

5.2.2. Microwave Processing Route

5.2.2.1. Results and Discussion

5.2.2.1.1. XRD

XRD patterns in Figure 5.7 shows pure perovskite phase for all microwave sintered KNN ceramics measured at room temperature for XRD angle (2θ) ranged from 10 to 80. There are two parts presented in Figure 5.7: part (a) relates to microwave sintered KNN ceramics manufactured with 700°C/4h calcination temperature and different sintering time (10, 15, 20, 25mins), and part (b) shows microwave sintered KNN ceramics prepared with 800°C/4h calcination temperature and different microwave sintering times (10, 15, 20, 25mins).

XRD results show that all microwave sintered KNN ceramic specimens have pure perovskite $K_{0.5}Na_{0.5}NbO_3$ phase, as expected, with no observed of secondary phases, as presented in Figure 5.7. XRD results are in good agreement with ICDD no 04-017-0216, with no changes in the peaks shifting and shapes (Figure 5.7 (c) and (d)), which indicates the orthorhombic structure at room temperature. The peak splitting identified between 45 and 47 ° 2θ to two peaks, showing homogeneous solid solution and orthorhombic structure of KNN ceramics, (Rani, Yadav, & Prakash, 2012; Chaiyo et al., 2009; Ramajo, Taub, & Castro, 2014). The XRD results are in good agreement with the previous studies of Jean et al. (Jean et al., 2018), Ramajo and group (Ramajo et al., 2014), Agustinawati and group (Agustinawati et al., 2017) and Nuraini and group (Nuraini et al., 2018). In addition, the XRD results for microwave sintered KNN ceramics are consistent with those of solid-state sintered KNN ceramics, as presented in Figure 5.7 and Figure 5.2, respectively.

XRD results of pure microwave and solid-state sintered KNN ceramics exhibit no changes in the peak position and peak shape for a strong peak identified between 31 and 33 degree, which shows a good consistent with orthorhombic structure corresponding to ICDD no 04-017-0216, for KNN ceramics manufactured by microwave and solid-state sintering processing, as shown in Figure 5.8.

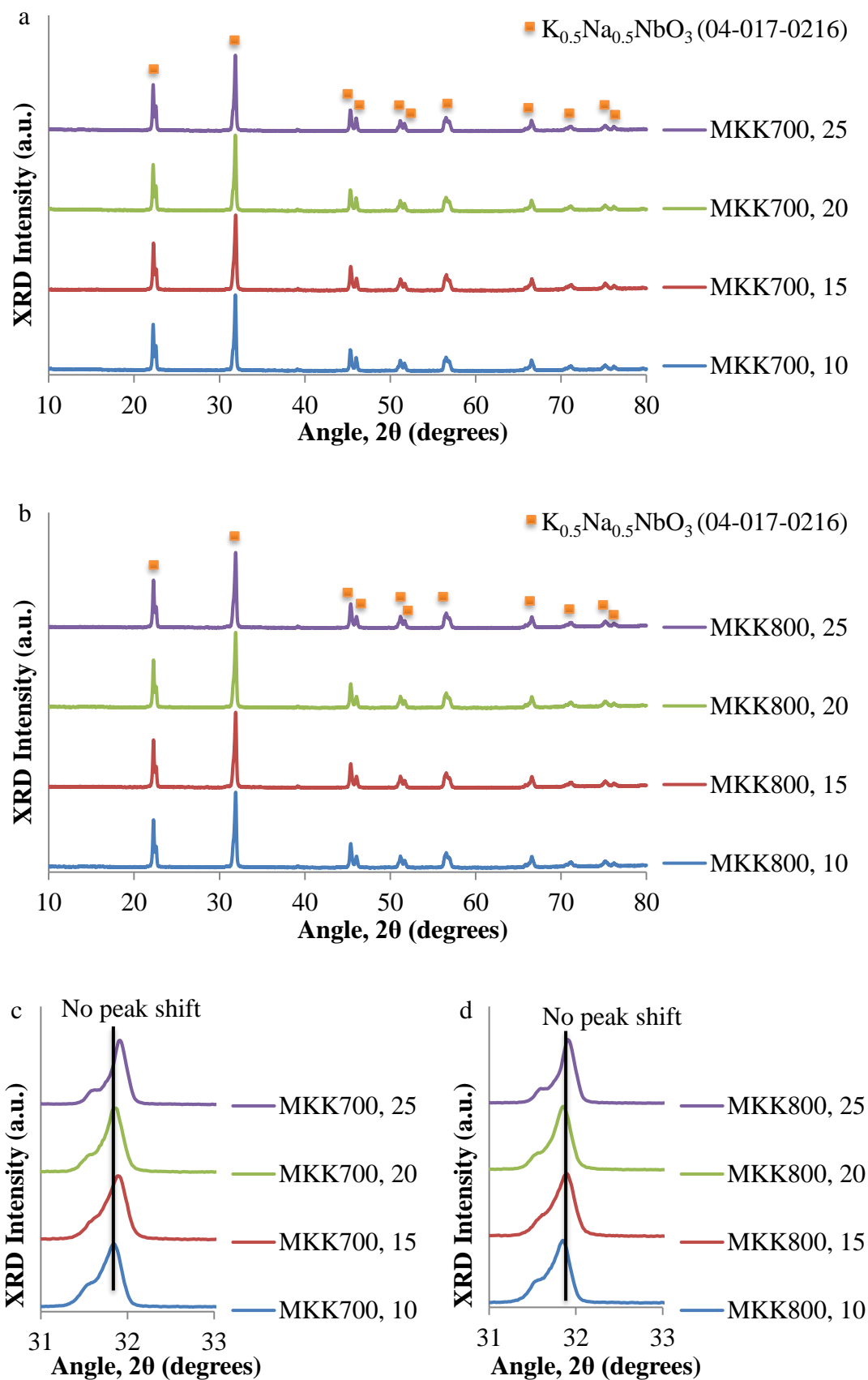


Figure 5.7. X-Ray diffraction patterns for microwave sintered KNN ceramics with (a) 700°C/4h calcination temperature and (b) 700°C/4h calcination temperature, and different sintering times as shown.

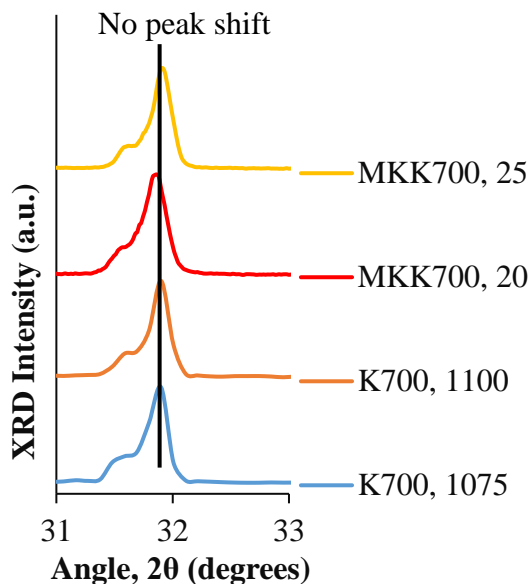


Figure 5.8. X-Ray diffraction patterns for microwave and solid-state sintered KNN ceramics with peak position (2 theta) shifting.

5.2.2.1.2. Raman Spectroscopy

Figure 5.9 shows Raman results for microwave sintered KNN ceramics measured at room temperature with Raman shift ranged from 100 to 1000 cm^{-1} . Raman spectra are presented as four regions with eight bands for all microwave sintered KNN ceramics. Figure 5.9 contains two parts; part (a) shows KNN prepared with 700°C/4h calcination temperature and different sintering times (10, 15, 20, 25mins), and part (b) shows microwave sintered KNN ceramics manufactured with 800°C/4h calcination temperature and different sintering times (10, 15, 20, 25mins).

Raman spectra exhibited three strong regions between 150 and 1000 cm^{-1} Raman shift and one weak peak between 100 and 150 cm^{-1} at room temperature, for all microwave sintered KNN ceramics samples, as shown in the Figure 5.9. The strong regions contain sharp peaks that marked as ν_1 to ν_6 , which are assigned to vibrational modes relating to NbO_6 octahedra. The region situated between 300 and 800 cm^{-1} corresponds to ν_1 to ν_3 modes. The vibrational bending modes are low Raman shift, for example the region between 150 and 300 cm^{-1} showing ν_4 to ν_6 modes (Wang et al., 2016; Wu et al., 2014). The ideal Raman spectra are presented in Figure 5.8, confirming the presence of typical perovskite $\text{K}_{0.5}\text{Na}_{0.5}\text{TiO}_3$ structure as reported by Lingfei and group (Lingfei et al., 2009) and Singh and group (Singh et al., 2013). An orthorhombic phase is demonstrated through a shoulder observed between the ν_1 and ν_2 vibrational modes (Yan et al., 2018). A translational mode of the K^+ cation and rotations of the NbO_6 octahedra can be assigned at lower energy (less than 200 cm^{-1}), which is located

at a ν_6 vibrational mode placed on a shoulder underneath the ν_5 vibrational mode (Singh et al., 2013). The weak peak formed between 100 and 150 cm^{-1} can be assigned to Na^+/K^+ cations versus rotation of NbO_6 octahedron (Liu et al., 2013). The Raman spectra show the absence of cubic phase of pure KNN perovskite due to the formation a peak located between 800 and 900 cm^{-1} assigned to an association of ν_1 and ν_5 (Nb-O) vibrational modes (Chen et al., 2018; Yan et al., 2018). Good agreement is presented for Raman results for microwave sintered KNN and solid-state sintered KNN ceramics, due to the existence of orthorhombic phase in the ceramic structure, as shown in Figure 5.9 and Figure 5.3, respectively.

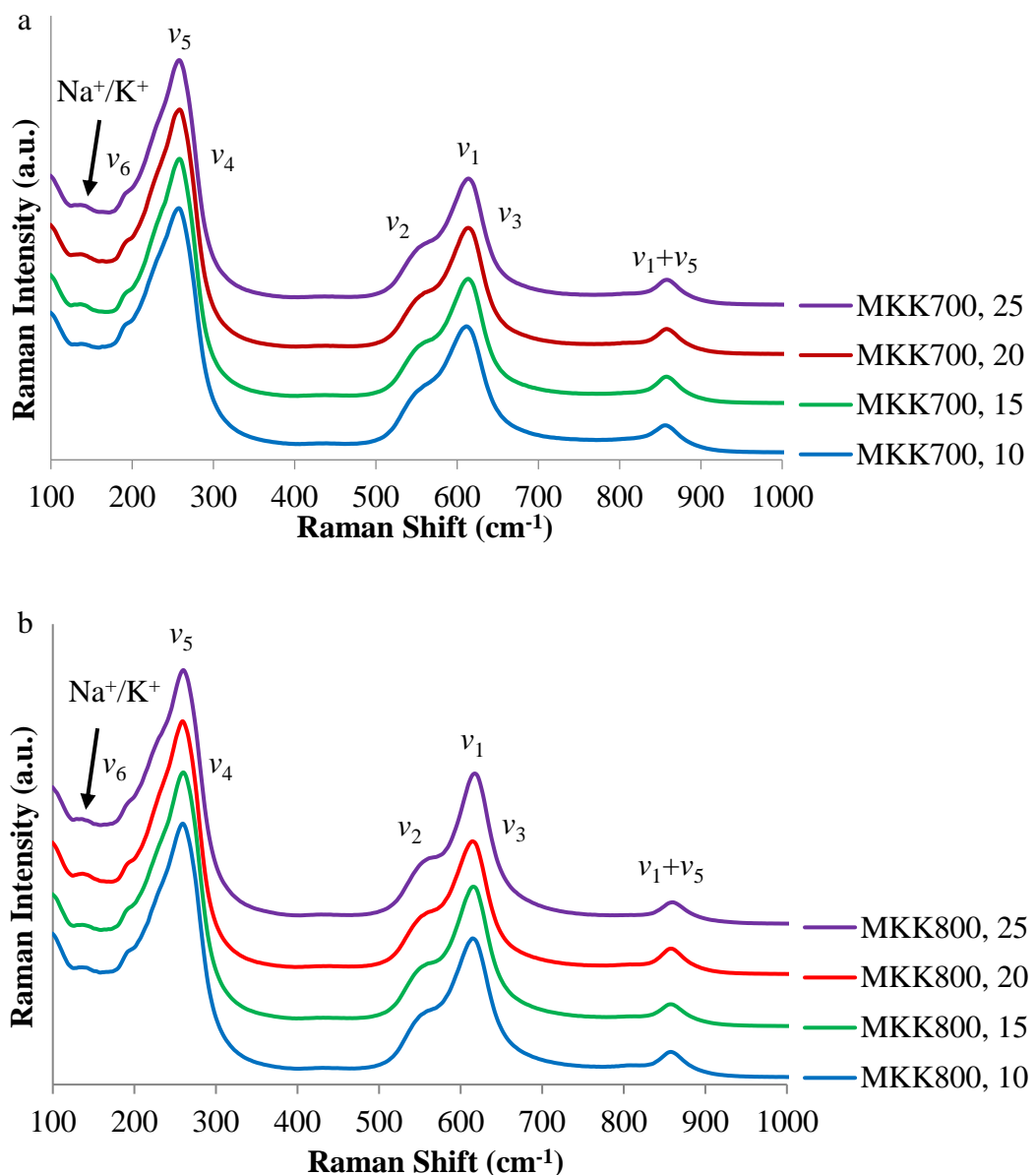


Figure 5.9. Raman spectrum for microwave sintered KNN ceramics with (a) 700°C/4h calcination temperature and (b) 700°C/4h calcination temperature, and different sintering temperatures as shown.

5.2.2.1.3. Electron Microscopy

Figure 5.10 shows secondary SEM micrographs for microwave sintered KNN ceramics analysed at room temperature with 8000x magnification and 20 μm scale. Smaller grains are present for microwave sintered KNN ceramics prepared at a shorter sintering time of 10mins, and then grains become larger with increasing sintering time, as shown.

The SEM technique has been used to investigate the microstructure of microwave sintered KNN ceramics, showing inhomogeneous size distribution for each sample, as shown in Figure 5.9. The average grain size increases from approximately 200 nm to approximately 3 μm with increasing the microwave sintering time from 10 to 25 mins. SEM images show the separate grains are achieved at lower microwave sintering time of 10 mins, and then the grains agglomerated and melting occurs to generate flat areas without boundaries at higher microwave sintering time of 15-25 mins, possibly resulting from increasing microwave heating temperature with increasing microwave sintering time, as presented in Figure 5.9. The densification level in the SEM micrographs demonstrates qualitative agreement with the relative density of microwave sintered KNN ceramic pellets sintered at the different microwave sintering times. This shown by rous ceramics with smaller grain sizes with lower relative density (approximately 69% of theoretical density) and more densified ceramics with larger grain sizes showing higher relative density (approximately 91% of theoretical density), sintered at microwave sintering times of 10 to 25 mins respectively, as shown in Figure 5.9 and Table 5.2. The higher average grain size of approximately 3 μm in the current work displays good agreement with the previous study of 3 μm (Ponraj & Varma, 2016), however, it is smaller than the 5 μm presented in the present chapter for solid-state sintered KNN ceramics, ones presented by Alkoy and Berksoy-Yavuz (Alkoy & Berksoy-Yavuz, 2012) and 8 μm (Byun et al., 2018), for pure KNN ceramics.

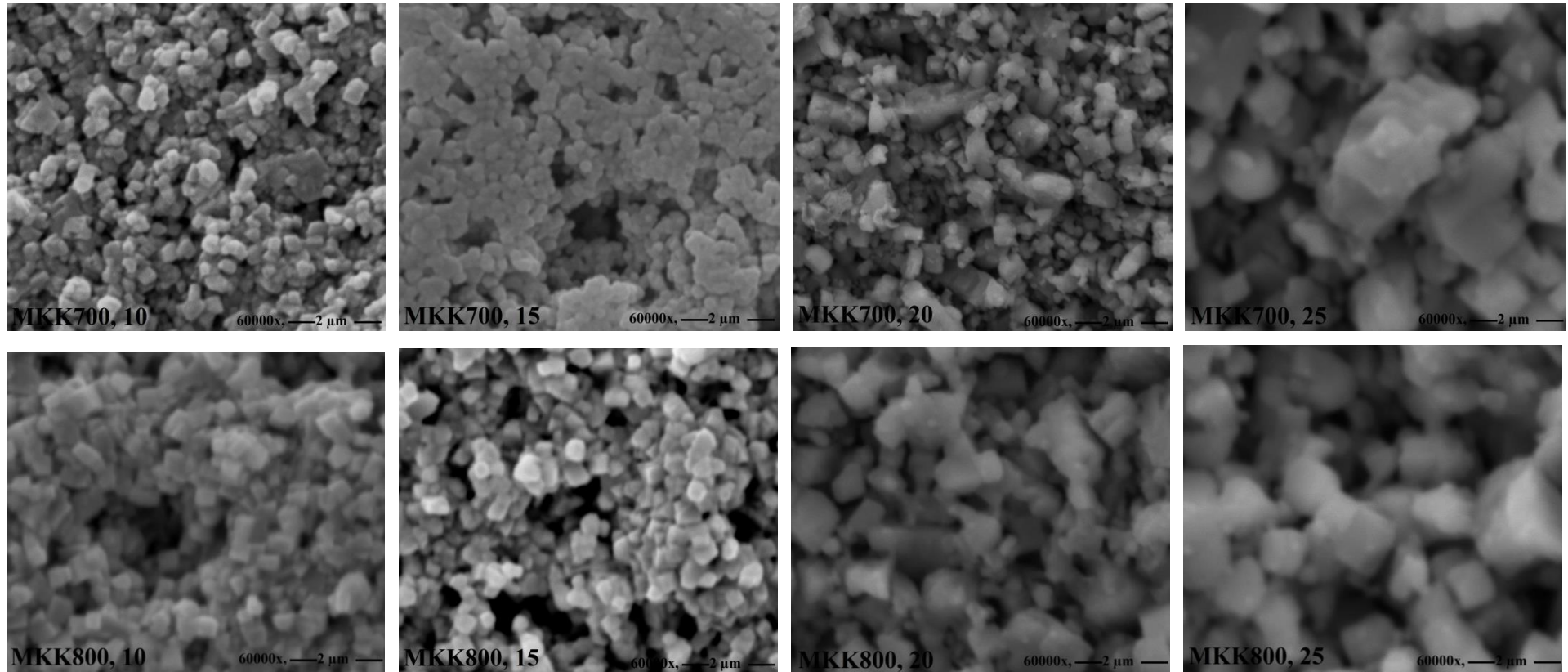


Figure 5.10. Secondary SEM images for microwave sintered KNN ceramics with different calcination temperatures and sintering temperatures, as shown.

5.2.2.1.4. Density

Table 5.2 presents relative density results for all microwave sintered KNN ceramics prepared with different calcination and microwave sintering times.

The relative density of microwave sintered KNN ceramics increases with increasing sintering time (Table 5.2). As can be anticipated, the lower relative density of approximately 68% of theoretical density occurs at lower 10 mins microwave sintering time (MKK700, 10) ceramic calcined at 700°C, and higher relative density of approximately 92% of theoretical density occurs at the upper 25 mins microwave sintering time (K700, 1100) ceramic calcined at 700°C. The higher relative density (approximately 90.6% of theoretical density) demonstrates good improvement in comparison with those of approximately 84% of theoretical density reported by Agustinawati and group (Agustinawati, Isnaini, & Suasmoro, 2017), however, it is lower than those of 91.2 %, 94% and 98% as presented in Table 5.1 (K700, 1000), from Lopez-Juarez and group (Lopez-Juarez et al., 2015) and He and group report (He et al., 2013) respectively, for pure solid-state sintered KNN ceramics.

Table 5.2. Relative density results of microwave sintered KNN ceramics with different calcination and sintering temperatures, as presented.

Sample names	Bulk density (g/cm ³)	Relative density (%)	Sample names	Bulk density (g/cm ³)	Relative density (%)
MKK700, 10	3.06±0.01	68.2±0.1	MKK800, 10	3.18±0.01	70.8±0.1
MKK700, 15	3.61±0.01	80.3±0.1	MKK800, 15	3.66±0.01	81.4±0.1
MKK700, 20	3.97±0.01	88.4±0.1	MKK800, 20	3.88±0.01	86.4±0.1
MKK700, 25	4.07±0.01	90.6±0.1	MKK800, 25	4.06±0.01	90.5±0.1

5.2.2.1.5. Electrical Properties

Figure 5.11 presents hysteresis (P-E) loops of microwave sintered KNN ceramics measured at room temperature, 40kV/cm electric field and 1 Hz frequency in a bipolar field. It can be observed that Figure 5.11 is divided into two parts: part (a) shows microwave sintered KNN ceramics manufactured with 700°C/4h calcination temperature and different microwave sintering times (10, 15, 20, 25mins), and part (b) shows microwave sintered KNN ceramics prepared with 800°C/4h calcination

temperature and various microwave sintering times (10, 15, 20, 25 mins). It is observed that the saturated hysteresis P-E loops are detected at longer microwave sintering time of 25 mins for all microwave sintered KNN ceramics.

The hysteresis loop shape can be affected by microwave sintering time, densification and higher relative density. The ideal hysteresis loop shape indicating ferroelectricity behaviour occurs at higher microwave sintering (25 mins) time and relative density (higher than approximately 90% of theoretical density). On the other hand, a lemon-shaped hysteresis loop corresponding to high conductivity occurs at low microwave sintering (20 mins) time and relative density (less than approximately 88% of theoretical density). Hysteresis loops were not observed at lower microwave sintering (less than 15 mins) time and relative density (less than 82% of theoretical density), due to passing current through pores in the KNN samples (current leakage), and leakage resulting from oxygen vacancies (Wiegand et al., 2012, Woo et al., 2017). The higher remnant polarization of approximately $17 \mu\text{C}/\text{cm}^2$ for MKK800, 25 ceramics shows improvement comparing with $10\mu\text{C}/\text{cm}^2$ (Ponraj & Varma, 2016), however it is less than $33 \mu\text{C}/\text{cm}^2$ for K700, 1100 ceramics and $26\mu\text{C}/\text{cm}^2$ (Tian & Du, 2014), for pure KNN ceramics.

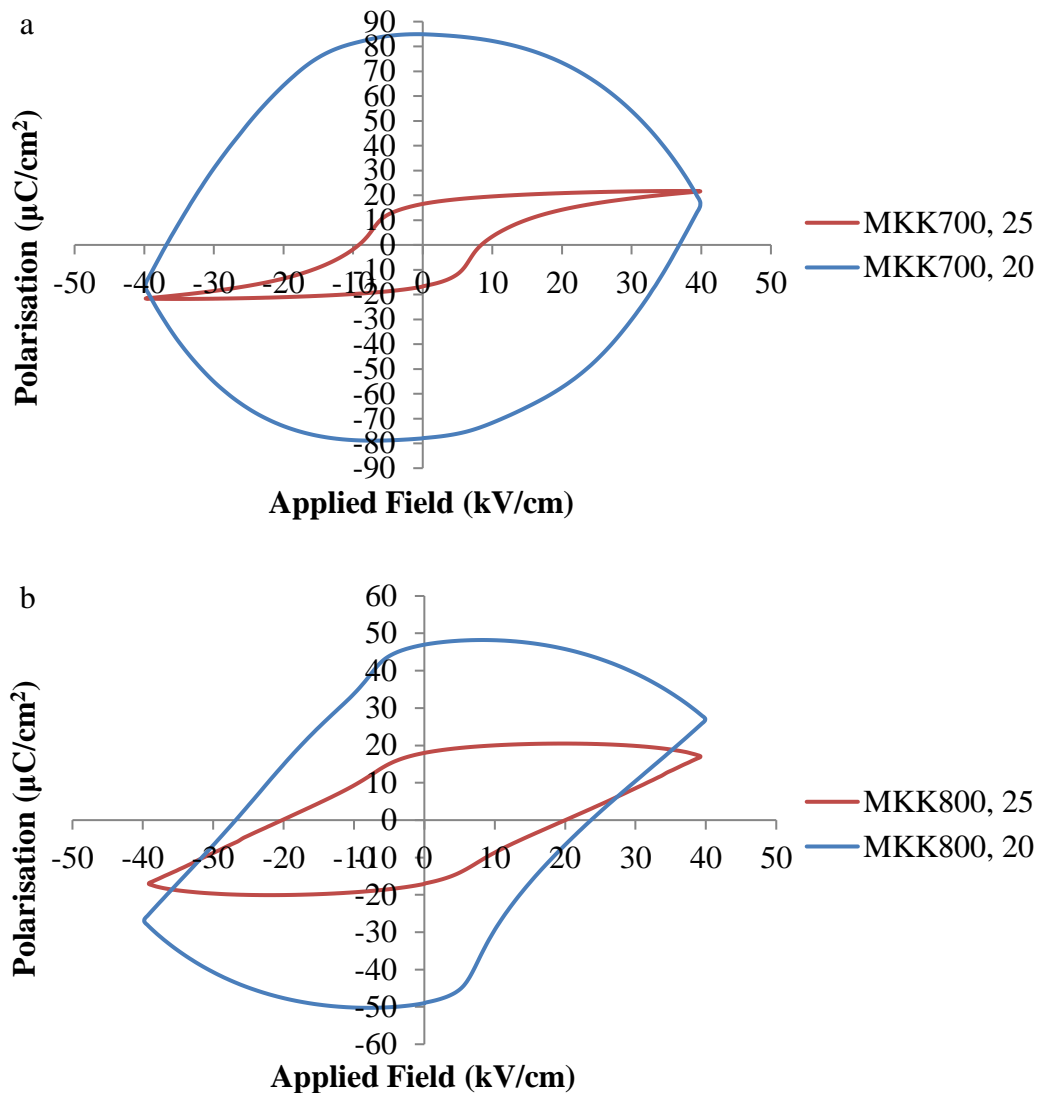


Figure 5.11. Polarisation vs electric field response at room temperature and 1Hz frequency using the bipolar measurement of microwave sintered KNN ceramics with (a) 700°C/4h calcination temperature and (b) 700°C/4h calcination temperature, and different sintering temperatures.

Figure 5.12 presents strain-electric field (S-E) loops for microwave sintered KNN ceramics analysed at room temperature, 40kV/cm electric field and 1 Hz frequency in a bipolar field. Figure 5.12 contains two parts: part (a) shows microwave sintered KNN ceramics made with 700°C/4h calcination temperature and different microwave sintering times (10, 15, 20, 25mins), and part (b) shows microwave sintered KNN ceramics prepared with 800°C/4h calcination temperature and various microwave sintering times (10, 15, 20, 25 mins). The butterfly P-E loops shown at lower and maximum strain% are obtained at 20 and 25 mins of microwave sintered KNN ceramics, respectively.

The maximum strain increased from approximately 0.052% to 0.075% with increasing microwave sintering time from 20 to 25 mins. The typical butterfly S-E loop shape, indicating ferroelectric behaviour is shown for microwave sintered KNN ceramics sintered at 20 and 25 mins (Priya & Nahm, 2011). On the other hand, S-E loops do not appear for lower microwave sintering (less than 15 mins) time and relative density (less than 82% of theoretical density), due to current leakage. The maximum strain of approximately 0.075% for MKK700, 25 ceramics shows good improvement compared with 0.06% for K700, 1100 ceramics and 0.05% (Du et al., 2017), however, it is less than 0.012% (Dahiya, Thakur, & Juneja, 2013), 0.09% (Palei, Sonia, & Kumar, 2012) and 0.08% (Matsubara, Yamaguchi, Kikuta, & Hirano, 2005).

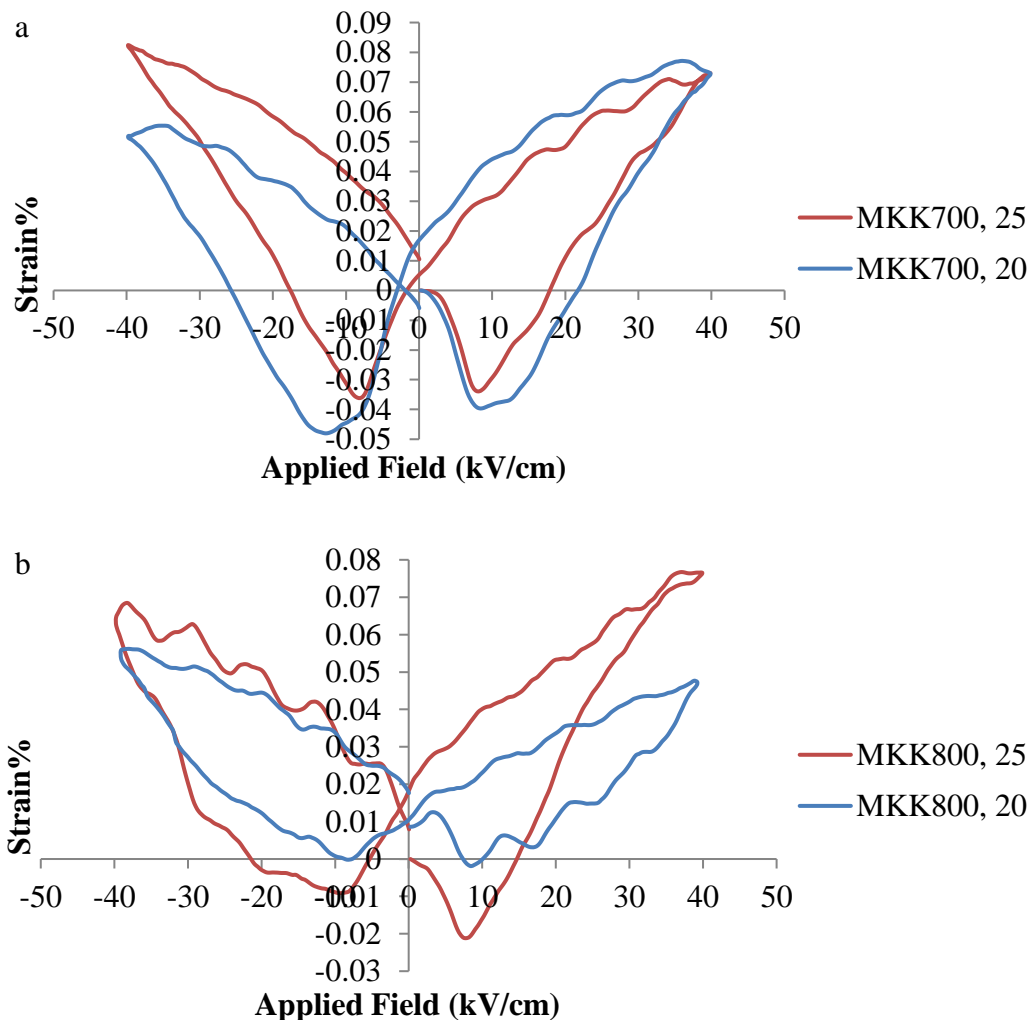


Figure 5.12. Electric field induced strain at room temperature and 1Hz frequency using the bipolar measurement of microwave sintered KNN ceramics with (a) 700°C/4h calcination temperature and (b) 700°C/4h calcination temperature, and different sintering temperatures.

5.2.3. Melt Processing Route

5.2.3.1. Potassium Niobium Borate glasses

Potassium niobium borate glasses were prepared by melt processing to use as a baseline to prepare potassium sodium niobium borate ceramics. The potassium niobium borate glass compositions prepared by melt quenching are shown in Figure 5.13. Two compositions gave completely glassy samples, whilst three compositions crystallised completely and one sample was partly amorphous (partly glass), as shown in Figure 5.13.

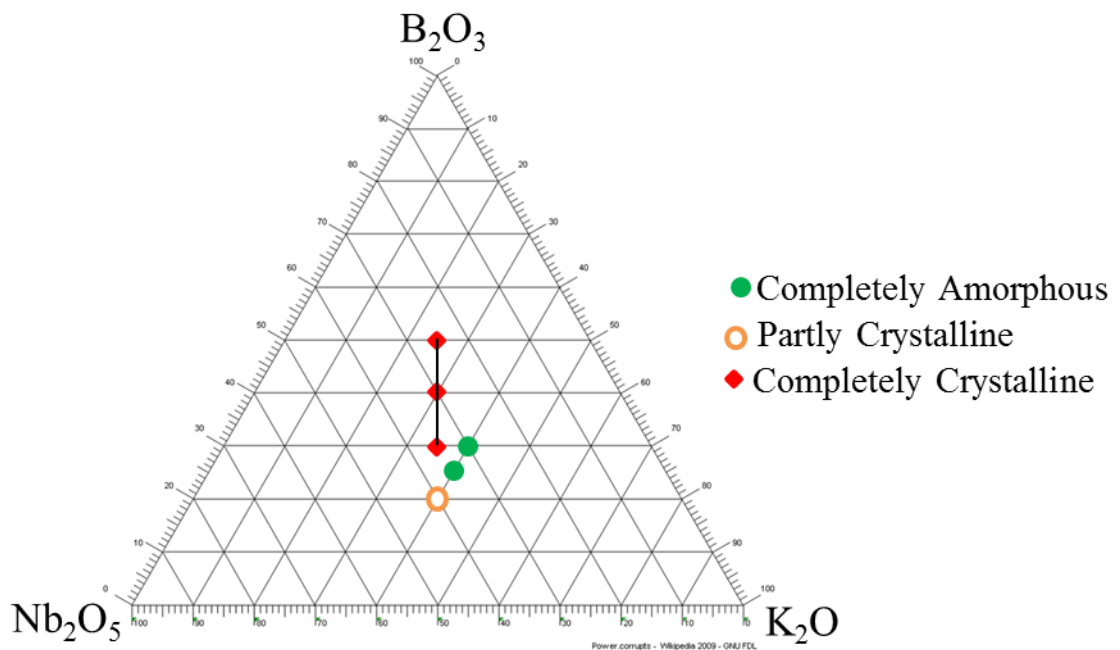


Figure 5.13. Phase diagram for potassium niobium borate glasses showing nominal compositions prepared.

The main purpose in the present work is to preper KNN glass-ceramics through crystallisation, so these glasses have not been analysed.

5.2.3.2. Potassium Sodium Niobium Silicate Glasses

5.2.3.2.1. Results and Discussion

5.2.3.2.1.1. XRD

Potassium sodium niobium silicate glassy samples were ground to a fine powder and placed into XRD sample metallic holders to analyse the crystalline structures using XRD analysis. At room temperature, XRD analysis applied at 10 to 80 °2θ and shows

one crystalline phase and amorphous phase for all potassium sodium niobium silicate crystalline glasses, as shown in Figure 5.14.

XRD results (Figure 5.14) for potassium sodium niobium silicate glassy samples exhibited sharp peaks for all samples at room temperature, indicating partly or mostly crystalline glasses. All peaks stated in the present work correspond to ICDD no 01-074-2025 and ICDD no 01-073-7471, showing $K_{0.90}Na_{0.10}NbO_3$ and $K_{2.6}Nb_{11.6}O_{30}$ phases, respectively.

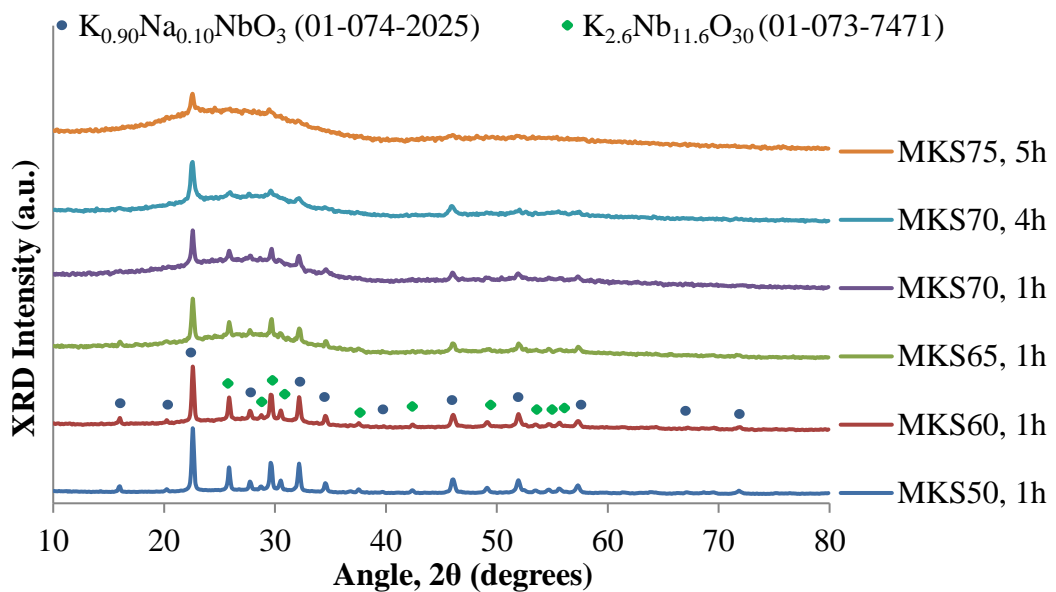


Figure 5.14. XRD patterns for potassium sodium niobium silicate glasses.

5.2.3.2.1.2. Raman Spectroscopy

Raman results for potassium sodium niobium silicate glasses measured at room temperature with Raman shift from 100 to 1500 cm^{-1} , are shown in Figure 5.15. Raman spectra show a broad band at lower than 450 cm^{-1} and a sharp, strong peak at 450-800 cm^{-1} .

Raman spectra have been collected for KNN silicate glass samples at 100 to 1500 cm^{-1} , as shown in Figure 5.15. Three main peaks are shown for all samples. The first four bands are located between 100 and 800 cm^{-1} , marked as ν_1 , ν_3 , ν_5 and ν_6 , corresponding to octahedral NbO_6 (Kioka et al., 2011b). although niobium dominated spectra for the glassy samples, another band located between 700 and 1000 cm^{-1} can be assigned as NbO_6 octahedra that is fully dissolved in the silicate glass matrix via Nb-O-Si bond (Kioka, Honma, & Komatsu, 2011a; Lipovskii, Kaganovskii, Melehin,

Tagantsev, & Yanush, 2008; Möncke et al., 2017), resulting from much higher polarizability of Nb^{5+} ions, $\alpha(\text{Nb}^{5+})=0.262\text{\AA}^3$, compared to only $\alpha(\text{Si}^{4+})=0.033\text{\AA}^3$ for Si^{4+} ions, niobium-related bands dominate the Raman spectra. (The Raman scattering cross-section of Nb-O related bonds is so much higher than for Si-O related bonds because the Raman intensity of a vibrational mode is proportional to the square of the polarizability derivative with respect to the normal coordinate of the mode (e.g., bond stretching)) (Dimitrov & Komatsu, 2010; Möncke et al., 2017).

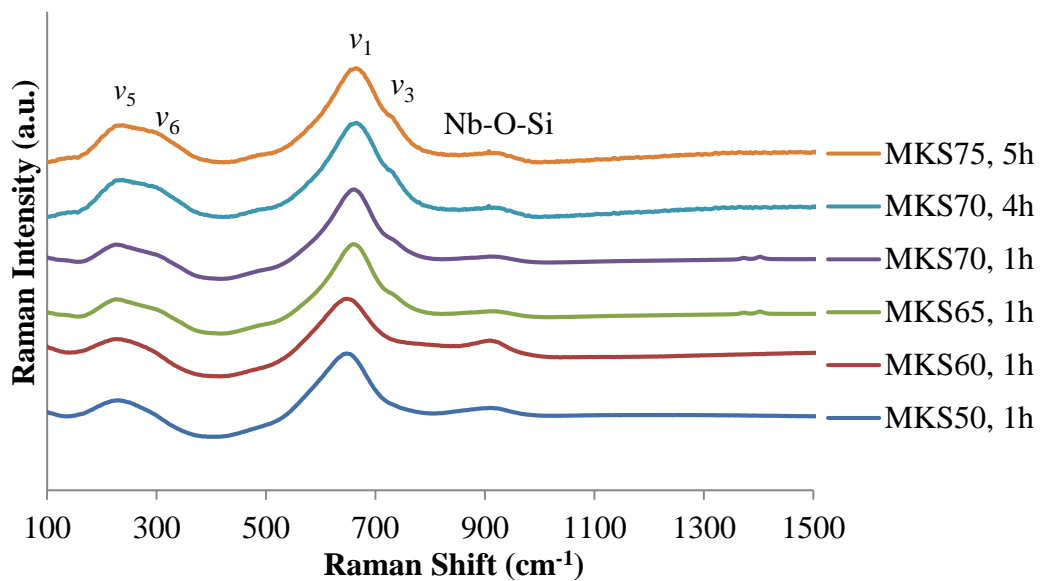


Figure 5.15. Raman spectra for potassium sodium niobium silicate glasses.

5.2.3.2.1.3. Electron Microscopy

Secondary SEM micrographs for potassium sodium niobium silicate glassy samples measured at room temperature with 20,000x magnification and 10 μm scale. All glassy samples reveal inhomogeneous shapes and sizes of detected grains on the surface, as presented in Figure 5.16.

Secondary detection SEM micrographs (Figure 5.16) for potassium sodium niobium silicate glassy samples show grain growth on the surface of the sample, indicating the formation of partly or completely crystalline glasses. Larger grain sizes were obtained for MKS60, 1h samples and smaller grain sizes were obtained for MKS70, 1h samples.

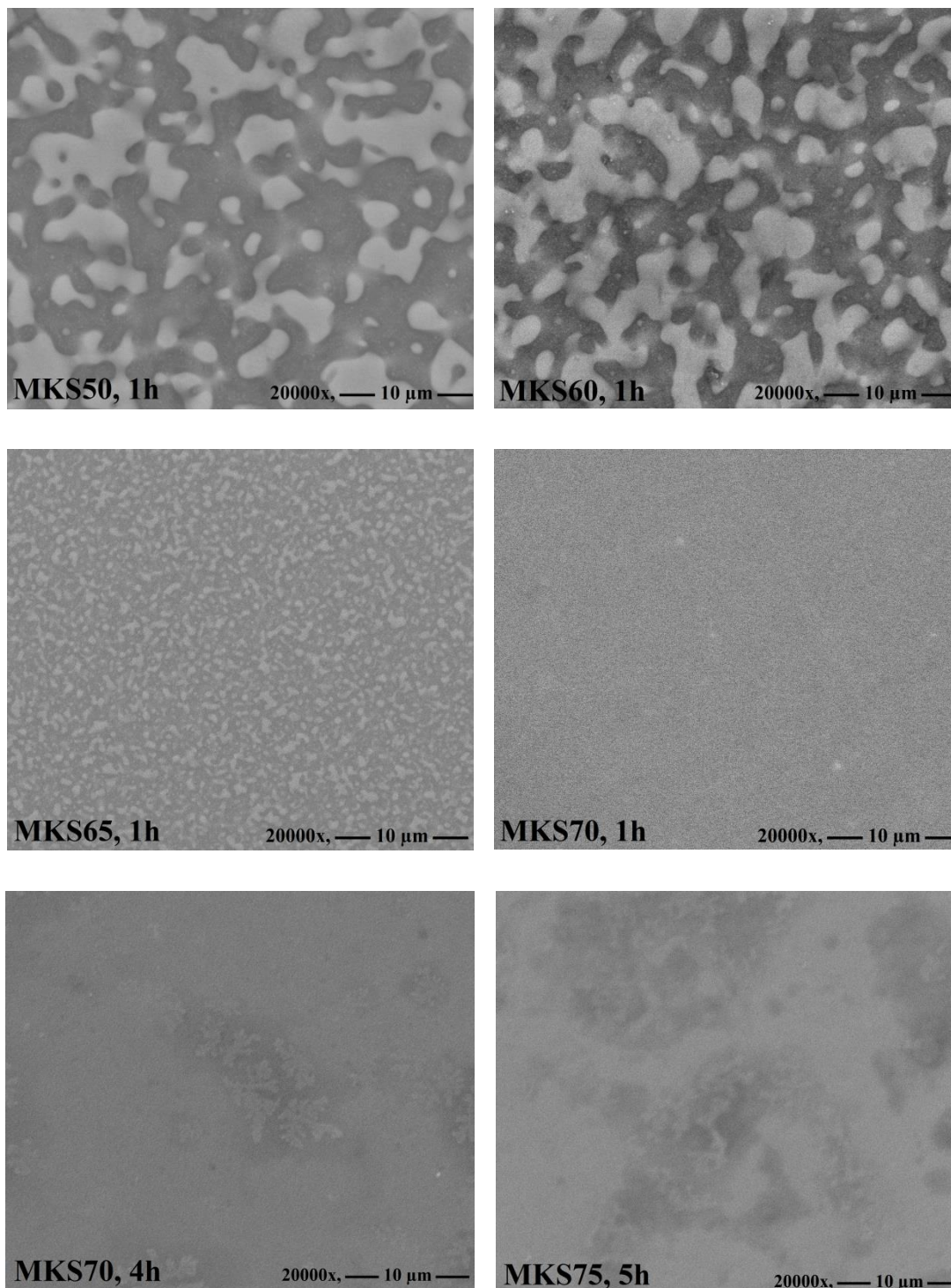


Figure 5.16. SEM images for potassium sodium niobium silicate glasses.

5.2.3.2.1.4. Density

Table 5.3 shows the dependence of bulk densities of potassium sodium niobium silicate glassy samples as a function of composition. Bulk density decreases with increasing SiO_2 content, as expected on the basis of the lower density of Si compared with Nb.

Bulk densities of potassium sodium niobium silicate glassy samples present a higher density of 3.26 g/cm³ and lower density of 2.83 g/cm³ of samples MKS50, 1h and MBS75, 5h, respectively. It can be shown from Table 6.6; the bulk density of potassium sodium niobium silicate glassy samples has decreased with increasing of SiO₂ and decreasing of K₂O, Na₂O and Nb₂O₅ contents.

Table 5.3. Bulk density results of potassium sodium niobium silicate glasses.

Sample name	Bulk density (gm/cm ³)
MKS50, 1h	3.26±0.3
MKS60, 1h	3.16±0.3
MKS65, 1h	3.05±0.3
MKS70, 1h	2.96±0.3
MKS70, 4h	2.94±0.3
MKS75, 5h	2.83±0.3

5.2.3.3. Potassium Sodium Niobium Borate Glass-Ceramics

Potassium sodium niobium borate glasses and glass-ceramics were manufactured by melt processing. The potassium niobium borate glass compositions prepared by melt quenching are shown in Figure 5.17. Two compositions gave completely glassy samples, whilst one sample was partly amorphous, as shown in Figure 5.17.

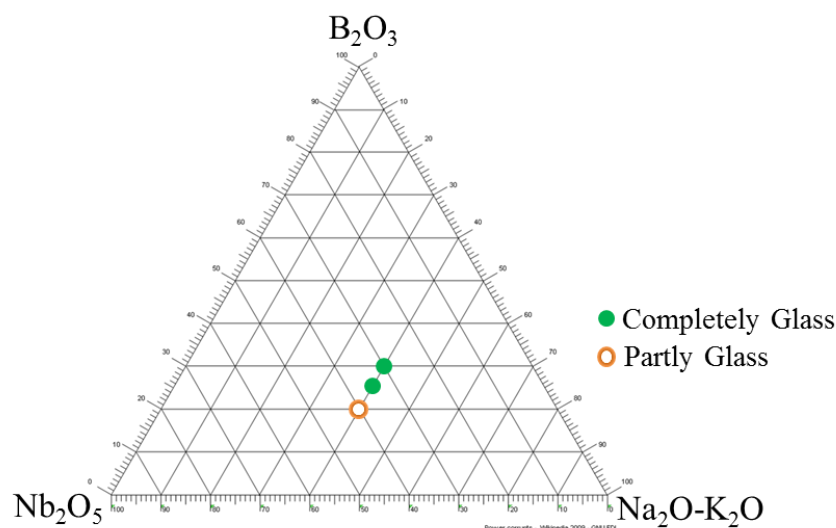


Figure 5.17. Phase diagram for potassium sodium niobium borate glasses and glass-ceramics showing composition prepared.

5.2.3.3.1. Results and Discussion

5.2.3.3.1.1. DTA

Figure 5.17 shows the DTA data for potassium sodium niobium borate glasses. DTA analysis was used to determine exothermic peaks corresponding to the crystallisation temperatures (T_C) and identified two crystallisation temperatures as shown.

It is known that preparing glass-ceramics from glasses requires determination of the crystallisation temperature (T_C) of the glasses. In the present work, DTA analysis has been used to determine the crystallisation temperatures by identifying the exothermic peaks of KNNB glasses, as shown in Figure 5.18. Two main exothermic peaks related the crystallisation temperatures are presented for each component of the two prepared KNNB glasses, the first crystallisation temperature assigned as T_{C1} and second crystallisation temperature assigned as T_{C2} , as shown in the Figure 5.18. Increasing Nb_2O_5 content from 30 to 35mol% and reducing B_2O_5 content from 30 to 25mol% shifted both crystallisation temperatures to higher temperatures. The primary purpose of determining the crystallisation temperatures is to prepare glass-ceramics by heat treatment of the prepared glasses at these crystallisation temperatures. Heat treatment at the indicated T_C for a period of time leads to rearrangement of the random bonds to be ordered bonds (Behrens et al., 2018; Hunger, Carl, & Rüssel, 2010; Kioka et al., 2011; Trégouët et al., 2017; Wang, Honma, & Komatsu, 2014). For example, heat treatment of the two prepared KNNB glasses, random B-O-Nb bonds are broken and redistributed in ordered $NaNb_3O_8$ at T_{C1} and ordered $K_{0.5}Na_{0.5}NbO_3$ and $K_{5.75}Nb_{10.85}O_{30}$ at T_{C2} , while borate entities form the remaining glass phase, as identified by XRD results shown in the Figure 5.20.

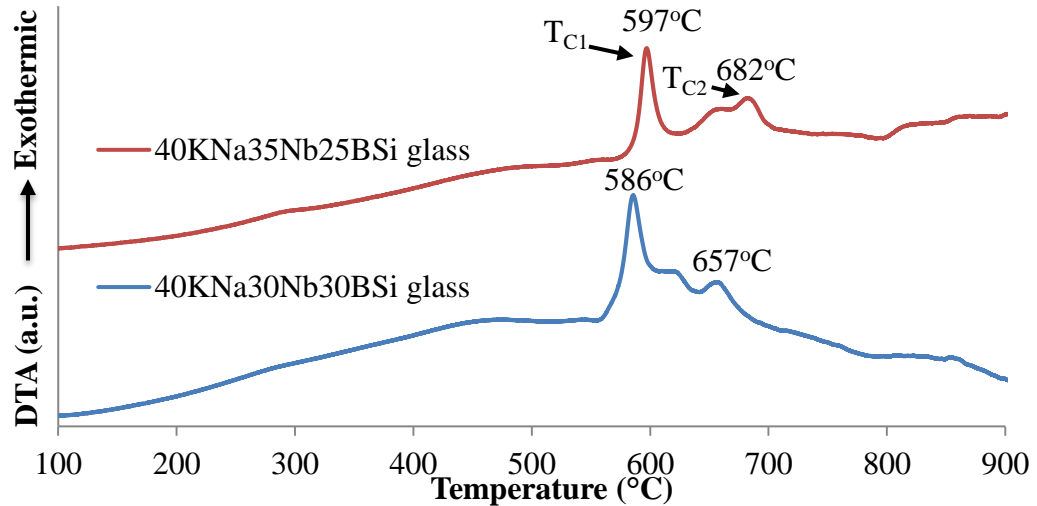


Figure 5.18. DTA traces for KNN borate glass compositions.

5.2.3.3.1.2. XRD

Figure 5.19 and Figure 5.20 present XRD results for potassium sodium niobium borate (KNNB) glasses and glass-ceramics, respectively. XRD results in Figure 5.19 present broad peaks like humps without any sharp peaks, however, sharp peaks occur for one of the KNNB glasses. On the other hand, XRD results in Figure 5.20 showed sharp peaks without existing humps for the KNNB glass-ceramic samples presented.

All KNN borate glasses were investigated with XRD analysis to identify the amorphous or crystalline phases present. As shown in Figure 5.19, XRD analysis showed non-crystalline structure due to the existence of a broad hump with no crystallinity or sharp peaks. This confirmed fully amorphous and glassy samples for two KNN borate glasses (40KNa35Nb25B and 40KNa40Nb20B), however the third KNN borate glass (40KNa30Nb30B) had crystallized and the sharp peaks are attributed to ICDD no 01-074-2025, $K_{0.90}Na_{0.10}NbO_3$ (Das et al., 2017; Hao & Dai, 2017; Samudrala et al., 2018). The two completely amorphous KNN borate glasses were heat treated at T_{C1} and T_{C2} (shown in Figure 5.18) temperatures exhibited crystalline phases as displayed in the Figure 5.20. The formation of ceramic phases from glass phases resulted from devitrification during heat treatment (Bouchouicha et al., 2016). The glassy content decreases with increasing heat treatment temperature. The first crystalline phase formed by heat treatment at lower T_{C1} is $NaNb_3O_8$ according to ICDD no 01-078-2007 (Figure 5.20(a)), resulting from the higher crystallization tendency of the Na_2O and Nb_2O_5 contents with the glassy melt (Hmood, Guenster, & Heinrich, 2015; Tréguoët et al., 2017). The main $K_{0.5}Na_{0.5}NbO_3$ crystalline phase was

successfully formed during heat treatment at higher T_{C2} . The $K_{0.5}Na_{0.5}NbO_3$ crystalline phase corresponds to ICDD no 04-016-7531, and exhibits a non-ferroelectric anorthic crystalline structure at room temperature. In addition, a secondary phase ($K_{5.75}Nb_{10.85}O_{30}$) related ICDD no 00-038-0297 was introduced with the main KNN phase at higher T_{C2} for all KNN borate glass ceramics, as shown in Figure 5.20(b) (Yongsiri, Sirisoonthorn, & Pengpat, 2015). This may be due to the high volatilization of alkali oxides during melting processing (Ramajo, Taub, & Castro, 2014).

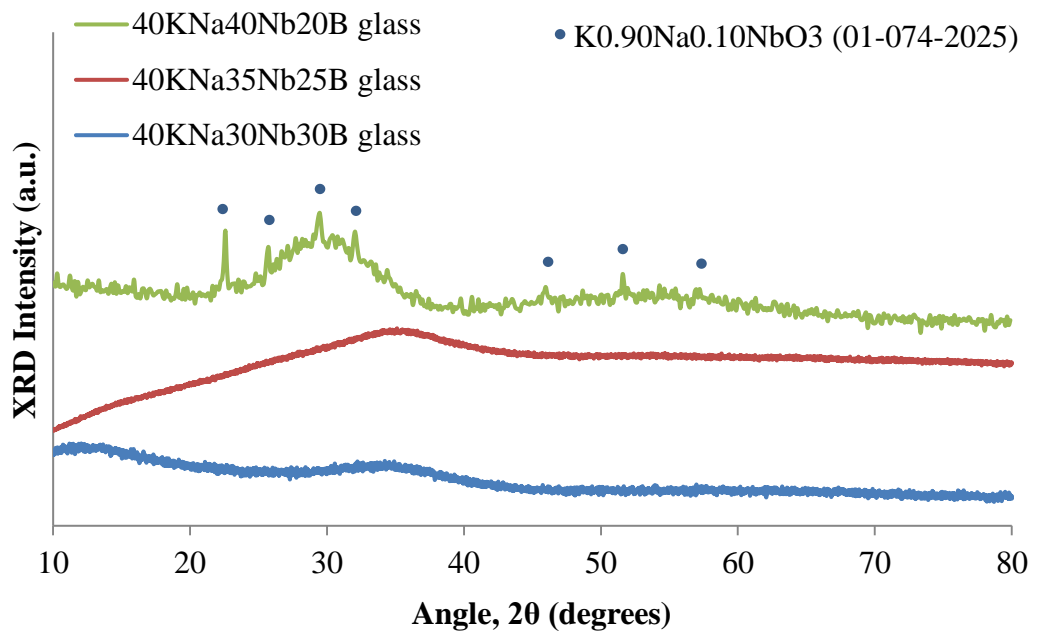


Figure 5.19. XRD results of KNN borate glass compositions.

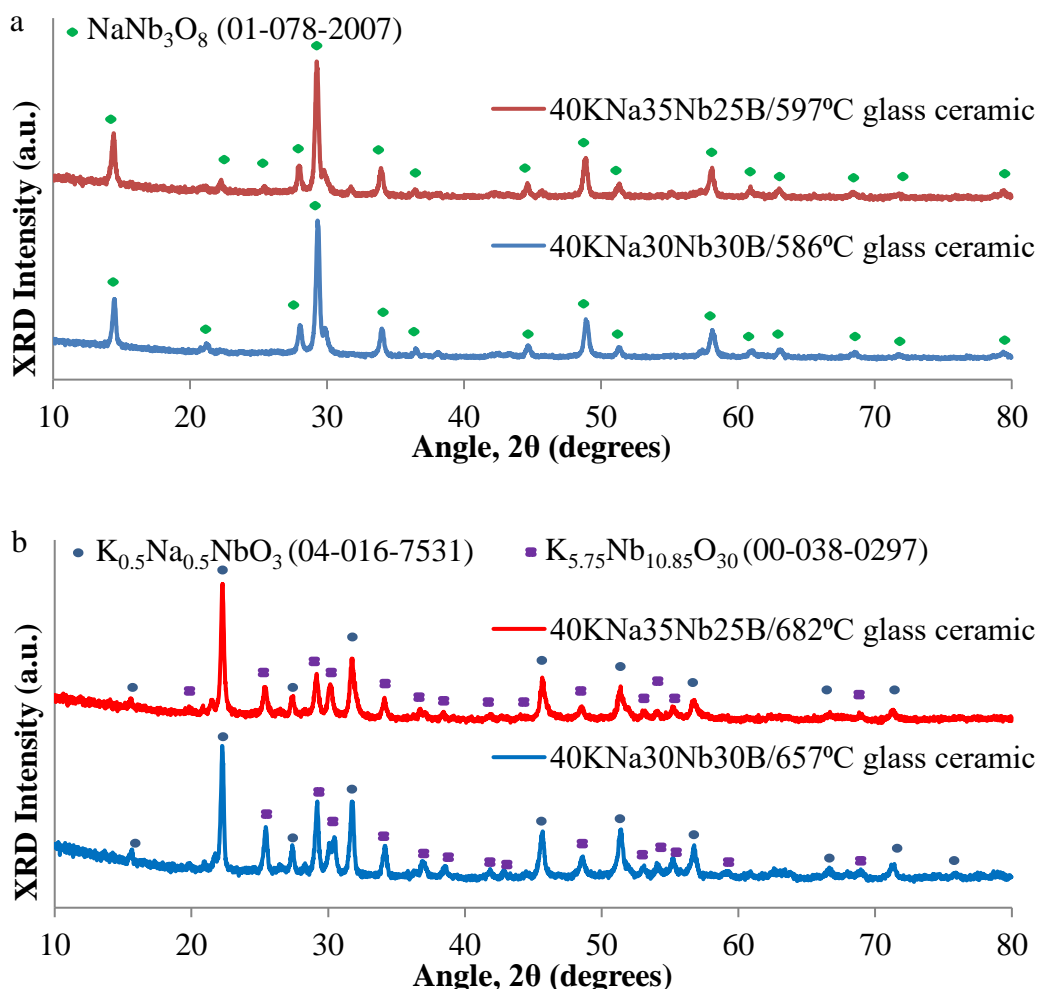


Figure 5.20. XRD patterns for KNN borate glass-ceramics heat treated at (a) T_{C1} and (b) T_{C2} , for 7.30.

5.2.3.3.1.3. Raman Spectroscopy

Figure 5.21 and Figure 5.22 show Raman results for potassium sodium niobium borate (KNNB) glasses and glass-ceramics, respectively. Strong bands are detected at $350\text{-}750\text{ cm}^{-1}$ for 40KNa30Nb30B glassy sample, however, a strong band detected at $750\text{-}1000\text{ cm}^{-1}$ for both 40KNa35Nb25B and 40KNa40Nb20B glasses, is shown in Figure 5.21. On the other hand, Raman results presented strong peaks with sharp tips at $350\text{-}750\text{ cm}^{-1}$ for both 40KNa35Nb25B and 40KNa40Nb20B glass-ceramic samples, as shown in Figure 5.22.

Raman spectra measured at room temperature in the range $100\text{-}1500\text{ cm}^{-1}$ for all KNN borate glasses, are shown in Figure 5.21. Each spectrum has three main bands. The first band is assigned to a ν_5 band in the region of 100 and 300 cm^{-1} and is assigned as a vibrational bending mode, corresponding to NbO_6 octahedra. The second main band is observed in the region of 300 and 750 cm^{-1} , attributed to vibrational stretching

mode is marked as ν_1 and ν_2 , where the ν_1 band is assigned to less-distorted NbO_6 octahedra (Kioka et al., 2011b) and the shoulder in the ν_2 band corresponds to octahedral NbO_6 (Zhu et al., 2012). The third band is observed in the region of 750 to 1000 cm^{-1} , attributed to a stretching mode with metastable phase and could be assigned as Nb-O-B in pyroborate units (Baek et al., 2017; Cheng, Wan, & Liang, 2001).

After heat treatment of the KNN borate glasses, peaks in the Raman spectra occurred in sharp lines instead of broad shapes, which demonstrate conversion of the KNN borate glasses to KNN borate glass-ceramics, as shown in Figure 5.22. The sharp bands exhibited as vibrational modes are marked ν_1 to ν_6 corresponding to NbO_6 octahedra. The vibrational stretching modes are assigned as ν_1 to ν_3 , which are shown at higher Raman shift (300 and 750 cm^{-1}) and the vibrational bending modes are assigned as ν_4 to ν_6 which are displayed at lower Raman shift (150 and 300 cm^{-1}) (Wang et al., 2016; Wu et al., 2014). Where a shoulder is identified at ν_6 vibrational mode (less than 195 cm^{-1} Raman shift), this could be assigned as a translational mode of K^+ cation and rotations of the NbO_6 octahedra. Also, the weak peak identified at 110 cm^{-1} (Figure 5.22(b)) can be matched to the Na^+/K^+ cations versus NbO_6 octahedra. However, the splitting of one weak peak to two weak peaks in the region of 750 and 1000 cm^{-1} may be due to the substitution the B^{3+} in the same site of Nb^{5+} (Singh et al., 2013; Wang et al., 2016; Zhu et al., 2012). The highest Raman intensity was confirmed for peak allocated in the region of 300 cm^{-1} , and 750 cm^{-1} for both 40KNa40Nb20B glass (Figure 5.20) and KNN borate glass-ceramics (figure 5.22), as well as the similarity in Raman spectral shape for 40KNa40Nb20B glasses (Figure 5.21) and KNN borate glass-ceramics (Figure 5.22). The highest Raman intensity and similarity in Raman spectra shape maybe gives evidence for some level of crystallization of 40KNa40Nb20B glasses.

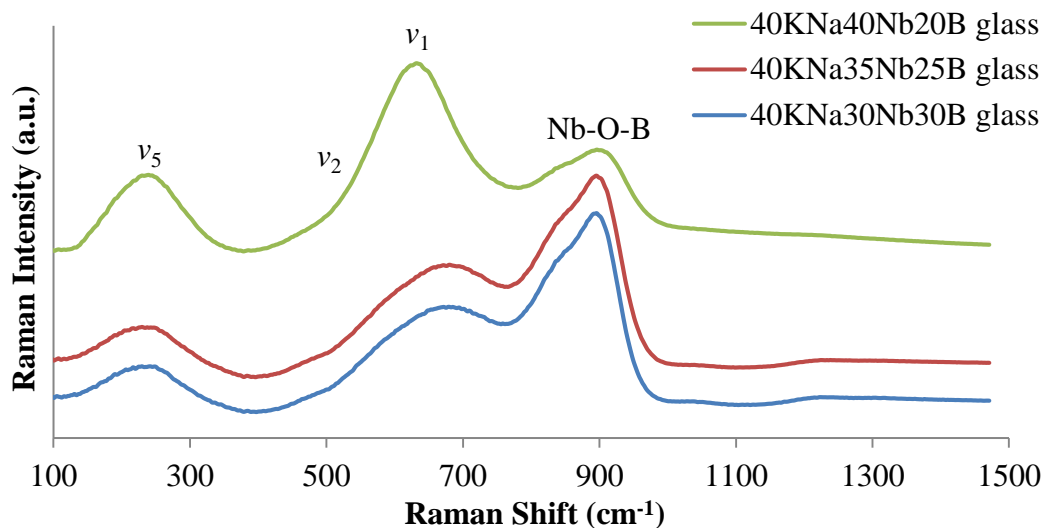


Figure 5.21. Raman spectra for KNN borate glass compositions.

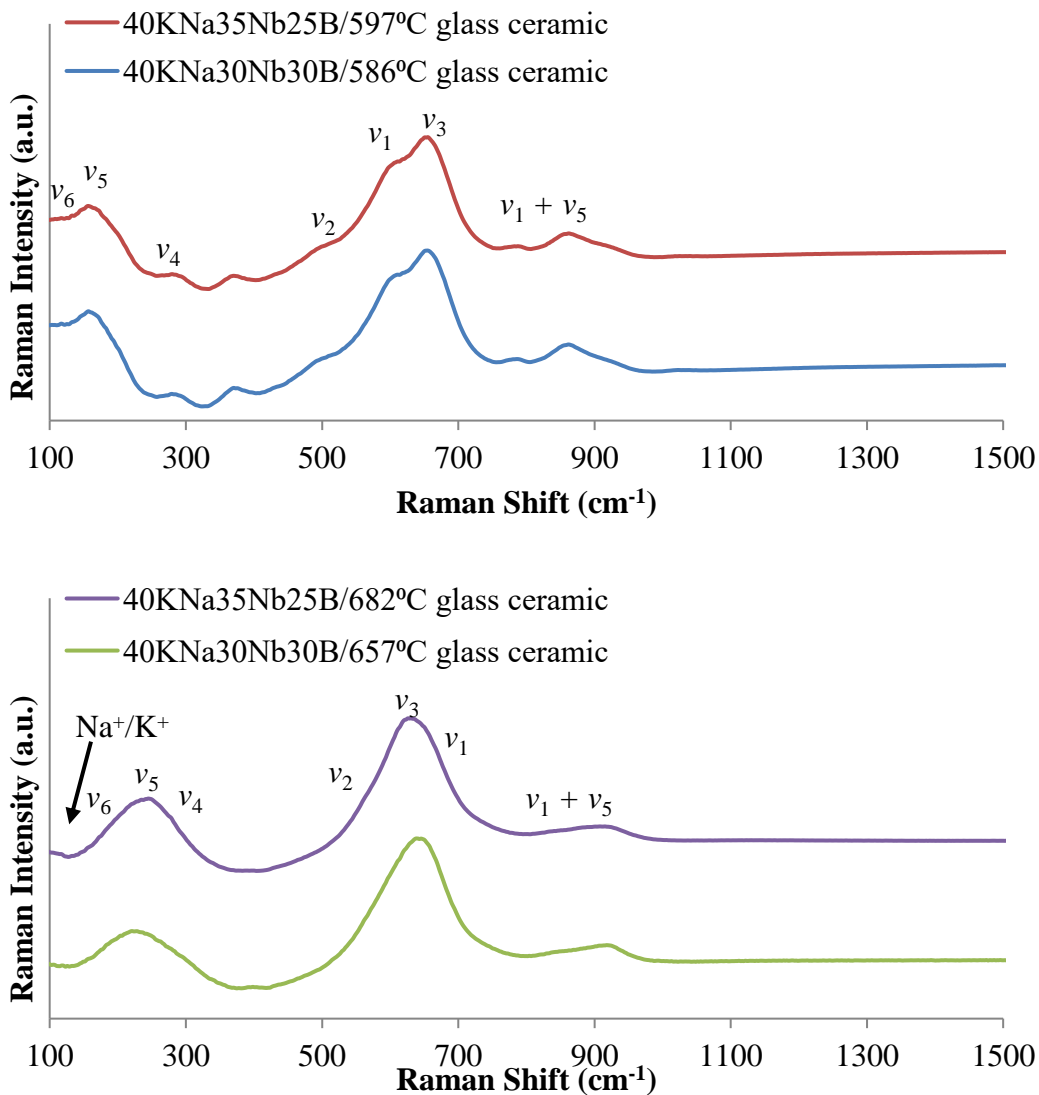


Figure 5.22. Raman spectra KNN borate glass-ceramic compositions heat treated at (a) T_{C1} and (b) T_{C2} , for the 7.30h period.

5.2.3.3.1.4. Electron Microscopy

Figure 5.23 shows secondary SEM micrographs for KNN borate glasses and glass-ceramics analysed at room temperature with 20,000x magnification and 10 μm scale. A flat surface with no observed grains appeared for all KNN borate glasses except 40KNa40Nb20B glass, in which, grains were identified on the surface.

SEM micrographs confirmed the amorphous nature of 40KNa30Nb30B and 40KNa35Nb25B glasses due to the absence grains or grain-boundaries on the glass surface. They confirmed the crystalline nature of the 40KNa40Nb20B glasses showing the presence of grains. Many crystallites appeared on the surface of the KNN borate glass-ceramic samples after heat treatment. Inhomogeneous average grain sizes ranged from about 100 nm to 200 nm for KNN borate glass-ceramics heat treated at T_{C1} and T_{C2} respectively, indicating the successful crystallisation and formation of KNN glass borate ceramics.

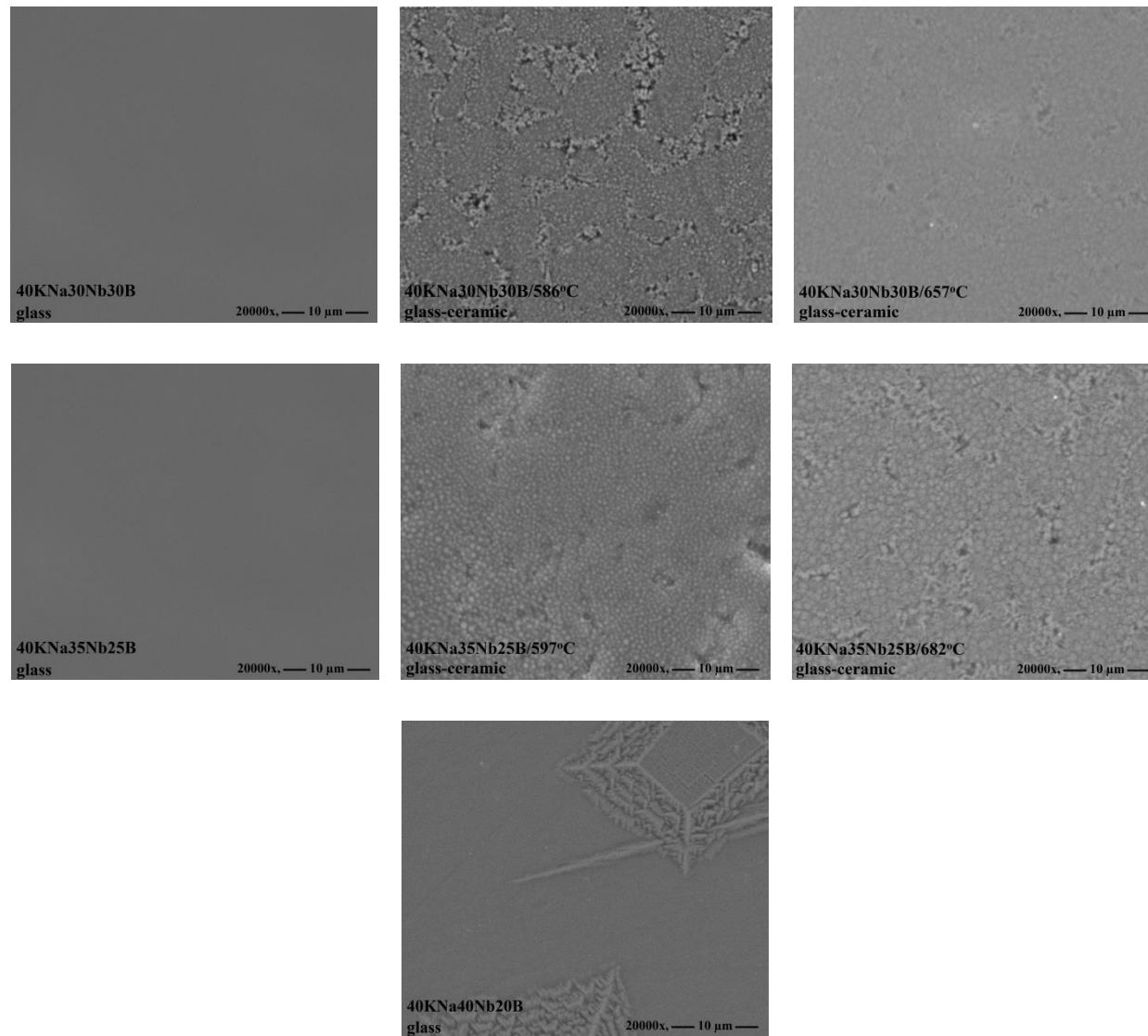


Figure 5.23. SEM images of KNN borate glass and glass-ceramics.

5.2.3.3.1.5. Density

Table 5.4 shows the dependence of bulk densities of potassium sodium niobium borate glasses and glass-ceramics as a function of composition. The minimum bulk density of 3.13 g/cm³ of 40KNa30Nb30B glass and maximum density of 3.51 g/cm³ of 40KNa35Nb25B/682°C glass- ceramic are observed.

The bulk density increased from 3.13 to 3.42 g/cm³ with increasing content of Nb₂O₅ from 30 to 40mol%, as shown in Table 5.4. Ganvir and Gedam (Ganvir & Gedam, 2017) stated that the increasing or decreasing of bulk density could be affected by molecular weight. Therefore the increase in bulk density is due to the higher molecular weight of Nb₂O₅ (265.81 gm/mol) than B₂O₃ (69.62 gm/mol) in the KNN borate glasses. It is observed that the bulk density exhibited a lower value of 3.13 g/cm³ for 40KNa30Nb30B glass and higher value of 3.51 g/cm³ for 40KNa35Nb25B/682°C glass ceramic. It can be assumed that the maximum bulk density of 40KNa35Nb25B/682°C glass ceramic (3.51 g/cm³) resulted from grain growth of KNN crystals as clearly observed in SEM (Figure 5.22) during the crystallisation of KNa35Nb25B glass at 682°C heat treatment (Yongsiri et al., 2012).

Table 5.4. Bulk density results for potassium sodium niobium borate glasses and glass ceramics.

Sample Name	Bulk density (g/cm ³)
40KNa30Nb30B glass	3.13±0.1
40KNa35Nb25B glass	3.22±0.1
40KNa40Nb20B glass	3.42±0.1
40KNa30Nb30B/586°C glass-ceramic	3.26±0.1
40KNa30Nb30B/657°C glass-ceramic	3.31±0.1
40KNa35Nb25B/597°C glass-ceramic	3.32±0.1
40KNa35Nb25B/682°C glass-ceramic	3.51±0.1

5.2.3.3.1.6. Electrical Properties

Figure 5.24 shows the polarisation versus applied electric field (P-E hysteresis) loops measured at room temperature, and 1Hz applied frequency. Unsaturated and slimmed hysteresis loops for KNN borate glass-ceramics heat treated at T_{C2} are shown.

The P-E hysteresis loops reveal slimmed loop shapes could be related to a linear dielectric property. The tendency of polarisation against the electric field is consistent with the formation of non-ferroelectric $K_{0.5}Na_{0.5}NbO_3$ (anorthic) phase during the crystallisation of KNN borate glass ceramics. The remnant polarisation increased from 0.04 to 0.1 $\mu C/cm^2$ with increasing Nb_2O_5 content from 30 to 35mol% and reducing B_2O_3 content from 30 to 25mol%, respectively. The absence of typical ferroelectric P-E loop shape may be due to the existence of residual glasses or secondary non-ferroelectric phases ($K_{5.75}Nb_{10.85}O_{30}$) or anorthic $K_{0.5}Na_{0.5}NbO_3$ phase at room temperature or any combination of these.

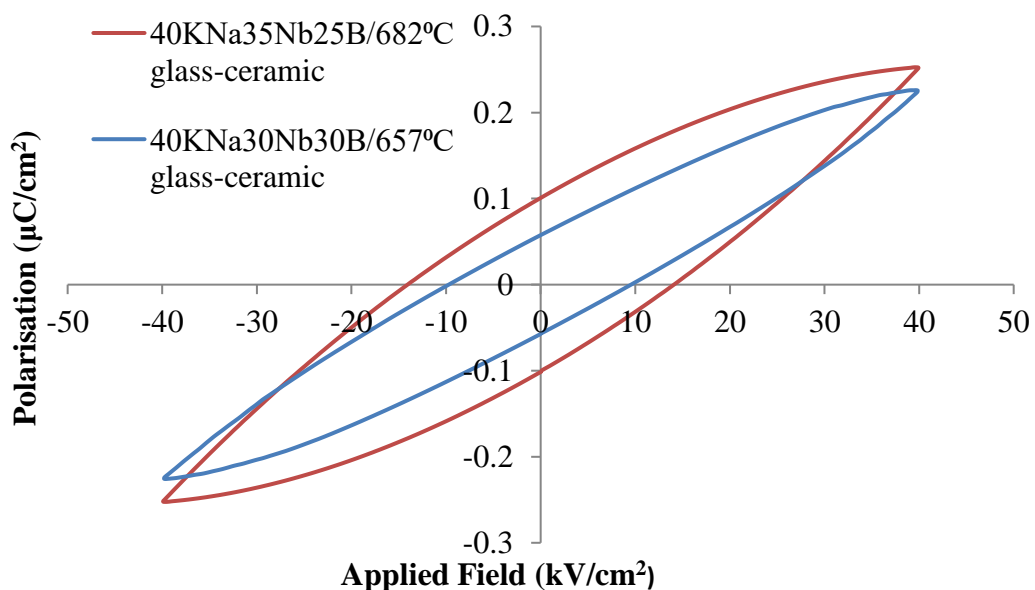


Figure 5. 24. Hysteresis (P-E) loop of KNN borate glass-ceramic compositions heat treated at T_{C2} , for 7.30h, measured at room temperature and 1Hz frequency.

5.2.3.4. Potassium Sodium Niobium Borosilicate Glass-Ceramics

Potassium sodium niobium borosilicate glasses and glass-ceramics were manufactured by melt processing. The potassium niobium borosilicate glass compositions prepared by melt quenching are shown in Figure 5.25. Two compositions gave completely glassy samples, whilst one sample was partly amorphous (partly glass), as shown in Figure 5.25.

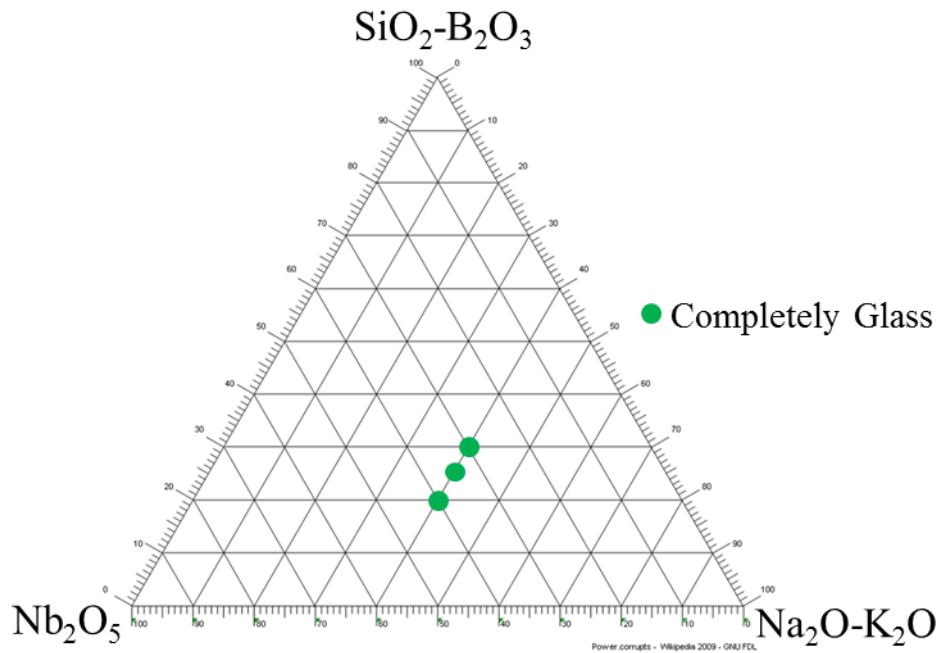


Figure 5.25. Phase diagram for potassium sodium niobium borosilicate glasses and glass-ceramics, showing compositions of prepared samples.

5.2.3.4.1. Results and Discussion

5.2.3.4.1.1. DTA

Figure 5.26 shows the DTA traces for potassium sodium niobium borosilicate glasses. DTA analysis has been used to determine exothermic peaks referring to the crystallisation temperatures (T_C) and has detected two crystallisation temperatures.

DTA traces for KNNBSi glasses have been used to determine the exothermic peaks at different temperatures, which in Figure 5.26 are referred to as the crystallisation temperatures (T_C). Each composition of the three prepared KNNBSi glasses exhibited two main crystallisation temperatures, first crystallisation temperature (T_{C1}) and second crystallisation temperature (T_{C2}). The exothermic peaks shift to higher temperatures, from 608 to 617°C, as the Nb_2O_5 content is raised from 30 to 40mol% on account of the combined SiO_2 and B_2O_3 content, which is reduced from 30 to 20mol%. The T_{C1} peaks shift only slightly, first from 760 to 762°C then down to 757°C as the Nb_2O_5 content increases. The main purpose of determining the crystallisation temperatures was to find the best temperatures for the subsequent heat treatment when preparing the glass-ceramics from the glasses. As shown by earlier studies, it is expected that crystallisation at T_C for a period of time leads to the redistribution of the random ionic bonds found typically in niobate glasses in more ordered bonds, e.g. in

niobate crystals. In this process, Si-O-Nb and B-O-Nb bonds are broken, and diffusion will lead to an agglomeration of niobate octahedra to form the first cluster and then crystals of Na/KNbO₃ while silicate and borate entities constitute for most the remaining glass phase. Earlier studies showed that the first crystallisation temperature T_{C1} , leads foremost to the crystallisation of potassium niobates, as identified by XRD. Sodium niobates crystallise at the higher crystallisation temperature T_{C2} . These findings indicate that the potassium-niobium oxides have a higher crystallisation tendency than other sodium-niobium oxides (Behrens et al., 2018; Hunger et al., 2010; Kioka et al., 2011; Trégouët et al., 2017; Wang et al., 2014).

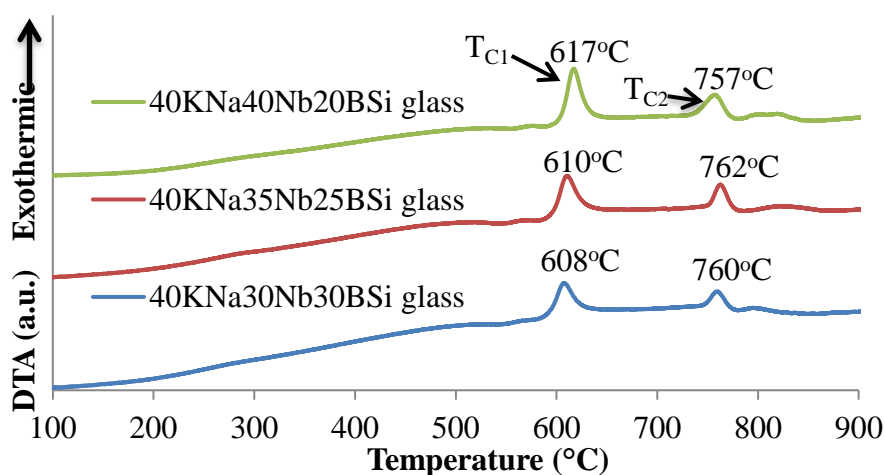


Figure 5.26. DTA traces for KNN borosilicate glass compositions.

5.2.3.4.1.2. XRD

Figure 5.27 and Figure 5.28 show XRD patterns for potassium sodium niobium borosilicate (KNNBSi) glasses and glass-ceramics, respectively. XRD patterns in Figure 5.27 exhibit broad peaks like humps with no presence of any sharp peaks for all KNNBSi glass samples, However XRD results in Figure 5.28 revealed sharp peaks with no presence of amorphous for humps of all KNNBSi glass-ceramic samples.

All KNN borosilicate glasses in the current study are XRD amorphous without any inclusion of crystalline phases. As seen from Figure 5.27, XRD patterns for all three glasses show only a broad hump without any indication of crystallinity which would be related in the presence of sharp peaks (Das et al., 2017; Y. Hao & Dai, 2017; Samudrala et al., 2018). However, as shown in Figure 5.28, all KNN borosilicate samples that have

been heating treated at T_{C1} and T_{C2} display sharp peaks in their XRD patterns, corresponding to various crystalline phases. XRD confirms, therefore, the successful formation of glass–ceramic phases from the purely amorphous glass phases through devitrification during the heat treatment of KNN borosilicate glassy samples (Bouchouicha et al., 2016). It is apparent that the glassy content decreases with increasing temperature of the applied heat treatment. The first crystalline phase of KNN borosilicate glass-ceramics formed by heat treatment at lower temperatures below T_{C1} is NaNb_3O_8 phase related to ICDD no 01-078-2007 (Figure 5.28(a)), reflecting the higher crystallisation tendency of the sodium-niobate system from the glassy melt (Hmood et al., 2015; Trégouët et al., 2017). As can be seen from Figure 5.28(b), the main $\text{K}_{0.5}\text{Na}_{0.5}\text{NbO}_3$ crystalline phase was successfully formed during heat treatment at the higher temperature corresponding to T_{C2} . The $\text{K}_{0.5}\text{Na}_{0.5}\text{NbO}_3$ crystalline phase corresponds to ICDD no 04-016-7531, showing non-ferroelectric anorthic crystalline structure at room temperature. In addition, a secondary phase ($\text{K}_{5.75}\text{Nb}_{10.85}\text{O}_{30}$) corresponding to ICDD no 00-038-0297 was introduced with main KNN phase at higher T_{C2} for all KNN borosilicate glass-ceramics, as shown in Figure 5.28(b) (Yongsiri, Sirisoonthorn, & Pengpat, 2015). This could result from the volatilization of alkali oxides during melting processing (Ramajo et al., 2014).

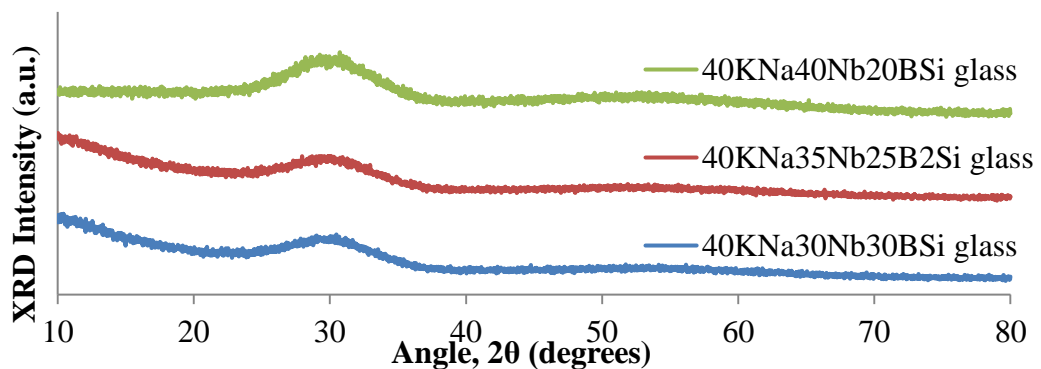


Figure 5. 27. XRD patterns for KNN borosilicate glass compositions.

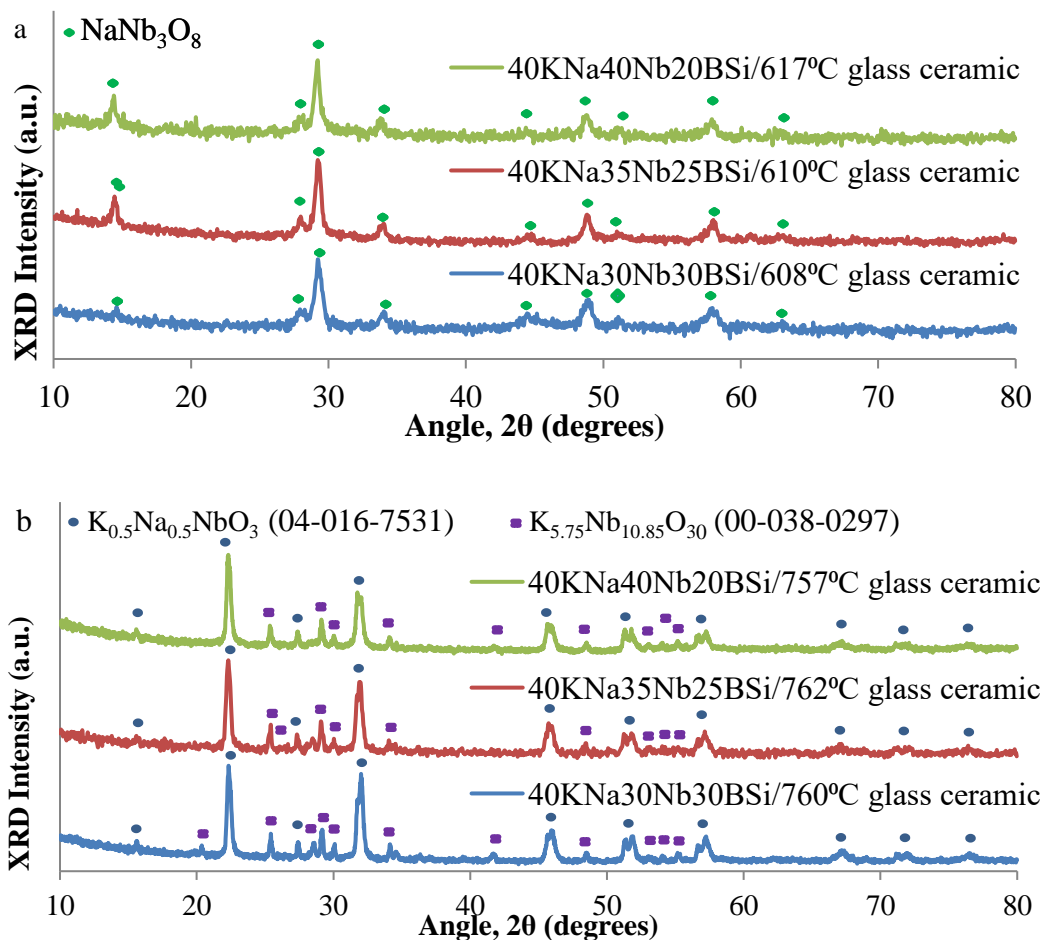


Figure 5.28. XRD patterns for KNN borosilicate glass-ceramic compositions heat treated at (a) T_{C1} and (b) T_{C2} , for 7.30 h.

5.2.3.4.1.3. Raman Spectroscopy

Figure 5.29 and Figure 5.30 show Raman spectra for potassium sodium niobium borosilicate (KNNBSi) glasses and glass-ceramics, respectively. Raman spectra exhibit broad peaks like humps for all KNNBSi glass samples, as shown in Figure 5.29. However, Raman results identified sharp peaks for all KNNBSi glass-ceramic samples, as presented in Figure 5.30.

Raman spectra have been investigated for KNN borosilicate glasses and glass-ceramics at 100 to 1500 cm^{-1} . Figure 5.29 shows Raman spectra for KNN borosilicate glasses that include three main broad bands corresponding to amorphous materials. Broad bands between 100 and 750 cm^{-1} marked as ν_1 , ν_2 and ν_5 , are assigned as octahedral NbO_6 units where the first main band allocated between 100 and 300 cm^{-1} presents a vibrational bending mode and the second main band between 300 and 750 cm^{-1} presents a vibrational stretching mode (Kioka et al., 2011b). Although niobium dominates in spectra for the glassy samples, the third broad band placed between 750

and 1000 cm^{-1} , can be assigned as NbO_6 octahedra that is fully dissolved in the borosilicate glass matrix via Nb-O-Si and Nb-O-B bonds (Kioka et al., 2011a; Lipovskii et al., 2008; Möncke et al., 2017). Due to the much higher polarizability of Nb^{5+} ions, $\alpha(\text{Nb}^{5+})=0.262\text{Å}^3$, compared to only $\alpha(\text{B}^{3+})=0.003\text{Å}^3$ for B^{3+} or $\alpha(\text{Si}^{4+})=0.033\text{Å}^3$ for Si^{4+} ions, niobium-related bands dominate the Raman spectra. The Raman scattering cross-section of Nb-O related bonds is so much higher than for Si-O related bonds because the Raman intensity of a vibrational mode is proportional to the square of the polarizability derivative with respect to the normal coordinate of the mode (e.g., bond stretching)) (Dimitrov & Komatsu, 2010; Möncke et al., 2017). According to the Manara group report (Manara, Grandjean, & Neuville, 2009) B-O⁻ bonds are allocated between 1250 and 1500 cm^{-1} and Si-O Q species placed between 910 and 1190 cm^{-1} , so that the sharp peak identified at 1210 cm^{-1} could potentially be assigned as a Si-O-B bond. Figure 5.30 shows exhibits Raman spectra for KNN borosilicate glass-ceramics that include three main sharp peaks. The heat treatment of KNN borosilicate glasses significantly affected the peak shape and intensity, for example, the third peak at $750\text{-}1000\text{ cm}^{-1}$ is weak (Figure 5.30) for KNN borosilicate glass-ceramics, comparing with being the strongest peak (Figure 5.29) for KNN borosilicate glasses. Also, a sharp peak in Figure 5.29 for KNN borosilicate glasses disappeared after heat treatment (Figure 5.30) to form KNN borosilicate glass-ceramics. Raman spectra display eight peaks for KNN borosilicate glass-ceramics. Peaks at $100\text{-}300\text{ cm}^{-1}$ show vibrational modes and peaks at $300\text{-}750\text{ cm}^{-1}$ show vibrational stretching modes (Wang et al., 2016; Wu et al., 2014). Peaks marked as ν_1 to ν_5 are assigned as NbO_6 octahedra, and a shoulder marked as ν_6 at less than 200 cm^{-1} could be identified as a translational mode of K^+ cation and rotations of the NbO_6 octahedra, as well as the weak peak at 135 cm^{-1} could be assigned as Na^+/K^+ cations versus NbO_6 octahedra. The weak splitting peak allocated at 750 and 1000 cm^{-1} could be assigned as a association of ν_1 and ν_5 corresponding to octahedral NbO_6 , the reason of splitting may be due to the substitution of Si and B in the same site of Nb (Singh et al., 2013; Wang et al., 2016; Zhu et al., 2012). Typical Raman spectra are shown in Figure 5.30(b), showing an ideal shape for $\text{K}_{0.5}\text{Na}_{0.5}\text{TiO}_3$ phase, consistent with the existence of $\text{K}_{0.5}\text{Na}_{0.5}\text{TiO}_3$ phase as shown by stating in the XRD patterns (Figure 5.28(b)).

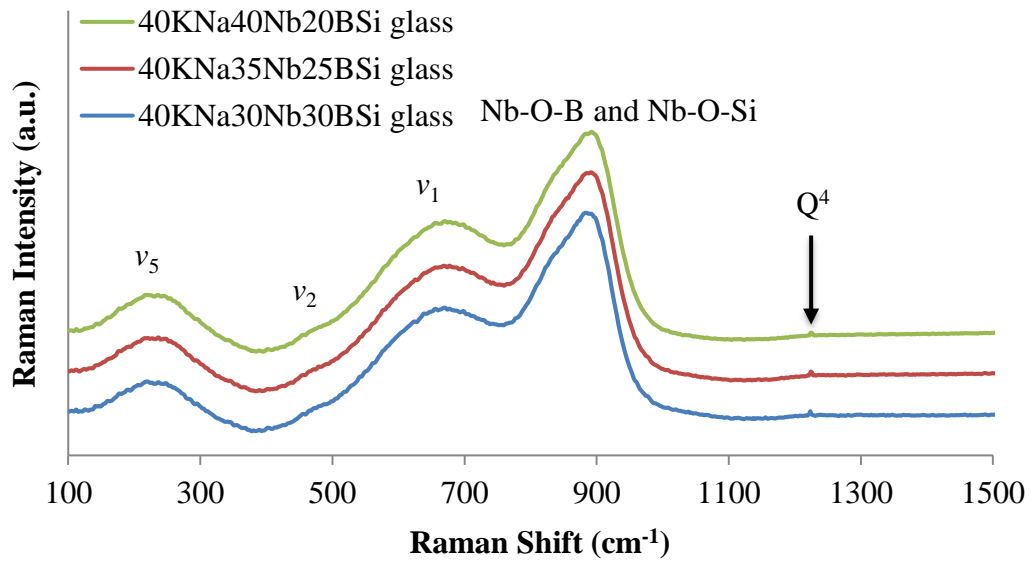


Figure 5.29. Raman spectra for KNN borosilicate glass compositions.

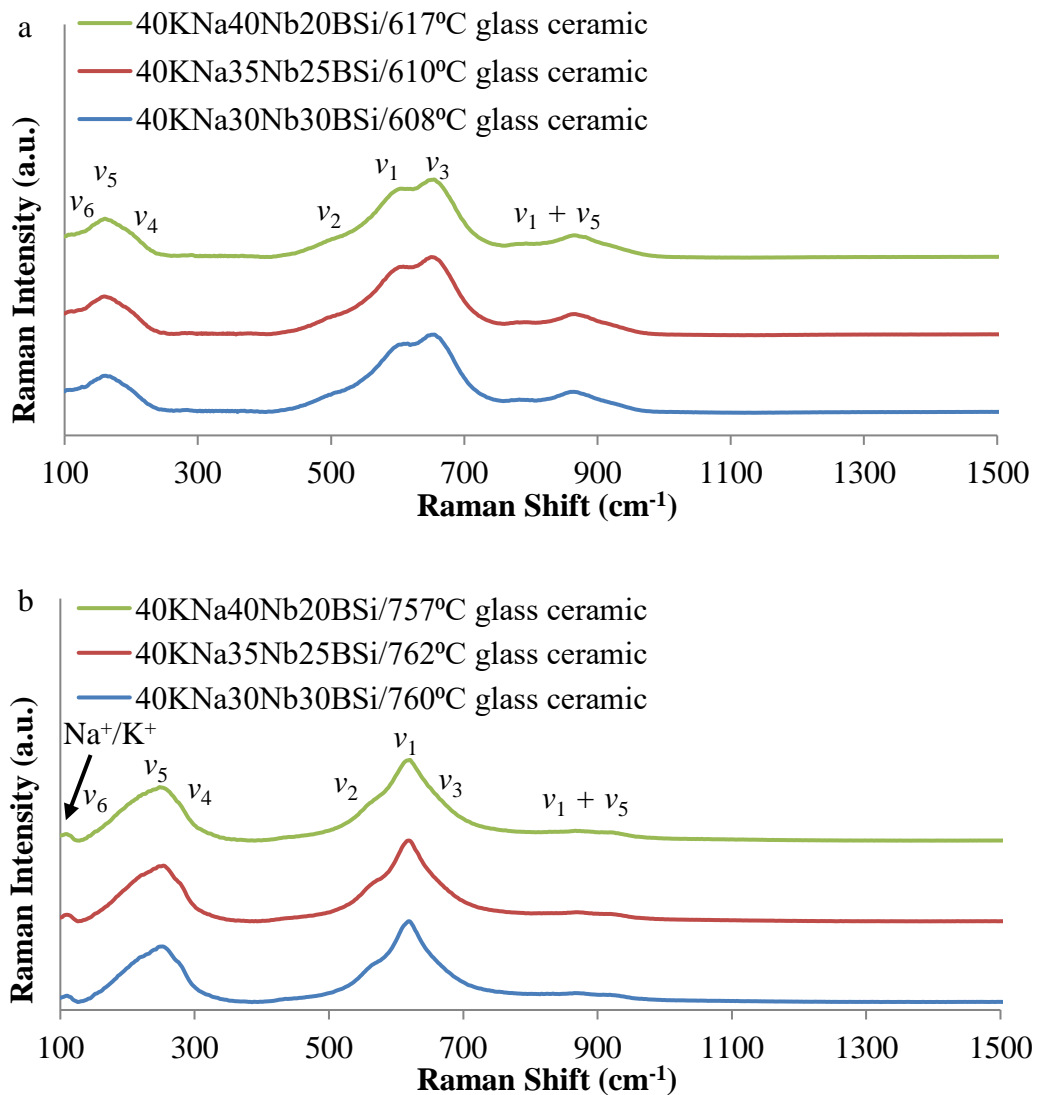


Figure 5.30. Raman spectra for KNN borosilicate glass-ceramic compositions heat treated at (a) T_{C1} and (b) T_{C2} , for 7.30 h.

5.2.3.4.1.4. Electron Microscopy

Figure 5.31 shows secondary SEM micrographs for KNN borosilicate glasses and glass-ceramics analysed at room temperature with 4,000x magnification and 50 μm scales. Flat surface with no grains appeared for KNN borosilicate glasses; on the other hand, grains were detected on the surface of KNN borosilicate glass-ceramics, as shown.

The microstructure of KNN borosilicate glasses was studied under the Scanning Electron Microscope (SEM), and selected micrographs are shown in Figure 5.31. The absence of grains or grain-boundaries on the glass surface of the three glass samples are consistent with the amorphous nature of the samples before heat treatment and agree with the XRD (Figure 5.27) and Raman (Figure 5.29) data. In contrast, many crystallites appear on the surface of heat treated KNN borosilicate glass-ceramic samples. Inhomogeneous grains, mostly in cubic-like shape with sizes ranging from 6.8 μm to 260 nm formed on the surface of the samples heat treated at T_{C1} . Inhomogeneous finer grains, again mostly of cubic-like shape, with sizes ranging from 1.1 μm to 100 nm were identified on the surface of the samples heat treated at T_{C2} . The micrographs confirm the successful crystallisation and formation of KNN borosilicate glass ceramics in agreement with XRD (Figure 5.28(a and b)) and Raman results (Figure 5.30(a and b)). The selected heat treatment temperature, chosen in accordance with the crystallisation peaks determined by DTA (Figure 5.26) affected the grain sizes of the crystals that formed. Larger grains formed when heat treated at the lower T_{C1} temperature, while smaller grains formed after heat treatment of the glasses at the higher T_{C2} temperature.

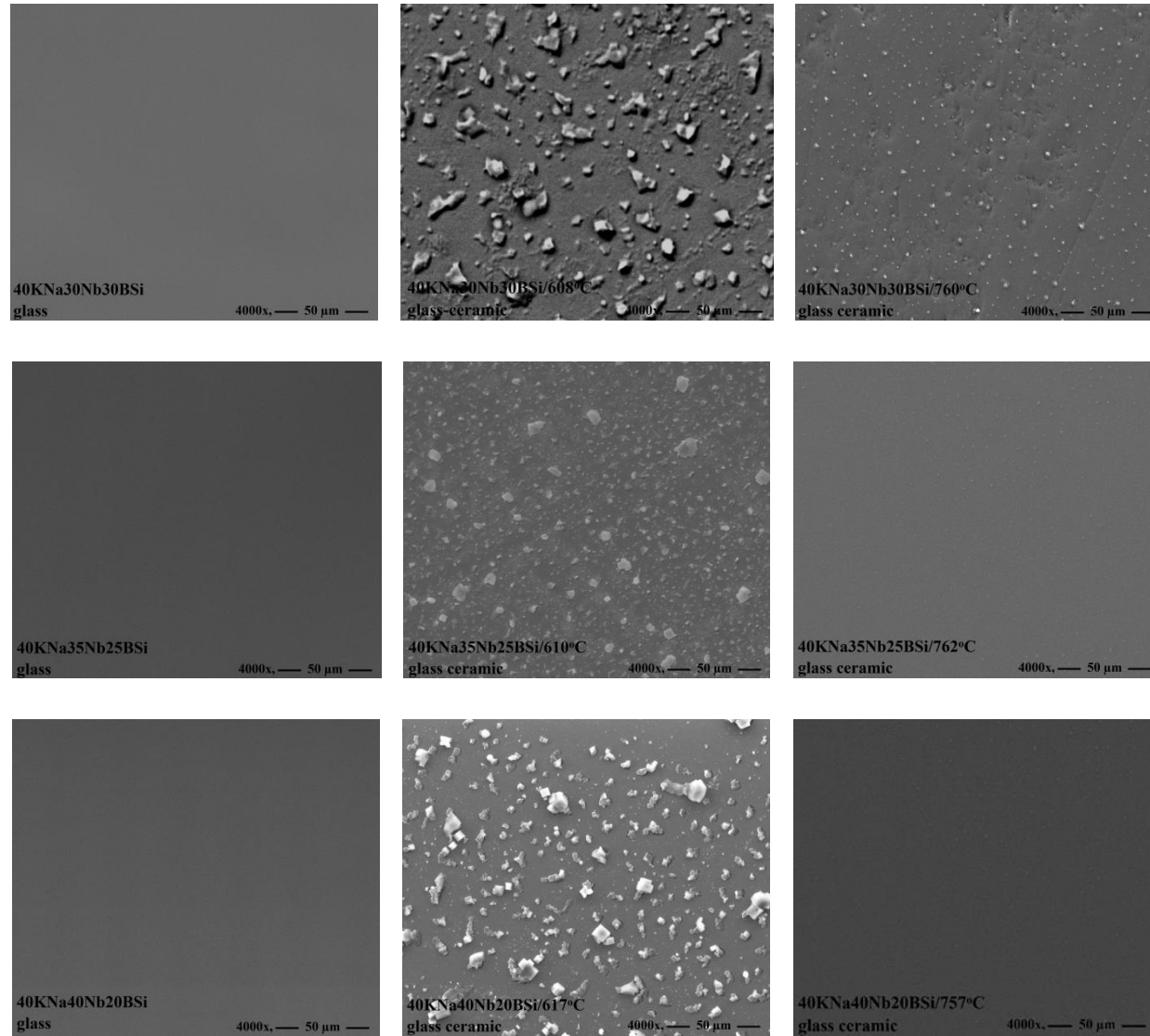


Figure 5.31. SEM images of KNN borosilicate glasses and glass ceramics.

5.2.3.4.1.5. Density

Table 5.5 shows the dependence of bulk densities of potassium sodium niobium borosilicate glasses and glass-ceramics as a function of composition. As can be seen, the minimum bulk density of 3.15 g/cm³ of 40KNa30Nb30BSi glass and maximum of 3.75 g/cm³ of 40KNa40Nb20BSi/757°C glass- ceramic.

As shown in the Table 5.5, the bulk density of 40KNa30Nb30BSi, 40KNa35Nb25BSi and 40KNa40Nb20BSi glasses increased gradually from 3.15 to 3.43 g/cm³ with increasing the amount of Nb₂O₅ from 30 to 40mol%, respectively. The increase in bulk density is due to the higher molecular weight of Nb₂O₅ (265.81 gm/mol) compared to SiO₂ (60.09 gm/mol) and B₂O₃ (69.62 gm/mol). The bulk density has lower values for KNN borosilicate glasses compared to the more dense KNN borosilicate glass ceramics, reaching a maximum bulk density of 3.75 g/cm³ for the 40KNa40Nb20BSi/757°C glass-ceramic. It is generally observed that crystals with their highly ordered structure have a higher density than disordered glasses (Das et al., 2017; Kioka et al., 2011b). As apparent from the SEM micrograph (Figure 5.30) and XRD (Figure 5.27(b)), the formation of crystals on the surface of 40KNa40Nb20BSi/757°C glass ceramic, has affected density increasing (Yongsiri et al., 2012).

Table 5.5. Bulk density results for potassium sodium niobium borosilicate glasses and glass ceramics.

Sample Name	Bulk density (g/cm ³)
40KNa30Nb30BSi glass	3.15±0.1
40KNa35Nb25BSi glass	3.31±0.1
40KNa40Nb20BSi glass	3.43±0.1
40KNa30Nb30BSi/608°C glass ceramic	3.24±0.1
40KNa30Nb30BSi/760°C glass ceramic	3.46±0.1
40KNa35Nb25BSi/610°C glass ceramic	3.38±0.1
40KNa35Nb25BSi/762°C glass ceramic	3.58±0.1
40KNa40Nb20BSi/617°C glass ceramic	3.51±0.1
40KNa40Nb20BSi/757°C glass ceramic	3.75±0.1

5.2.3.4.1.6. Electrical Properties

Figure 5.32 shows the polarisation versus applied electric field (P-E) hysteresis loops measured at room temperature, and 1Hz frequency applied. Unsaturated and pinched hysteresis loops are observed for KNN borosilicate glass-ceramics heat treated at T_{C2} .

The P-E hysteresis loops presented slimmed loop may be corresponding to a linear dielectric property. The tendency of polarisation against the electric field is characterised by the formation of non-ferroelectric $K_{0.5}Na_{0.5}NbO_3$ (anorthic) phase during the crystallisation of KNN borosilicate glass-ceramics. The remnant polarisation increased from 0.19 to 0.39 $\mu C/cm^2$ with increasing Nb_2O_5 from 30 to 40mol% and reducing $SiO_2+B_2O_3$ from 30 to 20mol%, respectively. The absence of a typical ferroelectric P-E loop shape could be due to the presence of residual glasses or secondary non-ferroelectric phases ($K_{5.75}Nb_{10.85}O_{30}$) or anorthic $K_{0.5}Na_{0.5}NbO_3$ phase at room temperature.

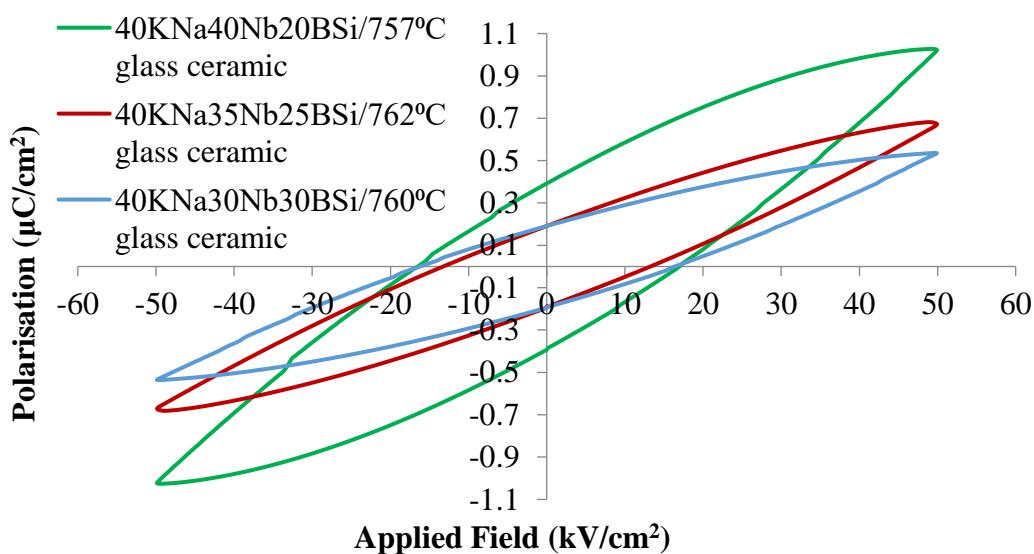


Figure 5.32. Hysteresis (P-E) loops of KNN borosilicate glass-ceramic compositions heat processed at T_{C2} , for 7.30 h measured at room temperature and 10Hz frequency.

5.2.3.5. Potassium Sodium Niobium Borosilicate Glass-Ceramic Fibres

5.2.3.5.1. Results and Discussion

5.2.3.5.1.1. DTA

Figure 5.33 displays DTA traces of potassium sodium niobium borosilicate glasses. DTA analysis has been used to estimate exothermic peaks indicating the crystallization temperatures (T_C), and has exhibited two crystallization temperatures.

DTA is the main technique has been used to identify the crystallization temperature (T_C) through determining of exothermic peaks. In the present work, DTA has been used to analyse the exothermic peaks of KNNBSi glasses, in order to prepare KNNBSi glass-ceramics fibres through heat treating KNNBSi glass fibres at for a T_C period of time. The DTA curve for KNNBSi glasses (Figure 5.33) detected two important crystallization peaks for each of the three prepared KNNBSi glasses. T_{C1} refers to lower crystallization temperature and T_{C2} refers to higher crystallization temperature of each specific glass composition in the DTA curve.

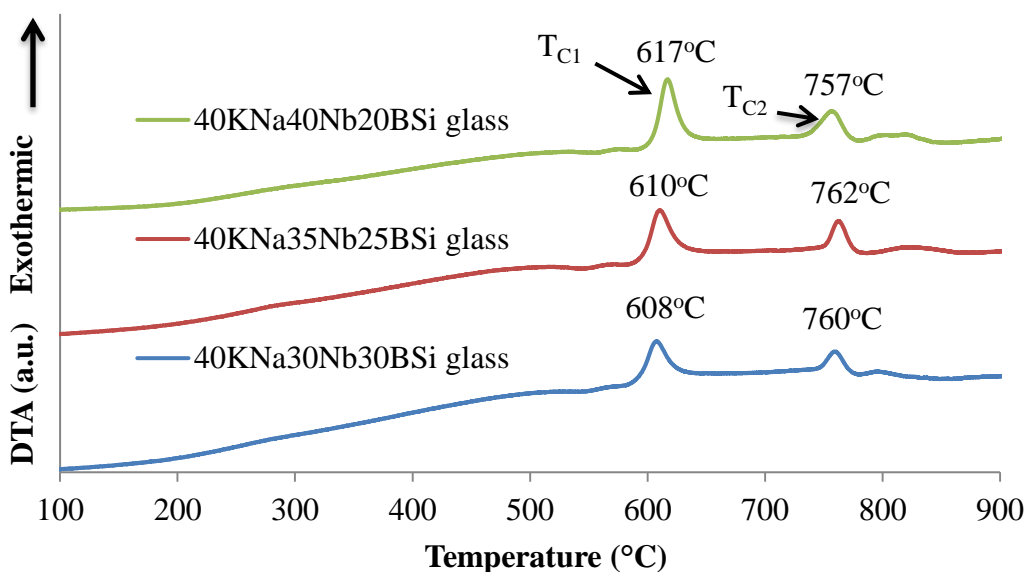


Figure 5.33. DTA results for KNN borosilicate glass compositions.

5.2.3.5.1.2. XRD

Figure 5.34 and Figure 5.35 show XRD patterns for potassium sodium niobium borosilicate (KNNBSi) glass and glass-ceramic fibres, respectively. XRD patterns in Figure 5.34 display weak and broad humps for all KNNBSi glass fibres. However, Figure 5.35 shows sharp peaks for all KNNBSi glass-ceramic fibres. XRD confirms that all untreated glass fibres were X-ray amorphous.

XRD results for all KNNBSi glass fibres are shown in Figure 5.34, showing weak, broad humps with no presence of any sharp peaks indicating an X-ray amorphous material (Das et al., 2017; Hao & Dai, 2017; Samudrala et al., 2018). However, as can be seen in Figure 5.35, sharp peaks are presented by XRD results of glass fibres heat treated at T_{C1} and T_{C2} , which confirms the successful formation of glass-ceramic fibres

(Bouchouicha et al., 2016). The NaNb_3O_8 phase fitted to ICDD no 01-078-2007 (Figure 5.35(a)) was obtained by heat treatment at lower crystallization temperature (T_{C1}), referring to the higher crystallization tendency of the sodium and niobium oxides rather than potassium oxide during heat treatment at T_{C1} of glass fibres (Hmood et al., 2015; Trégouët et al., 2017). The main $\text{K}_{0.5}\text{Na}_{0.5}\text{NbO}_3$ crystalline phase fitted to ICDD no 04-016-7531 was successfully produced during heat treatment at the higher crystallisation T_{C2} temperature, which is stated to be a non-ferroelectric anorthic crystalline structure at room temperature. However, the secondary phase ($\text{K}_{5.75}\text{Nb}_{10.85}\text{O}_{30}$) fitted to ICDD no 00-038-0297 was developed with the main KNN phase at T_{C2} for all KNN borosilicate glass-ceramic fibres, as revealed in Figure 5.35(b) (Yongsiri, Sirisoonthorn, & Pengpat, 2015). The presence of $\text{K}_{5.75}\text{Nb}_{10.85}\text{O}_{30}$ phase could be produced from the high evaporation of alkali sodium oxide during melt processing (Ramajo et al., 2014).

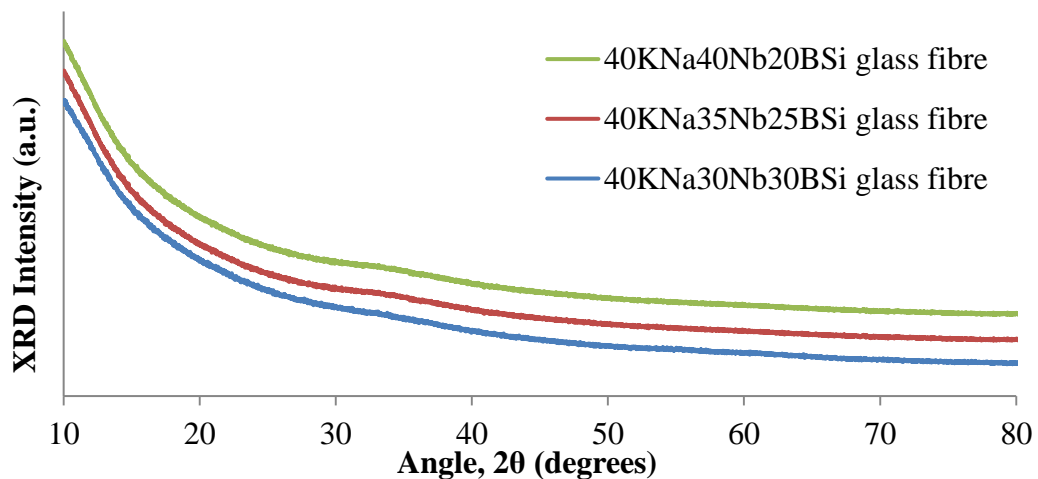


Figure 5. 34. XRD patterns for KNN borosilicate glass compositions.

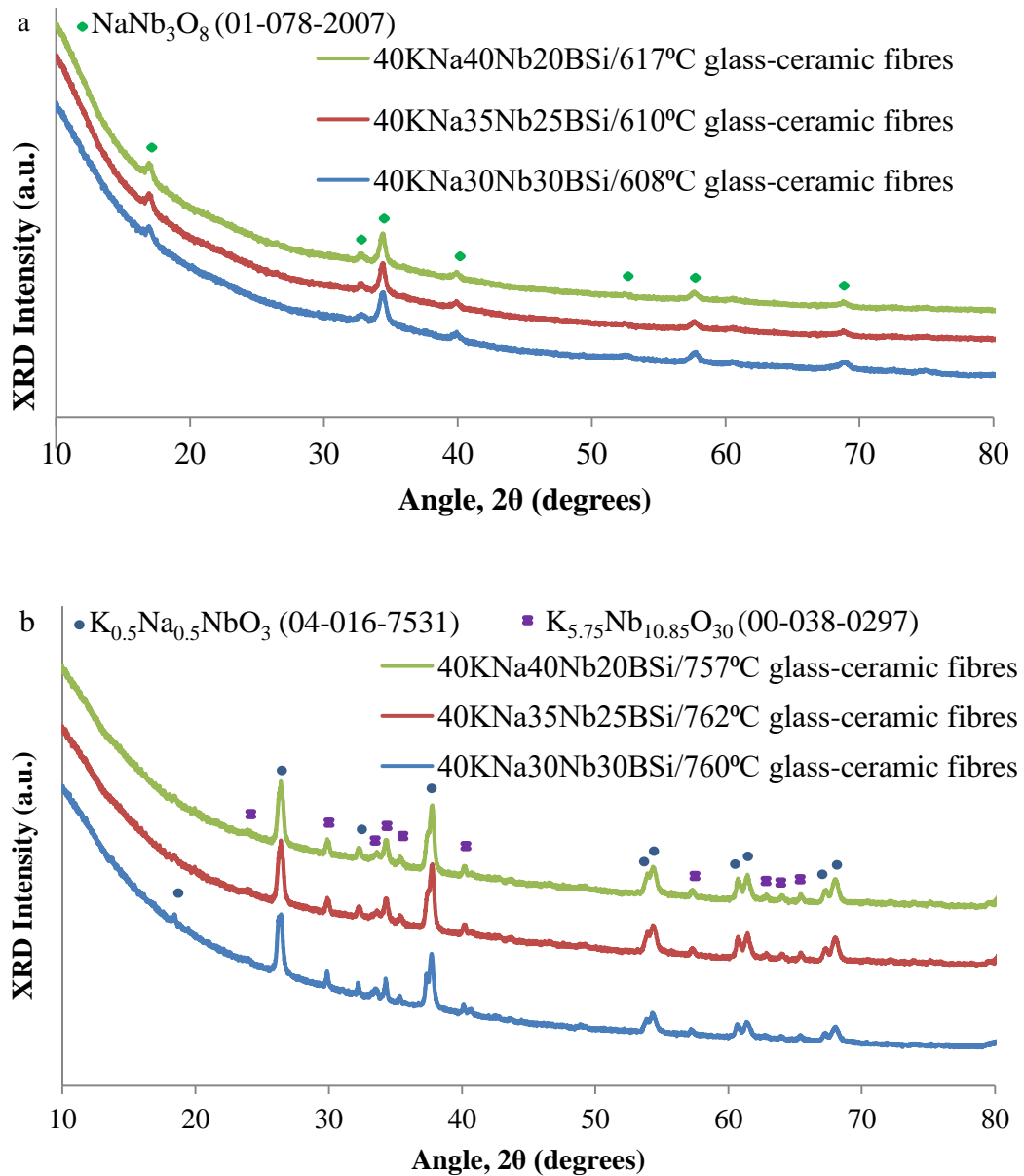


Figure 5.35. XRD patterns for KNN borosilicate glass-ceramic compositions heat treated at (a) T_{C1} and (b) T_{C2} , for 7.30 h.

5.2.3.5.1.3. Raman Spectroscopy

Figure 5.36 and Figure 5.37 show Raman spectra for potassium sodium niobium borosilicate (KNNBSi) glass and glass-ceramic fibres, respectively. Raman results show broad bands for all KNNBSi glass fibres, as shown in Figure 5.36. On the other hand, Raman results detected sharp peaks of all KNNBSi glass-ceramic fibres, as shown in Figure 5.37.

Raman spectra of all KNNB borosilicate glass and glass-ceramic fibres have been measured at room temperature at Raman shifts of 100-1500 cm^{-1} . As can be seen from

Figure 5.36, each Raman spectrum shows three broad peaks and one sharp peak. The first and second broad peaks in the region $100\text{-}750\text{ cm}^{-1}$ assigned as ν_1 , ν_2 and ν_5 appeared as vibrational modes, identified as NbO_6 octahedra (Kioka et al., 2011b). The third broad, strongest band and vibration stretching mode, is placed in the region $750\text{-}1000\text{ cm}^{-1}$ and is assigned to dominant Nb-O-B and Nb-O-Si bands, due to higher polarizability of Nb^{5+} (0.262\AA^3) than B^{3+} (0.003\AA^3) and Si^{4+} (0.033\AA^3) (Dimitrov & Komatsu, 2010; Möncke et al., 2017). The sharp peak identified at 1005 cm^{-1} could be potentially Si allocated as Q^3 species (Manara et al., 2009). The heat treatment of KNN borosilicate glass fibres has considerably affected the third peak intensity at $750\text{-}1000\text{ cm}^{-1}$ Raman shift, showing a weak peak (Figure 5.37) in the Raman spectra of KNN borosilicate glass-ceramic fibres, compared with strongest peak (Figure 5.36) in Raman spectra of KNN borosilicate glass fibres. In addition, the fourth sharp peak appeared at above 1000 cm^{-1} Raman shift in the Raman spectra of KNN borosilicate glass fibres (Figure 5.35) has disappeared after heat treatment (Figure 5.37). It can be seen in Figure 5.37, the Raman spectra present eight peaks of KNN borosilicate glass-ceramics fibres. Peaks marked as ν_1 to ν_5 is corresponding to the NbO_6 octahedron (Kioka et al., 2011b), where peaks marked as ν_1 to ν_3 show vibrational stretching modes, but peaks marked as ν_4 to ν_6 present vibrational bending modes (Wang et al., 2016; Wu et al., 2014). A shoulder marked as a ν_6 place less than 200 cm^{-1} Raman shift could be identified as a translational mode of K^+ cation and rotations of the NbO_6 octahedron, as well as the weak peak places at 135 cm^{-1} Raman shift could be identified as Na^+/K^+ cations versus NbO_6 octahedron. The splitting weak peak allocated at 750 and 1000 cm^{-1} Raman shift could be assigned as association of ν_1 and ν_5 corresponding to the octahedral NbO_6 , the reason of splitting may be due to the substitution of SiO_2 and B_2O_3 in the same site of Nb_2O_5 (Singh et al., 2013; Wang et al., 2016; Zhu et al., 2012). The typical Raman spectra are shown in Figure 5.37(b), referring to the presence $\text{K}_{0.5}\text{Na}_{0.5}\text{TiO}_3$ phase, demonstrating existence $\text{K}_{0.5}\text{Na}_{0.5}\text{TiO}_3$ phase that stating in the XRD results (Figure 5.35(b)).

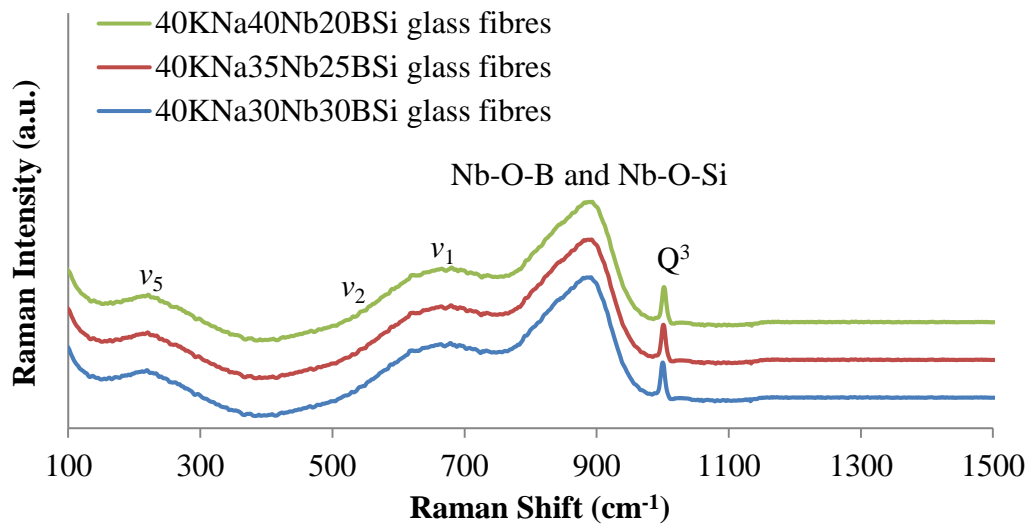


Figure 5.36. Raman results of KNN borosilicate glass compositions.

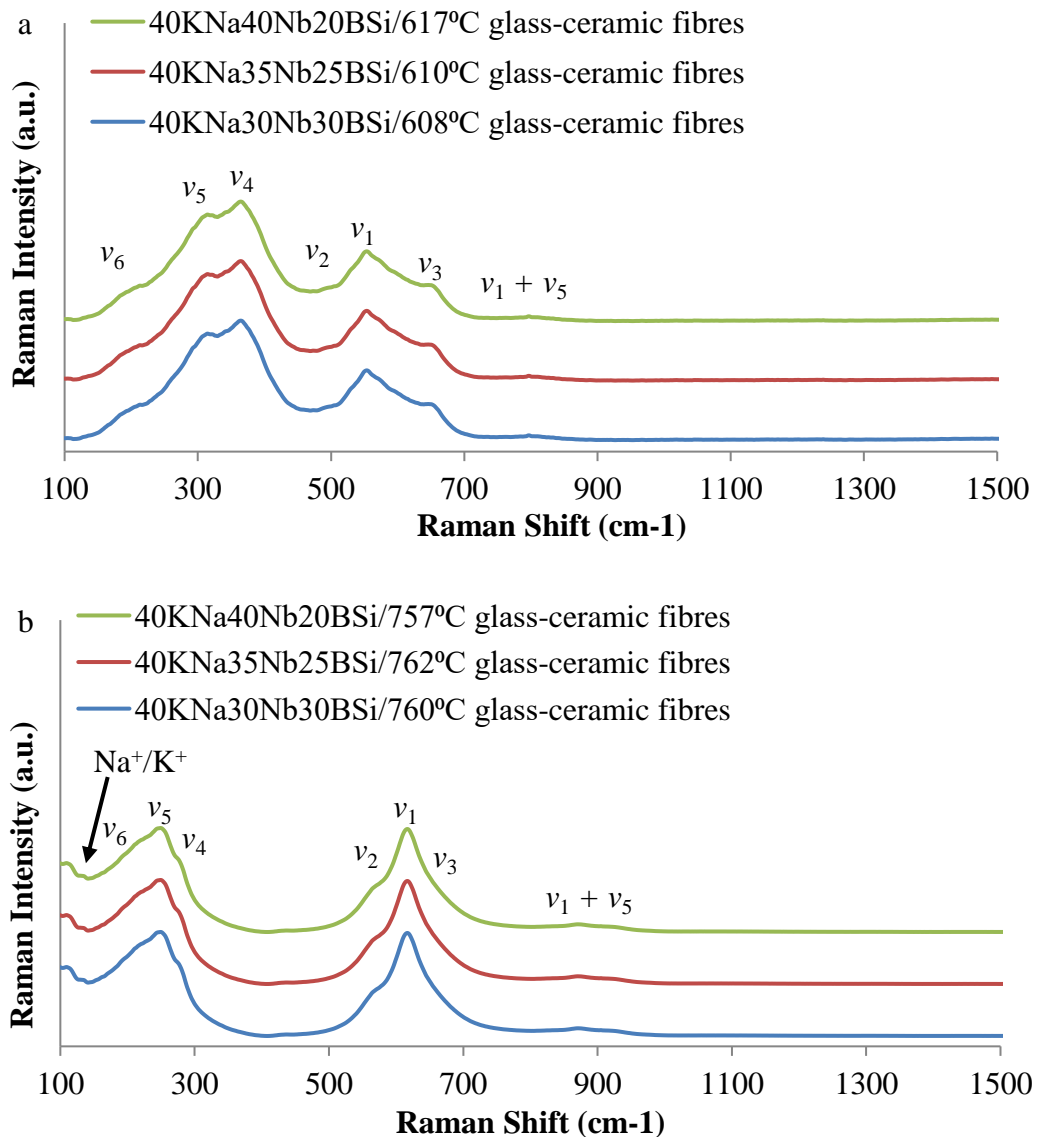


Figure 5.37. Raman results of KNN borosilicate glass-ceramic compositions heat treated at (a) T_{C1} and (b) T_{C2} , for 7.30 h period, as shown above.

5.2.3.5.1.4. Electron Microscopy

Figure 5.38 displays secondary SEM micrographs for KNN borosilicate glass and glass-ceramic fibres investigated at room temperature with 500x magnification and 300 μm scales.

The surface morphology of KNN borosilicate glass and glass-ceramic fibres was investigated under the Scanning Electron Microscope (SEM), as shown in Figure 5.38. Flat and shiny surfaces were shown for all KNN borosilicate glass fibres. However, the surface of heat treated glass-ceramic fibres shows the formation of white dust and tends to be rough and opaque surface, indicating partly or completely crystallised of KNN borosilicate glass-ceramic fibres.

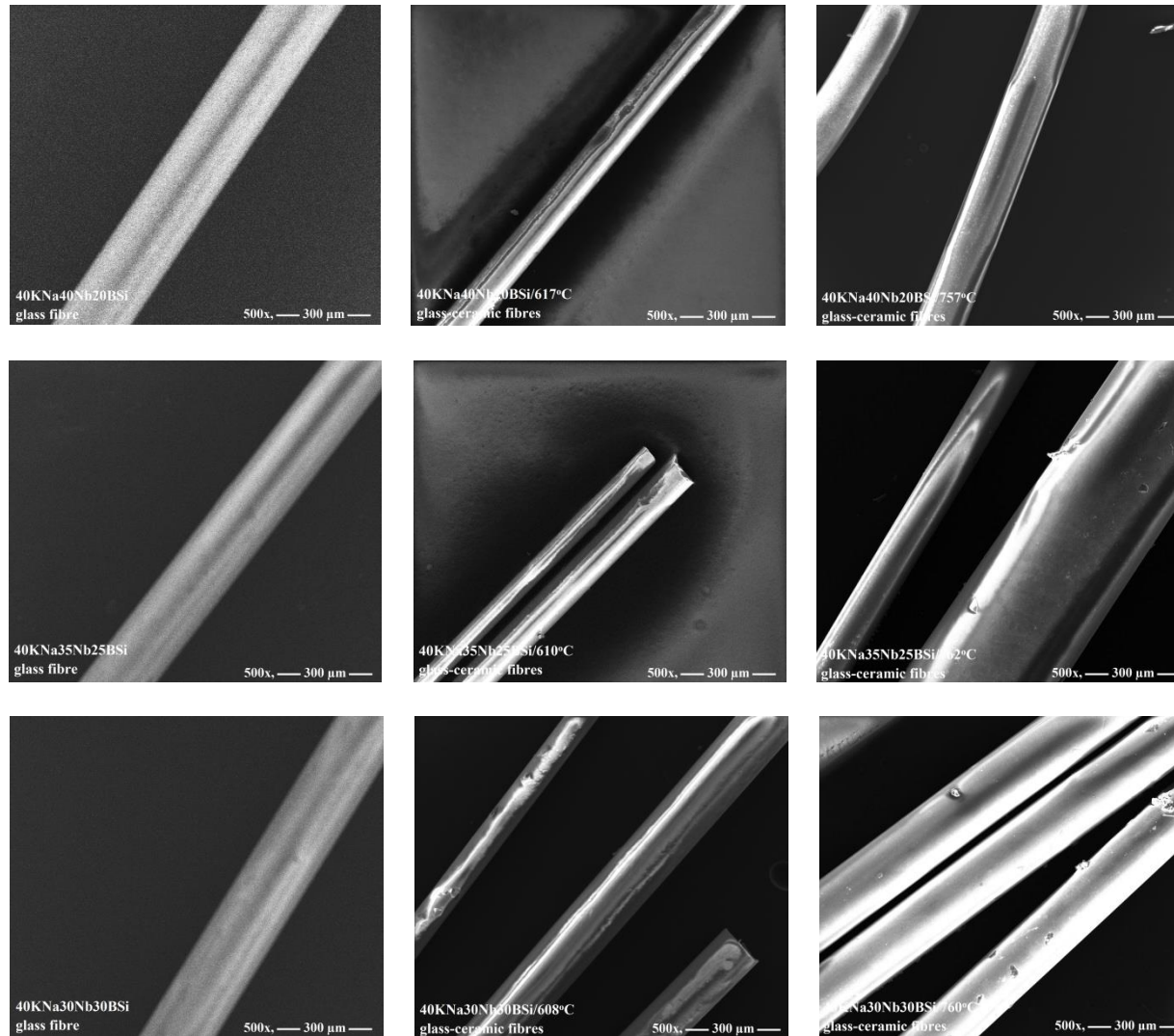


Figure 5.38. Secondary SEM images of KNN borosilicate glasses and glass ceramics, as shown above.

5.3. Iron-Doped Potassium Sodium Niobate Ceramics

5.3.1. Solid State Processing Route

5.3.1.1. Results and Discussion

5.3.1.1.1. XRD

Figure 5.39 shows diffraction patterns for all iron-doped KNN ceramics measured at room temperature with 2θ ranged from 10 to 80°. Phase analysis identified single phase $K_{0.5}Na_{0.5}NbO_3$ (04-017-0216) for 2mol% iron doped KNN ceramics; however it is detected three phases are $K_{0.5}Na_{0.5}NbO_3$ (04-017-0216), K_2FeO_4 (00-025-0652) and Fe_2O_3 (032-0469) for 2.5-10mol% iron doped KNN ceramics.

A homogeneous solid solution of KNN ceramics has achieved according to the splitting peak to two peaks that specified in between 45 and 47 (XRD angle, 2θ), as presented in Figure 5.39 and stated by Rani and group (Rani et al., 2012) and Chaiyo and group (Chaiyo et al., 2009), as well as by referring to the indicated splitting can show the orthorhombic structure as reported by Ramajo and group (Ramajo et al., 2014), indicating to the orthorhombic structure at room temperature.

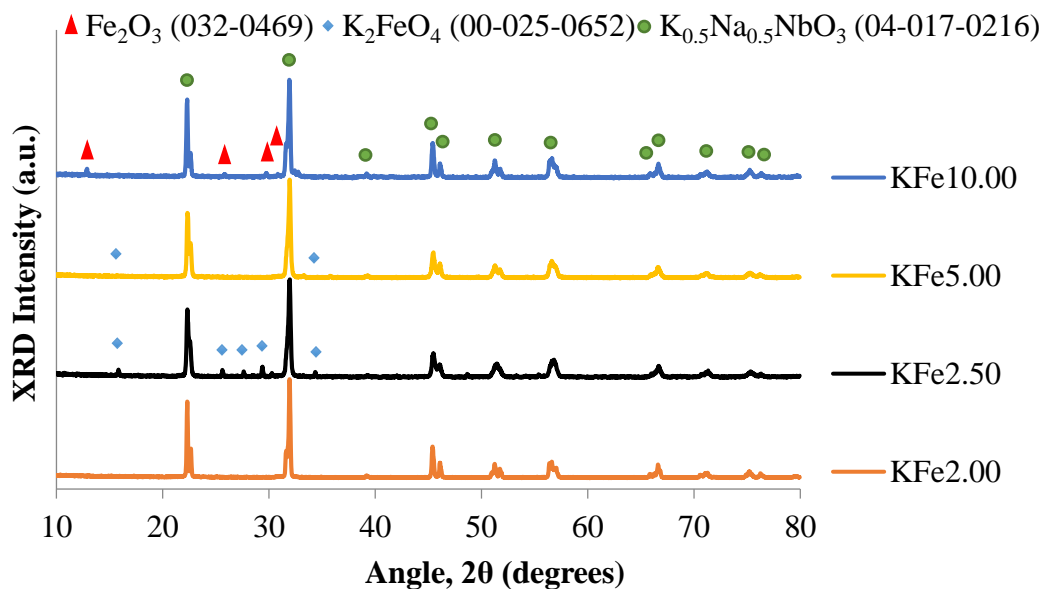


Figure 5.39. X-Ray diffraction patterns for solid-state sintered $K_{0.5}Na_{0.5}Nb_{1-x}Fe_xO_{3-x}$ ceramics ($x = 0.020-0.100$).

5.3.1.1.2. Raman Spectroscopy

Figure 5.40 shows Raman spectra for iron doped KNN ceramics analysed at room temperature with Raman shift from 100 to 1000 cm^{-1} . Raman spectra show four regions with eight bands for all KNN ceramic samples.

Raman spectra exhibited three strong regions between 150 and 1000 cm^{-1} Raman shift and one weak peak between 100 and 150 cm^{-1} Raman shift, where measured at room temperature, for all solid-state sintered Fe-KNN ceramic samples, as shown in Figure 5.40. The strong regions contain sharp peaks that marked as ν_1 to ν_6 , which display vibrational modes fitting to the NbO_6 octahedron. It is clearly seen that, the vibrational stretching modes are located at high Raman shift, such that region situated between 300 and 800 cm^{-1} Raman shift by corresponding to ν_1 to ν_3 modes, on the other hand, the vibrational bending modes are placed at low Raman shift, for example set that region between 150 and 300 cm^{-1} Raman shift by indicating to ν_4 to ν_6 modes (Wang et al., 2016; Wu et al., 2014). An orthorhombic phase has demonstrated through a shoulder observed between ν_1 and ν_2 vibrational modes (Yan et al., 2018). A translational mode of K^+ cation and rotations of the NbO_6 octahedron could be assigned at lower energy (less than 200 cm^{-1} Raman shift), which is located at a ν_6 vibrational mode that placed on the beginning of shoulder underneath ν_5 vibrational mode (Singh et al., 2013). The weak peak formed between 100 and 150 cm^{-1} Raman shift could be indicated to the Na^+/K^+ cations versus rotation NbO_6 octahedron (Liu et al., 2013). The present Raman spectra show the absence of cubic phase for iron modified KNN perovskite structure due to the formation a peak that located between 800 and 900 cm^{-1} Raman shift, which is assigned an association of ν_1 and ν_5 (Nb_2O_5) vibrational modes (Chen et al., 2018; Yan et al., 2018).

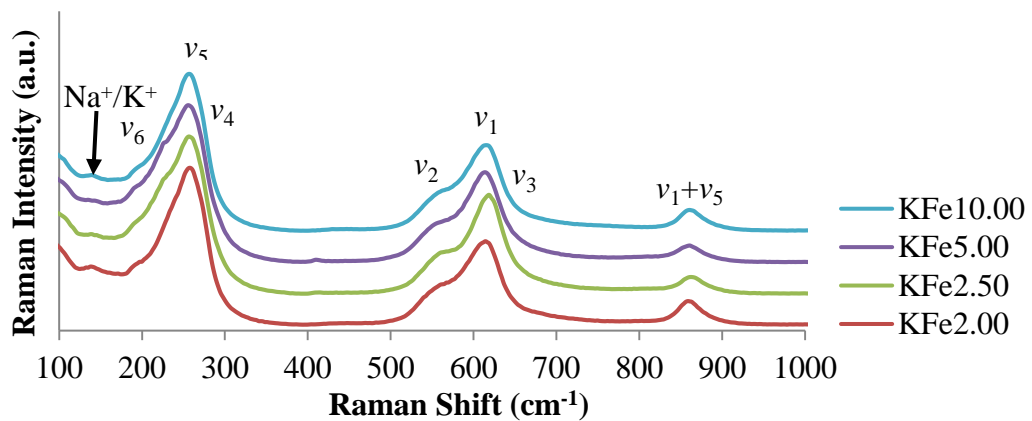


Figure 5.40. Raman spectra for solid-state sintered $\text{K}_{0.5}\text{Na}_{0.5}\text{Nb}_{1-x}\text{Fe}_x\text{O}_{3-x}$ ceramics ($x = 0.020-0.100$).

5.3.1.1.3. Density

Bulk and relative density results for pure and iron modified KNN ceramics are presented in Table 5.9.

The relative density results display increasing the relative density with increasing iron oxide content for iron doped KNN ceramics prepared by solid-state sintering processing, as shown in Table 5.9. Lower relative density (73%) occurred 2mol%Fe doped KNN ceramics, and then increased reaching a value of about 86% relative density for 10mol% Fe-KNN ceramic.

Table 5.6. Relative density for solid-state sintered $\text{Bi}_{0.5}\text{Na}_{0.5}\text{Ti}_{1-x}\text{Fe}_x\text{O}_{3-x}$ ceramics ($x = 0.000-0.100$).

Sample Names	Bulk density (g/cm^3)	Relative Density (%)
KFe0.00	3.30	73.4
KFe2.00	3.34	74.2
KFe2.50	3.42	76.2
KFe5.00	3.67	81.4
KFe10.00	3.89	86.1

5.4. Conclusions

Pure potassium sodium niobate (KNN) ceramics were successfully manufactured using solid state and microwave sintering processing routes. However it was challenging to produce single phase KNN glass-ceramics using melt processing route, due to only partial crystallisation of all glassy silicate samples. The relative density displays maximum value of 91.2% of the theoretical density for solid-state sintered KNN ceramics, in comparison with these of 90.6% of the theoretical density for pure microwave sintered KNN ceramics. However, the bulk density increased with increasing K_2O , Na_2O and Nb_2O_5 contents with reducing SiO_2 . SEM imaging exhibited enhancing densification of ceramic specimens during increasing the sintering temperatures (solid-state sintering processing) and microwave sintering time (microwave sintering one), also, showing a higher average of grain sizes of ca 5 μm and 3 μm for solid-state sintering and microwave sintering processing routes, respectively. SEM imaging showed the presence of grains on the surfaces of KNN silicate glassy

samples indicating to the crystallisation of samples. The saturated hysteresis (P-E) loops were observed at higher sintering temperature (1100°C, solid-state sintering processing) and time (25 mins, microwave sintering processing), with lower remnant polarization of $17 \mu\text{C}/\text{cm}^2$ stated for microwave sintered KNN (MKK700, 25) ceramics than $33 \mu\text{C}/\text{cm}^2$ identified for solid-state sintered KNN (K700, 1100) ceramics. The butterfly S-E loops shape have introduced at higher sintering temperatures (1075-1100°C, solid-state sintering processing) and time (25 mins, microwave sintering processing), and strain% of ca 7.5 % stated for microwave sintered KNN (MKK700, 25) ceramics then of 6% exhibited for solid-state sintered KNN (K700, 1100) ceramics.

Potassium sodium niobium borosilicate glass and glass-ceramic fibres have successfully produced using novel melt processing. XRD results showed the completely amorphous phase of all KNN borosilicate glass fibres. However they show crystalline phases including $\text{K}_{0.5}\text{Na}_{0.5}\text{NbO}_3$, NaNb_3O_8 and $\text{K}_{5.75}\text{Nb}_{10.85}\text{O}_{30}$ of heat treated KNNBSi glass-ceramic fibres. Raman spectra exhibit broad band for glass fibres and sharp peaks indicating to the crystallinity for glass-ceramic fibres. SEM results show shiny and flat surface for KNNBSi glass fibres and formation of white places with the rough and opaque surface for KNNBSi glass-ceramic fibres.

Iron-doped KNN ceramics were prepared by solid-state sintering. A single $\text{K}_{0.5}\text{Na}_{0.5}\text{NbO}_3$ phase was obtained for only one iron-doped sample, $\text{K}_{0.5}\text{Na}_{0.5}\text{Nb}_{0.98}\text{Fe}_{0.02}\text{O}_{2.98}$. Adding iron to KNN ceramics increased the relative density from 73% of the theoretical density for undoped KNN ceramics to 86% of the theoretical density for $\text{K}_{0.5}\text{Na}_{0.5}\text{Nb}_{0.9}\text{Fe}_{0.1}\text{O}_{2.9}$.

Chapter Six

Conclusions and Future Work

Chapter eight considers conclusions and future work for present research work.

6.1. Conclusions

In the present project, microwave sintering processing has been used to enable sintering of ceramics in short times and with low energy consumption, aimed at solving problems with interrupted electricity supplies in many countries including the author's home country, Iraq. Ceramics produced using this novel processing method have shown comparable properties with those prepared using conventional solid-state sintering processing.

In the present project, pure bismuth sodium titanate (BNT) ceramics have been prepared by three processing routes: solid-state sintering, microwave sintering and melt processing. Single phase $\text{Bi}_{0.5}\text{Na}_{0.5}\text{TiO}_3$ ceramics were successfully produced using solid-state and microwave sintering processing routes, whilst a $\text{Ti}_2\text{Bi}_2\text{O}_7$ phase was produced by the melt processing route. A maximum relative density of 94.6% of the theoretical density was obtained for pure BNT ceramics manufactured by solid-state sintering. SEM micrographs exhibited increasing densification and increasing the average grain size of ceramic pellets with increasing sintering temperatures (solid-state sintering processing) and microwave sintering time (microwave sintering one). Higher average grain size of ca 2 μm was obtained for solid-state sintered BNT ceramics sintered at 1100°C, in comparison with the lower average grain size of 900 nm for microwave sintering BNT ceramics, sintered per 25 mins. However, SEM micrographs showed the presence of grains on the surface of BNT silicate glasses indicating crystallisation of samples. Ferroelectric behaviour was successfully produced for pure BNT ceramics sintered at 1075-1100°C, solid-state sintering processing and higher microwave sintering time (25 mins). A higher remnant polarisation of 42.2 $\mu\text{C}/\text{cm}^2$ was obtained microwave sintered BNT (sample MKB700, 25) ceramics, compared with 40 $\mu\text{C}/\text{cm}^2$ identified for solid-state sintered BNT (sample B700, 1100). The butterfly S-E loops shapes were obtained for pure BNT ceramics sintered at 1050-1100°C, solid-state sintering processing, and higher microwave sintering time (25 mins). A maximum strain of about 0.083% presented for microwave sintered BNT (sample MKB700, 25)

ceramics, compared with 0.08% presented for solid-state sintered BNT (sample B700, 1100) ceramics.

$\text{Bi}_{0.5}\text{Na}_{0.5}\text{Ti}_{1-x}\text{Fe}_x\text{O}_{3-0.5x}$ ceramics were prepared by two processing routes, solid-state sintering and microwave sintering, where x ranged from 0.0 to 0.1. Adding iron to the BNT ceramics enhanced the densification to up to 97% of relative density at lower sintering temperatures of 900°C and microwave sintering times of 20 mins. XRD patterns presented single phase $\text{Bi}_{0.5}\text{Na}_{0.5}\text{TiO}_3$ ceramics for all studied Fe dopant levels. SEM imaging showed increasing average grain size with increasing iron concentration, to reach a maximum average grain size of 4 μm for $\text{Bi}_{0.5}\text{Na}_{0.5}\text{Ti}_{0.9}\text{Fe}_{0.1}\text{O}_{2.95}$. However, slimmed P-E hysteresis loops indicating relaxor behaviour were presented for all studied iron doped BNT ceramics.

Pure potassium sodium niobate (KNN) ceramics have been produced by three processing routes, solid-state sintering, microwave sintering and melt processing. Pure phase $\text{K}_{0.5}\text{Na}_{0.5}\text{NbO}_3$ ceramic was successfully produced using solid-state and microwave sintering processing routes. On the other hand, the main $\text{K}_{0.5}\text{Na}_{0.5}\text{NbO}_3$ phase and additional $\text{K}_{5.75}\text{Nb}_{10.85}\text{O}_{30}$ phase were obtained by heat treatment of KNN borate, KNN borosilicate glass-ceramics and KNN borosilicate glass-ceramic fibres manufactured by melt processing and heat treatment to form glass-ceramics. A maximum relative density of 91.2% of the theoretical density was achieved for pure KNN ceramics prepared by solid-state sintering. The bulk density increased with increasing K_2O , Na_2O and Nb_2O_5 contents and with reducing B_2O_3 and SiO_2 . SEM images present improving densification of ceramic pellets and increasing average grain size with increasing sintering temperature (solid-state sintering processing) and microwave sintering time (microwave sintering processing). The higher average grain size of ca 5 μm was occurred for solid-state sintered BNT ceramics sintered at 1100°C, in comparison with a lower average grain size of 3 μm for microwave sintering KNN ceramics sintered at 25 mins. SEM micrographs showed the presence of grains on microstructure surfaces of BNT silicate glasses, KNN borate and KNN borosilicate glass-ceramics, and the rough and opaque surface was obtained for KNN borosilicate glass-ceramic fibres, indicating crystallisation of samples. Ferroelectric behaviour was successfully obtained for pure KNN ceramics sintered at higher sintering temperatures (1100°C, solid-state sintering processing) and higher microwave sintering time (25 mins, microwave sintering processing). A higher remnant polarisation of 33 $\mu\text{C}/\text{cm}^2$ presented for solid-state sintered KNN (named as K700, 1100) ceramics, compared with 17

$\mu\text{C}/\text{cm}^2$ stated for microwave sintered KNN (named as MKK700, 25) ceramics. However, relaxor behaviour has obtained for KNN borate glass-ceramics and KNN borosilicate glass-ceramics. Butterfly S-E loops shapes were obtained for pure KNN ceramics sintered at 1075-1100°C, solid-state sintering processing and higher microwave sintering time (25 mins). A maximum strain of about 0.075% was obtained for microwave sintered KNN (named as MKB700, 25) ceramics, compared with 0.06% presented for solid-state sintered KNN (named as K700, 1100) ceramics.

$\text{Bi}_{0.5}\text{Na}_{0.5}\text{Nb}_{1-x}\text{Fe}_x\text{O}_{3-x}$ ceramics were manufactured by solid-state sintering. Pure perovskite $\text{K}_{0.5}\text{Na}_{0.5}\text{NbO}_3$ phase was obtained for only $\text{K}_{0.5}\text{Na}_{0.5}\text{Nb}_{0.98}\text{Fe}_{0.02}\text{O}_{2.98}$ ceramics. The relative density has increased with increasing iron doped content to reach a maximum value of 86% of the theoretical density for $\text{K}_{0.5}\text{Na}_{0.5}\text{Nb}_{0.9}\text{Fe}_{0.1}\text{O}_{2.9}$.

According to the main results and discussion above, longer sintering times and conductive heating for the ceramics produced using conventional solid-state sintering lead to increased average grain size, and reductions in residual porosity, that provide higher relative density for the resulting ceramics. XRD results show broad peaks for BNT ceramics prepared at lower sintering temperatures, which may be due to smaller crystallite sizes.

6.2. Future Work

Additional work is suggested in future to build on the work in this thesis, as follows:

1. Optimisation of microwave susceptor linings that can be placed inside a standard microwave oven to generate temperatures greater than approximately 1100°C within 20 mins or less heating time.
2. Optimisation the hysteresis P-E loops, strain vs electric field loops, relative density (densification) and single phase KNN and BNT ceramics by adding different dopants such as Dy_2O_3 , Er_2O_3 , Eu_2O_3 , Pr_6O_{11} , MnO_2 , TiO_2 , ZrO_2 and CuO for KNN and BNT ceramics using microwave sintering processing.
3. Measuring dielectric constant and dielectric loss factor over a range of temperatures above room temperature, with various applied frequencies for all electrical ceramics and glass-ceramics considered in the present project.
4. Develop more KNN glass compositions to try to obtain single-phase $\text{K}_{0.5}\text{Na}_{0.5}\text{NbO}_3$ glass-ceramics using the melt processing and heat treatment route.

5. XRD analyses for all KNN borate and KNN borosilicate glass samples at above room temperature to 1200°C to discover a single phase KNN with crystallisation temperature.
6. Further electrical, microstructure and physical measurements such as XRD, Raman spectroscopy, scan electron microscopy, bulk density, differential thermal analysis, dielectric constant and dielectric loss factor at room temperature for potassium niobium borate and bismuth sodium titanium glasses and glass-ceramics.

References

- Abdul Razak, K., Yip, C. J., & Sreekantan, S. (2011). Synthesis of $(\text{Bi}_{0.5}\text{Na}_{0.5})\text{TiO}_3$ (BNT) and Pr doped BNT using the soft combustion technique and its properties. *Journal of Alloys and Compounds*, 509(6), 2936-2941.
- Agrawal, D. (2010). Microwave sintering of ceramics, composites and metal powders. In *Sintering of advanced materials* (pp. 222-248). Woodhead Publishing.
- Aksel, E., Erdem, E., Jakes, P., Jones, J. L., & Eichel, R. (2010). Defect structure and materials “hardening” in Fe_2O_3 -doped $(\text{Bi}_{0.5}\text{Na}_{0.5})\text{TiO}_3$ ferroelectrics. *Applied Physic Letters*, 97(1), 012903.
- Alkathy, M. S., Gayam, R., Hazra, B. K., & Raju, K. C. J. (2017). Effect of sintering on structural and physical properties of nickel and lithium co-substituted barium titanate ceramics. *Ceramics International*, 43(6), 4937-4949.
- Alkoy, E. M., & Berksoy-Yavuz, A. (2012). Electrical properties and impedance spectroscopy of pure and copper-oxide-added potassium sodium niobate ceramics. *IEEE Transactions on Ultrasonics, Ferroelectrics, and Frequency Control*, 59(10), 2121-2128.
- Anton, E.M., Schmitt, L.A., Hinterstein, M., Trodahl, J., Kowalski, B., Jo, W., Kleebe, H.J., Rödel, J. and Jones, J.L., 2012. Structure and temperature-dependent phase transitions of lead-free $\text{Bi}_{1/2}\text{Na}_{1/2}\text{TiO}_3$ – $\text{Bi}_{1/2}\text{K}_{1/2}\text{TiO}_3$ – $\text{K}_{0.5}\text{Na}_{0.5}\text{NbO}_3$ piezoceramics. *Journal of Materials Research*, 27(19), pp.2466-2478.
- Anthoniappen, J., Tu, C. S., Chen, P., Chen, C., Idzerda, Y. U. & Chiu, S. -. (2015). Raman spectra and structural stability in B-site manganese doped $(\text{Bi}_{0.5}\text{Na}_{0.5})_{0.925}\text{Ba}_{0.075}\text{TiO}_3$ relaxor ferroelectric ceramics. *Journal of the European Ceramic Society*, 35(13), 3495-3506.
- Baek, C., Kim, M., Kwon, O., Choi, H., & Yang, Y. (2017). Formation of $\text{Ba}_2\text{NaNb}_5\text{O}_{15}$ crystal and crystallization kinetics in BaO – Na_2O – Nb_2O_5 – SiO_2 – B_2O_3 glass. *Crystal Growth & Design*, 17(11), 5684-5690.
- Bai, S., Zhang, J., Chen, Z., Wang, Y., Hong, M., & Karaki, T. (2017). Near-room-temperature synthesis of niobate hydrate particles with hexagonal-plate-like morphologies. *Materials Chemistry and Physics*, 199, 230-238.
- Bai, W., Zheng, P., Wen, F., Zhang, J., Chen, D., Zhai, J., & Ji, Z. (2017). Lead-free BNT-based composite materials: Enhanced depolarization temperature and electromechanical behavior. *Dalton Transactions*, 46(44), 15340-15353.
- Bai, W., Shen, B., Zhai, J., Liu, F., Li, P., Liu, B., & Zhang, Y. (2016). Phase evolution and correlation between tolerance factor and electromechanical properties in BNT-based ternary perovskite compounds with calculated end-member $\text{Bi}(\text{Me}_{0.5}\text{Ti}_{0.5})\text{O}_3$ (Me = Zn, Mg, Ni, Co). *Dalton Transactions*, 45(36), 14141-14153.
- Bai, W., Hao, J., Fu, F., Li, W., Shen, B., & Zhai, J. (2013). Structure and strain behavior of textured BNT-based ceramics by template grain growth. *Materials Letters*, 97, 137-140.

- Bansal, N. P. & Doremus, R. (1986). *Handbook of glass properties*. London: Academic Press.
- Birla, S. L., & Pitchai, K. (2017). Simulation of microwave processes. In *The Microwave Processing of Foods* (pp. 407-431). Woodhead Publishing.
- Bouchouicha, H., Panczer, G., De Ligny, D., Guyot, Y., Baesso, M., Andrade, L., Ternane, R. (2016). Synthesis and luminescent properties of Eu_3/Eu_2 co-doped calcium aluminosilicate glass-ceramics. *Journal of Luminescence*, 169, 528-533.
- Buchanan, R. C. (1986). *Ceramic materials for electronics: Processing, properties and applications*. New York: Dekker.
- Busca, G. (2014). In Busca G. (Ed.), *Chapter 2 - preparation of solid catalysts: A short summary*. Amsterdam: Elsevier.
- Butnoi, P., Manotham, S., Jaita, P., Pengpat, K., Eitssayeam, S., Tunkasiri, T., & Rujijanagul, G. (2017). Effects of processing parameter on phase transition and electrical properties of lead-free BNKT piezoelectric ceramics. *Ferroelectrics*, 511(1), 42-51.
- Bykov, Y. V., Rybakov, K., & Semenov, V. (2001). High-temperature microwave processing of materials. *Journal of Physics D: Applied Physics*, 34(13), R55.
- Byun, J., Hyun, J. W., Kim, Y. J., & Bobor, K. (2018). Fabrication of lead-free $(\text{K}_{0.5}\text{Na}_{0.5})_{1-x}\text{Ag}_x\text{NbO}_3$ ferroelectric ceramics and their dielectric properties. *Journal of the Korean Physical Society*, 72(6), 726-730.
- Carter, C. B., & Norton, M. G. (2007). *Ceramic materials: Science and engineering*. New York: Springer Science & Business Media.
- Cernea, M., Trupina, L., Dragoi, C., Vasile, B. S., & Trusca, R. (2012). Structural and piezoelectric characteristics of BNT-BT_{0.05} thin films processed by sol-gel technique. *Journal of Alloys and Compounds*, 515, 166-170.
- Chae, M. S., Lee, K. S., & Koh, J. H. (2013). Influence of calcination temperature on the piezoelectric properties of Ag_2O doped $0.94(\text{K}_{0.5}\text{Na}_{0.5})\text{NbO}_3-0.06\text{LiNbO}_3$ ceramics. *Ceramics International*, 39, S25-S29.
- Chan, I., Sun, C., Houg, M., & Chu, S. (2011). Sb doping effects on the piezoelectric and ferroelectric characteristics of lead-free $\text{Na}_{0.5}\text{K}_{0.5}\text{Nb}_{1-x}\text{Sb}_x\text{O}_3$ piezoelectric ceramics. *Ceramics International*, 37(7), 2061-2068.
- Chandrasekaran, S., Ramanathan, S., & Basak, T. (2012). Microwave material processing—a review. *AIChE Journal*, 58(2), 330-363.
- Chandrasekhar, M., & Kumar, P. (2016a). Synthesis and characterizations of NaNbO_3 modified BNT-BT-BKT ceramics for energy storage applications. *Physica B: Condensed Matter*, 497, 59-66.
- Chandrasekhar, M., & Kumar, P. (2016b). Processing and characterizations of BNT-KNN ceramics for actuator applications. *Processing and Application of Ceramics*, 10(2), 73-77.

Cheng, C., Chen, K., & Yang, F. (2012). Effect of sintering temperature on piezoelectric and ferroelectric properties of lead-free piezoelectric Ta-modified ($\text{K}_{0.5}\text{Na}_{0.5}$) NbO_3 ceramics. *Ferroelectrics*, 435(1), 46-54.

Cheng, K., Wan, J., & Liang, K. (2001). Crystallization of $\text{R}_2\text{O}-\text{MgO}-\text{Al}_2\text{O}_3-\text{B}_2\text{O}_3-\text{SiO}_2-\text{F}$ (R= K, Na) glasses with different fluorine source. *Materials Letters*, 47(1-2), 1-6.

Cheng, R., Duan, Y., Chu, R., Hao, J., Du, J., Xu, Z., & Li, G. (2015). Investigation of structural and electrical properties of B-site complex ion ($\text{Nd}_{1/2}\text{Ta}_{1/2}$)₄ - doped $\text{Bi}_{1/2}\text{Na}_{1/2}\text{TiO}_3$ lead-free piezoelectric ceramic. *Journal of Materials Science: Materials in Electronics*, 26(7), 5409-5415.

Cheng, X., Brow, R. K., & Chen, G. (2017). The dissolution behavior in alkaline solutions of a borosilicate glass with and without P_2O_5 . *Journal of the American Ceramic Society*, 100(10), 4519-4532.

Chiang, H., Lee, Y., & Gaik, T. L. (2013). Effect of microwave sintering on the microstructure and piezoelectric properties of ZnO-doped $\text{Bi}_{0.5}\text{Na}_{0.5}\text{TiO}_3$ ceramics. *Journal of the Ceramic Society of Japan*, 121(1413), 430-436.

Chou, C., Chen, J., Yang, R., & Chou, S. (2010). The effects of MgO doping and sintering temperature on the microstructure of the lead-free piezoelectric ceramic of $\text{Bi}_{0.5}\text{Na}_{0.5}\text{TiO}_3$. *Powder Technology*, 202(1), 39-45.

Chou, C., Liu, C., Hsiung, C., & Yang, R. (2011). Preparation and characterization of the lead-free piezoelectric ceramic of $\text{Bi}_{0.5}\text{Na}_{0.5}\text{TiO}_3$ doped with CuO. *Powder Technology*, 210(3), 212-219.

Chu, S. Y., Chen, T. Y., Tsai, I. T., & Water, W. (2004). Doping effects of Nb additives on the piezoelectric and dielectric properties of PZT ceramics and its application on SAW device. *Sensors and Actuators A: Physical*, 113(2), 198-203.

Coondoo, I., Panwar, N., Maiwa, H., & Kholkin, A. L. (2015). Improved piezoelectric and energy harvesting characteristics in lead-free Fe_2O_3 modified KNN ceramics. *Journal of Electroceramics*, 34(4), 255-261.

Dai, B., Hu, X., Yin, R., Bai, W., Wen, F., Deng, J., Qin, H. (2017). Piezoelectric grain-size effects of BaTiO_3 ceramics under different sintering atmospheres. *Journal of Materials Science: Materials in Electronics*, 28(11), 7928-7934.

Dargham, S. A., Ponchel, F., Zaatari, Y., Assaad, J., Remiens, D., & Zaouk, D. (2016). Synthesis and characterization of BNT thin films prepared by Sol-Gel method. *Materials Today: Proceedings*, 3(3), 810-815.

Das, S., Madheshiya, A., Gautam, S., & Gautam, C. (2017). Fabrication and optical characterizations of lead calcium titanate borosilicate glasses. *Journal of Non-Crystalline Solids*, 478, 16-22.

Dimitrov, V., & Komatsu, T. (2010). An interpretation of optical properties of oxides and oxide glasses in terms of the electronic ion polarizability and average single bond strength. *Journal of the University of Chemical Technology and Metallurgy*, 45(3), 219-250.

- Dong, G., Fan, H., Shi, J., & Li, M. (2015). Composition- and Temperature-Dependent large strain in $(1-x)(_{0.8}\text{Bi}_{0.5}\text{Na}_{0.5}\text{TiO}_3-_{0.2}\text{Bi}_{0.5}\text{K}_{0.5}\text{TiO}_3)-x\text{NaNbO}_3$ ceramics. *Journal of the American Ceramic Society*, 98(4), 1150-1155.
- Du, J., Xu, Z., Chu, R., Hao, J., Li, W., Jiang, G., & Zheng, P. (2017). Rare-earth doped $(\text{K}_{0.5}\text{Na}_{0.5})\text{NbO}_3$ multifunctional ceramics. *Journal of Materials Science: Materials in Electronics*, 28(7), 5288-5294.
- Duong, T. A., Han, H. S., Hong, Y. H., Park, Y. S., Nguyen, H. T. K., Dinh, T. H., & Lee, J. S. (2018). Dielectric and piezoelectric properties of $\text{Bi}_{1/2}\text{Na}_{1/2}\text{TiO}_3$ - SrTiO_3 lead-free ceramics. *Journal of Electroceramics*, 41(1-4), 73-79.
- Duran, P., & Moure, C. (1986). Piezoelectric Ceramics. *Materials chemistry and physics*, 15(3-4), 193-211.
- Ebnesajjad, S. (2011). In Ebnesajjad S. (Ed.), *4 - surface and material characterization techniques*. Oxford: William Andrew Publishing.
- Epp, J. (2016). 4 - X-ray diffraction (XRD) techniques for materials characterization. In G. Hübschen, I. Altpeter, R. Tschuncky, & H. Herrmann (Eds.), *Materials characterization using nondestructive evaluation (NDE) methods* (pp. 81-124) Woodhead Publishing.
- Fanelli, E., Pernice, P., Xiao, M., Aronne, A., & Sigaev, V. (2011). Crystallization behaviour and nanostructuring in alkali niobosilicate glasses. *Journal of Materials Science & Technology*, 27(2), 189-192.
- Feizpour, M., Bafrooei, H. B., Hayati, R., & Ebadzadeh, T. (2014). Microwave-assisted synthesis and sintering of potassium sodium niobate lead-free piezoelectric ceramics. *Ceramics International*, 40(1), 871-877.
- Fisher, J. G., Bencan, A., Kosec, M., Vernay, S., & Rytz, D. (2008). Growth of dense single crystals of potassium sodium niobate by a combination of solid-state crystal growth and hot pressing. *Journal of the American Ceramic Society*, 91(5), 1503-1507.
- Fujii, I., Ito, Y., Suzuki, T., & Wada, T. (2016). Ferroelectric and piezoelectric properties of $(\text{Bi}_{1/2}\text{Na}_{1/2})\text{TiO}_3$ - BiFeO_3 ceramics. *Journal of Materials Research*, 31(01), 28-35.
- Fukuchi, E., Kimura, T., Tani, T., Takeuchi, T., & Saito, Y. (2002). Effect of potassium concentration on the grain orientation in bismuth sodium potassium titanate. *Journal of the American Ceramic Society*, 85(6), 1461-1466.
- Gallegos-Melgar, A., Espinosa-Arbelaez, D. G., Flores-Ruiz, F. J., Lahmar, A., Dellis, J., Lemée, N., Muñoz-Saldaña, J. (2015). Ferroelectric properties of manganese doped $(\text{Bi}_{1/2}\text{Na}_{1/2})\text{TiO}_3$ and $(\text{Bi}_{1/2}\text{Na}_{1/2})\text{TiO}_3$ - BaTiO_3 epitaxial thin films. *Applied Surface Science*, 359, 923-930.
- Ganvir, V., & Gedam, R. (2017). Influence of Sm_2O_3 addition on electrical properties of lithium borosilicate glasses. *Integrated Ferroelectrics*, 185(1), 102-108.
- Goldstein, G. I.; Newbury, D. E.; Echlin, P.; Joy, D. C.; Fiori, C.; Lifshin, E. (1981). *Scanning electron microscopy and x-ray microanalysis*. New York: Plenum Press.

- Hamid, A., Farahin, N., Osman, R. A. M., Idris, M. S., & Tan, T. Q. (2015). Studied on Structural Characterization of Lanthanum doped Barium Titanium ceramics. In *Materials Science Forum* (Vol. 819, pp. 198-203). Trans Tech Publications.
- Agrawal, D. (2013). Microwave sintering of metal powders. *Advances in powder metallurgy* (pp. 361-379). Elsevier.
- Hao, H., Tan, G., Ren, H., Xia, A., & Xiong, P. (2014). Hydrothermal-assisted synthesis and sintering of $K_{0.5}Na_{0.5}NbO_3-xLiTaO_3$ lead-free piezoelectric ceramics. *Ceramics International*, 40(7), 9485-9491.
- Hao, Y., & Dai, Y. (2017). Influence of Y_2O_3 on the structure and luminescence of Eu^{2+} doped borosilicate glasses. *Journal of Non-Crystalline Solids*, 474, 32-36.
- He, F., Chen, X., Chen, J., Wang, Y., Zhou, H., & Fang, L. (2013). $(K_{0.5}Na_{0.5})NbO_3-Bi(Mg_{0.5}Ti_{0.5})O_3$ solid solution: Phase evolution, microstructure and electrical properties. *Journal of Materials Science: Materials in Electronics*, 24(11), 4346-4350.
- Hmood, F. J., Guenster, J., & Heinrich, J. G. (2015). Sintering and piezoelectric properties of $K_{0.5}Na_{0.5}NbO_3$ glass microspheres. *Journal of the European Ceramic Society*, 35(15), 4143-4151.
- Hollenstein, E., Damjanovic, D., & Setter, N. (2007). Temperature stability of the piezoelectric properties of Li-modified KNN ceramics. *Journal of the European Ceramic Society*, 27(13-15), 4093-4097.
- Hu, B., Fan, H., Ning, L., Gao, S., Yao, Z., & Li, Q. (2018). Enhanced energy-storage performance and dielectric temperature stability of $(1-x)(0.65Bi_{0.5}Na_{0.5}TiO_3-0.35Bi_{0.1}Sr_{0.85}TiO_3)-xKNbO_3$ ceramics. *Ceramics International*, 44(9), 10968-10974.
- Ingham, B., & Toney, M. F. (2014). X-ray diffraction for characterizing metallic films. In *Metallic Films for Electronic, Optical and Magnetic Applications* (pp. 3-38). Woodhead Publishing.
- Inoue, K., Sakida, S., Nanba, T., & Miura, Y. (2006). Structure and optical properties of TiO₂-containing oxide glasses. *Materials Science and Technology*, 3, 583-593.
- Ivanov, M., Macutkevicius, J., Grigalaitis, R., & Banys, J. (2018). General view of ferroelectrics: Origin of ferroelectricity in metal oxide ferroelectrics and ferroelectric properties. *Magnetic, ferroelectric, and multiferroic metal oxides* (pp. 5-33). Elsevier.
- Jaffe, B., Cook Jr, W. R., & Jaffe, H. (1971). *Piezoelectric ceramics*. London: Academic Press INC.
- Jenko, D., Bencan, A., Malic, B., Holc, J., & Kosec, M. (2005). Electron microscopy studies of potassium sodium niobate ceramics. *Microscopy and Microanalysis*, 11(06), 572-580.
- Jiang, X., Wang, B., Luo, L., Li, W., Zhou, J., & Chen, H. (2014). Electrical properties of $(1-x)(Bi_{0.5}Na_{0.5})TiO_3-xKNbO_3$ lead-free ceramics. *Journal of Solid-State Chemistry*, 213, 72-78.
- Jones, G., & Thomas, P. (2002). Investigation of the structure and phase transitions in the novel A-site substituted distorted perovskite compound $Na_{0.5}Bi_{0.5}TiO_3$. *Acta Crystallographica Section B: Structural Science*, 58(2), 168-178.

Kakroo, S., Kumar, A., Mishra, S., Singh, V., & Singh, P. K. (2016). The effect of CuO and NiO doping on dielectric and ferroelectric properties of $\text{Na}_{0.5}\text{Bi}_{0.5}\text{TiO}_3$ lead-free ceramics. *Phase Transitions*, 89(3), 211-220.

Kamakshi, T., Rao, P. S. V. S., & Rao, T. P. (2015). Effect of (Na and K) ion substitutions on the micro structural, dielectric and electrical properties of PZT ceramics. *Materials Today: Proceedings*, 2(4-5), 2896-2901.

Kambale, K., Shroff, S., Butee, S., Singh, R., & Kulkarni, A. (2017). Effect of addition of V_2O_5 on the densification, dielectric and ferroelectric behavior of lead-free potassium sodium niobate ceramics. *Ferroelectrics*, 518(1), 94-102.

Kang, C., Park, J., Shen, D., Ahn, H., Park, M., & Kim, D. (2011). Growth and characterization of $(\text{K}_{0.5}\text{Na}_{0.5})\text{NbO}_3$ thin films by a sol-gel method. *Journal of Sol-Gel Science and Technology*, 58(1), 85-90.

Khamman, O. (2014). Phase formation and dielectric properties of Ge doped $(\text{Bi}_{0.5}\text{Na}_{0.5})\text{TiO}_3$ ceramics. *Ferroelectrics*, 458(1), 43-48.

Kim, J., Kim, J., Han, S., Kang, H., Lee, H., & Cheon, C. (2016). (K, Na) NbO_3 -based ceramics with excess alkali oxide for piezoelectric energy harvester. *Ceramics International*, 42(4), 5226-5230.

Kimura, M., Ando, A., & Sakabe, Y. (2010). 2 - lead zirconate titanate-based piezo-ceramics. In K. Uchino (Ed.), *Advanced piezoelectric materials* (pp. 89-110). Woodhead Publishing.

Kingery, W. D. (1958). *Ceramic fabrication processes*. New York: John Wiley & Sons.

Kingery, W. D. (1959). Densification during sintering in the presence of a liquid phase. I. Theory. *Journal of Applied Physics*, 30(3), 301-306.

Kioka, K., Honma, T., & Komatsu, T. (2011a). Formation and laser patterning of perovskite-type KNbO_3 crystals in aluminoborate glasses. *Optical Materials*, 33(3), 267-274.

Kioka, K., Honma, T., & Komatsu, T. (2011b). Fabrication of (K, Na) NbO_3 glass-ceramics and crystal line patterning on glass surface. *Optical Materials*, 33(8), 1203-1209.

Klančnik, G., Medved, J., & Mrvar, P. (2010). Differential thermal analysis (DTA) and differential scanning calorimetry (DSC) as a method of material investigation diferenčna termična analiza (DTA) in diferenčna vrstična kalorimetrija (DSC) kot metoda za raziskavo materialov. *RMZ-Materials and Geoenvironment*, 57(1), 127-142.

Koruza, J., Venkataraman, L. K., & Malič, B. (2018). Lead-free perovskite ferroelectrics. In *Magnetic, ferroelectric, and multiferroic metal oxides* (pp. 51-69). Elsevier.

Kreiselt, J., Glazer, A. M., Jones, G., Thomas, P. A., Abello, L., & Lucazeau, G. (2000). An x-ray diffraction and Raman spectroscopy investigation of A-site substituted perovskite compounds: The $(\text{Na}_{1-x}\text{K}_x)_{0.5}\text{Bi}_{0.5}\text{TiO}_3$ ($0 = x = 1$) solid solution. *Journal of Physics Condensed Matter*, 12(14), 3267-3280.

Kumar, A., Sharma, A., Kumar, R., Vaish, R., & Bowen, C. (2016). Performance of $K_{0.5}Na_{0.5}NbO_3$ - $LiSbO_3$ - $CaTiO_3$ ceramics in acoustic energy harvesting exposed to sound pressure. *Ferroelectrics*, 504(1), 149-159.

Larkin, P. J. (2018). Chapter 1 - introduction: Infrared and Raman spectroscopy. In P. J. Larkin (Ed.), *Infrared and Raman spectroscopy (second edition)* (pp. 1-5) Elsevier.

Li, F., Gou, Q., Xing, J., Tan, Z., Jiang, L., Xie, L., Zhu, J. (2017). The piezoelectric and dielectric properties of sodium–potassium niobate ceramics with new multiphase boundary. *Journal of Materials Science: Materials in Electronics*, 28(23), 18090-18098.

Li, H., Kang, J., Guo, F., Qu, Y., & Yang, D. (2013). Effect of the Nb_2O_5 content on electrical properties of lead-free $BaTiO_3$ - $Bi_{0.5}Na_{0.5}TiO_3$ ceramics. *Ceramics International*, 39(7), 7589-7593.

Lidjici, H., Lagoun, B., Berrahal, M., Rguitti, M., Hentatti, M. A., & Khemakhem, H. (2015). XRD, Raman and electrical studies on the $(1-x)(Na_{0.5}Bi_{0.5})TiO_3$ - $xBaTiO_3$ lead-free ceramics. *Journal of Alloys and Compounds*, 618, 643-648.

Lin, C., Wu, X., Lin, M., Huang, Y., & Li, J. (2017). Optical, luminescent and optical temperature sensing properties of $(K_{0.5}Na_{0.5})NbO_3$ - $ErBiO_3$ transparent ceramics. *Journal of Alloys and Compounds*, 706, 156-163.

Lin, D. e. a. (2007). Structure and electrical properties of $K_{0.5}Na_{0.5}NbO_3$ - $LiSbO_3$ lead-free piezoelectric ceramics. *Journal of Applied Physics*, 101(7), 074111(6).

Lipovskii, A., Kaganovskii, Y., Melehin, V., Tagantsev, D., & Yanush, O. (2008). Electrooptical kerr phenomenon and Raman spectroscopy of one lithium–niobium–silicate glass-forming system. *Journal of Non-Crystalline Solids*, 354(12-13), 1245-1249.

Liu, Z., Ren, W., Peng, P., Guo, S., Lu, T., Liu, Y., Wang, G. (2018). High performance $Bi_{0.5}Na_{0.5}TiO_3$ - $BiAlO_3$ - $K_{0.5}Na_{0.5}NbO_3$ lead-free pyroelectric ceramics for thermal detectors. *Applied Physics Letters*, 112(14), 142903.

Lopez-Juarez, R., Gomez-Vidales, V., Cruz, M. P., & Villafuerte-Castrejon, M. E. (2015). Dielectric, ferroelectric, and piezoelectric properties of Mn-doped $K_{0.5}Na_{0.5}NbO_3$ lead-free ceramics. *Journal of Electronic Materials*, 44(8), 2862-2868.

Lu, W., Wang, Y., Fan, G., Wang, X., & Liang, F. (2011). The structural and electric properties of Li- and K-substituted $Bi_{0.5}Na_{0.5}TiO_3$ ferroelectric ceramics. *Journal of Alloys and Compounds*, 509(6), 2738-2744.

Lusiola, T., Soppelsa, A., Rubio-Marcos, F., Fernandez, J. F., & Clemens, F. (2016a). The impact of microstructure in $(K, Na)NbO_3$ -based lead-free piezoelectric fibres: From processing to device production for structural health monitoring. *Journal of the European Ceramic Society*, 36(11), 2745-2754.

Ma, X., Xue, L., Wan, L., Yin, S., Zhou, Q., & Yan, Y. (2013). Synthesis, sintering, and characterization of BNT perovskite powders prepared by the solution combustion method. *Ceramics International*, 39(7), 8147-8152.

- Ma, Y. J., Cho, J. H., Lee, Y. H., & Kim, B. I. (2006). Hydrothermal synthesis of $(\text{Bi}_{1/2}\text{Na}_{1/2})\text{TiO}_3$ piezoelectric ceramics. *Materials Chemistry and Physics*, 98(1), 5-8.
- Madheshiya, A., Gautam, C., & Upadhyay, S. (2018). Preparation, optical and electrical properties of bismuth-substituted lead titanate borosilicate glass and glass ceramics. *Journal of Non-Crystalline Solids*, 502, 118-127.
- Malic, B., Bernard, J., Holc, J., Jenko, D., & Kosec, M. (2005). Alkaline-earth doping in $(\text{K}, \text{Na})\text{NbO}_3$ based piezoceramics. *Journal of the European Ceramic Society*, 25(12), 2707-2711.
- Malič, B., Kuščer, D., Vrabelj, M., & Koruza, J. (2018). 5 - review of methods for powder-based processing. In B. D. Stojanovic (Ed.), *Magnetic, ferroelectric, and multiferroic metal oxides* (pp. 95-120) Elsevier.
- Manara, D., Grandjean, A., & Neuville, D. (2009). Advances in understanding the structure of borosilicate glasses: A Raman spectroscopy study. *American Mineralogist*, 94(5-6), 777-784.
- Maqbool, A., Hussain, A., Rahman, J. U., Park, J. K., Park, T. G., Song, J. S., & Kim, M. H. (2014). Ferroelectric and piezoelectric properties of SrZrO_3 -modified $\text{Bi}_{0.5}\text{Na}_{0.5}\text{TiO}_3$ lead-free ceramics. *Transactions of Nonferrous Metals Society of China*, 24, s146-s151.
- Marghussian, V. (2015). In Marghussian V. (Ed.), *3 - ferroelectric and electro-optical properties of nano-glass ceramics*. Oxford: William Andrew Publishing.
- Moulson, A. J., & Herbert, J. M. (2003). *Electroceramics: materials, properties, applications*. England: John Wiley & Sons.
- Möncke, D., Ehrt, R., Palles, D., Efthimiopoulos, I., Kamitsos, E. I., & Johannes, M. (2017). A multi-technique study of a new lithium disilicate glass-ceramic spray-coated on ZrO_2 substrate for dental restoration. *Biomedical Glasses*, 3(1), 41-55.
- Nayak, S., Sahoo, B., Chaki, T. K., & Khastgir, D. (2014). Facile preparation of uniform barium titanate (BaTiO_3) multipods with high permittivity: Impedance and temperature dependent dielectric behavior. *RSC Advances*, 4(3), 1212-1224.
- Pal, V., Dwivedi, R. K., & Thakur, O. P. (2014). Synthesis and ferroelectric behavior of Gd-doped BNT ceramics. *Current Applied Physics*, 14(1), 99-107.
- Pan, H., Zhang, J., Jia, X., Xing, H., He, J., Wang, J., & Wen, F. (2018). Large electrostrictive effect and high optical temperature sensing in $\text{Bi}_{0.5}\text{Na}_{0.5}\text{TiO}_3$ - BaTiO_3 - $(\text{Sr}_{0.7}\text{Bi}_{0.18}\text{Er}_{0.02})\text{TiO}_3$ luminescent ferroelectrics. *Ceramics International*, 44(5), 5785-5789.
- Panda, P., & Sahoo, B. (2015). PZT to lead-free piezo ceramics: A review. *Ferroelectrics*, 474(1), 128-143.
- Pardo, L., Villafuerte-Castrejón, M. E., Morán, E., Reyes-Montero, A., Vivar-Ocampo, R., & Gonzalez, A. M. (2018). In Stojanovic B. D. (Ed.), *9 - ecological, lead-free ferroelectrics* Elsevier.
- Parija, B., Badapanda, T., Senthil, V., Rout, S., & Panigrahi, S. (2012). Diffuse phase transition, piezoelectric and optical study of $\text{Bi}_{0.5}\text{Na}_{0.5}\text{TiO}_3$ ceramic. *Bulletin of Materials Science*, 35(2), 197-202.

Parija, B., Rout, S., Cavalcante, L., Sim, A., Panigrahi, S., Longo, E., & Batista, N. (2012). Structure, microstructure and dielectric properties of $100-x$ $(\text{Bi}_{0.5}\text{Na}_{0.5})\text{TiO}_3-x[\text{SrTiO}_3]$ composites ceramics. *Applied Physics A*, *109*(3), 715-723.

Patel, S., Chauhan, A., & Vaish, R. (2014). Enhancing electrical energy storage density in anti-ferroelectric ceramics using ferroelastic domain switching. *Materials Research Express*, *1*(4), 045502.

Pattipaka, S., James, A., & Dobbidi, P. (2018). Dielectric, piezoelectric and variable range hopping conductivity studies of $\text{Bi}_{0.5}(\text{Na}, \text{K})_{0.5}\text{TiO}_3$ ceramics. *Journal of Electronic Materials*, *47*(7), 3876-3890.

Pattipaka, S., Peddigari, M., & Dobbidi, P. (2017). *Effect of ce on structural and dielectric properties of lead-free $(\text{Bi}_{0.5}\text{Na}_{0.5})\text{TiO}_3$ ceramics*.

Petrovic, M. M. V., & Bobic, J. D. (2018). Perovskite and aurivillius: Types of ferroelectric metal oxides. *Magnetic, ferroelectric, and multiferroic metal oxides* (pp. 35-49) Elsevier.

Ponraj, B., & Varma, K. B. R. (2016). Enhancement in the physical properties of $\text{K}_{0.5}\text{Na}_{0.5}\text{NbO}_3$ ceramics by the addition of $0.5\text{Li}_2\text{O}-0.5\text{K}_2\text{O}-2\text{B}_2\text{O}_3$ glass. *Integrated Ferroelectrics*, *176*(1), 257-267.

Pourianejad, S., & Movahedi, B. (2015). Solid-state synthesis of modified $(\text{Bi}_{0.5}\text{Na}_{0.5})\text{TiO}_3$ piezoelectric nanocrystalline ceramics and evaluating their properties. *Materials Science in Semiconductor Processing*, *29*, 337-344.

Prado-Espinosa, A., Castro, M., & Ramajo, L. (2017). Influence of secondary phases on ferroelectric properties of $\text{Bi}_{0.5}\text{Na}_{0.5}\text{TiO}_3$ ceramics. *Ceramics International*, *43*(7), 5505-5508.

Priya, S., & Nahm, S. (2011). *Lead-free piezoelectrics* Springer Science & Business Media.

Pu, Y., Yao, M., Liu, H., & Frömling, T. (2016). Phase transition behavior, dielectric and ferroelectric properties of $(1-x)(\text{Bi}_{0.5}\text{Na}_{0.5})\text{TiO}_3-x\text{Ba}_{0.85}\text{Ca}_{0.15}\text{Ti}_{0.9}\text{Zr}_{0.1}\text{O}_3$ ceramics. *Journal of the European Ceramic Society*, *36*(10), 2461-2468.

Qin, Y., Zhang, J., Yao, W., Wang, C., & Zhang, S. (2015). Domain structure of Potassium-Sodium niobate ceramics before and after poling. *Journal of the American Ceramic Society*, *98*(3), 1027-1033.

Rahaman, M. N. (2003). *Ceramic processing and sintering*. New York: CRC press.

Rahman, J. U., Hussain, A., Maqbool, A., Song, T. K., Kim, W. J., Kim, S. S., & Kim, M. H. (2014). Dielectric, ferroelectric and field-induced strain response of lead-free BaZrO_3 -modified $\text{Bi}_{0.5}\text{Na}_{0.5}\text{TiO}_3$ ceramics. *Current Applied Physics*, *14*(3), 331-336.

Rajkumar, K., & Aravindan, S. (2009). Microwave sintering of copper-graphite composites. *Journal of Materials Processing Technology*, *209*(15-16), 5601-5605.

Ramajo, L. A., Taub, J., & Castro, M. S. (2014). Effect of ZnO addition on the structure, microstructure and dielectric and piezoelectric properties of $K_{0.5}Na_{0.5}NbO_3$ ceramics. *Materials Research*, 17(3), 728-733.

Ramajo, L., Taub, J., & Castro, M. S. (2014). Influence of zirconium addition on final properties of $K_{0.5}Na_{0.5}NbO_3$ -based ceramics. *Journal of Materials Science: Materials in Electronics*, 25(1), 168-173.

Ramana, M. V., Kiran, S. R., Ramamanohar Reddy, N., Siva Kumar, K. V., Murthy, V. R. K., & Murty, B. S. (2011). Synthesis of lead-free sodium bismuth titanate (NBT) ceramic by conventional and microwave sintering methods. *Journal of Advanced Dielectrics*, 1(01), 71-77.

Rao, K. J., Vaidhyanathan, B., Ganguli, M., & Ramakrishnan, P. A. (1999). Synthesis of inorganic solids using microwaves. *Chemistry of Materials*, 11(4), 882-895.

Razak, K. A., Yip, C. J., & Sreekantan, S. (2011). Synthesis of $(Bi_{0.5}Na_{0.5})TiO_3$ (BNT) and Pr doped BNT using the soft combustion technique and its properties. *Journal of Alloys and Compounds*, 509(6), 2936-2941.

Rezazadeh, L., Baghshahi, S., Golikand, A. N., & Hamnabard, Z. (2014). Structure, phase formation, and wetting behavior of $BaO-SiO_2-B_2O_3$ based glass-ceramics as sealants for solid oxide fuel cells. *Ionics*, 20(1), 55-64.

Rietveld, H. (1969). A profile refinement method for nuclear and magnetic structures. *Journal of applied Crystallography*, 2(2), 65-71.

Richerson, D. W. (2005). *Modern ceramic engineering: properties, processing, and use in design*. CRC press.

Rodríguez-Carvajal, J. (1993). Recent advances in magnetic structure determination by neutron powder diffraction. *Physica B: Condensed Matter*, 192(1-2), 55-69.

Rödel, J., Jo, W., Seifert, K. T., Anton, E., Granzow, T., & Damjanovic, D. (2009). Perspective on the development of lead-free piezoceramics. *Journal of the American Ceramic Society*, 92(6), 1153-1177.

Rout, D., Moon, K., Kang, S. L., & Kim, I. (2010). Dielectric and Raman scattering studies of phase transitions in the $(100-x)Na_{0.5}Bi_{0.5}TiO_3-x SrTiO_3$ system. *Journal of Applied Physics*, 108(8), 084102.

Rout, S., Raj, A., & Ghosh, S. (2017). Compositional effect on dielectric and ferroelectric properties of lead-free Zr modified BNT ceramic. *Ferroelectrics*, 518(1), 66-72.

Samudrala, R., Azeem, P. A., Penugurti, V. R., & Bramanandam, M. (2018). In vitro evaluation of niobia added soda lime borosilicate bioactive glasses. *Journal of Alloys and Compounds*,

Shannon, R. D. (1976). Revised effective ionic radii and systematic studies of interatomic distances in halides and chalcogenides. *Acta Crystallographica Section A: Crystal Physics, Diffraction, Theoretical and General Crystallography*, 32(5), 751-767.

Shannon, R. D., & Prewitt, C. T. (1969). Coordination and volume changes accompanying high-pressure phase transformations of oxides. *Materials Research Bulletin*, 4(1), 57-62.

Sharma, S. K., Chauhan, V. S., & Kumar, A. (2016). Detection of electromagnetic radiation in ferroelectric ceramics for non-contact sensing applications. *Journal of Alloys and Compounds*, 662, 534-540.

Shelby, J. E. (2005). *Introduction to glass science and technology*. New York: Royal Society of Chemistry.

Shen, Z., Zhao, Y., Tian, Z., Huang, W., Wu, J., & Lin, H. (2018). Effect of doping La_2O_3 on the structure and properties of the titanium barium silicate glass. *Journal of Non-Crystalline Solids*, 499, 17-24.

Shi, J., Fan, H., Liu, X., & Li, Q. (2014). Giant strain response and structure evolution in $(\text{Bi}_{0.5}\text{Na}_{0.5})_{0.945-x}(\text{Bi}_{0.2}\text{Sr}_{0.7}\square_{0.1})_x\text{Ba}_{0.055}\text{TiO}_3$ ceramics. *Journal of the European Ceramic Society*, 34(15), 3675-3683.

Shrout, T. R., & Zhang, S. J. (2007). Lead-free piezoelectric ceramics: Alternatives for PZT? *Journal of Electroceramics*, 19(1), 113-126.

Singh, R., Kambale, K., Kulkarni, A. R., & Harendranath, C. S. (2013). Structure composition correlation in KNN-BT ceramics-an X-ray diffraction and Raman spectroscopic investigation. *Materials Chemistry and Physics*, 138(2-3), 905-908.

Sinha Ray, S. (2013). 3 - structure and morphology characterization techniques. In S. S. Ray (Ed.), *Clay-containing polymer nanocomposites* (pp. 39-66). Amsterdam: Elsevier.

Smart, L. E., & Moore, E. A. (2016). *Solid state chemistry: An introduction*. New York: CRC press.

Stewart, M., Cain, M., & Hall, D. (1999). *Ferroelectric hysteresis measurement and analysis* National Physical Laboratory Teddington.

Sumang, R., Bongkarn, T., Kumar, N., & Kamnoy, M. (2017). Investigation of a new lead-free (1-xy) BNT-xBKT-yBZT piezoelectric ceramics. *Ceramics International*, 43, S102-S109.

Surowiak, Z., Kupriyanov, M. F., & Czekaj, D. (2001). Properties of nanocrystalline ferroelectric PZT ceramics. *Journal of the European Ceramic Society*, 21(10-11), 1377-1381.

Takao, H., Saito, Y., Aoki, Y., & Horibuchi, K. (2006). Microstructural evolution of Crystalline-Oriented $(\text{K}_{0.5}\text{Na}_{0.5})\text{NbO}_3$ piezoelectric ceramics with a sintering aid of CuO. *Journal of the American Ceramic Society*, 89(6), 1951-1956.

Tan, X., Aulbach, E., Jo, W., Granzow, T., Kling, J., Marsilius, M., Rödel, J. (2009). Effect of uniaxial stress on ferroelectric behavior of $(\text{Bi}_{1/2}\text{Na}_{1/2})\text{TiO}_3$ -based lead-free piezoelectric ceramics. *Journal of Applied Physics*, 106(4), 044107.

Tian, A., & Du, H. (2014). Enhanced ferroelectric property of manganese doped lead-free $(\text{K}_{0.5}\text{Na}_{0.5})\text{NbO}_3$ ceramics. *Ferroelectrics*, 463(1), 72-77.

Tiwari, V., & Srivastava, G. (2015). The effect of Li_2CO_3 addition on the structural, dielectric and piezoelectric properties of PZT ceramics. *Ceramics International*, 41(2, Part B), 2774-2778.

Tou, T., Hamaguti, Y., Maida, Y., Yamamori, H., Takahashi, K., & Terashima, Y. (2009). Properties of $(\text{Bi}_{0.5}\text{Na}_{0.5})\text{TiO}_3\text{-BaTiO}_3\text{-(Bi}_{0.5}\text{Na}_{0.5})(\text{Mn}_{1/3}\text{Nb}_{2/3})\text{O}_3$ lead-free piezoelectric ceramics and its application to ultrasonic cleaner. *Japanese Journal of Applied Physics*, 48(7S), 07GM03.

Trégouët, H., Caurant, D., Majérus, O., Charpentier, T., Lerouge, T., & Cormier, L. (2017). Exploration of glass domain in the $\text{SiO}_2\text{-B}_2\text{O}_3\text{-La}_2\text{O}_3$ system. *Journal of Non-Crystalline Solids*, 476, 158-172.

Trelcat, J., d'Astorg, S., Courtois, C., Champagne, P., Rguiti, M., & Leriche, A. (2011). Influence of hydrothermal synthesis conditions on BNT-based piezoceramics. *Journal of the European Ceramic Society*, 31(11), 1997-2004.

Turi, E. (2012). *Thermal characterization of polymeric material*. New York: Academic Press.

Amman Ullah, A., Ishfaq, M., Won Ahn, C., Ullah, A., Ehsan Awan, S., & Won Kim, I. (2015). Relaxor behavior and piezoelectric properties of $\text{Bi}(\text{Mg}_{0.5}\text{Ti}_{0.5})\text{O}_3$ -modified $\text{Bi}_{0.5}\text{Na}_{0.5}\text{TiO}_3$ lead-free ceramics. *Ceramics International*, 41(9), 10557-10564.

Vendrell, X., Garcia, J., Cerdeiras, E., Ochoa, D., Rubio-Marcos, F., Fernández, J., & Mestres, L. (2016). Effect of lanthanide doping on structural, microstructural and functional properties of $\text{K}_{0.5}\text{Na}_{0.5}\text{NbO}_3$ lead-free piezoceramics. *Ceramics International*, 42(15), 17530-17538.

Vendrell, X., García, J. E., Bril, X., Ochoa, D. A., Mestres, L., & Dezanneau, G. (2015). Improving the functional properties of $(\text{K}_{0.5}\text{Na}_{0.5})\text{NbO}_3$ piezoceramics by acceptor doping. *Journal of the European Ceramic Society*, 35(1), 125-130.

Vijaya, M. S. (2013). *Piezoelectric materials and devices: applications in engineering and medical sciences*. Boca Raton: Taylor & Francis Group.

Villafuerte-Castrejón, M., Morán, E., Reyes-Montero, A., Vivar-Ocampo, R., Peña-Jiménez, J., Rea-López, S., & Pardo, L. (2016). Towards lead-free piezoceramics: Facing a synthesis challenge. *Materials*, 9(1), 21.

Wang, J., Guo, F., Yang, B., Zhang, S., Zheng, L., Wu, F., & Cao, W. (2018). Electrical properties of $0.94\text{Bi}_{0.5}\text{Na}_{0.5}\text{TiO}_3\text{-}0.06\text{Ba}(\text{Zr}_{0.055}\text{Ti}_{0.945})\text{O}_3$ lead-free ceramics with high thermal stability. *Journal of Materials Science: Materials in Electronics*, 29(3), 2357-2362.

Wang, Y., Yu, E., Yang, H., & Zhang, Q. (2016). Growth behaviour of Li & Sb doped alkali niobate synthesised by hydrothermal method. *Materials & Design*, 110, 51-59.

Wang, Y., Zhang, Q., Hu, L., Yu, E., & Yang, H. (2016). Synthesis of alkalis niobate nanorods and their enhanced piezoelectric properties. *Journal of Alloys and Compounds*, 685, 1-7.

Wang, J., Zhou, Z., & Xue, J. (2006). Phase transition, ferroelectric behaviours and domain structures of $(\text{Na}_{1/2}\text{Bi}_{1/2})_{1-x}\text{TiPb}_x\text{O}_3$ thin films. *Acta Materialia*, 54(6), 1691-1698.

Wang, X. X., Murakami, K., Sugiyama, O., & Kaneko, S. (2001). Piezoelectric properties, densification behaviour and microstructural evolution of low temperature sintered PZT ceramics with sintering aids. *Journal of the European Ceramic Society*, 21(10-11), 1367-1370.

Watcharapasorn, A., Jiansirisomboon, S., & Tunkasiri, T. (2007). Sintering of Fe-doped $\text{Bi}_{0.5}\text{Na}_{0.5}\text{TiO}_3$ at $<1000^\circ\text{C}$. *Materials Letters*, 61(14-15), 2986-2989.

Wei, Q., Zhu, M., Li, L., Guo, Z., Zheng, M., & Hou, Y. (2018). Large electric field induced strain in new lead-free binary $(\text{Bi}_{1/2}\text{Na}_{1/2})\text{TiO}_3\text{-Ba}(\text{Zn}_{1/3}\text{Nb}_{2/3})\text{O}_3$ solid solution. *Journal of Alloys and Compounds*, 731, 631-635.

Wiegand, S., Flege, S., Baake, O., & Ensinger, W. (2012). Influence of different heat treatment programs on properties of sol-gel synthesized $(\text{Na}_{0.5}\text{K}_{0.5})\text{NbO}_3$ (KNN) thin films. *Bulletin of Materials Science*, 35(5), 745-750.

Woo, J. W., Baek, S., Song, T. K., Lee, M. H., Rahman, J. U., Kim, W., Lee, S. (2017). Nonstoichiometric effects in the leakage current and electrical properties of bismuth ferrite ceramics. *Journal of the Korean Ceramic Society*, 54(4), 323-330.

Xie, H., Liu, G., Yang, L., Pang, S., Yuan, C., Zhang, X., Wang, H., Zhou, C. and Xu, J. (2018). Excellent optical, dielectric, and ferroelectric properties of $\text{Sr}(\text{In}_{0.5}\text{Nb}_{0.5})\text{O}_3$ modified $\text{K}_{0.5}\text{Na}_{0.5}\text{NbO}_3$ lead-free transparent ceramics. *Journal of Materials Science: Materials in Electronics*, 29(22), 19123-19129.

Wu, L., Xiao, D., Zhou, F., Teng, Y., & Li, Y. (2011). Microstructure, ferroelectric, and piezoelectric properties of $(1-x-y)\text{Bi}_{0.5}\text{Na}_{0.5}\text{TiO}_3\text{-xBaTiO}_3\text{-yBi}_{0.5}\text{Ag}_{0.5}\text{TiO}_3$ lead-free ceramics. *Journal of Alloys and Compounds*, 509(2), 466-470.

Wu, W., Li, J., Xiao, D., Chen, M., Ding, Y., & Liu, C. (2014). Defect dipoles-driven ferroelectric behavior in potassium sodium niobate ceramics. *Ceramics International*, 40(8), 13205-13210.

Xu, Y., Liu, D., Lai, F., Zhen, Y., & Li, J. (2008). Fabrication of (K, Na) NbO_3 Lead-Free piezoceramic microrod arrays by Sol-Gel processing with micromachined silicon templates. *Journal of the American Ceramic Society*, 91(9), 2844-2847.

Xu, J., Yang, M., Gan, K., Qu, Y., Zhang, X., Ma, N., Yang, J. (2016). Enhanced piezoelectric properties of PZT ceramics prepared by direct coagulation casting via high valence counterions (DCC-HVCI). *Ceramics International*, 42(2), 2821-2828.

Yongsiri, P., Eitssayeam, S., Rujijanagul, G., Sirisoonthorn, S., Tunkasiri, T., & Pengpat, K. (2012). Fabrication of transparent lead-free KNN glass ceramics by incorporation method. *Nanoscale Research Letters*, 7(1), 136.

Yongsiri, P., Sirisoonthorn, S., & Pengpat, K. (2015). Effect of Er_2O_3 dopant on electrical and optical properties of potassium sodium niobate silicate glass-ceramics. *Materials Research Bulletin*, 69, 84-91.

Yuan, Y., Zhao, C., Zhou, X., Tang, B., & Zhang, S. (2010). High-temperature stable dielectrics in Mn-modified $(1-x)\text{Bi}_{0.5}\text{Na}_{0.5}\text{TiO}_3\text{-xCaTiO}_3$ ceramics. *Journal of Electroceramics*, 25(2-4), 212-217.

- Zannen, M., Lahmar, A., Dietze, M., Khemakhem, H., Kabadou, A., & Es-Souni, M. (2012). Structural, optical, and electrical properties of Nd-doped $\text{Na}_{0.5}\text{Bi}_{0.5}\text{TiO}_3$. *Materials Chemistry and Physics*, *134*(2-3), 829-833.
- Zhang, S. T., Kounga, A. B., Aulbach, E., Ehrenberg, H., & Rödel, J. (2007). Giant strain in lead-free piezoceramics $\text{Bi}_{0.5}\text{Na}_{0.5}\text{TiO}_3\text{-BaTiO}_3\text{-K}_{0.5}\text{Na}_{0.5}\text{NbO}_3$ system. *Applied Physics Letters*, *91*(11), 112906.
- Zhao, N., Fan, H., Ren, X., Gao, S., Ma, J., & Shi, Y. (2018). A novel $(\text{Bi}_{0.5}\text{Na}_{0.5})_{0.94}\text{Ba}_{0.06})_{1-x}(\text{K}_{0.5}\text{Nd}_{0.5})_x\text{TiO}_3$ lead-free relaxor ferroelectric ceramic with large electrostrains at wide temperature ranges. *Ceramics International*, *44*(1), 571-579.
- Zheng, H., Pu, Y., Liu, X., & Wan, J. (2016). Correlation between dielectric properties and crystallization treatment in potassium sodium niobate glass-ceramics for energy storage application. *Journal of Alloys and Compounds*, *674*, 272-276.
- Zheng, L., Huo, X., Wang, R., Wang, J., Jiang, W., & Cao, W. (2013). Large size lead-free $(\text{Na}, \text{K})(\text{Nb}, \text{Ta})\text{O}_3$ piezoelectric single crystal: Growth and full tensor properties. *CrystEngComm*, *15*(38), 7718-7722.
- Zheng, M., Hou, Y., Chao, L., & Zhu, M. (2018). Piezoelectric KNN ceramic for energy harvesting from mechanochemically activated precursors. *Journal of Materials Science: Materials in Electronics*, 1-6.
- Zheng, M., Hou, Y., Yan, X., Zhang, L., & Zhu, M. (2017). A highly dense structure boosts energy harvesting and cycling reliabilities of a high-performance lead-free energy harvester. *Journal of Materials Chemistry C*, *5*(31), 7862-7870.
- Zhu, W., Zhu, J., Wang, M., Zhu, B., Zhu, X., & Pezzotti, G. (2012). Raman tensor analysis of $(\text{K}_{0.5}\text{Na}_{0.5})\text{NbO}_3\text{-LiSbO}_3$ lead-free ceramics and its application to study grain/domain orientation. *Journal of Raman Spectroscopy*, *43*(9), 1320-1328.
- Zhu, Y., Zhang, Y., Xie, B., Fan, P., Marwat, M. A., Ma, W., Zhang, H. (2018). Large electric field-induced strain in AgNbO_3 -modified $0.76\text{Bi}_{0.5}\text{Na}_{0.5}\text{TiO}_3\text{-}0.24\text{SrTiO}_3$ lead-free piezoceramics. *Ceramics International*, *44*(7), 7851-7857.
- Zuo, R., Su, S., Wu, Y., Fu, J., Wang, M., & Li, L. (2008). Influence of A-site nonstoichiometry on sintering, microstructure and electrical properties of $(\text{Bi}_{0.5}\text{Na}_{0.5})\text{TiO}_3$ ceramics. *Materials Chemistry and Physics*, *110*(2), 311-315.
- Zuo, R., Wang, M., Ma, B., Fu, J., & Li, T. (2009). Sintering and electrical properties of $\text{Na}_{0.5}\text{K}_{0.5}\text{NbO}_3$ ceramics modified with lanthanum and iron oxides. *Journal of Physics and Chemistry of Solids*, *70*(3-4), 750-754.